

Spectroscopic Determination of Electrostatic and Hydrogen Bonding Interactions in Chemical and Biological Systems

by

Tapas Haldar
10CC16A26031

A thesis submitted to the
Academy of Scientific & Innovative Research
for the award of the degree of

DOCTOR OF PHILOSOPHY
In
SCIENCE

Under the supervision of
Dr. Sayan Bagchi



CSIR-National Chemical Laboratory, Pune

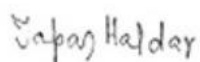


Academy of Scientific and Innovative Research
AcSIR Headquarters, CSIR-HRDC campus
Sector 19, Kamla Nehru Nagar,
Ghaziabad, U.P. – 201 002, India

May, 2021

Certificate

This is to certify that the work incorporated in this Ph.D. thesis entitled, "*Spectroscopic Determination of Electrostatic and Hydrogen Bonding Interactions in Chemical and Biological Systems*", submitted by Tapas Haldar to the Academy of Scientific and Innovative Research (AcSIR) in fulfillment of the requirements for the award of the Degree of *Doctor of Philosophy in Science*, embodies original research work carried-out by the student. We, further certify that this work has not been submitted to any other University or Institution in part or full for the award of any degree or diploma. Research material(s) obtained from other source(s) and used in this research work has/have been duly acknowledged in the thesis. Image(s), illustration(s), figure(s), table(s) etc., used in the thesis from other source(s), have also been duly cited and acknowledged.



Tapas Haldar
(Research Student)

25/5/2021

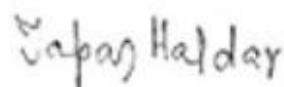


Dr. Sayan Bagchi
(Research Supervisor)

25/5/2021

STATEMENTS OF ACADEMIC INTEGRITY

I Tapas Haldar, a Ph.D. student of the Academy of Scientific and Innovative Research (AcSIR) with Registration No. 10CC16A26031 hereby undertake that, the thesis entitled “Spectroscopic Determination of Electrostatic and Hydrogen Bonding Interactions in Chemical and Biological Systems” has been prepared by me and that the document reports original work carried out by me and is free of any plagiarism in compliance with the UGC Regulations on “*Promotion of Academic Integrity and Prevention of Plagiarism in Higher Educational Institutions (2018)*” and the CSIR Guidelines for “*Ethics in Research and in Governance (2020)*”.



Signature of the Student

Date : 25.05.2021

Place : Pune

It is hereby certified that the work done by the student, under my/our supervision, is plagiarism-free in accordance with the UGC Regulations on “*Promotion of Academic Integrity and Prevention of Plagiarism in Higher Educational Institutions (2018)*” and the CSIR Guidelines for “*Ethics in Research and in Governance (2020)*”.



Signature of the Supervisor

Dr. Sayan Bagchi

Date : 25.05.2021

Place : Pune

*This thesis is dedicated to
My mother, Mrs. Bandana Haldar, & Father, Mr.
Sadhan Chandra Haldar for their endless support
and inspiration.*

Acknowledgments

During the entire period of my doctoral research, I have been acquainted, accompanied, and supported by many people. Herein I take this privilege to express my heartfelt gratitude and appreciation to all of them.

First of all, I would like to express my sincere gratitude to my supervisor, Dr. Sayan Bagchi, for his constant support and guidance throughout this journey. His precious knowledge, wise advice about life, and generous help have significantly shaped the course of my doctoral journey and made me grow, not only as a researcher but also as a wise and responsible human being. I feel immensely privileged to be a part of his esteemed research group at CSIR-National Chemical Laboratory. It is this very place where I have learned to nurture a blend of hard work and discipline to shape my professional and personal aspects of life. Under his supervision and guidance, I have learned not only the art of culturing science but also the art of thinking out of the box. What I have gained and learned from him can never be repaid in any possible form. I believe, a better way of thanking him would be through my future contributions to the scientific community. I would finally say that working with him was a wonderful opportunity in my life.

I would like to sincerely thank my doctoral advisory committee (DAC) members, Dr. Narendra Kadoo, Dr. Santosh Kumar Jha, and Dr. Jayaraj Nithyanandhan, for their constant support extended with guidance and suggestions throughout my Ph.D. I am thankful to the student academic office of NCL for all the support. I acknowledge Dr. Sunita Barve, Mr. Gati Krushna Nayak and other staff members of the library for all kind of support and for giving access to the library. I would also like to thank the staffs who are the part of NCL administrative section for extending their support whenever I required.

I am grateful to Prof. Dr. Ashish K. Lele (Director, CSIR-NCL), Prof. Dr. Ashwini K. Nangia (Former Director, CSIR-NCL), Prof. Dr. Sourav Pal (Former Director, CSIR-NCL), Dr. P. A. Joy (Former HoD, Division of Physical & Materials Chemistry, CSIR-NCL) and Dr. B. L. V Prasad (HoD, Division of Physical & Materials

Chemistry, CSIR-NCL) for giving me this opportunity and providing me with advanced research infrastructure and facilities.

I would also like to thank Prof. Sanjib Bagchi (IISER Kolkata), under the guidance of whom I have completed my M. Sc. Dissertation and gained immense knowledge in fundamental physical chemistry and spectroscopy. I express my special appreciation to Dr. Partha Hazra (IISER Pune), Dr. Suman Chakrabarty (SNBNCBS, Kolkata) for their generous support.

It's my immense pleasure to thank my lab mates Somnath, Pranab, Sushil, Samadhan, Srijan, Deborin da, Kaushik da and Madhumita di for devoting their precious time and providing me with valuable suggestions.

No words are sufficient to acknowledge my prized friends in and out of NCL who have helped me at various stages of my life and my research work. First of all, I don't know how to quantify the amount of love and support I have got from my roommates Tamal Das, Subhrashis Banerjee, Debranjana Mandal, Sajal Maity, Sayantan Acharya to complete this PhD journey. I would love to thank Dr. Achintya Dutta, Dr. Krisahnu Shaw, Dr. Anup Bhuniya, Dr. Saibal Bera, Dr. Subrata Mukherjee, Dr. Sivaprasad Midya, Dr. Manjur Oyasim Akram, Dr. Arunava Maity, Dr. Shantigopal Mondal, Dr. Monoj Nandi, Dr. Bipul Biswas, Dr. Sudip Sashmal, Dr. Atreyee Banerjee, Dr. Suvendu Karak, Kousik Maji, Asish Bera, Pronay Das, Rahul Chowdhury, Sandipan Jana, Himadri Sashmal, Anirban Sen, Amarnath Singham, Swapnil Halnor, Sanjukta Pahar, Pooja Dhorge, Milan Bisai, Anagh Mukherjee, Bittu Chandra, Ujjwal Nandi, Pankaj Shaw, Sutanu Nandi, Abhijeet Bera, Ananta Dey, Dr. Hriday Agarwal, Dr. Atanu Patra, Dr. Santanu Pattanyak for being a valuable part of my NCL family. I really enjoyed the time that I spent with these awesome people.

Without the funding that I have received, this Ph. D. would not have been possible. Hence I would like to express my sincere appreciation to CSIR for fellowship.

Words are inadequate to express my feelings and gratitude to my family for their unconditional love, care, and support throughout my life. I would not have achieved anything without my mom and dad's support, who gave me the freedom to explore my world and explore who I am. With immense gratitude and reverence, I acknowledge my mom, Mrs. Bandana Haldar, and my dad, Mr. Sadhan Chandra Haldar for

shaping my life and making me who I am today. I would also like to give special thanks to my elder brother Mr.Akshay Haldar and my sister Mrs.Anita Sen for their continuous support during my hard times. I would also like to express my sincere thanks to my brother in law Mr. Sanjoy Sen and sister in law, Mrs. Mitradyuti Haldar for his constant inspiration throughout my research journey. I would also to express appreciation to my special friend, Mon, for her tremendous support during my hard time.

My acknowledgement will be incomplete without acknowledging all my teachers who have played important roles in my life. I express my respect and gratitude to them.

I am indebted to the eminent scientific community, whose achievements are a constant source of inspiration for me.

Finally, with immense respect and gratitude, I bow down in front of the almighty for all that has been offered to me. I am and will remain thankful for everything that has ever happened in my PhD journey, the good and the bad, for everything that I have achieved and the few that I have lost. Some were blessings, and some were lessons worth learning.

Tapas Haldar

Table of Contents

Chapter 1	1
1.1 Non-covalent Interactions and its Significance.....	2
1.2 Electrostatics and its Significance	5
1.3 Hydrogen Bonding and its Significance.....	9
1.4 Outline of Thesis	12
1.5 References	17
Chapter 2	24
2.2 Fourier Transform Infrared Spectroscopy (FTIR)	28
2.3 UV-Visible Absorption Spectroscopy.....	30
2.4 Steady-State Fluorescence Spectral Measurement.....	31
2.4.1 Light sources.....	31
2.4.2 Gratings.....	31
2.6 Nuclear Magnetic Resonance (NMR) Spectroscopy	32
2.7 Molecular Dynamic Simulation	33
2.8 References	34
Chapter 3	37
3.1 Introduction	38
3.2 Materials and sample preparation	40
3.3 Results and discussion.....	40
3.3.1 Solvatochromism of Acetone	42
3.3.2 Solvatochromism of Ethyl Acetate	44
3.3.3 Solvatochromism of Conjugated Ketone	46
3.3.4 Explanation of n- π^* Absorption / IR Correlation.....	50
3.3.5 Electric Field / n- π^* Absorption Correlation.....	51
3.3.6 Carbonyl (C=O) H-bond Detection	54
3.4 Conclusion.....	58
3.5 References	59
Chapter 4	64
4.1 Introduction	65
4.2 Materials and sample preparation	67

4.3 Results and discussion.....	69
4.3.1 Cross- Correlation between Independent Spectroscopic Observables for Testosterone	70
4.3.2 Correlation between Independent Spectroscopic Observables with electrostatic Field for Testosterone	73
4.3.3 Estimation of Binding Constant of BSA-Testosterone Complex.....	76
4.3.4 Prediction of Electric Field inside Protein Interior	78
4.4 Conclusion.....	80
4.5 References	81
Chapter 5	84
5.1 Introduction	85
5.2 Materials and sample preparation	86
5.3 Results and discussion.....	86
5.3.1 Origin of $E_T(30)$ parameter	86
5.3.2 Validation of Stark consequence for $E_T(30)$ dye	90
5.4 Summary	104
5. 5 References	105
Chapter 6.....	109
6.1 Introduction	110
6.2 Materials and sample preparation	112
6.3 Results and discussion.....	112
6.3.1 Steady-State Fluorescence Measurements	112
6.3.2 Vibrational Solvatochromism	114
6.3.3 Electric Field-Vibrational Frequency Correlation	118
6.3.4 Fluorescence-IR Frequency Correlation.....	119
6.3.5 Fluorescence- Electric Field Correlation	121
6.3.6 Validation of Fluorescence/Field Correlation	122
6.3.7 Validation of Stark Tuning Rate	124
6.4 Summary	125
6.5 References	125
Chapter 7	131
7.1 Summary	132
7.2 Future Scope.....	133
7.3 References	136

List of Tables

Table 3.1 Absolute values and shifts in $n-\pi^*$ and C=O stretching frequencies of acetone in non-hydrogen-bonding and hydrogen-bonding solvation environments.	44
Table 3.2 Absolute values and shifts in $n-\pi^*$ and C=O stretching frequencies of ethyl acetate in non-hydrogen-bonding and hydrogen-bonding solvation environments.	46
Table 3.3 Absolute values and shifts in $n-\pi^*$ and C=O stretching frequencies of acetophenone (aromatic ketone) in non-hydrogen-bonding and hydrogen-bonding solvation environments.	48
Table 3.4 Absolute values and shifts in $n-\pi^*$ and C=O stretching frequencies of Mesityl oxide (aliphatic conjugated ketone) in non-hydrogen-bonding and hydrogen-bonding solvation environments.	49
Table 3.5 MD estimated electric fields experienced by the carbonyl (C=O) probe of acetone, acetophenone, ethyl acetate, mesityl oxide in different solvation environments.	53
Table 3.6 Comparison of predicted difference dipoles in $n-\pi^*$ transition from IR/ $n-\pi^*$ and field/ $n-\pi^*$ plots.	53
Table 3.7 Absolute values and shifts in emission peak positions of acetone(saturated ketone) in non-hydrogen-bonding and hydrogen-bonding solvation environments.	56
Table 3.8 Absorption and emission peak positions of camphor in different non-H-bonding and H-bonding solvation environments.	57
Table 4.1 $n-\pi^*$ absorption wavelength, C=O stretching frequencies and ^{13}C NMR chemical shifts for testosterone in non-hydrogen bonding and hydrogen bonding solvents	71

Table 4.2 MD estimated and corrected electric fields experienced by the carbonyl for testosterone in pure organic solvents and acetonitrile/water binary mixtures (v/v).	75
Table 5.1 Dipole moment in the ground and excited states, the angle (θ) between ground and the excited state dipole moments, and the change in dipole moment ($\Delta\vec{\mu}$) for the pyridinium N-phenolate betaine dye in different neat organic solvents with varying polarity.	88
Table 5.2 Absolute values of the absorption peak maxima and the MD estimated electric fields along the C-O axis for pyridinium N-phenolate betaine dye in different neat organic solvents with varying polarity.	90
Table 5.3 Absolute values of fluorescence peak maxima and C=O stretching frequencies of coumarin1 in non-hydrogen-bonding and hydrogen-bonding solvation environments.	95
Table 5.4 Absolute values of fluorescence peak maxima and C=O stretching frequencies of PRODAN in non-hydrogen-bonding and hydrogen-bonding solvation environments.	96
Table 5.5 MD estimated and corrected electric fields experienced by the carbonyl for PRODAN in neat organic solvents and dimethyl sulphoxide/water binary mixtures (v/v).	100
Table 6.1 Absolute values of fluorescence peak maxima and C \equiv N stretching frequencies of 4-Cyanoindole in non-hydrogen-bonding and hydrogen-bonding solvation environments.	117
Table 6.2 Absolute values of fluorescence peak maxima and C \equiv N stretching frequencies of 5-Cyanoindole in non-hydrogen-bonding and hydrogen-bonding solvation environments.	118
Table 6.3 Emission maxima ($\bar{\nu}_{emission}$) and nitrile stretch ($\bar{\nu}_{C\equiv N}$) of 5CNI and 4CNI along with predicted electrostatic field ($\vec{F}_{C\equiv N}$) from emission maxima of different micellar interfaces.	124

List of Figures

Figure 1.1 A) Determining the interaction energy between molecules is generally a quantum mechanical problem. However, if we focus on one molecule and consider it as a dipole interacting with the field created by all the other molecules, the chemical picture can be converted into an electrostatic one (B). This figure has been taken from Ref.4. 4

Figure 1.2. The reaction mechanism of catalysis by ketosteroid isomerase. In the first step, Asp40 removes a proton from the steroid to form a dienolate intermediate, stabilized by two H-bonds from Tyr16 and Asp103. This transformation results in an increase of the dipole moment along the C=O bond. E = enzyme; S = substrate; I = intermediate; P = product. This figure has been taken from Ref.29. 7

Figure 1.3. (A) Complex between KSI and the product-like inhibitor, 19-NT, used in this study to probe electric fields in the KSI active site. (B) Plot of 19-NT's C=O peak frequency, $\bar{\nu}_{C=O}$ against the calculated solvent electric field $|\vec{F}_{ext}|$ the C=O group experiences in different solvation environment. (C) The IR spectra of 19-nortestosterone in water (blue) and inside the active site of KSI (red) after binding. (D) Plot of enzymatic unimolecular free energy barrier against the electric field, 19-NT's C=O group experiences in each of the active sites of KSI variants. This figure has been taken from Ref.29. 8

Figure 1.4. Schematic representation of hydrogen bond. 10

Figure 2.1. Representation of vibrational solvatochromism. (A) VSE can be described in terms of anharmonicity. The anharmonic motion on the molecular potential energy surface shows that the bond will be slightly longer in their excited vibrational energy levels and thereby possess a slightly larger dipole moment. On the other hand, for a harmonic oscillator, $|\Delta\vec{\mu}| = 0$. (B) In the presence of an electric field (\vec{F}), both the vibrational energy states (i.e., the ground and the excited vibrational states) are stabilized differently, resulting in a shift in the transition energy (vibrational frequency). Vectors corresponding 26

to $\Delta\vec{\mu}$ (change in dipole moment) parallel, antiparallel, and perpendicular to the external electric field \vec{F}_{ext} are shown in red, blue, and green, respectively.

Figure 2.2: Schematic diagram of Fourier transform infrared (FTIR) spectrophotometer 29

Figure 2.3: Schematic diagram of UV-Visible absorption spectrophotometer. 30

Figure 2.4: Block diagram of a spectrofluorometer. 31

Figure 3.1 Schematic of molecular orbital diagram for a simple carbonyl group containing molecule (acetone). 38

Figure 3.2 (A) Energy diagram representation of the IR transition (a ground state phenomenon) and the $n-\pi^*$ transition (involves ground and excited electronic states). Solvatochromic (B) $n-\pi^*$ electronic absorption spectra and (C) IR absorption spectra of the C=O stretch of acetone in aprotic and protic solvation environments. (D) Shifts of $n-\pi^*$ absorption ($\Delta\bar{\nu}_{n-\pi^*}$) plotted against shifts of C=O IR stretching frequencies ($\Delta\bar{\nu}_{C=O}$) of acetone in different solvation environments. The black line indicates the best-fit line. The regression value (R^2) of the fitted lines is shown in the figure. 39

Figure 3.3 (A) $n-\pi^*$ electronic absorption spectra of ethyl acetate in non-hydrogen-bonding and hydrogen-bonding solvation environments. The polarity increases in the direction of the arrow. (B) Shifts of $n-\pi^*$ absorption ($\Delta\bar{\nu}_{n-\pi^*}$) plotted against shifts of C=O IR stretching frequencies ($\Delta\bar{\nu}_{C=O}$) of ethyl acetate in different solvation environments. The black line indicates the best-fit line. The regression value (R^2) of the fitted lines is shown in the figure. 45

Figure 3.4 (A) $n-\pi^*$ electronic absorption spectra of acetophenone (aromatic ketone) in non-hydrogen-bonding and hydrogen-bonding solvation environments. The solid black curves represent aprotic solvents [(1) hexanes, (2) tetrahydrofuran, (3) valeronitrile, (4) acetonitrile] and the solid red curves represent the fitted peak of acetophenone in aqueous acetonitrile solutions (v/v) [(5) 90% acetonitrile, (6) 80% acetonitrile (7) 70% acetonitrile, (8) 60% acetonitrile]. The polarity increases in the direction of the arrow. (B) Plots of $n-$ 47

π^* frequency shifts ($\Delta\bar{\nu}_{n-\pi^*}$) versus IR frequency shifts ($\Delta\bar{\nu}_{C=O}$) of acetophenone in different pure organic solvents and binary solvent mixtures. The black line indicates the best-fit line. The black solid circles represent aprotic solvents [(1) hexanes, (2) tetrahydrofuran, (3) valeronitrile, (4) acetonitrile] and red solid circles represent aqueous acetonitrile solutions (v/v) [(5) 90% acetonitrile, (6) 80% acetonitrile (7) 70% acetonitrile, (8) 60% acetonitrile, (9) 50% acetonitrile]. The regression values (R^2) of the fitted line is shown in the figure.

Figure 3.5 (A) $n-\pi^*$ electronic absorption spectra of mesityl oxide (aliphatic conjugated ketone) in non-hydrogen-bonding and hydrogen-bonding solvation environments. The solid black curves represent aprotic solvents [(1) hexanes, (2) tetrahydrofuran, (3) valeronitrile, (4) acetonitrile] and solid red curves represent the fitted peak of mesityl oxide in aqueous acetonitrile solutions (v/v) [(5) 90% acetonitrile, (6) 80% acetonitrile (7) 70% acetonitrile, (8) 60% acetonitrile]. The polarity increases in the direction of the arrow. (B) Plots of $n-\pi^*$ frequency shifts ($\Delta\bar{\nu}_{n-\pi^*}$) versus IR frequency shifts ($\Delta\bar{\nu}_{C=O}$) of mesityl oxide in different pure organic solvents and binary solvent mixtures. The black line indicates the best-fit line. The black solid circles represent aprotic solvents [(1) hexanes, (2) tetrahydrofuran, (3) valeronitrile, (4) acetonitrile] and red solid circles represent aqueous acetonitrile solutions (v/v) [(5) 90% acetonitrile, (6) 80% acetonitrile (7) 70% acetonitrile, (8) 60% acetonitrile, (9) 50% acetonitrile]. The regression values (R^2) of the fitted line is shown in the figure.

48

Figure 3.6 Shifts in $n-\pi^*$ absorption wavenumber ($\Delta\bar{\nu}_{n-\pi^*}$) versus shifts in C=O electrostatic fields ($\Delta\vec{F}_{C=O}$) for ethyl acetate, acetone, acetophenone, mesityl oxide. The solid circles represent the $[\Delta\bar{\nu}_{n-\pi^*}, \Delta\vec{F}_{C=O}]$ paired points, and the solid lines denote the best linear fits. The regression values (R^2) of the fitted lines are shown in the figure.

52

Figure 3.7 (A) Normalized fluorescence spectra of the acetone in non-hydrogen-bonding and hydrogen-bonding solvation environments. A:W represents acetonitrile-water solution (v/v). (B) Shifts in $n-\pi^*$ absorption ($\Delta\bar{\nu}_{n-\pi^*}$) versus shifts of emission wavenumber ($\Delta\bar{\nu}_{em}$) for acetone in protic

55

and aprotic solvation environments. Black solid circles represent aprotic solvents [(1) cyclohexane, (2) hexanes, (3) n-pentane, (4) diethyl ether, (5) tetrahydrofuran, (6) valeronitrile, (7) acetonitrile], red solid circles represent aqueous acetonitrile solutions (v/v) [(8) 80% acetonitrile, (9) 60% acetonitrile, (10) 40% acetonitrile, (11) 20% acetonitrile] and blue solid circle represent water. Black line indicates the best-fit line in different non-hydrogen-bonding aprotic solvents. The regression value (R^2) of the best fit equals to 0.97.

Figure 3.8 Experimentally obtained $n-\pi^*$ absorption frequencies of camphor are plotted against the corresponding emission frequencies in aprotic (black) and protic (red) solvation environments. Linear correlation is observed (dashed lines) 58 for ketones in aprotic solvents (non-H-bonded C=O), whereas, a deviation from linearity is observed in protic solvation environment (H-bonded C=O).

Figure 4.1 The absorbance of the amide-I IR band of BSA plotted against different concentrations of the protein (fixed path-length). The black line indicates best fit line. The regression value (R^2) of the fitted line is shown in the figure. The linear correlation verifies Beer-Lambert law and indicates that the 69 protein has not aggregated in the plotted concentration range. The dashed vertical line corresponds to the concentration of the protein at which the IR and UV experimental results of the BSA-testosterone complex have been reported.

Figure 4.2 (A): For carbonyls, the spectroscopic observables of IR spectroscopy, NMR spectroscopy, and UV/VIS absorption spectroscopy change with the solvent polarity. Figure 4.1A represents the shift (and the direction of the shifts) in the observables for testosterone with the varying solvent polarity. 70 (B) Normalized $n-\pi^*$ electronic absorption spectra of testosterone in non-hydrogen-bonding and hydrogen-bonding solvation environments. A:W represents acetonitrile-water solution (v/v). The polarity increases in the direction of the arrow.

Figure 4.3 Linear correlations exist among the three independent spectroscopic observables of testosterone, namely (A) C=O stretching frequency and $n-\pi^*$ 72 wavelength, (B) C=O stretching frequency and ^{13}C chemical shift of the C=O carbon, and (C) $n-\pi^*$ wavelength and ^{13}C chemical shift of the C=O carbon in

hydrogen bonding and non-hydrogen bonding solvents. The black lines denote the best-fit lines, the black circles represent aprotic solvents [(1) DBE, (2) THF, (3) VLN, (4) ACN] and red circles represent protic binary solvent mixtures [(5)A10W, (6)A20W, (7)A30W, (8)A40W, (9)A50W]. The regression values of the fitted lines are shown in the figures.

Figure 4.4 Carbonyl stretching frequency versus electrostatic field field exerted on the C=O of the testosterone calculated by MD simulation of testosterone dissolved in different non-hydrogen bonding and hydrogen bonding solvents. The black solid circles represent aprotic solvents [(1) dibutyl ether, (2) tetrahydrofuran, (3) valeronitrile, (4) acetonitrile] and red solid circles represent aqueous acetonitrile solutions (v/v) [(5) 90% acetonitrile, (6) 80% acetonitrile (7) 70% acetonitrile, (8) 60% acetonitrile, (9) 50% acetonitrile]. The regression values (R^2) of the fitted lines are shown in the figures. The black line denotes best fitted line. The equation for this best fitted line is $\bar{\nu}_{C=O} = 0.603 (F_{C=O}) + 1686.91$.

74

Figure 4.5 Carbonyl stretching frequency (A), $n-\pi^*$ electronic transition and ^{13}C Chemical shifts show linear sensitivities towards the corrected electric field exerted along the C=O bond of testosterone in both non-H-bonding and H-bonding environments. The black solid circles represent aprotic solvents [(1) dibutyl ether, (2) tetrahydrofuran, (3) valeronitrile, (4) acetonitrile] and red solid circles represent aqueous acetonitrile solutions (v/v) [(5) 90% acetonitrile, (6) 80% acetonitrile (7) 70% acetonitrile, (8) 60% acetonitrile, (9) 50% acetonitrile]. The regression values (R^2) of the fitted lines are shown in the figures. The black solid line denotes best fitted line.

76

Figure 4.6 Fluorescence quenching study of the tryptophan residues in BSA by testosterone. (A) Steady-state fluorescence spectra of BSA (10 μM) in 20mM aqueous phosphate buffer (pH 7.2) in the presence of testosterone with the concentration: (a) 0 μM , (b) 5 μM , (c) 7.5 μM , (d)12.5 μM , (e)15 μM , (f)17.5 μM , (g)20.0 μM , (h)22.5 μM . The fluorescence spectra were recorded in the wavelength range of 300-450 nm by exciting BSA at 290 nm. (B) Plot of $F_0/F_0 - F$ versus $1/[\text{Testosterone}]$ for tryptophan fluorescence quenching of the protein

77

by testosterone.

Figure 4.7 A cartoon of BSA-testosterone complex is shown in 4.7A. The protein is shown in green and the substrate is shown in red. (4.7B) The $n-\pi^*$ absorption spectra and (4.7C) the IR spectra of C=O stretch of testosterone in BSA-testosterone complex can be used to estimate the local polarity at the binding site of BSA using electric field (4.7D). The predicted electric fields from UV/VIS and IR experiments are within 0.7 MV/cm (error $\sim 3.5\%$). The dotted vertical lines in 4.7B and 4.7C represent the peak maxima of aprotic solvents and binary aqueous mixtures. The numbers (2, 4, 6, and 8) correspond to those in column 1 of Table 4.1. 79

Figure 5.1 $\pi-\pi^*$ absorption peak maxima plotted against electrostatic field along C-O axis of pyridinium N-phenolate betaine dye in different neat organic solvents (blue solid circles) of varying polarity. The regression values (R^2) of the fitted line is 0.97. The red solid line indicates best fit line. The equation for this best fitted line is $\bar{\nu}_{abs} = 256.1 |\vec{F}_{C=O}| + 9095.3$. 89

Figure 5.2 Molecular structure and abbreviations of the solvatochromic probes used. 91

Figure 5.3 Solvatochromic $\pi-\pi^*$ emission spectra of coumarin 1 (A) and PRODAN (B) in a number of neat organic solvents and water. The polarity increases in the direction of the arrow. 92

Figure 5.4 Solvatochromic IR studies of coumarin1 and PRODAN. (A) Area normalized FTIR absorption spectra of the C=O stretch of coumarin1 in non-hydrogen bonding solvation environments. (B) Fitted IR absorption spectra of the C=O stretch of coumarin1 in neat organic solvents of varying polarity. (C) Representative FTIR spectra of the C=O stretching band of PRODAN dissolved in a number of neat organic solvents at 10 mM concentration. 94

Figure 5.5 Experimentally obtained carbonyl stretching frequency of C1 is plotted against the corresponding emission peak maxima in non-H-bonding (blue line) and H-bonding (red dotted line) solvation environments. Linear correlation is observed (solid blue lines) for C1 in aprotic solvents (non H-bonded C=O), whereas, a deviation from linearity is observed in protic solvation environment 97

(H-bonded C=O). The red circles represent protic binary solvent mixtures [(1) 9:1 (D:W), (2) 4:1 (D:W), (7) 7:3 (D:W), (8) 3:2 (D:W), (9) 1:1 (D:W)].

Figure 5.6 (A) Carbonyl stretching frequency versus electrostatic field exerted on the C=O of the C1 calculated by MD simulation of C1 dissolved in different non-hydrogen bonding and hydrogen bonding solvents. The regression values (R^2) of the fitted lines are shown in the figures. The blue line denotes best fitted line. The equation for this best fitted line is $\bar{\nu}_{C=O} = 0.703 (F_{C=O}) + 1737.6$. (B) Plot of fluorescence peak maxima C1 in different solvation environments compared against the average electrostatic field C=O experiences in each solvents, as calculated by MD simulation. Blue (solid) and red (dotted) lines indicate best fitted line of the Non H-bonded and H-bonded solvents respectively. The red circles represent protic binary solvent mixtures [(1) 9:1 (D:W), (2) 4:1 (D:W), (3) 7:3 (D:W), (4) 3:2 (D:W), (5) 1:1 (D:W)]. The equation of the best fit line for C1 in non H-bonding solvents is $\bar{\nu}_{emission} = 74.8 (F_{C=O}) + 25138$, ($R^2 = 0.987$). 98

Figure 5.7 (A) Experimentally obtained carbonyl stretch of PRODAN is plotted against the corresponding emission peak maxima in non-H-bonding (blue line) solvation environments. Linear correlation is observed (solid blue lines) for PRODAN in aprotic solvents (non-H-bonded C=O). The regression value for best fit line is 0.98. (B) Carbonyl stretching frequency versus electrostatic field exerted on the C=O of the PRODAN calculated by MD simulation of PRODAN dissolved in different non-hydrogen bonding solvents. The regression value for best fit line is 0.99. The blue line denotes best fitted line. The equation for this best fitted line is $\bar{\nu}_{C=O} = 0.636 (F_{C=O}) + 1687.8$. (C) Plot of fluorescence peak maxima PRODAN in different solvation environments compared against the average electrostatic field C=O experiences in each solvents, as calculated by MD simulation. Blue (solid) and red (dotted) lines indicate best fitted line of the Non H-bonded and H-bonded solvents respectively. The red circles represent protic binary solvent mixtures [(1) 9:1 (D:W), (2) 4:1 (D:W), (3) 7:3 (D:W), (4) 3:2 (D:W), (5) 1:1 (D:W), (6) 2:3 (D:W), (7) 1:4 (D:W), (8) water]. The equation of the best fit line for PRODAN in non H-bonding solvents is $\bar{\nu}_{emission} = 377.7 (F_{C=O}) + 24824.2$, ($R^2 =$ 101

0.99).

Figure 5.8 (A) Emission spectra of PRODAN (10 μ M) as a function of HSA concentration. (B) Plot of $1/F-F_0$ versus $1/[HSA]$. (C) Emission spectra of PRODAN-HSA 1:1 complex in buffer and free PRODAN in buffer. (D) The predicted electrostatic fields from both emission and IR experiments are within 0.6 MV/cm. 103

Figure 6.0 Molecular structure and abbreviations of the solvatochromic probes used. The atom numbering is given for 4-cyano indole. 113

Figure 6.1 Solvatochromic π - π^* emission spectra of 4-cyano indole (A) and 5-cyano indole (B) in a number of organic solvents and water. The polarity increases in the direction of the arrow. 114

Figure 6.2 Normalized emission spectra of both (A) 4-cyano indole (λ_{ex} = 300nm) and (B) 5-cyano indole (λ_{ex} = 275nm) in various 8:2, 6:4, 4:6, 2:8 aqueous dimethyl sulphoxide solutions (v/v) (Dotted lines). Normalized emission spectra of both cyano-indoles in DMSO (solid orange line) and water (solid red line) are also shown for comparison. The polarity increases in the direction of the arrow. 115

Figure 6.3 Solvatochromic IR studies of 4-cyano indole. (A) Area normalized FTIR absorption spectra of the $C\equiv N$ stretch of 4-cyanoindole in non-hydrogen bonding solvation environments. (B) Fitted IR absorption spectra of the $C\equiv N$ stretch of 4-cyano indole in pure organic solvents. 116

Figure 6.4 (A) Representative FTIR spectra of the $C\equiv N$ stretching band of 5-cyano indole dissolved in a number of aprotic solvents and water at 10 mM concentration. (B) Representative FTIR spectra of the $C\equiv N$ stretch band of 5-cyanoindole in different DMSO-water (D: W) solutions (dotted lines). IR absorption spectra of the $C\equiv N$ stretch of 5-cyanoindole in DMSO (solid orange line) and water (red solid line) are also displayed for easy comparison. 117

Figure 6.5 Field-frequency calibration curves for (A) 4CNI and (B) 5CNI in H-bonding and non-H-bonding environments. The blue (solid) and red (dotted) 120

lines indicate the best fitted line in non H-bonding and H-bonding solvents respectively. The equations of the best-fit non-H-bonded lines for (A) 4CNI and (B) 5CNI are $\bar{\nu}_{C\equiv N} = -0.20 |\vec{F}_{C\equiv N}| + 2217.6$ ($R^2 = 0.99$) and $\bar{\nu}_{C\equiv N} = -0.40 |\vec{F}_{C\equiv N}| + 2226.8$ ($R^2 = 0.99$) respectively. The field-frequency paired points (red circle) for the nitriles dissolved in DMSO/water binary mixtures (v/v) (H-bonding environments) falls off the best-fit non-H-bonded lines. A linear correlation between C \equiv N stretching frequency and the electrostatic field exerted by the H-bonding environments exists for both the cyano-indoles. The equations of the best fit H-bonded lines for (A) 4CNI and (B) 5CNI are $\bar{\nu}_{C\equiv N} = 0.17 |\vec{F}_{C\equiv N}| + 2210$, ($R^2 = 0.98$) and $\bar{\nu}_{C\equiv N} = 0.27 |\vec{F}_{C\equiv N}| + 2210.9$, ($R^2 = 0.98$) respectively.

Figure 6.6 Experimentally obtained nitrile stretching frequencies of (A) 4CNI and (B) 5CNI are plotted against the corresponding π - π^* emission frequencies in non-H-bonding (blue line) and H-bonding (red line) solvation environments. Linear correlation is observed (solid blue lines) for cyano indoles in aprotic solvents (non-H-bonded C \equiv N), whereas, a deviation from linearity is observed in protic solvation environment (H-bonded C \equiv N).

121

Figure 6.7 Plot of fluorescence peak maxima of 4-cyano indole (A) and 5-cyano indole (B) in different solvation environments compared against the average electrostatic field C \equiv N experiences in each solvents, as calculated by MD simulation. Blue (solid) and red (dotted) lines indicate best fitted line of the Non H-bonded and H-bonded solvents respectively. The equations of the best fit lines for (A) 4-cyano indole and (B) 5-cyano indole in non H-bonding solvents are $\bar{\nu}_{emission} = -158.6 (|F_{C\equiv N}|) + 29072.6$, ($R^2 = 0.994$) and $\bar{\nu}_{emission} = -174.78 (|F_{C\equiv N}|) + 31526.7$, ($R^2 = 0.99$), respectively.

122

Figure 6.8 Shifts in emission wavenumber versus shifts in C=O electrostatic fields for 4-cyano indole (solid blue circle), 5-cyano indole (solid blue square), 6-cyano indole (solid blue triangle), 7-cyano indole (hollow triangle), *N*-acetyl-4-cyano tryptophan (hollow circle), *N*-acetyl-5-cyano indole (hollow square) in various non-hydrogen-bonding solvents. In purely electrostatic environment $\Delta\bar{\nu}_{emission}$ varies linearly with the electric field for various nitrile group

125

containing indole compounds. The black line indicates the best fitted line in non H-bonding solvents. The slope and intercept of best fit line for non H-bonded solvents are $-162.75 \text{ cm}^{-1}/|\text{MV/cm}|$ and 69.869 cm^{-1} respectively. The regression value of the fitted line is 0.98.

Figure 7.1 The empirically proposed Hammett equation is based on the ionization of benzoic acid in water at 25°C and is expressed as, $\log(k_X/k_H) = \rho\sigma_X$. The equation describing the linear correlation between a series of reactions with meta- and para- substituted aromatics and the hydrolysis of benzoic acids with the same substituents is known as the Hammett Equation (A). Ortho isomers do not fall on the line (B).

135

Figure 7.2 Cartoon demonstrating the influence of substituent on carbonyl vibration of acetophenone. In both cases (i.e. electron donating and withdrawing substituents) shown above, the carbonyl(C=O) vibration is a relatively local mode, indicated by the solid circle. The carbonyl group is conjugated with the highly polarizable benzene ring, and electron density can drift from benzene to the carbonyl group under the influence of a substituent. Therefore, the frequency of carbonyl is characteristic of the polarization of the entire benzene molecule.

136

Chapter 1

Introduction

1.1 Non-covalent Interactions and its Significance

Understanding the molecular details of the biological process is of critical consequence to modern biophysics. Most of the drugs are small organic molecules (ligands) that change biological processes by interacting (either through covalent or non-covalent interactions) with biomolecules (i.e. proteins, peptides, etc.). Illuminating the mechanism behind the binding of small ligands to proteins is therefore important in understanding biological process as well as for drug discovery. A fundamental knowledge of the ligand-binding process requires insight into the non-covalent interactions that stabilize a protein-ligand complex as well as the dynamics of the system. In this thesis, we focus on the impact of non-covalent interactions on various biological systems. A major difference between non-covalent interactions and covalent bonds is that no electrons are shared between the participating atoms in case of non-covalent interactions. Therefore non-covalent interactions are somewhat weaker than covalent bonds. The non-covalent interactions play a crucial role in biological systems by influencing the structure, dynamics and function of biomolecules.¹⁻² So understanding non-covalent interactions is essential for a detailed description of the bio-molecular processes.

Non-covalent interactions are ubiquitous in biological systems and play key roles in several processes like host-guest complexation, molecular recognition, nucleic acid base pairing, protein folding, enzyme catalysis, and self-assembly of nano-materials.²⁻⁵ Non-covalent interactions eventuate through a diversity of mechanisms, such as hydrogen bonding (H-bonding),⁶ electrostatic⁷⁻⁸ and hydrophobic interactions,⁹ van der Waals interactions,¹⁰ π - π stacking¹¹⁻¹² and X-H/ π interactions.¹³ Electrostatic

interactions are the Coulombic interactions between two permanently charged molecules, two polar molecules, or a permanently charged molecule and a polar molecule. Van der Waals interactions are weak interactions that happen between all molecules, and are influenced by London dispersion forces. Molecules interact with each other through interactions of permanent dipoles and dipole - induced dipole interactions. The H-bonds are established between a hydrogen (H) atom connected to an electronegative donor atom and a neighboring acceptor atom. H-bonding is a comparatively strong and directional non-covalent interaction, with its magnitude and directionality governed primarily by the electrostatic forces between the donor H-atom and the acceptor atom. The π - π stacking interactions refer to the interactions between aromatic rings containing π orbitals in three prototypical configurations: stacked, edge-to-face, and T-shaped. π - π stacking interactions are weaker than hydrogen bonding interactions. The X-H/ π interactions, in which the hydrogen of a NH or CH group is directed toward the face of an aromatic ring, also make important contributions to biomolecular structure and function. The propensity to understand and predict the interaction is essential because functions of the molecules are influenced by the interaction. However, experimentally it has been extremely problematic for chemists to identify and measure the non-covalent interaction in complex organized systems such as proteins. The most frequently used descriptor is the dissociation constant (K_D), but it lacks of microscopic insight.⁴ Binding constant value describes only the strength with which a ligand is bound to the macromolecules. But K_D value does not recognize what parts of the molecules are accountable for an interaction. To date, fluorescent probes have been extensively employed to interrogate the local polarity in biological cavities through dielectric constant (ϵ) based semi-empirical polarity parameters and scales.¹⁴⁻¹⁷ However, there are some limitations

such as, (a) dielectric constant is a bulk solvent property and cannot define the local microenvironment around the optical probe, and (b) the semi-empirical polarity parameters cannot account for the local specific intramolecular and intermolecular interactions like hydrogen bonding. It has been recently demonstrated that electric field, a fundamental concept from physics, can be the proxy to the local polarity within the biomolecular interior.⁴

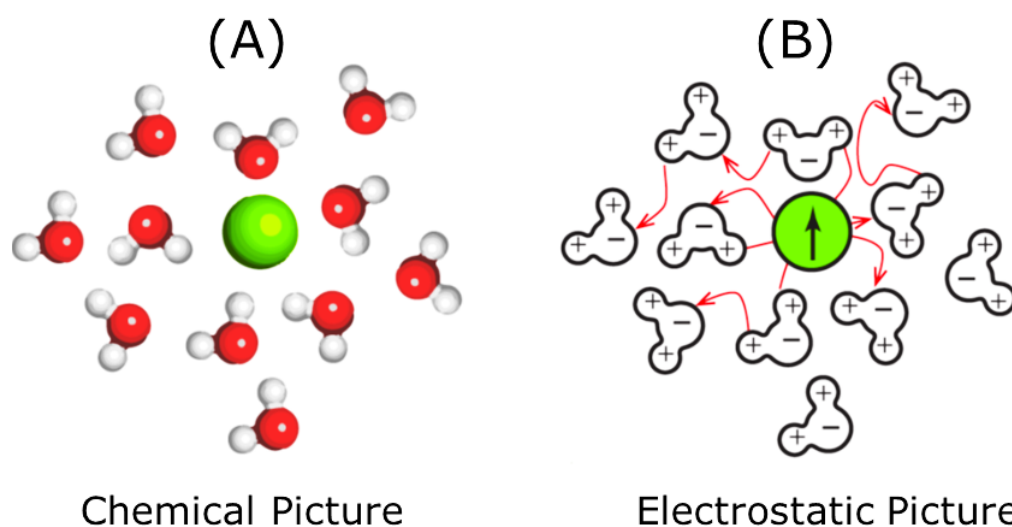


Figure 1.1 A) Determining the interaction energy between molecules is generally a quantum mechanical problem. However, if we focus on one molecule and consider it as a dipole interacting with the field created by all the other molecules, the chemical picture can be converted into an electrostatic one (B). This figure has been taken from Ref.4.

The electric field denotes the field due to the environment of any molecule excluding the atoms constituting the molecule. This is clearly understood from Figure 1.⁴ When dissolved in an aqueous solvent, the solute molecule becomes surrounded by the solvent molecules (Figure 1A). In solution, the solute molecule can be considered a point dipole or a collection of dipoles and the solvent molecules can be considered to create electric fields by their own charges, dipoles, induced dipoles, etc. (Figure 1B).

If the dipole moment of a solute molecule is $\vec{\mu}$ and the environmental field due to the surrounding solvents is \vec{F} , the interaction energy (U) between the solute and the solvents can be written as $U = -\vec{\mu} \cdot \vec{F}$. This simple electrostatic picture of interaction is quantitative and applicable as long as there is no covalent contribution to the interaction. However due to experimental limitations in obtaining a detailed quantitative description on electrostatic interaction field, most of our knowledge had been confined within the limits of theoretical calculations. Recently a wide attention has been drawn into vibrational spectroscopy, as infrared (IR) probes are sensitive reporters of the local electrostatic environments.^{4, 18-21} Vibrational Stark effect (VSE) spectroscopy allows us to predict the electric fields using vibrational probes incorporated into specific protein residues or ligands, providing a quantitative understanding of the non-covalent interactions.^{4, 22}

In this thesis, we have broadly focused on the impacting of electrostatic and H-bonding interactions on the various biological and chemical systems.

1.2 Electrostatics and its Significance

Local electrostatics within protein interiors affects protein's interactions with ligands, substrates, and other proteins, making it a critical determinant of structure, stability and activity.²³⁻²⁵ Also the electrostatic interaction has been extensively examined in understanding the enzyme catalysis.³ Since protein contains charged and polarizable atoms, the electrostatic energy of a group of charges inside the protein cavity or active site of the enzyme is composed of the following two contributions²⁶⁻²⁷:

(i) Charge - charge interaction:

$$V_{QQ} + V_{Qq} = \sum_{i>j} \frac{Q_i Q_j}{r_{ij}} + \sum_{ik} \frac{Q_i q_k}{r_{ik}} \quad [1.1]$$

Where, V represents the interaction energy inside the protein interior, Q and q designates the charges of inside and outside of the protein interior respectively, and r is the distance between the charges. Subscript, i , j and k corresponds to the different interacting atomic charges.

(ii) Inductive interactions between the charges and the induced dipoles on the protein atoms:

$$V_{ind} = -\frac{1}{2} \left[\sum_{i,k} \frac{Q_i \mu_k \vec{r}_{jk}}{r_{ik}^3} + \sum_{j,k} \frac{q_j \mu_k \vec{r}_{jk}}{r_{jk}^3} \right] \quad [1.2]$$

Where, V_{ind} represents the electrostatic potential energy due to the charge-induced dipole interaction on the enzyme active site and μ_k designates the induced dipoles of the system.

The physical basis of the catalytic properties of enzymes has been a fundamental objective in biochemical research. Enzymes catalyze the great majority of biological reactions and enhance the rate of these reactions by orders of magnitude compared to the uncatalyzed reactions. The origins of the enormous catalytic effect of enzymes are still not well known. Using both theoretical and experimental approaches, electrostatic stabilization has been extensively utilized to explain the high catalytic proficiency of enzymes.²⁸ The fundamental concept is that enzyme makes an electrostatic environment within a protein interior that preferentially stabilizes the charge distribution of the transition state (TS) more than that of the substrate to

stimulate the reaction. In this thesis, we will describe on one such example that will encourage us to interpret the significance of electrostatics on molecular function.

Bacterial Δ^5 -3-ketosteroid isomerase (KSI) from *Pseudomonas putida* has been broadly studied for understanding an enzyme catalyzed allylic isomerization reaction which is followed by intramolecular proton transfer.²⁹⁻³¹ KSI catalyzes the enolization process of β , γ - to α , β -unsaturated steroidal ketones via dienolate intermediate (anionic intermediate)³²⁻³³ (Figure2). Using computational method, Warshel et al. revealed that the major contribution towards the origin of large catalytic proficiency of KSI is electrostatics in nature.³⁰

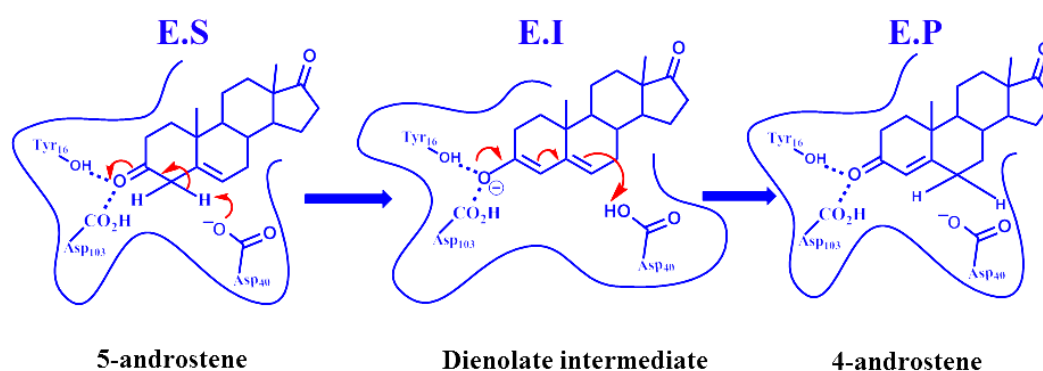


Figure 1.2. The reaction mechanism of catalysis by ketosteroid isomerase. In the first step, Asp40 removes a proton from the steroid to form a dienolate intermediate, stabilized by two H-bonds from Tyr16 and Asp103. This transformation results in an increase of the dipole moment along the C=O bond. E = enzyme; S = substrate; I = intermediate; P = product. This figure has been taken from Ref.29.

Direct experimental evidence of the electrostatic origin of enzyme catalysis in KSI has been demonstrated by Boxer and coworkers using VSE spectroscopy.²⁹ Linear VSE can be described as the linear shift in IR stretching frequencies ($\Delta\bar{\nu}$) of certain vibrations (such as C=O and C \equiv N stretches) with the change in the local electrostatic field ($\Delta\vec{F}$) experienced by a vibrational probe.³⁴⁻³⁷

$$\Delta\bar{\nu} = \Delta\vec{\mu} \cdot \Delta\vec{F} \quad [1.3]$$

Where, $\Delta\vec{\mu}$ is designated as the vibrational difference dipole or stark tuning rate (units of $\text{cm}^{-1}/(\text{MV}/\text{cm})$). The stark tuning rate signifies the sensitivity of the vibrational probe to an external electrostatic field (for details please see chapter 2). Equation 1.3 valid only if the interactions between the vibrational stretching frequency and electric field are electrostatic in nature.

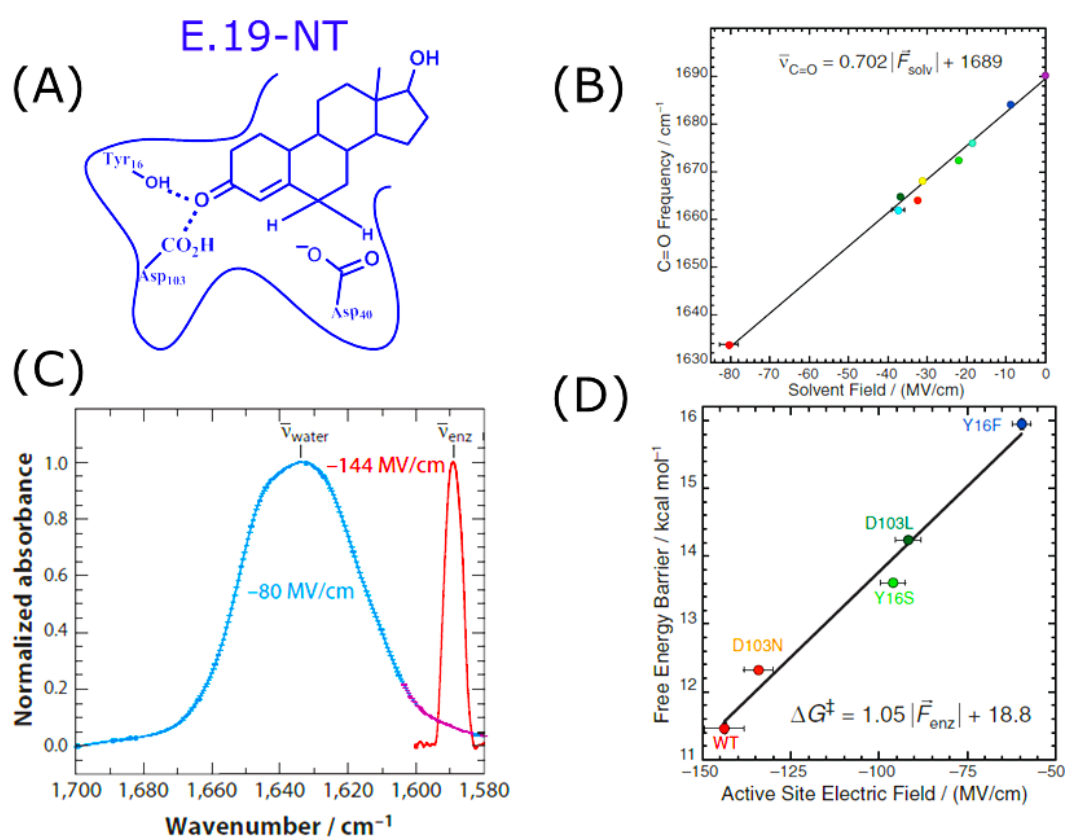


Figure 1.3 (A) Complex between KSI and the product-like inhibitor, 19-NT, used in this study to probe electric fields in the KSI active site. (B) Plot of 19-NT's C=O peak frequency, $\bar{\nu}_{\text{C=O}}$ against the calculated solvent electric field $|\vec{F}_{\text{ext}}|$ the C=O group experiences in different solvation environment. (C) The IR spectra of 19-nortestosterone in water (blue) and inside the active site of KSI (red) after binding. (D) Plot of enzymatic unimolecular free energy barrier against the electric field, 19-NT's C=O group experiences in each of the active sites of KSI variants. This figure has been taken from Ref.29.

Boxer et al. concentrated their study on the inhibitor 19-nortestosterone (19-NT) that binds to the enzyme active site (Figure 3A).²⁹ Although the C=O vibrational probe of 19-NT experiences a similar electrostatic environment as the substrate's C=O bond, 19-NT cannot perform the enzymatic reaction. This provides an inherent advantage to quantitatively measure the extreme electric field exerted on the carbonyl using vibrational solvatochromism and VSS. A calibration curve was obtained to calibrate the sensitivity of the C=O's vibrational frequency to the exerted electrostatic field from the solvation environments (Figure 3B). Using the calibration curve, an extremely large electric field was found to be exerted on the 19NT's C=O when bound to the wild type KSI. Moreover, the C=O bond being extremely narrow when bound to KSI also suggested a rigid environment that greatly reduces the fluctuations in the exerted electric field (Figure 3C). By exploring multiple mutants of KSI, Boxer et al. illustrated that the free energy barrier of the isomerization reaction varies linearly with the electric field (Figure 3D).²⁹ The linear correlation underpinned the intimate relation of the electric fields at the KSI active site to enzyme catalysis. Boxer and coworkers have also manifested in a different pursue that the electrostatic stabilization of TS is not only in KSI, but is also essential for catalytic processes in several other enzymes.³⁸ These results exhibited that local electrostatics executes an important role in molecular functions like enzyme catalysis.

1.3 Hydrogen Bonding and its Significance

Hydrogen-bonds (H-bonds) are ubiquitous specific chemical interactions that play a pivotal role toward molecular structure, function and stability.³⁹⁻⁴² H-bonding, of fundamental relevance in nature, has invaluable contribution to various chemical and biological processes that include molecular recognition, enzyme and organo-catalysis, protein folding, and drug-receptor interactions.^{29, 43-46} Conventional hydrogen bonds are

characterized as D-H...A, where the donor D and the acceptor A are generally very high electronegative (O, N and F are most ordinarily used) than the H (Figure 4).⁶ H-bonds are attractive intermolecular forces that generate due to the dipole-dipole interaction between a H atom that is covalently bound to a more electronegative atom and another highly electronegative atom which lies in the vicinity of the H atom. The H-bonds are weak compared to the covalent or ionic bonds and the dissociation energy of a H-bond varies between 0.5 - 40 kcal/ mol.⁶ The H-bond strength not only depends on the electronic environment around the donor (D) and acceptor (A) atoms but also depends on the geometry of such molecules which is involved in the H-bonding. Using X-ray crystallography and computational study, the geometrical criteria of H-bonding has been concluded which is based on the D-A distance and D-H-A angle cut-off. The D-A distance for H-bonding varies between 2.5- 4.0 Å and the D-H-A angle ranges from 180° to 150° for a H-bond.⁴⁷⁻⁴⁹

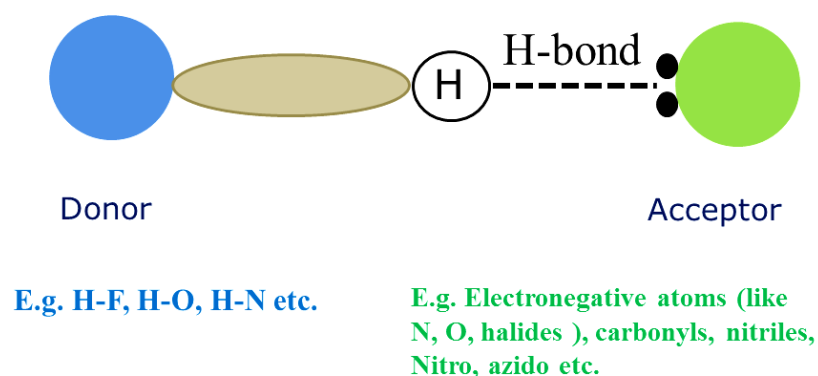


Figure 1.4 Schematic representation of hydrogen bond.

In 1920, the chemical concept of H-bonding is first attributed by Rodebush et.al.⁵⁰ But the physical nature of H-bonding interaction is being widely debated even today in the scientific community. Extensive theoretical researches have revealed different effects

like polarization, charge transfer and dispersion, as well as electrostatic interactions impart to the H-bonding interactions.⁵¹⁻⁵²

Carbonyl (C=O) H-bonds have profound mechanistic roles in many enzymatic and chemical reactions.³⁷ Hydrogen bond networks are exclusively universal within the active site of enzyme, which acts to stabilize the transition state of enzymatic reaction.⁴⁵ C=O H-bonds are play a critical role in stabilizing the enzyme-substrate conformation in the TS of enzymatic reactions. Recently, Boxer and coworkers has been reported that H-bonds in the KSI oxyanion hole provide a significant catalytic contribution through electrostatic interactions (Figure 2).²⁹ The carbonyl employs in short, strong H-bonds with the neighboring Asp103 and Tyr13, when bound to wild type KSI. KSI exerts an extremely large electric field on this C=O bond with a magnitude of 144 MV/cm.⁴⁶ When the reaction proceeds from its ground state to its transition state, the strength of H-bond increases due to the formation of dienolate like intermediate (anionic intermediate), resulting in enhancement of the catalytic power by stabilization of the TS to a large extent.⁴³ A site-directed mutagenesis experiment also proves that catalytic rate of KSI is greatly decreased upon removal of the oxyanion-hole H-bond donors. These results demonstrate that carbonyl H-bonding plays the pivotal role in enzyme catalytic activity.

So, understanding H-bond contributions toward molecular function and subsequent engineering of molecules with novel properties demand a definitive determination of the H-bonding status. X-ray and neutron diffraction methods can determine the exact locations of donor-acceptor groups, but generally assumes predefined standard geometries for H atom position.⁵³⁻⁵⁴ Currently, spectral shifts in NMR, IR, or Raman spectroscopies are utilized to comment on the H-bonding status of a chemical group. Similar spectral shifts arising from a single spectroscopic technique, however, have been

observed for both H-bonded and non-H-bonded scenarios that make the H-bond determination inconclusive. On the other hand, a dual experimental approach correlating shifts from two spectroscopic techniques with different sensitivities to the presence and absence of H-bonds can lead to a successful determination of the H-bonding status. Here, in this thesis we present a dual experimental approach for detection of both carbonyl (C=O) and nitrile (C≡N) H-bonds.

1.4 Outline of Thesis

In this thesis we have used a combination of different spectroscopic methods and molecular dynamic simulations to predict the electrostatic field and also investigate the hydrogen bonding interactions in the chemical and biological system. The organization of the thesis is as follows,

Chapter 2

Chapter 2 describes experimental and computational methods used in this thesis to understand and measure electrostatics interactions.

Chapter 3

Carbonyl $n-\pi^*$ electronic transitions are known to undergo blue shift in polar and hydrogen-bonding solvents. The anomalous solvatochromic blue shift of $n-\pi^*$ electronic transition has been of great interest for a long time, from both theoretical and experimental points of view. This results provides a direct experimental evidence of the anomalous solvatochromic behavior of carbonyl (C=O) $n-\pi^*$ electronic absorption bands, independent of any theoretical approximations. We present an experimental approach involving IR/ $n-\pi^*$ correlations to elucidate the electrostatic interactions are key toward the spectral shifts in both aprotic and protic solvation

environments. In the case of IR, there is a transition between the two vibrational levels in the ground electronic state (ground electronic state phenomenon). But in the case of $n-\pi^*$ electronic transition, there is a vertical transition between the ground and excited electronic state (according to Franck-Condon principle). So linear correlation between the $n-\pi^*$ electronic transition and IR frequency shifts of different carbonyl(C=O) compounds in both non-hydrogen-bonding and hydrogen-bonding solvation environments were observed, which emphasize that electrostatic interactions in the ground electronic state play a key role toward the $n-\pi^*$ blue shifts in carbonyls. Also $n-\pi^*$ shifts show linear sensitivity to calculated electrostatic-fields on carbonyls in both non-hydrogen-bonding and hydrogen-bonding solvation environments. These results support the electrostatic nature of C=O H-bonding interactions. We have also experimentally demonstrated the H-bonding status of the C=O using $n-\pi^*$ /fluorescence correlations. These results evoke the potential for $n-\pi^*$ absorption to quantify local polarity in biomolecules and to probe chemical reactions involving carbonyl activation/stabilization.

Chapter 4

Local electrostatics within protein interiors affects protein's interactions with ligands, substrates, and other proteins, making it a critical determinant of structure, stability and activity. Electrostatic interactions being prevalent in bio-molecular systems, research efforts have focused to quantify and describe local polarity within protein cavities and to further relate that to biological processes. Computational studies are not sufficient to determine the local polarity in protein interiors. In recent years, fluorescent probes have been extensively employed to interrogate the local polarity in biological cavities through dielectric constants or semi-empirical polarity scales. A choice of multiple spectroscopic methods that are not limited by fluorophores, along

with a molecular level description of microscopic polarity involving solute-solvent interactions, would allow more flexibility to pick and choose the experimental technique to determine the local polarity within protein interiors. In this chapter, we have concentrated on the non-invasive spectroscopic methods like infrared (IR) spectroscopy, nuclear magnetic resonance (NMR) spectroscopy, and ultraviolet/visible (UV/VIS) $n-\pi^*$ absorption spectroscopy that provide spectral signatures of the C=O moiety. Moreover, the spectroscopic observables like C=O IR frequencies, ^{13}C NMR chemical shifts of the C=O carbon or $n-\pi^*$ wavelengths are sensitive to the immediate surroundings of the C=O group and therefore should be ideal to report on the local polarity within protein. Here we have presented that excellent linear cross correlation between UV/VIS, IR, and ^{13}C NMR observables of carbonyl compound in various non-hydrogen-bonded as well as hydrogen bonded solvation environments. The local polarity at the binding site of a serum protein has been determined using the absorption wavelength as well as the carbonyl stretching frequency of its natural steroid substrate, testosterone. Excellent agreement is observed in the determined local polarity from two independent spectroscopic techniques. Therefore, we can pick and choose the spectroscopic method based on the molecular process under study.

Chapter 5

Solvatochromic dyes play a key role in the understanding of solvent polarity effects and are increasingly important as probes of complex biological systems. The $E_{\text{T}}(30)$ scale, derived from the electronic absorption of the betaine dye 2,6-diphenyl-4-(2,4,6-triphenylpyridinium-1-yl)phenolate (Reichardt's dye), has been the most widely applied empirical solvent polarity scale. The linear correlation between the emission peak maxima of a fluorophores and the corresponding $E_{\text{T}}(30)$ values in different

solvents allows us to determine the polarity within protein interiors. However, little has been understood regarding the origin of this universal correlation between $E_T(30)$ and almost any existing fluorophore, other than its solvent sensitivity is due to large dipolar difference between ground and excited state. In spite of the scarcity in adequate understanding behind its working principle, it has found its use in detecting polarity of active site of enzyme, solvation difference between minor and major groove of DNA, complex in-homogenous solvation environment inside a reverse micelle to name a few. However, for those distinct environments polarity on the basis of $E_T(30)$ parameter provides a vastly simplistic average picture and is inadequate to capture the micro heterogeneity due to specific interaction of charged and polar groups towards the fluorophore. We therefore need the understanding behind this remarkable solvent sensitivity and manage to find more microscopic details of heterogeneous solvent environment.

Since $E_T(30)$ scale has been derived from the electronic absorption of Reichardt's dye, it is worth investigating whether this semi-empirical polarity scale has electronic Stark effect as its origin. As the electronic absorption shows the characteristic of Stark effect, the electric field with varying solvent polarity should also correlate with the absorption value. In this chapter, a strong linear correlation is observed between $\pi-\pi^*$ absorption peak maxima across various solvation environment and calculated electrostatic field along C-O axis of pyridinium N-phenolate betaine dye using MD simulation.

Using VSE spectroscopy, it has been experimentally illustrated that carbonyl stretching frequencies are linearly sensitive towards the electrostatic field in both non H-bonding and H-bonding environments. If the $E_T(30)$ series is solely due to the sensing of local electrostatic then carbonyl moiety should also show a similar type of correlation between linear IR and fluorescence spectroscopy. In order to test our hypothesis, we have chosen carbonyl probe

containing various fluorophores. In this chapter we have shown that C=O IR absorption energies are linearly correlated with the $\pi \rightarrow \pi^*$ emission energies in aprotic solvents and a distinct deviation from linearity is observed in protic solvation environment. For hydrogen bonded environment, slope of the line changes indicating inherent sensitivity of fluorescence with H-bond. So from this dual experimental approach, we can easily to detect the coumarin1 C=O hydrogen bonding status. We also found that solvent-induced frequency shifts in C=O vibrations of various fluorophores correlate quantitatively with the ensemble-average electric field the C=O group experiences in the various solvation environments, as calculated by MD simulation. Using this fluorescence-electric field correlation, we can easily estimate $\vec{F}_{C=O}$ at the binding site of serum protein, human serum albumin (HSA).

Chapter 6

Nitrile ($C \equiv N$) groups are particularly powerful vibrational probes for investigating protein structure, interaction, and dynamics because it is highly intense, local and absorbs in the convenient region of the IR spectrum and that is useful as directional and sensitive probes of electric field in biological macromolecules. However, prediction of electric field in the biological macromolecule is very complicated using nitrile vibrational probe through IR absorption experiments.

Here in this chapter, we have illustrated that the correlation between nitrile stretching frequencies (ground electronic state phenomenon) and the fluorescence peak maxima (excited electronic state phenomenon) of different nitrile probe containing indole compounds to detect the nitrile H-bonding status. Also the fluorescence peak positions are strongly influenced towards the electric field through electronic stark effect. A strong linear correlation is observed between shifts of emission peak maxima across

non-hydrogen-bonding solvents and electric field calculated along C≡N molecular axis using MD simulation. But the slope of fluorescence/field correlation is changed for hydrogen-bonded solvation environment which indicates inherent sensitivity of fluorescence with specific interaction like hydrogen bonded. So from this fluorescence/field calibration curve, we can easily detect the nitrile hydrogen bonding status and also allows us to estimate $\vec{F}_{C\equiv N}$ using the experimentally measured $\bar{\nu}_{emission}$ in any unknown environment. Here we have experimentally determined $\vec{F}_{C\equiv N}$ along the C≡N bond axis of different cyano-indoles in the micelle-water interface using fluorescence spectroscopy.

This result cumulatively demonstrates that nitrile (C≡N) probes can quantitatively assess the electric fields involved in H-bonding interactions, making them promising for understanding the physical description of key bimolecular processes such as protein-ligand binding and organic catalysis. Also direct detection H-bonds can provide critical information regarding mechanistic understanding of organic and biological reactions.

1.5 References

1. Černý, J.; Hobza, P. Non-covalent interactions in biomacromolecules. *Phys. Chem. Chem. Phys.* **2007**, *9*, 5291-5303.
2. Lehn, J.-M. Supramolecular Chemistry—Scope and Perspectives Molecules, Supermolecules, and Molecular Devices (Nobel Lecture). *Angew. Chem., Int. Ed.* **1988**, *27*, 89-112.
3. Warshel, A.; Sharma, P. K.; Kato, M.; Xiang, Y.; Liu, H.; Olsson, M. H. M. Electrostatic Basis for Enzyme Catalysis. *Chem. Rev.* **2006**, *106*, 3210-3235.

4. Fried, S. D.; Boxer, S. G. Measuring Electric Fields and Noncovalent Interactions Using the Vibrational Stark Effect. *Acc. Chem. Res.* **2015**, *48*, 998-1006.
5. Warshel, A.; Aqvist, J. Electrostatic Energy and Macromolecular Function. *Annu. Rev. Biophys. Biophys. Chem.* **1991**, *20*, 267-298.
6. Arunan, E.; Desiraju, G. R.; Klein, R. A.; Sadlej, J.; Scheiner, S.; Alkorta, I.; Clary, D. C.; Crabtree, R. H.; Dannenberg, J. J.; Hobza, P.; Kjaergaard, H. G.; Legon, A. C.; Mennucci, B.; Nesbitt, D. J. Definition of the hydrogen bond (IUPAC Recommendations 2011). *Pure and Applied Chemistry* **2011**, *83*, 1637-1641.
7. Onsager, L. Electrostatic Interaction of Molecules. *J. Phys. Chem.* **1939**, *43*, 189-196.
8. Zhou, H.-X.; Pang, X. Electrostatic Interactions in Protein Structure, Folding, Binding, and Condensation. *Chem. Rev.* **2018**, *118*, 1691-1741.
9. Meyer, E. E.; Rosenberg, K. J.; Israelachvili, J. Recent progress in understanding hydrophobic interactions. *PNAS* **2006**, *103*, 15739.
10. Israelachvili, J. N. Van der Waals forces in biological systems. *Quarterly Reviews of Biophysics* **1973**, *6*, 341-387.
11. Zhuang, W.-R.; Wang, Y.; Cui, P.-F.; Xing, L.; Lee, J.; Kim, D.; Jiang, H.-L.; Oh, Y.-K. Applications of π - π stacking interactions in the design of drug-delivery systems. *Journal of Controlled Release* **2019**, *294*, 311-326.
12. Wheeler, S. E. Understanding Substituent Effects in Noncovalent Interactions Involving Aromatic Rings. *Acc. Chem. Res.* **2013**, *46*, 1029-1038.
13. Saggi, M.; Levinson, N. M.; Boxer, S. G. Experimental Quantification of Electrostatics in X-H \cdots π Hydrogen Bonds. *J. Am. Chem. Soc.* **2012**, *134*, 18986-18997.

14. Langhals, H. Polarity of Binary Liquid Mixtures. *Angew. Chem. Int. Ed. Engl.* **1982**, *21*, 724-733.
15. Kosower, E. M. The Effect of Solvent on Spectra. I. A New Empirical Measure of Solvent Polarity: Z-Values. *J. Am. Chem. Soc.* **1958**, *80*, 3253-3260.
16. Reichardt, C. Solvatochromic Dyes as Solvent Polarity Indicators. *Chem. Rev.* **1994**, *94*, 2319-2358.
17. Grunwald, E.; Winstein, S. The Correlation of Solvolysis Rates. *J. Am. Chem. Soc.* **1948**, *70*, 846-854.
18. Park, E. S.; Andrews, S. S.; Hu, R. B.; Boxer, S. G. Vibrational Stark Spectroscopy in Proteins: A Probe and Calibration for Electrostatic Fields. *J. Phys. Chem. B* **1999**, *103*, 9813-9817.
19. Thielges, M. C.; Case, D. A.; Romesberg, F. E. Carbon–Deuterium Bonds as Probes of Dihydrofolate Reductase. *J. Am. Chem. Soc.* **2008**, *130*, 6597-6603.
20. Ye, S.; Huber, T.; Vogel, R.; Sakmar, T. P. FTIR analysis of GPCR activation using azido probes. *Nature Chemical Biology* **2009**, *5*, 397-399.
21. Hu, W.; Webb, L. J. Direct Measurement of the Membrane Dipole Field in Bicelles Using Vibrational Stark Effect Spectroscopy. *J. Phys. Chem. Lett.* **2011**, *2*, 1925-1930.
22. Suydam, I. T.; Boxer, S. G. Vibrational Stark Effects Calibrate the Sensitivity of Vibrational Probes for Electric Fields in Proteins. *Biochemistry* **2003**, *42*, 12050-12055.
23. K A Sharp, a.; Honig, B. Electrostatic Interactions in Macromolecules: Theory and Applications. *Annu. Rev. Biophys. Biophys. Chem.* **1990**, *19*, 301-332.
24. Perutz, M. Electrostatic Effects in Proteins. *Science* **1978**, *201*, 1187-1191.

25. Warshel, A. Electrostatic Basis of Structure-Function Correlation in Proteins. *Acc. Chem. Res.* **1981**, *14*, 284-290.
26. Warshel, A.; Levitt, M. Theoretical studies of enzymic reactions: Dielectric, electrostatic and steric stabilization of the carbonium ion in the reaction of lysozyme. *J. Mol. Biol.* **1976**, *103*, 227-249.
27. Warshel, A. Energetics of enzyme catalysis. *Proc. Natl. Acad. Sci. U. S. A.* **1978**, *75*, 5250.
28. Schramm, V. L. Introduction: Principles of Enzymatic Catalysis. *Chem. Rev.* **2006**, *106*, 3029-3030.
29. Fried, S. D.; Bagchi, S.; Boxer, S. G. Extreme electric fields power catalysis in the active site of ketosteroid isomerase. *Science* **2014**, *346*, 1510.
30. Warshel, A.; Sharma, P. K.; Chu, Z. T.; Åqvist, J. Electrostatic Contributions to Binding of Transition State Analogues Can Be Very Different from the Corresponding Contributions to Catalysis: Phenolates Binding to the Oxyanion Hole of Ketosteroid Isomerase. *Biochemistry* **2007**, *46*, 1466-1476.
31. Pollack, R. M.; Thornburg, L. D.; Wu, Z. R.; Summers, M. F. Mechanistic Insights from the Three-Dimensional Structure of 3-Oxo- Δ^5 -steroid Isomerase. *Arch. Biochem. Biophys.* **1999**, *370*, 9-15.
32. Pollack, R. M. Enzymatic mechanisms for catalysis of enolization: ketosteroid isomerase. *Bio.org. Chem.* **2004**, *32*, 341-353.
33. Smith, S. B.; Richards, J. W.; Benisek, W. F. The purification and characterization of delta 5-3-ketosteroid isomerase from *Pseudomonas putida*, a cysteine-containing isomerase. *Journal of Biological Chemistry* **1980**, *255*, 2678-2684.

34. Fafarman, A. T.; Boxer, S. G. Nitrile Bonds as Infrared Probes of Electrostatics in Ribonuclease S. *J. Phys. Chem. B* **2010**, *114*, 13536-13544.
35. Boxer, S. G. Stark Realities. *J. Phys. Chem. B* **2009**, *113*, 2972-2983.
36. Andrews, S. S.; Boxer, S. G. Vibrational Stark Effects of Nitriles I. Methods and Experimental Results. *J. Phys. Chem. A* **2000**, *104*, 11853-11863.
37. Fried, S. D.; Bagchi, S.; Boxer, S. G. Measuring Electrostatic Fields in Both Hydrogen-Bonding and Non-Hydrogen-Bonding Environments Using Carbonyl Vibrational Probes. *J. Am. Chem. Soc.* **2013**, *135*, 11181-11192.
38. Schneider, S. H.; Boxer, S. G. Vibrational Stark Effects of Carbonyl Probes Applied to Reinterpret IR and Raman Data for Enzyme Inhibitors in Terms of Electric Fields at the Active Site. *J. Phys. Chem. B* **2016**, *120*, 9672-9684.
39. Berman, H. M. Hydrogen bonding in biological structures. *Biophys. J.* **1993**, *64*, 1976-1976.
40. Thomson, B.; Both, J.; Wu, Y.; Parrish, R. M.; Martínez, T. J.; Boxer, S. G. Perturbation of Short Hydrogen Bonds in Photoactive Yellow Protein via Noncanonical Amino Acid Incorporation. *J. Phys. Chem. B* **2019**, *123*, 4844-4849.
41. Oltrogge, L. M.; Boxer, S. G. Short Hydrogen Bonds and Proton Delocalization in Green Fluorescent Protein (GFP). *ACS Cent. Sci.* **2015**, *1*, 148-156.
42. Panigrahi, S. K.; Desiraju, G. R. Strong and weak hydrogen bonds in the protein–ligand interface. *Proteins: Structure, Function, and Bioinformatics* **2007**, *67*, 128-141.
43. Fried, S. D.; Boxer, S. G. Electric Fields and Enzyme Catalysis. *Annual Review of Biochemistry* **2017**, *86*, 387-415.

44. Wu, Y.; Fried, S. D.; Boxer, S. G. Dissecting Proton Delocalization in an Enzyme's Hydrogen Bond Network with Unnatural Amino Acids. *Biochemistry* **2015**, *54*, 7110-7119.
45. Levinson, N. M.; Boxer, S. G. A conserved water-mediated hydrogen bond network defines bosutinib's kinase selectivity. *Nat Chem Biol* **2014**, *10*, 127-132.
46. Sigala, P. A.; Fafarman, A. T.; Schwans, J. P.; Fried, S. D.; Fenn, T. D.; Caaveiro, J. M. M.; Pybus, B.; Ringe, D.; Petsko, G. A.; Boxer, S. G.; Herschlag, D. Quantitative dissection of hydrogen bond-mediated proton transfer in the ketosteroid isomerase active site. *Proc. Natl. Acad. Sci. U. S. A.* **2013**, *110*, E2552.
47. Torshin, I. Y.; Weber, I. T.; Harrison, R. W. Geometric criteria of hydrogen bonds in proteins and identification of 'bifurcated' hydrogen bonds. *Protein Engineering, Design and Selection* **2002**, *15*, 359-363.
48. Kabsch, W.; Sander, C. Dictionary of protein secondary structure: Pattern recognition of hydrogen-bonded and geometrical features. *Biopolymers* **1983**, *22*, 2577-2637.
49. Grabowski, S. J. Hydrogen bonding strength—measures based on geometric and topological parameters. *J. Phys. Org. Chem.* **2004**, *17*, 18-31.
50. Latimer, W. M.; Rodebush, W. H. Polarity and Ionization from the Standpoint of the Lewis Theory of Valence. *J. Am. Chem. Soc.* **1920**, *42*, 1419-1433.
51. Rendell, A. P. L.; Bacskay, G. B.; Hush, N. S. The validity of electrostatic predictions of the shapes of van der Waals dimers. *Chem. Phys. Lett.* **1985**, *117*, 400-408.
52. Grabowski, S. J. What Is the Covalency of Hydrogen Bonding? *Chem. Rev.* **2011**, *111*, 2597-2625.

53. Fucke, K.; Steed, J. W. X-ray and Neutron Diffraction in the Study of Organic Crystalline Hydrates. *Water* **2010**, *2*.
54. Nishiyama, Y.; Langan, P.; Chanzy, H. Crystal Structure and Hydrogen-Bonding System in Cellulose I β from Synchrotron X-ray and Neutron Fiber Diffraction. *J. Am. Chem. Soc.* **2002**, *124*, 9074-9082.

Chapter 2

Experimental and Computational Methods

2.1 Vibrational Stark Effect Spectroscopy

Vibrational Stark effect (VSE) spectroscopy has been successfully exploited to experimentally determine electrostatic interaction via quantitative estimation of the environment's electric field (\vec{F}).¹ An electric field is a vector quantity; it has both magnitude and direction. According to Coulomb's law², the magnitude of \vec{F} created by point charge (q) at a particular distance r in a vacuum is given by,

$$\vec{F} = \frac{q}{4\pi\epsilon_0 r^2} \vec{r} \quad [2.1]$$

where ϵ_0 is the dielectric constant of the medium.

To explain the vibrational Stark effect, we have chosen the molecular potential energy curve for a diatomic system such as CO (Figure2A). Since these potential energy curves are anharmonic, the bond length of a diatomic oscillator at the excited vibrational energy states is larger than that in the vibrational ground state (Figure2.1A).¹ For diatomic oscillators (CO) that possess a charge separation, the increase in the bond length results in a consequent increase in the dipole moment ($\vec{\mu}$). The two energy levels having different dipole moments will be stabilized to a different extent in the presence of an external field (\vec{F}_{ext}). In the presence of an external electric field, the energy gap between the ground and first excited vibrational states is modified by the scalar product of $\Delta\vec{\mu}$ and \vec{F}_{ext} vectors, i.e., $|\vec{F}||\Delta\vec{\mu}| \cos\theta$.³ Here θ is the angle between the vector representing the change in dipole moment ($\Delta\vec{\mu}$) and the direction of the external electric field (\vec{F}_{ext}). If $\Delta\vec{\mu}$ of the diatomic oscillator is oriented parallel to \vec{F}_{ext} (i.e. $\theta = 0^\circ$, $\cos\theta = 1$), the energy gap decreases and the band is shifted to the red. If the $\Delta\vec{\mu}$ is oriented perpendicular to \vec{F}_{ext} (i.e. $\theta = 90^\circ$, $\cos\theta = 0$), the energy levels will remain the same as in the absence of an external field. Finally, if the $\Delta\vec{\mu}$ is oriented antiparallel to \vec{F}_{ext} (i.e. $\theta = 180^\circ$, $\cos\theta = -1$), the

energy gap increases and the band is shifted towards the blue. Therefore, the applied electric field is capable of producing a shift in the vibrational transition energy, referred to as the vibrational Stark effect in this thesis.

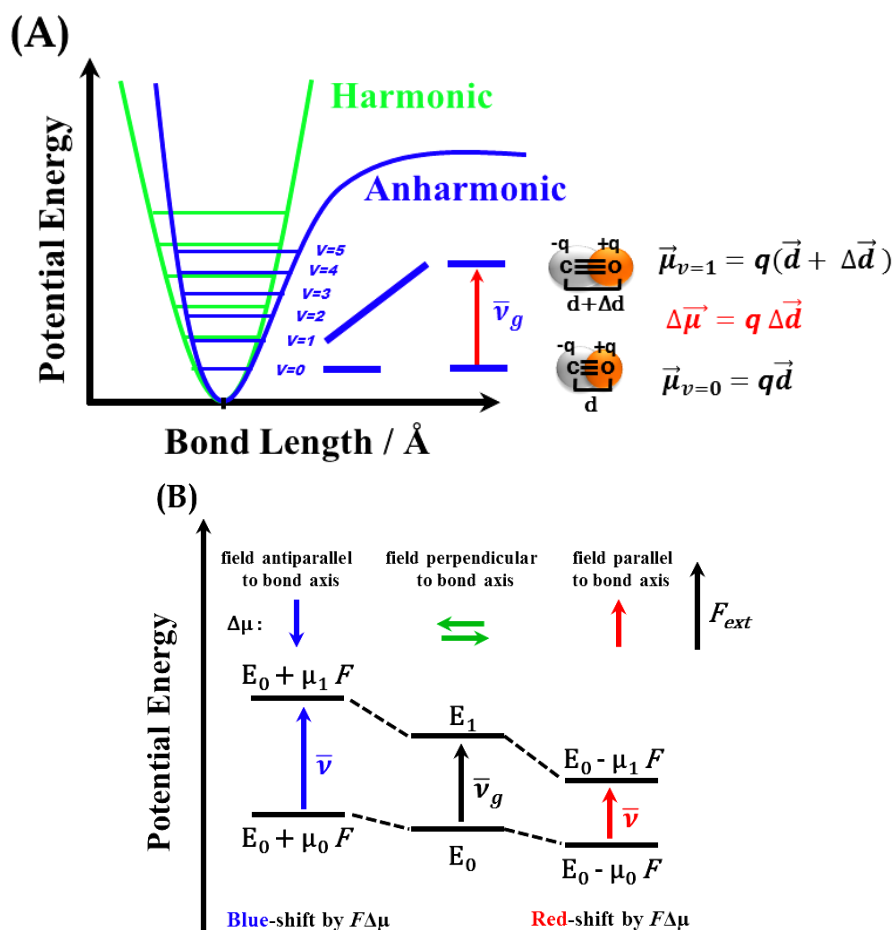


Figure 2.1. Representation of vibrational solvatochromism. (A) VSE can be described in terms of anharmonicity. The anharmonic motion on the molecular potential energy surface shows that the bond will be slightly longer in their excited vibrational energy levels and thereby possess a slightly larger dipole moment. On the other hand, for a harmonic oscillator, $|\Delta\vec{\mu}| = 0$. (B) In the presence of an electric field (\vec{F}), both the vibrational energy states (i.e., the ground and the excited vibrational states) are stabilized differently, resulting in a shift in the transition energy (vibrational frequency). Vectors corresponding to $\Delta\vec{\mu}$ (change in dipole moment) parallel, antiparallel, and perpendicular to the external electric field \vec{F}_{ext} are shown in red, blue, and green, respectively.

Since infrared (IR) spectroscopy probes the energy difference between the ground and the first excited vibrational state, the changes in the energy gap are observed as a shift in the vibrational frequency in electric field-dependent IR study. The vibrational Stark effect describes the linear dependence between the vibrational frequency shifts ($\Delta\bar{\nu}$) and the difference in electrostatic field ($\Delta\vec{F}$).³

$$\Delta\bar{\nu} = -(\Delta\vec{\mu} \cdot \Delta\vec{F}) \quad [2.2]$$

where, $\Delta\vec{\mu}$ is known as the Stark tuning rate, which gives the intrinsic sensitivity of the vibrational transition to an external electric field and can be expressed either in the unit of Debye or in the unit of $\text{cm}^{-1}/(\text{MV}/\text{cm})$. The latter unit corresponds to the IR frequency shift (in cm^{-1}) accompanied by the application of a unit electric field (1 MV/cm) projected along the vibrational axis. In vibrational Stark spectroscopy (VSS), the molecule containing the vibration of interest is dissolved in a glass-forming solvent [e.g., 2-methyl tetrahydrofuran (2-MeTHF)].⁴ The filled sample cell is rapidly immersed into liquid nitrogen.⁴ IR absorption spectrum of the sample is measured both in the presence and absence of the applied electric field. By analyzing small differences between the IR absorption spectra, $\Delta\vec{\mu}$ is estimated. Once the Stark tuning rate is determined, we can easily predict the site-specific electric field experienced by a vibrational probe from the surroundings using simple IR absorption experiments.

A method, easier than VSS, to determine the vibrational probe's sensitivity to the surrounding environments utilizes vibrational solvatochromism, where the molecule is dissolved in solvents of various polarities. The vibrational frequencies and the transition dipole moments of the vibrational probes are strongly affected by the local electric field (or solvent reaction field) generated by the surrounding solvent molecules.⁵⁻⁶ Common empirical models (such as the Onsager reaction field model⁷⁻⁸)

exist to specify the solvent electric field.⁹ However, the limitation of Onsager reaction field theory is that it does not consider the specific chemical interactions like hydrogen bonding. So another model is required which can provide more accurate field values inclusive of any specific interactions. Boxer and co-workers have developed a new method using an atomistic approach to calculate solvation fields by MD simulation.¹⁰ Correlating the solvent-by-solvent vibrational frequency shift for an individual solute against the average solvent electrostatic field calculated along the vibrational axis using MD simulation for each solvent has given a linear field-frequency correlation which is conceptually similar to that predicted by the vibrational Stark effect.¹⁰ In this thesis, we have determined the electrostatic interactions inside the biological systems using the solvatochromic approach.

2.2 Fourier Transform Infrared Spectroscopy (FTIR)

In FTIR, the frequencies from an infrared source are moderated using an interferometer. The source energy passes through a beam splitter in the interferometer, which splits it into two perpendicular beams, one undeflected and the other reflected at a 90° angle (Figure 2.2). The reflected beam goes to the fixed mirror and is returned to the beam splitter. The undeflected beam travels toward the moving mirror and is also comes back to the beam splitter. The motion of the mirror changes the path length of the second beam. When the two separate beams meet at the beam splitter, they recombine, but the two beams' path lengths are different, which cause both constructive and destructive interferences. The merged beam containing these interference motifs, referred to as an interferogram, which is finally directed at the sample position. After it passes through the sample, the sample simultaneously absorbs all of the wavelengths or frequencies. The modified interferogram signal that

reaches the detector contains information about the amount of energy absorbed at every wavelength. The time-domain interferogram obtained in the FTIR experiment can be converted to the frequency-domain signal (spectrum) by performing the Fourier transformation. IR absorption spectra mentioned in this thesis were recorded on a FTIR-Brucker Vertex 70 spectrometer with 2 cm^{-1} resolution at room temperature. For each sample, ~90 microliters of the sample solution were loaded into a demountable cell consisting of two windows (CaF_2 , 3 mm thickness, Shenzhen Laser Co. Ltd.), separated by a mylar spacer of 56 micrometers thickness. Each sample was dissolved independently in aprotic solvents and protic binary aqueous mixtures such that the final concentration of the liquid sample is 10 mM for the IR studies. A schematic diagram of a Fourier transform infrared spectrophotometer (FTIR) is shown in Figure 2.2.

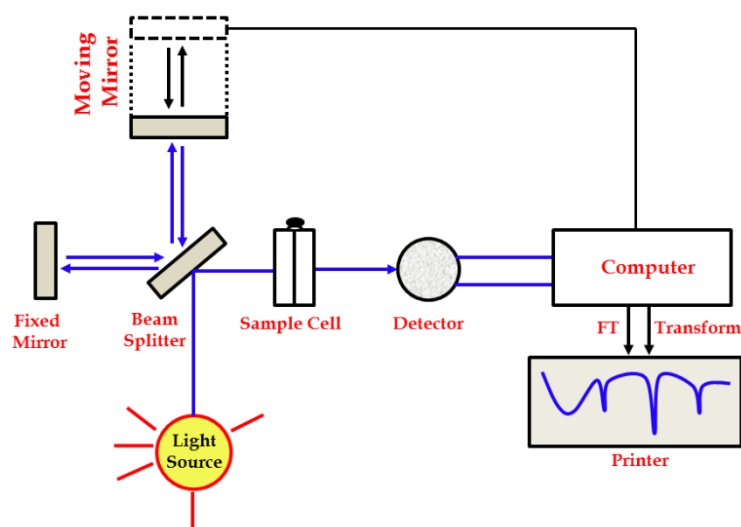


Figure 2.2: Schematic diagram of Fourier transform infrared (FTIR) spectrophotometer

2.3 UV-Visible Absorption Spectroscopy

All the steady-state absorption spectral measurements were performed in a Shimadzu UV 3600 Plus spectrophotometer using a quartz cuvette of 1 cm optical path length. A tungsten lamp has been used for the visible light source, and a deuterium lamp is utilized for the UV region. All the absorption measurements were performed using dilute solutions (ensured by $OD < 0.1$ at the excitation wavelength) to avoid aggregation and re-absorption effects. A schematic diagram of this spectrophotometer has been shown in figure 2.3.

For UV or visible absorption measurement instruments, the spectrophotometer has the following components:

- i. Light sources (UV and visible)
- ii. Wavelength selector (monochromator)
- iii. Sample containers
- iv. Detector
- v. Signal processor and readout.

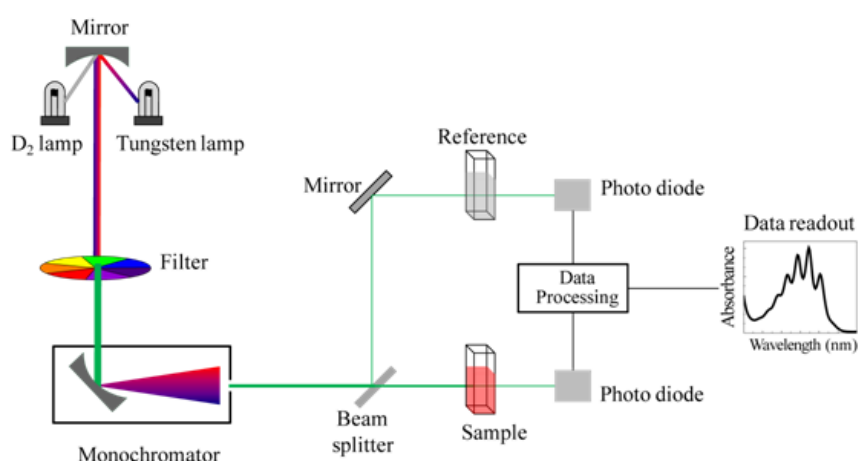


Figure 2.3: Schematic diagram of UV-Visible absorption spectrophotometer.

2.4 Steady-State Fluorescence Spectral Measurement

The steady-state fluorescence was measured in a calibrated Spectrofluorometer FS5 (Edinburgh Instruments) using quartz cell of 1 cm path length. A schematic diagram of the spectrofluorimeter is shown below (Figure 2.4)

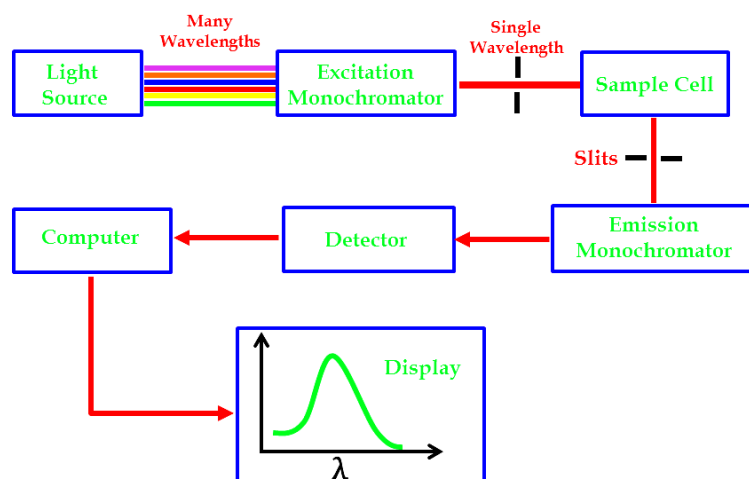


Figure 2.4: Block diagram of a spectrofluorometer.

2.4.1 Light sources

In the spectrofluorometer, gas discharge lamps like xenon lamps and high-pressure mercury lamps are commonly utilized, but there are also some other lamps like incandescent lamps (tungsten lamp), laser (tunable dye laser), etc.

2.4.2 Gratings

The monochromator, in most of the spectrofluorometer use diffraction gratings rather than prisms. The performance specifications of a monochromator include dispersion, efficiency, and stray light levels. Dispersion is usually given in nm/mm. The slit width is expressed in mm. A monochromator for fluorescence spectroscopy should have low stray light levels to avoid scattered or stray light problems.

2.6 Nuclear Magnetic Resonance (NMR) Spectroscopy

NMR spectroscopy is a commonly used spectroscopic technique that evaluates atoms and molecules' physical and chemical properties. NMR can provide detailed information about the structure, dynamics, reaction state, and molecules' chemical environment. The wide range of NMR spectroscopy applications to the study of proteins and nucleic acids has delivered specific information on these systems' dynamics and chemical kinetics. The most crucial feature of NMR spectroscopy is that it imparts information, at the atomic level, on the dynamics of proteins and nucleic acids in a wide range of time scales, ranging from seconds to pico-seconds. Besides, NMR can also provide atomic-level structural information of proteins and nucleic acids in solution. The methods depend on the intrinsic spin properties of nuclei. Nuclei spins are first exposed to a strong and constant magnetic field provided by the superconducting magnet, and then they are excited by a radiofrequency pulse sequence. The magnetic field's stability is achieved by the deuterium lock system, where a deuterated solvent is used to prepare the solution. The precession of the spins is recorded during the free induction decay of the NMR experiment and converted into a frequency spectrum after Fourier transformation. The spin properties of nuclei are susceptible to the surrounding environments, such as a change in electron density or hydrogen bonding interactions. The nuclei's sensitivity to both electrostatic contribution and hydrogen binding allows us to use this combination of IR-NMR spectroscopy to investigate the physical nature of hydrogen bond interaction. The ^{13}C NMR spectra of carbonyl compounds in different solvents are recorded on a 400 MHz JEOL ECX NMR spectrometer. To get an accurate chemical shift, final ^{13}C NMR spectra corrected based on the reference solvent ^{13}C chemical shift.

2.7 Molecular Dynamic Simulation

Molecular dynamics (MD) simulations (reported in this thesis) were carried out using the GROMACS¹¹⁻¹² (version: 4.6.5) software, and General AMBER force field (GAFF)¹³ was used to model vibrational probe (C=O, C≡N, etc.) containing ligand molecule. The force field parameters for all non-aqueous solvent molecules were obtained from virtualchemistry.org,¹⁴ which have been thoroughly tested and benchmarked for reliability. TIP3P water model¹⁵ was used in the simulations involving water molecules. A single vibrational probe containing solute molecule was solvated in 5 nm cubic box of the respective solvent molecule. Before each simulation, an energy minimization using the steepest descent algorithm was performed, followed by the equilibration in NVT ensemble at 300 K temperature for 100 ps using the velocity rescale thermostat,¹⁶ and equilibration in NPT ensemble at 300 K temperature and 1 bar pressure (using Parrinello-Rahman barostat¹⁷) for 1 ns. The coordinates were recorded for a 10-ns MD production run, with positions and forces on each atom being saved at every 0.2 ps and used for calculations of the average electric field exerted on the vibrational bond axis of the vibrational probe containing the solute molecule.

The electric field ($F_{C=O}$) exerted onto the C=O bond of acetone molecule by the environment was calculated by projecting the total electrostatic field due to the rest of the system onto the C=O bond vector following the same protocol as used by Boxer and co-workers.¹⁰ The equations used to define ($F_{C=O}$) are the following,

$$\vec{f}_{i, \text{electro}} = \vec{f}_{i, \text{total}} - \vec{f}_{i, \text{nonelectro}} \quad [2.3]$$

$$\vec{F}_i = \vec{f}_{i, \text{electro}} / q_i \quad [2.4]$$

$$F_{C=O} = \frac{1}{2} \langle \vec{F}_C \cdot \vec{\mu}_{CO} + \vec{F}_O \cdot \vec{\mu}_{CO} \rangle \quad [2.5]$$

Where i is indexed over the C-atom, and the O-atom of the C=O probe and \vec{F}_i designates the electrostatic field and $\vec{f}_{i, electro}$ designates total electrostatic (Coulomb) force applied on the i^{th} reference atom (C and O atoms of the C=O bond for acetone molecule), and q_i designates the partial charge acquired from the force field. $\vec{\mu}_{CO}$ is the unit vector across the C=O vibrational bond axis. Thus, the reported \vec{F}_{CO} or \vec{F}_{vib} values were averaged over both the C and O atoms and over the configurational ensemble across the MD trajectory until convergence was attained. For complete generality and consistent investigation of the electric field, the total exerted electric field was evaluated from the full solvation system.

2.8 References

1. Fried, S. D.; Boxer, S. G. Measuring Electric Fields and Noncovalent Interactions Using the Vibrational Stark Effect. *Acc. Chem.Res.* **2015**, *48*, 998-1006.
2. Halliday, D.; Resnick, R.; Walker, J. *Fundamentals of Physics, Extended 7th Edition.* **2004**; p 1328.
3. Boxer, S. G. Stark Realities. *J. Phys. Chem. B* **2009**, *113*, 2972-2983.
4. Suydam, I. T.; Boxer, S. G. Vibrational Stark Effects Calibrate the Sensitivity of Vibrational Probes for Electric Fields in Proteins. *Biochemistry* **2003**, *42*, 12050-12055.
5. Choi, J.-H.; Cho, M. Vibrational solvatochromism and electrochromism of infrared probe molecules containing C≡O, C≡N, C=O, or C-F vibrational chromophore. *J. Chem. Phys.* **2011**, *134*, 154513.

6. Liptay, W. Electrochromism and Solvatochromism. *Angew. Chem., Int. Ed.* **1969**, *8*, 177-188.
7. Bagchi, S.; Fried, S. D.; Boxer, S. G. A Solvatochromic Model Calibrates Nitriles' Vibrational Frequencies to Electrostatic Fields. *J. Am. Chem. Soc.* **2012**, *134*, 10373-10376.
8. Fafarman, A. T.; Sigala, P. A.; Herschlag, D.; Boxer, S. G. Decomposition of Vibrational Shifts of Nitriles into Electrostatic and Hydrogen-Bonding Effects. *J. Am. Chem. Soc.* **2010**, *132*, 12811-12813.
9. Fried, S. D.; Wang, L.-P.; Boxer, S. G.; Ren, P.; Pande, V. S. Calculations of the Electric Fields in Liquid Solutions. *J. Phys. Chem. B* **2013**, *117*, 16236-16248.
10. Fried, S. D.; Bagchi, S.; Boxer, S. G. Measuring Electrostatic Fields in Both Hydrogen-Bonding and Non-Hydrogen-Bonding Environments Using Carbonyl Vibrational Probes. *J. Am. Chem. Soc.* **2013**, *135*, 11181-11192.
11. Van Der Spoel, D.; Lindahl, E.; Hess, B.; Groenhof, G.; Mark, A. E.; Berendsen, H. J. C. GROMACS: Fast, flexible, and free. *Journal of Computational Chemistry* **2005**, *26*, 1701-1718.
12. Hess, B.; Kutzner, C.; van der Spoel, D.; Lindahl, E. GROMACS 4: Algorithms for Highly Efficient, Load-Balanced, and Scalable Molecular Simulation. *J. Chem. Theory Comput.* **2008**, *4*, 435-447.
13. Wang, J.; Wolf, R. M.; Caldwell, J. W.; Kollman, P. A.; Case, D. A. Development and testing of a general amber force field. *Journal of Computational Chemistry* **2004**, *25*, 1157-1174.
14. van der Spoel, D.; van Maaren, P. J.; Caleman, C. GROMACS molecule & liquid database. *Bioinformatics* **2012**, *28*, 752-753.

15. Horn, H. W.; Swope, W. C.; Pitner, J. W.; Madura, J. D.; Dick, T. J.; Hura, G. L.; Head-Gordon, T. Development of an improved four-site water model for biomolecular simulations: TIP4P-Ew. *J. Chem. Phys.* **2004**, *120*, 9665-9678.
16. Bussi, G.; Donadio, D.; Parrinello, M. Canonical sampling through velocity rescaling. *J. Chem. Phys.* **2007**, *126*, 014101.
17. Parrinello, M.; Rahman, A. Polymorphic Transitions in Single Crystals: A New Molecular Dynamics Method. *Journal of Applied Physics* **1981**, *52*, 7182-7190.

Chapter 3
Electrostatic Interactions Are Key to
C=O n- π^* Shifts: An Experimental
Proof

3.1 Introduction

Solute-solvent interactions are known to have remarkable effects on the behavior of molecular systems. In the near-ultraviolet (UV) region, anomalous solvatochromic shifts of carbonyl (C=O) $n\text{-}\pi^*$ electronic absorption bands to shorter wavelengths with increasing solvent polarity were first reported in the 1920s.¹ The bands arising from $n\text{-}\pi^*$ absorption may be distinguished easily from those arising from $\pi\text{-}\pi^*$ absorption by a large blue shift on changing the solvent polarity. An $n\text{-}\pi^*$ electronic transition involves the promotion of a non-bonding (n) electron from the lone pair orbital (symmetric to the molecular plane) of C=O oxygen to a vacant anti-bonding π^* molecular orbital (anti-symmetric to the molecular plane) (Figure 3.1).²⁻³

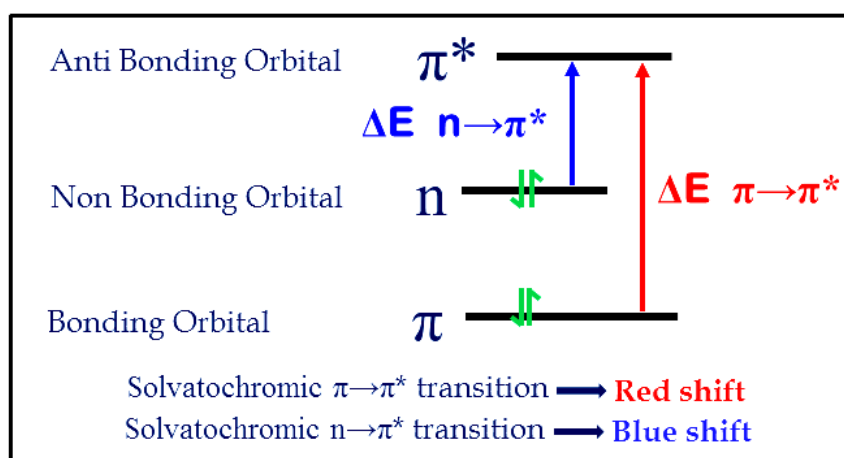


Figure 3.1 Schematic of molecular orbital diagram for a simple carbonyl group containing molecule (acetone).

The high sensitivity to solvents appears when the lone pair on C=O is available for hydrogen-bonding (H-bonding) in protic solvents. This anomalous solvatochromic blue shift of $n\text{-}\pi^*$ electronic transition has been of keen interest for a long time from theoretical and experimental research viewpoints. Several factors (change in the

dipole moment and H-bonding in the excited state,⁴ size of the solvent molecules,⁴ H-bonding between solute and solvent,⁵ Frank-Condon principle and the diversities in H-bond strength upon excitation⁶) have been proposed to cause the solvatochromic blue-shifts in C=O n- π^* transition. Various semi-empirical expressions have been developed to dissect the role of H-bonding and electrostatic interactions towards the n- π^* blue shifts in carbonyls.⁷⁻⁸ Recently, Catalan and coworkers have put forward a new photophysical model that includes solvent acidity (SA), dipolarity (SDP), and polarizability (SP) to explain the spectroscopic data.⁹ Several other theoretical studies have also contributed to understanding the solvatochromic blue shifts of n- π^* transitions of carbonyls.¹⁰⁻¹² It has been postulated from the theory that the solute-solvent interactions in the excited state do not significantly contribute to the blue shift of the n- π^* transitions.¹³ To the best of our knowledge, a direct experimental proof of the origin of the anomalous solvatochromic blue-shift in n- π^* transitions has never been revealed. As carbonyl (C=O) is one of the most abundant chemical groups present in chemical/biological molecules, experimental determination of the interactions leading to the blue shift will have an enormous effect on the molecular level mechanistic understanding of chemical/biological reactions involving C=O stabilization/activation by the catalyst/solvent.¹⁴⁻¹⁶

The C=O chromophore is imaginably a versatile spectroscopic probe to intermolecular interactions through UV, IR, ¹³C NMR, and Raman spectroscopy. The high sensitivity of the spectroscopic observables involved in spectroscopic transitions localized on C=O towards polarity (dielectric constant) of various solvents, H-bonding, and donor-acceptor complex formation have been reported.¹⁷⁻¹⁸ These shifts have been discussed either through theoretical calculations or through indirect semi-empirical models deduced from experimental data. In the present study, we report

direct experimental approaches using IR/ $n\text{-}\pi^*$ correlations on different C=O group containing molecules to explore the C=O $n\text{-}\pi^*$ solvatochromic shifts. Our experimental results manifest a unique correlation for both protic and aprotic solvents to understand the electrostatic nature of carbonyl H-bonds in a consistent manner. Moreover, we demonstrate that the H-bonding status of C=O can be experimentally probed using deviations in $n\text{-}\pi^*$ /fluorescence correlations.

3.2 Materials and sample preparation

Acetone was obtained from Sigma Aldrich and used after purification. Acetophenone, mesityl oxide, ethyl acetate, solvents like n-hexanes, tetrahydrofuran, valeronitrile, and acetonitrile were obtained from Sigma Aldrich and used without further purification. Each carbonyl compound was dissolved independently in aprotic solvents and protic binary aqueous mixtures (acetonitrile/water) such that the final concentration of the liquid sample is 10 mM for the IR studies. The concentration of the solutions used for the absorption experiments is 20 mM for all C=O containing molecules. The binary solvent mixtures are reported in terms of volume ratios. Fluorescence spectra are collected separately for the solvents and the solutions. For each solution, the corresponding solvent spectrum was subtracted from the solution spectrum in the same solvent to obtain the final peak positions.

3.3 Results and discussion

Ground state electrostatic interactions have been hypothesized to cause the solvatochromic blue shift in C=O $n\text{-}\pi^*$ transitions from direct reaction field (DRF) calculations.¹³ From an experimental viewpoint, parameters derived from the solvent dielectric constant (ϵ) have shown a reasonable linear correlation with the shift in $n\text{-}\pi^*$ transition frequencies in a selected set of aprotic solvents.⁷⁻⁸ However, using the semi-

empirical parameter, a similar correlation could not be seen for protic solvents that can form H-bond with the carbonyl. C=O stretching frequencies have also been reported to show linear sensitivity with similar semi-empirical expressions for aprotic solvents.¹⁹ Other semi-empirical polarity parameters/scales like Kosower's *Z* scale and Onsager reaction field have been extensively used to correlate the solvent effects on $n-\pi^*$ and C=O stretching frequencies.²⁰⁻²¹ However, H-bonding poses a challenging task to describe solute-solvent interactions. The continuum semi-empirical models do not account for the microscopic nature of the solvent and thereby cannot describe specific chemical interactions like H-bonding. Electrostatic field can serve as a quantitative and microscopic descriptor of solute-solvent interactions.²² Stark effect provides calibration of the transition frequency to the electrostatic field in terms of the difference dipole associated with the transition. Recent studies from the vibrational Stark effect (VSE, arising from IR transitions) have demonstrated that the field arising from electrostatic interactions varies linearly with C=O IR frequency in both H-bonding and non-H-bonding environments.²³ However, deviations from linear field-frequency correlation have been observed for nitriles in protic solvents.²⁴⁻²⁶ As both the solvatochromic shifts in C=O IR frequencies and $n-\pi^*$ frequencies have shown linear sensitivity to multiple semi-empirical expressions for aprotic solvents, we wanted to check whether a linear correlation exists between $n-\pi^*$ and IR shifts in carbonyls. Based on the results of VSE on C=O, we hypothesized that a correlation between IR shift (ground electronic state phenomenon) and $n-\pi^*$ shift (involves both ground and excited states) would provide a model-free direct experimental evidence of the role of ground state electrostatic interactions towards the solvatochromic blue shifts observed for carbonyls (Figure 3.2A). Incorporating both protic and aprotic solvents in our study will enable us to confirm if electrostatic interactions are

fundamental toward the spectral shifts in both H-bonding and non-H-bonding solvation environments.

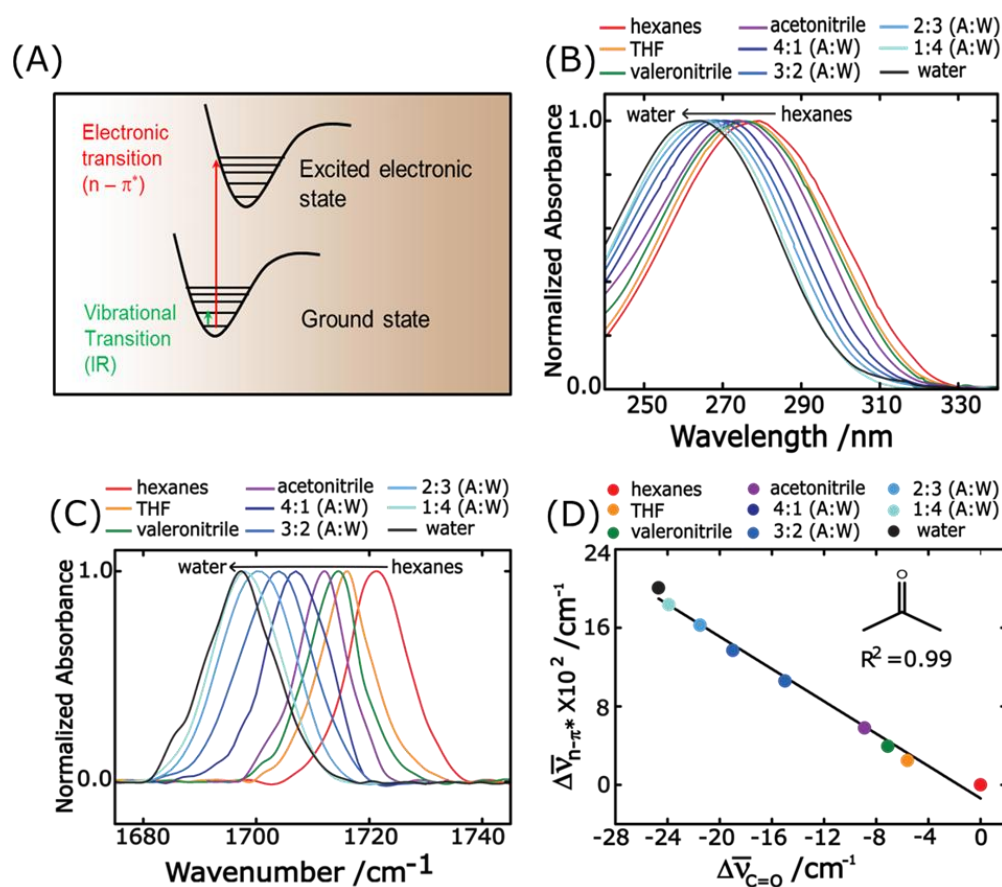


Figure 3.2 (A) Energy diagram representation of the IR transition (a ground state phenomenon) and the $n-\pi^*$ transition (involves ground and excited electronic states). Solvatochromic (B) $n-\pi^*$ electronic absorption spectra and (C) IR absorption spectra of the C=O stretch of acetone in aprotic and protic solvation environments. (D) Shifts of $n-\pi^*$ absorption ($\Delta\bar{\nu}_{n-\pi^*}$) plotted against shifts of C=O IR stretching frequencies ($\Delta\bar{\nu}_{\text{C=O}}$) of acetone in different solvation environments. The black line indicates the best-fit line. The regression value (R^2) of the fitted lines is shown in the figure.

3.3.1 Solvatochromism of Acetone

Acetone is chosen as the model carbonyl as the C=O stretching frequencies and $n-\pi^*$ frequencies of acetone have been extensively characterized in various solvents of varying polarity.^{9, 27-29} As previously reported, we observe a gradual increase in $n-\pi^*$

frequencies and a decrease in C=O stretching frequencies with increasing polarity of the aprotic solvents (Figures 3.2B and C). The $n-\pi^*$ peak positions are obtained using the methodology based on the center of gravity of the whole absorption band provided by Renge.²⁹ The overall frequency dispersion observed from the aprotic non-polar solvent hexane to the aprotic polar solvent acetonitrile in the IR experiment is ca. 9 cm^{-1} (Table 3.1). For $n-\pi^*$ transitions, the dispersion is ca. 579 cm^{-1} (Table 3.1). When acetone is dissolved in water, where the C=O can form a H-bond, a further red shift and blue shift are observed in IR and $n-\pi^*$ frequencies, respectively. To further understand the interactions in the H-bonding environment, we have scanned the polarity range between acetonitrile and water using acetonitrile/water solutions, where the percentage of water is gradually increased by 20% (v/v) increments. The C=O IR and $n-\pi^*$ frequencies of acetone in various pure organic solvents/ solvent mixtures are tabulated in Table 3.1. The reported frequency shifts (as shown in Table 3.1) are computed with respect to hexane as it is the most non-polar solvent in the solvatochromic series. Moreover, theoretical calculations have predicted \sim zero electrostatic field along the C=O bond axis of acetone in hexane.²³ The solvatochromic red-shifts in IR frequencies exhibit a linear correlation with the corresponding $n-\pi^*$ blue shifts (Figure 3.2 D). The linear sensitivity, as seen in aprotic solvents, where the interactions are predominantly electrostatic, continues in protic solvation environments, and the regression value of the best-fit line is 0.99. The solvatochromic C=O stretching frequency shifts have been previously revealed to arise from VSE, where the local electric field from the solvation environment affects the frequencies of the carbonyl (C=O) vibrational probe. Thus, the observed linear correlation between a ground state phenomenon and $n-\pi^*$ shifts in Figure 3.2 D

illustrates that the electrostatic interactions play a key role towards the acetone n- π^* blue shift in both H-bonding and non-H-bonding environments.

Table 3.1 Absolute values and shifts in n- π^* and C=O stretching frequencies of acetone in non-hydrogen-bonding and hydrogen-bonding solvation environments.

Solvent	Carbonyl stretch ($\bar{\nu}_{C=O}$) /cm ⁻¹	($\Delta\bar{\nu}_{C=O}$) ^b /cm ⁻¹	n- π^* wavelength ($\lambda_{n-\pi^*}$) /nm	n- π^* wave-number ($\bar{\nu}_{n-\pi^*}$) /cm ⁻¹	($\Delta\bar{\nu}_{n-\pi^*}$) /cm ⁻¹
Hexanes	1721.6	0.0	278.0	35971	0.0
Tetrahydrofuran	1716.0	-5.6	276.1	36219	248
Valeronitrile	1714.5	-7.1	275.0	36364	393
Acetonitrile	1712.7	-8.9	273.6	36550	579
4:1 A:W ^a	1706.6	-15.0	270.0	37030	1059
3:2 A:W ^a	1702.6	-19.0	267.8	37341	1370
2:3 A:W ^a	1700.1	-21.5	266.0	37598	1627
1:4 A:W ^a	1697.7	-23.9	264.5	37807	1836
Water	1696.9	-24.7	263.3	37979	2008

a: A:W represents acetonitrile-water solution (v/v), b: the negative sign represents red shift with respect to hexane.

To check the generality of the role of electrostatics toward the n- π^* blue-shifts in carbonyls, we have carried out similar solvatochromic UV and IR absorption experiments on other molecules containing the C=O moiety.

3.3.2 Solvatochromism of Ethyl Acetate

Ethyl acetate (ester carbonyl compound) has been studied to check the validity of the IR/ n- π^* correlation in similar sets of solvents/ solvent mixtures. As the n- π^* absorption frequency of ethyl acetate is within the solvent cut-off limit in most solvents, the solvatochromic response of ethyl acetate has been studied in hexane, acetonitrile, water, and acetonitrile/water solutions (Figure 3.3 A). Here, we observe a

gradual increase in the $n-\pi^*$ frequencies (blue shift) of ethyl acetate with the increasing polarity of the different solvation environments (Figure 3.3A). The excellent IR/ $n-\pi^*$ correlation in ethyl acetate as displayed in Figure 3.3B demonstrates that electrostatic stabilization of the ground state also determines the $n-\pi^*$ blue-shifts of ester C=O.

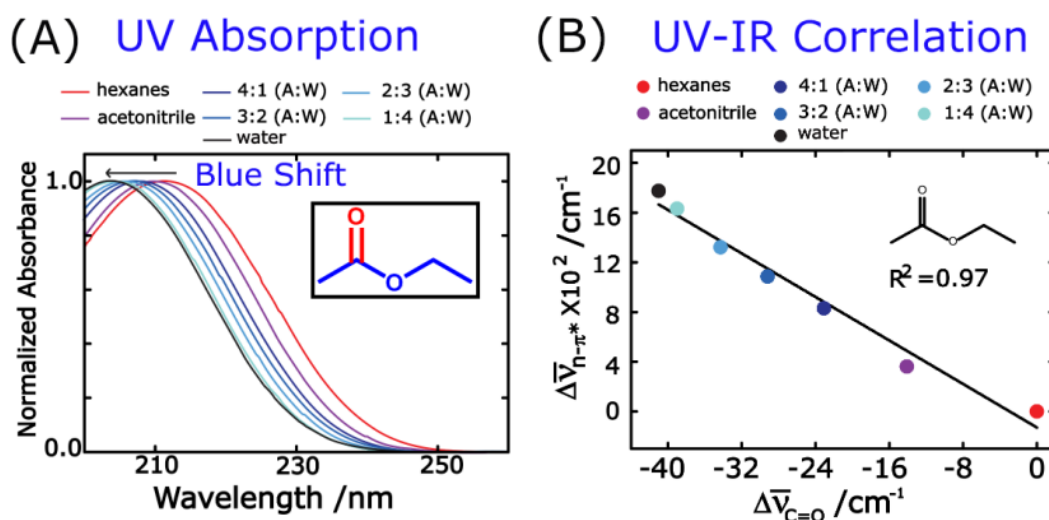


Figure 3.3 (A) $n-\pi^*$ electronic absorption spectra of ethyl acetate in non-hydrogen-bonding and hydrogen-bonding solvation environments. The polarity increases in the direction of the arrow. (B) Shifts of $n-\pi^*$ absorption ($\Delta\bar{\nu}_{n-\pi^*}$) plotted against shifts of C=O IR stretching frequencies ($\Delta\bar{\nu}_{C=O}$) of ethyl acetate in different solvation environments. The black line indicates the best-fit line. The regression value (R^2) of the fitted lines is shown in the figure.

Table 3.2 Absolute values and shifts in n- π^* and C=O stretching frequencies of ethyl acetate in non-hydrogen-bonding and hydrogen-bonding solvation environments.

Solvent	Carbonyl stretch ($\bar{\nu}_{C=O}$) /cm ⁻¹	($\Delta\bar{\nu}_{C=O}$) ^b /cm ⁻¹	n- π^* wavelength ($\lambda_{n-\pi^*}$) /nm	n- π^* wave-number ($\bar{\nu}_{n-\pi^*}$) /cm ⁻¹	($\Delta\bar{\nu}_{n-\pi^*}$) /cm ⁻¹
Hexanes	1749.5	0.0	211.3	47317	0.0
Acetonitrile (ACN)	1735.4	-14.1	209.7	47678	361
4:1 A:W ^a	1726.4	-23.1	207.7	48146	829
3:2 A:W ^a	1720.3	-29.2	206.6	48403	1086
2:3 A:W ^a	1715.2	-34.3	205.6	48638	1321
1:4 A:W ^a	1710.5	-39.0	204.3	48948	1631
Water	1708.5	-41.0	203.7	49092	1775

a: A:W represents acetonitrile-water solution (v/v), b: the negative sign represents red-shift from hexane.

3.3.3 Solvatochromism of Conjugated Ketone

Solvatochromic n- π^* absorption experiments are also performed on two different carbonyl group containing conjugated ketone compounds, acetophenone (aromatic ketone) and mesityl oxide (aliphatic α,β -unsaturated ketone) in various H-bonding (protic) and non-H-bonding (aprotic) solvation environments. The C=O moieties, both aromatic and aliphatic, show a gradual monotonic increase in the n- π^* absorption frequencies (blue shift) with increasing polarity of both aprotic and protic solvents (Figure 3.4A & 3.5A). Moreover, the carbonyl stretching frequency ($\bar{\nu}_{C=O}$) of both the ketones gradually decreases (red shift) with increasing the polarity of the solvation environments. A plot of n- π^* frequency shifts ($\Delta\bar{\nu}_{n-\pi^*}$) versus IR frequency shifts ($\Delta\bar{\nu}_{C=O}$) in the different non-hydrogen bonding and hydrogen bonding solvation environments shows an excellent linear correlation for the ketones mentioned above. The n- π^* electronic absorption spectra of acetophenone and mesityl oxide in non-H-

bonding and H-bonding solvation environments are presented in Figures 3.4A & 3.5A. However, due to the intrinsic overlap of the $n-\pi^*$ and $\pi-\pi^*$ bands of acetophenone and mesityl oxide in polar protic solvation environments, the conjugated ketones have been studied up to 1:1 acetonitrile/water (50% v/v). For both the ketones, the water concentration in binary solvent mixtures has been increased by 10% (v/v) to maintain the same number of data points in the linear fit. The IR and $n-\pi^*$ frequencies for acetophenone and Mesityl oxide, along with their shifts with respect to hexane, are listed in Tables 3.3 and 3.4.

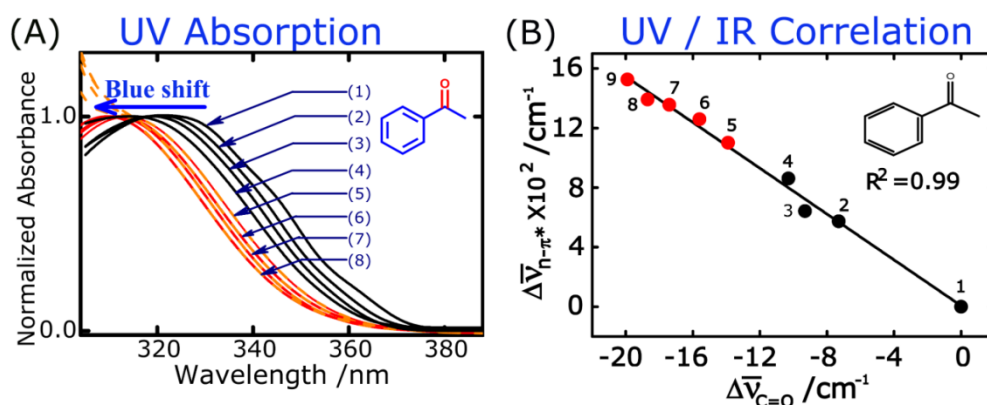


Figure 3.4 (A) $n-\pi^*$ electronic absorption spectra of acetophenone (aromatic ketone) in non-hydrogen-bonding and hydrogen-bonding solvation environments. The solid black curves represent aprotic solvents [(1) hexanes, (2) tetrahydrofuran, (3) valeronitrile, (4) acetonitrile] and the solid red curves represent the fitted peak of acetophenone in aqueous acetonitrile solutions (v/v) [(5) 90% acetonitrile, (6) 80% acetonitrile (7) 70% acetonitrile, (8) 60% acetonitrile]. The polarity increases in the direction of the arrow. (B) Plots of $n-\pi^*$ frequency shifts ($\Delta\bar{\nu}_{n-\pi^*}$) versus IR frequency shifts ($\Delta\bar{\nu}_{C=O}$) of acetophenone in different pure organic solvents and binary solvent mixtures. The black line indicates the best-fit line. The black solid circles represent aprotic solvents [(1) hexanes, (2) tetrahydrofuran, (3) valeronitrile, (4) acetonitrile] and red solid circles represent aqueous acetonitrile solutions (v/v) [(5) 90% acetonitrile, (6) 80% acetonitrile (7) 70% acetonitrile, (8) 60% acetonitrile, (9) 50% acetonitrile]. The regression values (R^2) of the fitted line is shown in the figure.

Table 3.3 Absolute values and shifts in n- π^* and C=O stretching frequencies of acetophenone (aromatic ketone) in non-hydrogen-bonding and hydrogen-bonding solvation environments.

Solvent	Carbonyl stretch ($\bar{\nu}_{C=O}$) / cm^{-1}	($\Delta\bar{\nu}_{C=O}$) ^b / cm^{-1}	n- π^* wavelength ($\lambda_{n-\pi^*}$) /nm	n- π^* wave-number ($\bar{\nu}_{n-\pi^*}$) / cm^{-1}	($\Delta\bar{\nu}_{n-\pi^*}$) / cm^{-1}
Hexanes	1696.4	0.0	324.8	30785	0.0
Tetrahydrofuran (THF)	1689.1	-7.3	318.9	31358	573
Valeronitrile (VLN)	1687.1	-9.3	318.2	31427	642
Acetonitrile (ACN)	1686.1	-10.3	316.0	31646	861
90%ACN+10%Water	1682.5	-13.9	313.6	31886	1101
80%ACN+20%Water	1680.8	-15.6	312.1	32044	1259
70%ACN+30%Water	1679.0	-17.4	311.1	32141	1356
60%ACN+40%Water	1677.7	-18.7	310.8	32177	1392
50%ACN+50%Water	1676.5	-19.9	309.4	32310	1525

b: the negative sign represents red-shift from hexane.

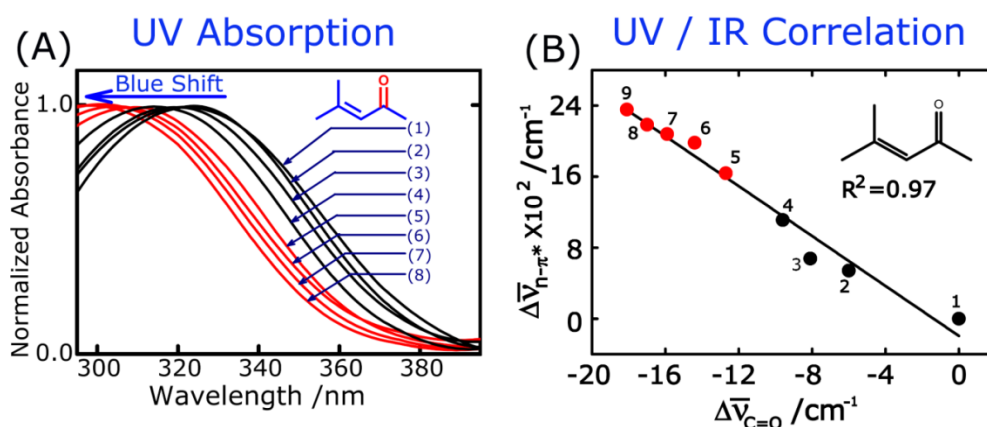


Figure 3.5 (A) n- π^* electronic absorption spectra of mesityl oxide (aliphatic conjugated ketone) in non-hydrogen-bonding and hydrogen-bonding solvation environments. The solid black curves represent aprotic solvents [(1) hexanes, (2) tetrahydrofuran, (3) valeronitrile, (4) acetonitrile] and solid red curves represent the fitted peak of mesityl oxide in aqueous acetonitrile solutions (v/v) [(5) 90%

acetonitrile, (6) 80% acetonitrile (7) 70% acetonitrile, (8) 60% acetonitrile]. The polarity increases in the direction of the arrow. (B) Plots of n- π^* frequency shifts ($\Delta\bar{\nu}_{n-\pi^*}$) versus IR frequency shifts ($\Delta\bar{\nu}_{C=O}$) of mesityl oxide in different pure organic solvents and binary solvent mixtures. The black line indicates the best-fit line. The black solid circles represent aprotic solvents [(1) hexanes, (2) tetrahydrofuran, (3) valeronitrile, (4) acetonitrile] and red solid circles represent aqueous acetonitrile solutions (v/v) [(5) 90% acetonitrile, (6) 80% acetonitrile (7) 70% acetonitrile, (8) 60% acetonitrile, (9) 50% acetonitrile]. The regression values (R^2) of the fitted line is shown in the figure.

Table 3.4 Absolute values and shifts in n- π^* and C=O stretching frequencies of Mesityl oxide (aliphatic conjugated ketone) in non-hydrogen-bonding and hydrogen-bonding solvation environments.

Solvent	Carbonyl stretch ($\bar{\nu}_{C=O}$) / cm^{-1}	($\Delta\bar{\nu}_{C=O}$) ^b / cm^{-1}	n- π^* wavelength ($\lambda_{n-\pi^*}$) /nm	n- π^* wave-number ($\bar{\nu}_{n-\pi^*}$) / cm^{-1}	($\Delta\bar{\nu}_{n-\pi^*}$) / cm^{-1}
Hexanes	1697.0	0.0	327.7	30516	0.0
Tetrahydrofuran (THF)	1691.0	-6.0	322	31056	540
Valeronitrile (VLN)	1688.9	-8.1	320.6	31192	676
Acetonitrile (ACN)	1687.4	-9.6	316.2	31626	1110
90%ACN+10%Water	1684.3	-12.7	311.0	32154	1638
80%ACN+20%Water	1682.6	-14.4	307.7	32499	1983
70%ACN+30%Water	1681.1	-15.9	306.8	32595	2079
60%ACN+40%Water	1680.0	-17.0	305.8	32701	2185
50%ACN+50%Water	1678.9	-18.1	304.2	32873	2357

b: the negative sign represents red-shift from hexane.

3.3.4 Explanation of $n-\pi^*$ Absorption / IR Correlation

The explanation of the above-mentioned experimental correlation is as follows. During the ultrafast $n-\pi^*$ excitation process, the solvent shells cannot reorient and adapt to the excited state dipole, and thus, the carbonyl moiety in the excited state is surrounded by the solvent molecules adapted to the ground state electrostatic interactions. A better stabilization of the ground state C=O dipole in a polar solvation environment compared with a non-polar solvent leads to the $n-\pi^*$ blue-shift with increasing solvent polarity. This stability can be associated with a greater electrostatic field exerted by the solvents along the C=O bond dipole through VSE. The larger stability in the protic solvation environments of C=O can be rationalized by considering that a H-bond positions a large dipole near the IR probe due to the small van der Waals radius of hydrogen, which in turn exerts a greater stabilizing electrostatic field on the C=O. The linear sensitivity of IR frequency shifts with that of $n-\pi^*$ frequency in a range of different C=O compounds demonstrates that electrostatic interactions in the ground electronic state play a key role toward the $n-\pi^*$ blue-shifts in carbonyls. As the electrostatic field is a function of partial charges and the coordinates of the individual atoms of the solvent molecules, electrostatic field provides a microscopic description of the solute-solvent interaction. The electrostatic field accounts for specific chemical interactions like H-bonding. Thus the IR/ $n-\pi^*$ linearity obtained in the aprotic solvents can be extended to the protic solvation environments. Boxer and coworkers have recently demonstrated a linear correlation between electrostatic field and C=O IR stretching frequencies using VSE, consistently for both H-bonding and non-H-bonding solvents.²³ Theoretical calculations have predicted a redistribution of electron density along the C=O bond in the excited-state leading to a reduced dipole moment, which reduces the electrostatic

interactions.³⁰ A smaller dipole moment would result in a blue shift with increasing solvent polarity through the electronic Stark effect. In Stark effect interpretation, the slope of the IR/ $n-\pi^*$ plot would be related to the difference dipoles of the two transitions. Considering the slopes of the IR/ $n-\pi^*$ plots along with the reported values of the difference dipoles for IR transitions (from VSE), the difference dipoles for the C=O $n-\pi^*$ transitions are in the order of $\sim 3-5$ Debye, which is consistent with the reported values for other electronic transitions.³¹ The similarity in difference dipoles supports the argument that the observed linear correlations arise from the underlying solvent electrostatic field.

3.3.5 Electric Field / $n-\pi^*$ Absorption Correlation

To further establish this point, we have estimated the average electrostatic field at the midpoint of the C=O ($\vec{F}_{C=O}$) of the above-mentioned ketones in all the different solvation environments using atomistic molecular dynamics (MD) simulations. The electric fields calculated from MD simulations for different carbonyl containing molecules in various solvents are tabulated in Table 3.5. An excellent linear correlation is obtained between experimentally recorded $n-\pi^*$ shifts and shifts in electrostatic fields (Figure 3.6) for different C=O containing molecules in both protic and aprotic solvation environments. However, earlier studies involving semi-empirical scales could not accommodate specific interactions like H-bonding, and thus the linearity between absorption frequencies and the polarity parameter was confined within a selected set of non-H-bonding solvents. The slopes of the best-fit lines in Figure 3.6 also provide us an estimate of the difference dipole for the C=O $n-\pi^*$ transitions. The values of the slopes obtained using the calculated electrostatic fields are smaller by a factor of ~ 2.5 . This factor is consistent with the correction

factor arising from the local field effect. The slopes of the best fit lines in Figure 3.6 for different carbonyl molecules and correction factors are given in Table 3.6.

Our experimental results show that the linearity is extendable from non-H-bonding to H-bonding environments of C=O. Thus it is unnecessary to consider the contribution from electrostatic interactions and H-bonding interactions for C=O spectroscopic probes separately. These results support the electrostatic nature of C=O H-bonding interactions.¹⁷ As both the axes in IR/n- π^* correlation are experimental observables, there are no assumptions involved in elucidating the highly debated origin of the n- π^* blue-shifts. The only assumption is whether the C=O is H-bonded in acetonitrile/water solutions.

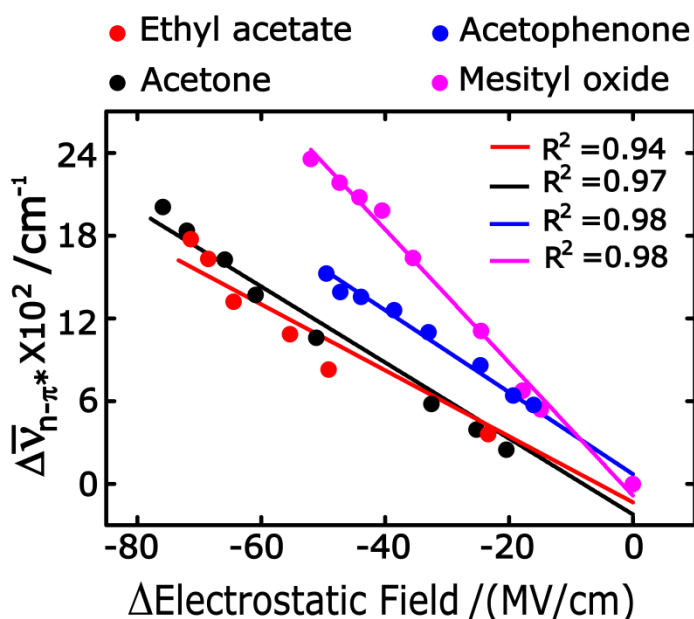


Figure 3.6 Shifts in n- π^* absorption wavenumber ($\Delta \bar{\nu}_{n-\pi^*}$) versus shifts in C=O electrostatic fields ($\Delta \vec{F}_{C=O}$) for ethyl acetate, acetone, acetophenone, mesityl oxide. The solid circles represent the $[\Delta \bar{\nu}_{n-\pi^*}, \Delta \vec{F}_{C=O}]$ paired points, and the solid lines denote the best linear fits. The regression values (R^2) of the fitted lines are shown in the figure.

Table 3.5 MD estimated electric fields experienced by the carbonyl (C=O) probe of acetone, acetophenone, ethyl acetate, mesityl oxide in different solvation environments.

Solvents	MD estimated electric field / (MV/cm)			
	Acetone	Acetophenone	Ethyl acetate	Mesityl oxide
Hexanes	-0.17	-0.129	-0.095	-0.11
Tetrahydrofuran	-20.39	-16.12	-	-14.96
Valeronitrile	-25.24	-19.44	-	-17.91
Acetonitrile	-32.49	-24.71	-23.325	-24.58
90%ACN+10%Water	-	-33.12	-	-35.57
80%ACN+20%Water	-51.06	-38.65	-49.1	-40.58
70%ACN+30%Water	-	-43.97	-	-44.25
60%ACN+40%Water	-60.86	-47.32	-55.31	-47.43
50%ACN+50%Water	-	-49.60	-	-51.95
40%ACN+60%Water	-65.82	-	-64.51	-
20%ACN+80%Water	-71.96	-	-68.51	-
Water	-75.85	-	-71.32	-

Table 3.6 Comparison of predicted difference dipoles in $n-\pi^*$ transition from IR/ $n-\pi^*$ and field/ $n-\pi^*$ plots.

C=O compound	Slope of IR/ $n-\pi^*$	Difference dipole in IR transition (Debye)	Predicted difference dipole in $n-\pi^*$ transition (Debye)	Slope of field/ $n-\pi^*$	Predicted difference dipole in $n-\pi^*$ transition from previous column (Debye)	Correction Factor
Acetone	82.42	0.048	3.96	27.56	1.65	2.4
Acetophenone	76.95	0.063	4.85	29.73	1.78	2.7
Ethyl Acetate	43.78	0.084	3.67	23.93	1.44	2.5

3.3.6 Carbonyl (C=O) H-bond Detection

To experimentally prove this assumption, we have performed UV/fluorescence covariance of acetone in protic and aprotic solvents. An acetone molecule that is H-bonded in the ground state cannot probably sustain the H-bond in the excited state as one of the electrons in the n-orbital is removed during the n- π^* transition. Two lone pairs on C=O oxygen can presumably form two H-bonds. However, an earlier study reported negligible contribution of solvent acidity to fluorescence solvatochromism of acetone. Acetone shows a gradual monotonic blue shift in the n- π^* absorption frequencies with increasing polarity of both aprotic and protic solvents (Figure 3.2B). Similar monotonicity is observed in n- π^* emission frequencies for the non-H-bonded ketone C=O dissolved in aprotic solvents. In a protic solvation environment, however, the trend is reversed, and a red shift in emission frequencies compared to that in the polar aprotic solvent, acetonitrile, is observed. For aprotic solvents, both the ground and excited states are not H-bonded and are stabilized by the electrostatic interactions by the surrounding solvent molecules leading to a linear correlation between n- π^* shifts and fluorescence shifts. According to this explanation, a plot of n- π^* shifts versus fluorescence shifts will maintain a linear correlation for aprotic solvents. In contrast, a deviation from linearity will occur for H-bonding protic solvents/solvent mixtures (Figure 3.7B), where the ground state involves a specific chemical interaction (H-bonding) missing in the excited state. A plot of ($\Delta\bar{\nu}_{n-\pi^*}$) versus fluorescence (emission) shifts ($\Delta\bar{\nu}_{em}$) demonstrates a deviation from the linear correlation for all acetonitrile/water mixtures, thereby providing evidence that C=O is H-bonded in binary aqueous solutions of acetonitrile.

The non-monotonicity in emission frequencies upon H-bonding compared to a monotonic blue shift in $n-\pi^*$ absorption frequencies, interestingly, enables us to use absorption and emission techniques in tandem for C=O H-bond detection. Moreover, a similar trend in saturated C=O of acetone emphasizes the dual experimental approach is independent of the structure of the C=O molecule.

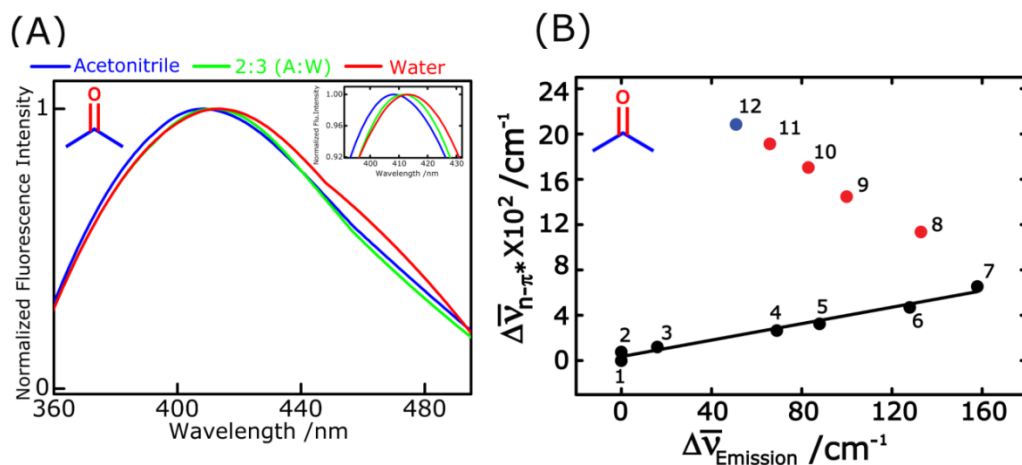


Figure 3.7 (A) Normalized fluorescence spectra of the acetone in non-hydrogen-bonding and hydrogen-bonding solvation environments. A:W represents acetonitrile-water solution (v/v). (B) Shifts in $n-\pi^*$ absorption ($\Delta\bar{\nu}_{n-\pi^*}$) versus shifts of emission wavenumber ($\Delta\bar{\nu}_{em}$) for acetone in protic and aprotic solvation environments. Black solid circles represent aprotic solvents [(1) cyclohexane, (2) hexanes, (3) n-pentane, (4) diethyl ether, (5) tetrahydrofuran, (6) valeronitrile, (7) acetonitrile], red solid circles represent aqueous acetonitrile solutions (v/v) [(8) 80% acetonitrile, (9) 60% acetonitrile, (10) 40% acetonitrile, (11) 20% acetonitrile] and blue solid circle represent water. Black line indicates the best-fit line in different non-hydrogen-bonding aprotic solvents. The regression value (R^2) of the best fit equals to 0.97.

Table 3.7 Absolute values and shifts in emission peak positions of acetone(saturated ketone) in non-hydrogen-bonding and hydrogen-bonding solvation environments.

Solvent	Fluorescence wavelength ($\lambda_{emission}$) /nm	Fluorescence wave number ($\bar{\nu}_{emission}$) /cm ⁻¹	($\Delta\bar{\nu}_{emission}$) /cm ⁻¹
Cyclohexane	409.3	24434	0
Hexane	409.3	24434	0
Diethyl ether	408.1	24503	69
Tetrahydrofuran	407.8	24522	88
Valeronitrile (VLN)	407.1	24562	128
Acetonitrile (ACN)	406.6	24592	158
4:1 A:W ^a	407.1	24567	133
3:2 A:W ^a	407.6	24534	100
2:3 A:W ^a	407.9	24517	83
1:4 A:W ^a	408.2	24500	66
Water	408.4	24485	51

a: A:W represents acetonitrile-water solution (v/v).

Camphor, a biologically relevant unsaturated ketone, is the natural substrate of cytochrome P450cam that catalyzes the regio- and stereospecific hydroxylation of camphor to 5-exo-hydroxycamphor.³²⁻³³ The hydrogen bond between the hydroxyl group of Tyr96 and the C=O oxygen of camphor play a critical mechanistic role in enzymatic catalysis.³⁴ Although P450cam was one of the first members of the P450 superfamily whose three-dimensional structure was determined when bound to camphor, direct experimental identification of the camphor's H-bonding status C=O in other P450 variants would lead to newer avenues in the mechanistic understanding of the enzymatic reaction. Similar solvatochromic absorption and emission experiments are carried out on camphor to check the viability of the prediction of the camphor C=O H-bond (Table 3.6). The covariance of solvatochromic emission and absorption frequencies of camphor shows deviation from linearity upon H-bonding (Figure 3.8), as seen for acetone, thereby

allowing conclusive determination of the H-bonding status of the camphor C=O. This result validates the generality of the dual experimental approach to detect saturated C=O H-bonds. This observation is quite intriguing and may help to contribute new insights in the arena of mechanistic study of organic and biomolecular reactions involving saturated C=O.

Table 3.8 Absorption and emission peak positions of camphor in different non-H-bonding and H-bonding solvation environments.

Solvents	n-π^* wavelength ($\lambda_{n-\pi^*}$) /nm	n-π^* wavenumber ($\bar{\nu}_{n-\pi^*}$) / cm^{-1}	Fluorescence wavelength ($\lambda_{emission}$) /nm	Fluorescence wavenumber ($\bar{\nu}_{emission}$) / cm^{-1}
n-hexanes	289.5	34542	416.5	24010
Diethyl ether	288.7	34638	415.9	24039
Tetrahydrofuran	287.9	34734	415.3	24079
Acetonitrile	287.5	34783	414.9	24099
1:1 A:W ^a	283.7	35249	415.3	24079
Water	280.1	35702	417.7	23941
Methanol	285.3	35051	415.0	24095

a: A:W represents acetonitrile-water solution (v/v).

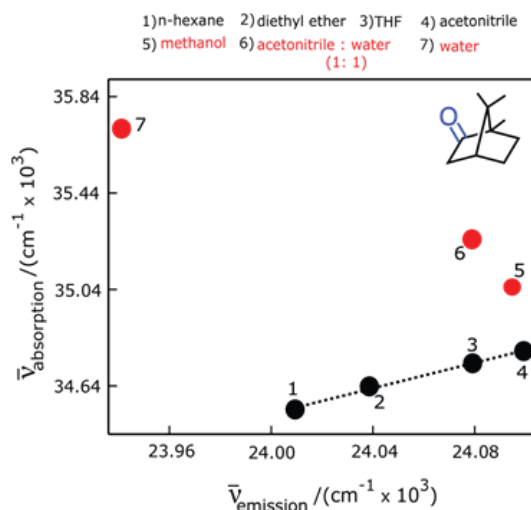


Figure 3.8 Experimentally obtained $n-\pi^*$ absorption frequencies of camphor are plotted against the corresponding emission frequencies in aprotic (black) and protic (red) solvation environments. Linear correlation is observed (dashed lines) for ketones in aprotic solvents (non-H-bonded C=O), whereas, a deviation from linearity is observed in protic solvation environment (H-bonded C=O).

3.4 Conclusion

In summary, using IR/ $n-\pi^*$ correlations in a range of different compounds with C=O functionalities, we have provided the first experimental evidence regarding the origin of the C=O $n-\pi^*$ solvatochromic blue shifts. Our results demonstrate that increasing solute-solvent electrostatic interactions in the ground electronic state is the key to the blue-shifts in $n-\pi^*$ transitions. We have also experimentally demonstrated the H-bonding status of the C=O using $n-\pi^*$ /fluorescence correlations. The implications of these results are manifold. These results demonstrate that $n-\pi^*$ frequencies can predict the electrostatic fields experienced by the carbonyl moiety. The electrostatic field has been recently proposed to be a microscopic and quantitative descriptor of non-covalent interactions and local polarity.²³ To date, IR spectroscopy has been used to predict electrostatic fields through the vibrational Stark effect. However, the intrinsic overlap of the ligand C=O frequency with the amide-I band of the protein makes it

extremely difficult to determine the C=O stretching frequency of the carbonyl experimentally.¹⁶ On the other hand, long-wavelength n- π^* transition of ligand carbonyls (e.g., in steroids) has considerably less overlap with the protein absorption and can be a suitable alternative for determining the local polarity at the binding site of the protein. Moreover, several organic reactions are predicted to involve C=O activation through H-bond. Metal-free organocatalysis has seen tremendous growth in recent times.³⁵ Recently, n- π^* frequencies have been shown to correlate with organic reaction rates.³⁶ Our results might provide a mechanistic understanding of these organic reactions.

3.5 References

1. Scheibe, G. Influencing of Absorption Spectrum, Reaction Rate and Equilibrium by Solvents. *Ber. Dtsch. Chem. Ges. B* **1927**, *60*, 1406-1419.
2. McConnell, H. Effect of Polar Solvents on the Absorption Frequency of n - π^* Electronic Transitions. *J. Chem. Phys* **1952**, *20*, 700-704.
3. Kasha, M. Characterization of Electronic Transitions in Complex Molecules. *Discuss. Faraday Soc.* **1950**, (9), 14-19.
4. Bayliss, N. S.; McRae, E. G. Solvent Effects in the Spectra of Acetone, Crotonaldehyde, Nitromethane and Nitrobenzene. *J. Phys. Chem.* **1954**, *58*, 1006-1011.
5. Brealey, G. J.; Kasha, M. The Rôle of Hydrogen Bonding in the n \rightarrow π^* Blue-shift Phenomenon. *J. Am. Chem. Soc.* **1955**, *77*, 4462-4468.
6. Pimentel, G. C. Hydrogen Bonding and Electronic Transitions - the Role of the Franck-Condon Principle. *J. Am. Chem. Soc.* **1957**, *79*, 3323-3326.

7. Ito, M.; Inuzuka, K.; Imanishi, S. Effect of Solvent on n- π^* Absorption Spectra of Ketones. *J. Am. Chem. Soc.* **1960**, *82*, 1317-1322.
8. McRae, E. G. Theory of Solvent Effects on Molecular Electronic Spectra - Frequency Shifts. *J. Phys. Chem.* **1957**, *61*, 562-572.
9. Catalan, J.; Pablo Catalan, J. Questioning the Photophysical Model for the Indole Chromophore in the Light of Evidence Obtained by Controlling the Non-specific Effect of the Medium with 1-chlorobutane as Solvent. *Phys. Chem. Chem. Phys.* **2011**, *13*, 15022-15030.
10. Grozema, F. C.; van Duijnen, P. T. Solvent Effects on the n- π^* Transition of Acetone in Various Solvents: Direct Reaction Field Calculations. *J. Phys. Chem. A* **1998**, *102*, 7984-7989.
11. Martin, M. E.; Sanchez, M. L.; del Valle, F. J. O.; Aguilar, M. A. A Multiconfiguration Self-Consistent Field/Molecular Dynamics Study of the n- π^* Transition of Carbonyl Compounds in Liquid Water. *J. Chem. Phys.* **2000**, *113*, 6308-6315.
12. Aidas, K.; Kongsted, J.; Osted, A.; Mikkelsen, K. V.; Christiansen, O. Coupled Cluster Calculation of the n- π^* Electronic Transition of Acetone in Aqueous Solution. *J. Phys. Chem. A* **2005**, *109*, 8001-8010.
13. Van Duijnen, P. T.; de Vries, A. H. Direct Reaction Field Force Field: A Consistent Way to Connect and Combine Quantum-Chemical and Classical Descriptions of Molecules. *Int. J. Quantum Chem.* **1996**, *60*, 1111-1132.
14. Wittkopp, A.; Schreiner, P. R. Metal-Free, Noncovalent Catalysis of Diels-Alder Reactions by Neutral Hydrogen Bond Donors in Organic Solvents and in Water. *Chem. - Eur. J.* **2003**, *9*, 407-414.

15. Tuerkmen, Y. E.; Rawal, V. H. Exploring the Potential of Diarylacetylenediols as Hydrogen Bonding Catalysts. *J. Org. Chem.* **2013**, *78*, 8340-8353.
16. Fried, S. D.; Bagchi, S.; Boxer, S. G. Extreme Electric Fields Power Catalysis in the Active Site of Ketosteroid Isomerase. *Science* **2014**, *346*, 1510-1514.
17. Kashid, S. M.; Bagchi, S. Experimental Determination of the Electrostatic Nature of Carbonyl Hydrogen-Bonding Interactions Using IR-NMR Correlations. *J. Phys. Chem. Lett.* **2014**, *5*, 3211-3215.
18. Balasubramanian, A.; Rao, C. N. R. Evaluation of Solute-Solvent Interactions from Solvent Blue-shifts of $n \rightarrow \pi^*$ Transitions of C=O, C=S, NO₂ and N=N Groups: Hydrogen Bond Energies of Various Donor-acceptor Systems. *Spectrochim. Acta* **1962**, *18*, 1337-1352.
19. Inuzuka, K. z.; Ito, M.; Imanishi, S. Effect of Solvent on Carbonyl Stretching Frequency of Ketones. *Bull. Chem. Soc. Jpn* **1961**, *34*, 467-471.
20. Dilling, W. L. The Effect of Solvent on the Electronic Transitions of Benzophenone and Its o- and p-Hydroxy Derivatives. *J. Org. Chem.* **1966**, *31*, 1045-1050.
21. Elenewski, J. E.; C Hackett, J. Solvatochromism and the Solvation Structure of Benzophenone. *J. Chem. Phys.* **2013**, *138*, 224308.
22. Fried, S. D.; Boxer, S. G. Measuring Electric Fields and Noncovalent Interactions Using the Vibrational Stark Effect. *Acc. Chem. Res.* **2015**, *48*, 998-1006.
23. Fried, S. D.; Bagchi, S.; Boxer, S. G. Measuring Electrostatic Fields in Both Hydrogen-Bonding and Non-Hydrogen-Bonding Environments Using Carbonyl Vibrational Probes. *J. Am. Chem. Soc.* **2013**, *135*, 11181-11192.

24. Fafarman, A. T.; Sigala, P. A.; Herschlag, D.; Boxer, S. G. Decomposition of Vibrational Shifts of Nitriles into Electrostatic and Hydrogen-Bonding Effects. *J. Am. Chem. Soc.* **2010**, *132*, 12811-12813.
25. Bagchi, S.; Fried, S. D.; Boxer, S. G. A Solvatochromic Model Calibrates Nitriles' Vibrational Frequencies to Electrostatic Fields. *J. Am. Chem. Soc.* **2012**, *134*, 10373-10376.
26. Deb, P.; Halder, T.; Kashid, S. M.; Banerjee, S.; Chakrabarty, S.; Bagchi, S. Correlating Nitrile IR Frequencies to Local Electrostatics Quantifies Noncovalent Interactions of Peptides and Proteins. *J. Phys. Chem. B* **2016**, *120*, 4034-4046.
27. Kun Cha, D.; A. Kloss, A.; C. Tikanen, A.; Ronald Fawcett, W. Solvent-Induced Frequency Shifts in the Infrared Spectrum of Acetone in Organic Solvents. *Phys. Chem. Chem. Phys.* **1999**, *1*, 4785-4790.
28. Nyquist, R. A. Infrared Studies of Ketones: Parameters Affecting the Induced Carbonyl Stretching Vibration by Solute/Solvent Interaction. *Appl. Spectrosc.* **1990**, *44*, 433-438.
29. Renge, I. Solvent Dependence of $n-\pi^*$ Absorption in Acetone. *J. Phys. Chem. A* **2009**, *113*, 10678-10686.
30. Pasteka, L. F.; Melichercik, M.; Neogady, P.; Urban, M. CASPT2 and CCSD(T) Calculations of Dipole Moments and Polarizabilities of Acetone in Excited States. *Mol. Phys.* **2012**, *110*, 2219-2237.
31. Boxer, S. G. Stark Realities. *J. Phys. Chem. B* **2009**, *113*, 2972-2983.
32. Katagiri, M.; Ganguli, B. N.; Gunsalus, I. C. A Soluble Cytochrome P-450 Functional in Methylene Hydroxylation. *J. Biol. Chem.* **1968**, *243*, 3543-3546.
33. Poulos, T. L.; Finzel, B. C.; Howard, A. J. High-resolution crystal structure of cytochrome P450cam. *J. Mol. Biol.* **1987**, *195*, 687-700.

34. Prasad, S.; Mitra, S. Role of Protein and Substrate Dynamics in Catalysis by *Pseudomonas putida* Cytochrome P450cam. *Biochemistry* **2002**, *41*, 14499-14508.
35. Sohtome, Y.; Nagasawa, K. The Design of Chiral Double Hydrogen Bonding Networks and Their Applications to Catalytic Asymmetric Carbon-Carbon and Carbon-Oxygen Bond-Forming Reactions. *Synlett* **2010**, *2010*, 1-22.
36. Walvoord, R. R.; Huynh, P. N. H.; Kozlowski, M. C. Quantification of Electrophilic Activation by Hydrogen-Bonding Organocatalysts. *J. Am. Chem. Soc.* **2014**, *136*, 16055-16065.

Chapter 4
Quantification of Local Electrostatics
Inside Protein Interior Using $n-\pi^*$
Absorption Spectroscopy

4.1 Introduction

The polarity within protein interiors affects protein's interactions with ligands, substrates, and other proteins, making it a critical determinant of protein structure, stability and activity. As electrostatic interactions are prevalent in any bio-molecular system,¹⁻³ computational and experimental studies have focused to describe local electrostatics and polarity within biological cavities. Protein polarity is often described by a low dielectric constant ($\epsilon = 2-4$), however, electrostatics calculations suggest large electric fields are produced by charged and polar groups in folded proteins that can vary from site to site in magnitude and direction.⁴⁻⁶ Experimental studies for protein polarity determination have mostly relied on the sensitivity of the fluorescent probes to the microenvironment.⁷⁻⁸ These studies are informative and report on protein polarity by correlating peak emission wavelength to dielectric constant or semi-empirical solvent polarity parameters and scales.⁹⁻¹² However, there are a few limitations: (a) polarity measurement in protein depends on efficient fluorophores insertion, thus limited by the affinity of the ligand binding site, (b) fluorescent probe might alter the molecular architecture of the native protein and there-by change the function and stability, (c) dielectric constant is a bulk solvent property and cannot define the local microenvironment around the optical probe, and (d) most of the semi-empirical polarity parameters (with a few exceptions, e.g. $E_T(30)$) cannot account for the specific intramolecular and intermolecular interactions like hydrogen bonding. We therefore require a non-invasive label free spectroscopic method that probes chemical groups preferably either present in the native proteins or in their natural substrates. We would also require a microscopic and quantitative descriptor of electrostatic interactions inside proteins that is dependent on the molecular architecture of the biomolecule and the coordinates of the surrounding

solvent molecules. Moreover, a direct coupling, understood on a theoretical basis and independently verified by experiments, should exist between the spectroscopic observable and the local electrostatics descriptor.

Carbonyl (C=O) groups are ubiquitous in biomolecules and are also common in the natural sub-strates of the proteins. Probing C=O moieties paves the way to use label free spectroscopic techniques. Here, we focus on the non-invasive spectroscopic methods like infrared (IR) spectroscopy, nuclear magnetic resonance (NMR) spectroscopy, and ultraviolet/visible (UV/VIS) $n-\pi^*$ absorption spectroscopy that provide spectral signatures of the C=O moiety. Moreover, the spectroscopic observables like C=O IR frequencies, ^{13}C NMR chemical shifts of the C=O carbon or $n-\pi^*$ wavelengths are sensitive to the immediate surroundings of the C=O group and therefore should be ideal to report on the local electrostatics within proteins.¹³⁻¹⁶ The electric field estimated at any point inside protein depends on the distances of all the other atoms in the system (both solute and solvent atoms) from that point as well as the residual partial charges on each atom and has been reported to influence every aspect of protein function.¹⁷⁻¹⁸ As biomolecules consist of polar, polarizable, and charged residues, electric field experienced by C=O from its environment can provide microscopic insight about how enzymes function within the highly heterogeneous protein environment.¹⁴ For example, a small change in the environment, like a modification in the protonation state or a conformational rearrangement upon ligand binding would result in a change in the electric field experienced by C=O. Moreover, as C=O hydrogen bonding interactions are electrostatic,^{15, 19} electric field at C=O includes specific solute-solvent interactions like hydrogen bonding. In this work, we have shown independent linear correlations of IR, NMR and UV/VIS spectroscopic observables to the electric field exerted on C=O vibrational probe. Depending on the

bio molecular system, we can pick and choose the spectroscopic method to determine local electric field within the interior of biomolecules.

Serum albumins, one of the most abundant proteins in the circulatory system, maintain osmotic pressure and pH of blood and transport several lipophilic compounds like fatty acids, drugs and steroid hormones. Testosterone, a steroid hormone, is one of the natural substrates of serum albumins. The association of testosterone with serum proteins regulates its biological activity. The steroid-protein interaction has a major biological implication and the local electric field at the testosterone binding site of bovine serum albumin (BSA) has been probed in the present work.

4.2 Materials and sample preparation

Testosterone, bovine serum albumin (BSA), solvents like dibutyl ether (DBE), tetrahydrofuran (THF), valeronitrile (VLN), acetonitrile (ACN), and D₂O were obtained from Sigma Aldrich and used without further purification. Testosterone was dissolved independently in pure organic solvents and protic binary aqueous mixtures (acetonitrile/water) such that the final concentration of liquid sample is 10 mM for the solvatochromic IR studies. As testosterone is not soluble (or sparingly soluble) in neat water or in acetonitrile/water mixtures (with high water content (> 70% v/v)), we have reported spectroscopic results up to 50% acetonitrile/water (v/v). For recording the IR spectra of testosterone in each solvent (or solvent mixture) 100 scans were collected.

The IR absorption spectrum of testosterone bound BSA solution (in buffer) was recorded on a Vertex 70 (Bruker) spectrometer. The solution contained 1 mM testosterone added to 1.5 mM BSA in phosphate buffer. Multiple spectra of the protein-ligand complex (in deuterated phosphate buffer) and the background spectra

of BSA in deuterated phosphate buffer were collected and background was carefully subtracted to obtain the C=O IR peak of testosterone. The C=O peak was reproducible and the error bar in the estimated peak position was found to be 0.6 cm⁻¹.

The concentration of testosterone used for solvatochromic absorption experiments was 5 mM. For the UV absorption experiment of testosterone bound BSA, the concentrations of the ligand and the protein were the same as the IR experiment.

In order to check if the protein aggregates at 1.5mM concentration (experimental condition), the absorbance at the peak maximum of the amide-I band of BSA at different concentrations were plotted against the corresponding concentrations. These points could be fitted to a straight line with a regression (R^2) value of 0.99 (Figure 4.1). This illustrates that Beer-Lambert law is being obeyed at the experimental concentration of the protein.

The ¹³C NMR spectra were obtained on a 400 MHz JEOL ECX NMR spectrometer. Here peak positions are informed as the maximum value.

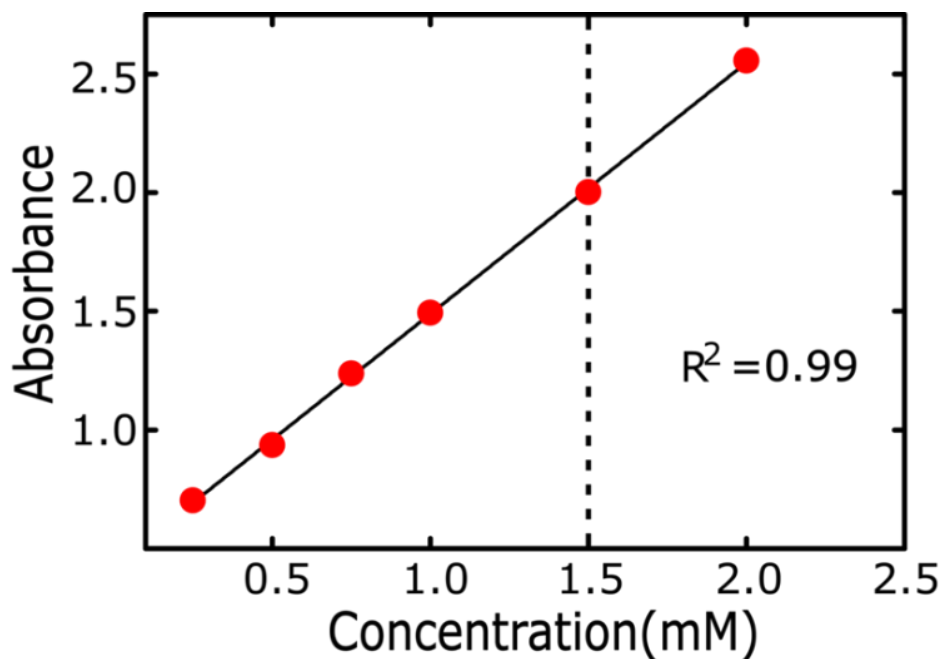


Figure 4.1 The absorbance of the amide-I IR band of BSA plotted against different concentrations of the protein (fixed path-length). The black line indicates best fit line. The regression value (R^2) of the fitted line is shown in the figure. The linear correlation verifies Beer-Lambert law and indicates that the protein has not aggregated in the plotted concentration range. The dashed vertical line corresponds to the concentration of the protein at which the IR and UV experimental results of the BSA-testosterone complex have been reported.

4.3 Results and discussion

To interrogate the local electrostatics at the binding site of BSA, solvatochromic IR, ^{13}C NMR, and UV/VIS experiments were performed for testosterone in a wide range solvation environments of varying polarity. Testosterone was dissolved in various pure organic solvents and binary aqueous mixtures of acetonitrile/water (v/v) to mimic non-hydrogen bonding and hydrogen bonding solvation environments of the substrate. Due to the change in polarity, a shift in the respective peak positions is observed in each of the spectroscopic techniques (Figure 4.1A).

4.3.1 Cross- Correlation between Independent Spectroscopic Observables for Testosterone

The $n-\pi^*$ absorption wavelength of testosterone shows a monotonic blue-shift with the increasing polarity of the aprotic solvents and the protic aqueous binary mixtures (with increasing water content) (Figure 4.1B). The C=O stretching frequency of testosterone shows a monotonic red shift with the increasing polarity of the same set of neat solvents/ solvent mixtures (Table 4.1). The ^{13}C NMR chemical shift of the carbonyl carbon shows a downfield shift with the increasing polarity of the solvation environment (Table 4.1). The $n-\pi^*$ absorption wavelength, C=O stretching frequencies and ^{13}C NMR chemical shifts for testosterone in various pure organic solvents/ solvent mixtures are tabulated in Table 4.1.

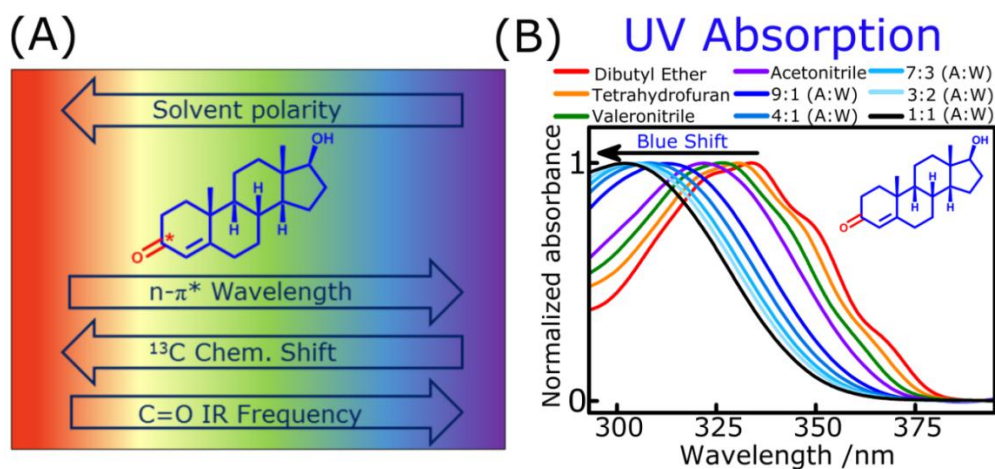


Figure 4.2 (A): For carbonyls, the spectroscopic observables of IR spectroscopy, NMR spectroscopy, and UV/VIS absorption spectroscopy change with the solvent polarity. Figure 4.1A represents the shift (and the direction of the shifts) in the observables for testosterone with the varying solvent polarity. (B) Normalized $n-\pi^*$ electronic absorption spectra of testosterone in non-hydrogen-bonding and hydrogen-bonding solvation environments. A:W represents acetonitrile-water solution (v/v). The polarity increases in the direction of the arrow.

We observe linear cross correlations within the spectroscopic observables in various non-hydrogen bonded as well as hydrogen bonded environment (Figures 4.3A, 4.3B, and 4.3C). This result illustrates that measurement of one of the spectroscopic observables can directly predict the other observables from the calibrations shown in Figure 4.3. To verify the generality of the linear correlation between independent spectroscopic variables as seen for testosterone C=O, we have performed solvatochromic experiments on small molecule ketones, esters, and amides and the results show similar trends as found in testosterone (Figure 4.4). Thus, a direct coupling of any of these spectroscopic variables to the local electric field within the bio-molecular interior would allow us to quantify local electrostatics by performing any one of the above mentioned non-invasive spectroscopic experiments.

Table 4.1 n- π^* absorption wavelength, C=O stretching frequencies and ^{13}C NMR chemical shifts for testosterone in non-hydrogen bonding and hydrogen bonding solvents.

Serial No.	Solvent	n- π^* wavelength /nm	carbonyl stretch /cm $^{-1}$	^{13}C chemical shift /ppm
1	Dibutyl ether (DBE)	333.47	1682.4	No peak
2	Tetrahydrofuran (THF)	330.39	1676.8	196.79
3	Valeronitrile (VLN)	326.50	1673.3	198.02
4	Acetonitrile (ACN)	322.80	1670.1	199.39
5	90%ACN+10%Water (A10W)	312.57	1660.5	201.39
6	80%ACN+20%Water (A20W)	308.50	1657.7	201.99
7	70%ACN+30%Water (A30W)	304.93	1653.9	202.31
8	60%ACN+40%Water (A40W)	303.77	1652.6	202.73
9	50%ACN+50%Water (A50W)	301.37	1649.4	203.08

(A) UV / IR Correlation (B) IR / NMR Correlation (C) UV / NMR Correlation

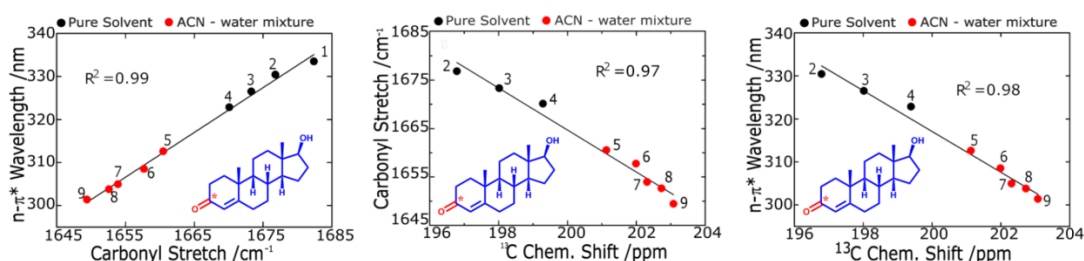


Figure 4.3 Linear correlations exist among the three independent spectroscopic observables of testosterone, namely (A) C=O stretching frequency and $n-\pi^*$ wavelength, (B) C=O stretching frequency and ^{13}C chemical shift of the C=O carbon, and (C) $n-\pi^*$ wavelength and ^{13}C chemical shift of the C=O carbon in hydrogen bonding and non-hydrogen bonding solvents. The black lines denote the best-fit lines, the black circles represent aprotic solvents [(1) DBE, (2) THF, (3) VLN, (4) ACN] and red circles represent protic binary solvent mixtures [(5)A10W, (6)A20W, (7)A30W, (8)A40W, (9)A50W]. The regression values of the fitted lines are shown in the figures.

Interestingly, the C=O IR frequencies are known to show linear sensitivity towards electrostatic field through vibrational Stark effect (VSE).²⁰ A change in the local environment modifies the electrostatic field exerted on the IR probe, thereby causing a shift in the IR transition energy. Moreover, vibrational Stark tuning rate, the change in IR frequency caused by a unit change in field, can be measured independently from vibrational Stark effect (VSE) spectroscopy. For a diatomic chemical moiety like C=O, the varying electrostatic field along the C=O bond in solvatochromic experiments polarizes the charge density and changes the perpendicular elements of the shielding tensor.²¹ The change in charge density changes the shielding on the C=O carbon nucleus and the ^{13}C chemical shift has been reported to vary linearly with the

field. Thus while the linear sensitivity of C=O to electrostatic field is the difference dipole (from VSE) that for ^{13}C NMR is the shielding polarizability. As both C=O stretching frequencies and ^{13}C chemical shifts of the C=O carbon show linear sensitivity toward electrostatic field, the electrical and magnetic properties of the ground electronic state tend to vary linearly (Figure 4.3 B). The linear correlation between C=O IR frequencies and the n- π^* absorption wavelengths arises as the solvent shell orientation in the Frank Condon state is adapted to the electrostatic interactions of the ground state. The excitation process is much faster than the solvent shell reorientation process, and the solvatochromic shifts of the n- π^* transitions are dominated by the ground state electrostatic stabilization of the spectroscopic probe.²²

4.3.2 Correlation between Independent Spectroscopic Observables with electrostatic Field for Testosterone

The Stark tuning rate of 19-Nortestosterone (19-NT) has been experimentally measured and reported by Boxer and coworkers.¹⁴ 19-NT is a steroid with a very similar structure and connectivity, especially around the C=O moiety. Using atomistic molecular dynamics (MD) simulations, we have calculated the electrostatic field at the mid-point of the C=O of testosterone in all the different solvation environments of the solvatochromic experiments. C=O stretching frequencies of testosterone when plotted against the electrostatic fields show a linear sensitivity with a slope of ~ 0.6 . The slope is theoretically equivalent to the experimentally measured Stark tuning rate of $1.4 \text{ cm}^{-1}/(\text{MV}/\text{cm})$.¹⁴ Thus the calculated electrostatic fields were scaled down by a factor of 2.32 to make the slope equal to the experimentally measured value. This divergence appears from the local field effect and is compatible with the reported value of the local field correction factor, $f \sim 2$. The electrostatic fields calculated from

MD simulations for all the different solvation environments, along with the corresponding corrected field values are listed in Table 4.2 and equations of the best fit line of the plot using the corrected field is given in the caption of Figure 4.4.

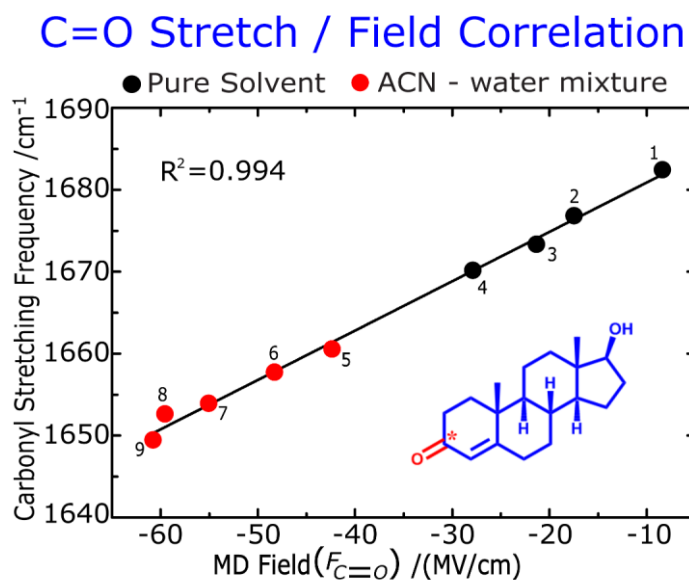


Figure 4.4 Carbonyl stretching frequency versus electrostatic field field exerted on the C=O of the testosterone calculated by MD simulation of testosterone dissolved in different non-hydrogen bonding and hydrogen bonding solvents. The black solid circles represent aprotic solvents [(1) dibutyl ether, (2) tetrahydrofuran, (3) valeronitrile, (4) acetonitrile] and red solid circles represent aqueous acetonitrile solutions (v/v) [(5) 90% acetonitrile, (6) 80% acetonitrile (7) 70% acetonitrile, (8) 60% acetonitrile, (9) 50% acetonitrile]. The regression values (R^2) of the fitted lines are shown in the figures. The black line denotes best fitted line. The equation for this best fitted line is $\bar{\nu}_{C=O} = 0.603 (F_{C=O}) + 1686.91$.

Table 4.2 MD estimated and corrected electric fields experienced by the carbonyl for testosterone in pure organic solvents and acetonitrile/water binary mixtures (v/v).

Serial Number	Solvents	MD estimated electric field / (MV/cm)	*Corrected electric field / (MV/cm)
1	Dibutyl ether	-8.36	-3.60
2	Tetrahydrofuran	-17.47	-7.53
3	Valeronitrile	-21.33	-9.19
4	Acetonitrile(ACN)	-27.86	-12.01
5	90%ACN+10%Water	-42.35	-18.25
6	80%ACN+20%Water	-48.28	-20.81
7	70%ACN+30%Water	-55.05	-23.73
8	60%ACN+40%Water	-59.55	-25.67
9	50%ACN+50%Water	-60.78	-26.20

*: MD estimated fields are divided by a correction factor of 2.32 for testosterone to get the corresponding corrected electric fields.

In my previous chapter 3, it has been shown that $n-\pi^*$ electronic transition varies linearly with electrostatic fields for different C=O containing molecules (Figure 3.6) in both protic and aprotic solvation environments. ^{13}C NMR chemical shifts of the C=O carbon and the $n-\pi^*$ absorption wavelengths also show similar linear sensitivities to the corrected electrostatic fields exerted on the C=O axis of testosterone. The straight lines shown in Figure 4.5A, 4.5B, 4.5C can independently calibrate the sensitivities of C=O IR frequency, ^{13}C chemical shift and $n-\pi^*$ wavelength to the electrostatic field exerted on the carbonyl at the testosterone binding site of the serum protein.

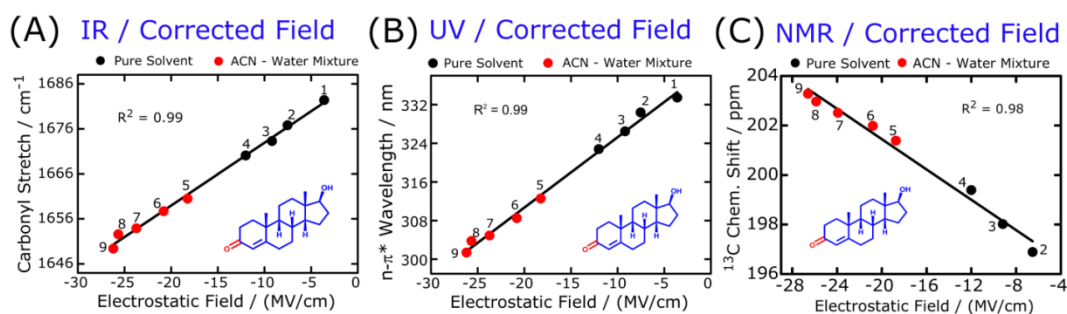


Figure 4.5 Carbonyl stretching frequency (A), n- π^* electronic transition and ¹³C Chemical shifts show linear sensitivities towards the corrected electric field exerted along the C=O bond of testosterone in both non-H-bonding and H-bonding environments. The black solid circles represent aprotic solvents [(1) dibutyl ether, (2) tetrahydrofuran, (3) valeronitrile, (4) acetonitrile] and red solid circles represent aqueous acetonitrile solutions (v/v) [(5) 90% acetonitrile, (6) 80% acetonitrile (7) 70% acetonitrile, (8) 60% acetonitrile, (9) 50% acetonitrile]. The regression values (R²) of the fitted lines are shown in the figures. The black solid line denotes best fitted line.

4.3.3 Estimation of Binding Constant of BSA-Testosterone Complex

Fluorescence quenching measurements have been extensively utilized to study the interaction of organic dyes with protein. In this case, the interaction of testosterone with bovine serum protein (BSA) was studied by the fluorescence measurement at the room temperature. Figure 4.6A shows the effect of increasing concentration of testosterone on the emission spectrum of BSA (Concentration of BSA is 10 μ M). The fluorescence intensity of BSA decreased regularly upon addition of testosterone and there was almost no shift of the emission wavelength with the addition of testosterone. The binding constant is calculated for the quantitative representation of testosterone–BSA binding affinity using the following equation (modified Stern-Volmer equation)²³:

$$\frac{F_0}{F_0 - F} = \frac{1}{f_a} + \frac{1}{K_a f_a [Q]}$$

Where K_a is the effective quenching constant for the accessible fluorophores and f_a is the fraction of accessible fluorescence, $(F_0 - F)$ or ΔF is the difference in steady-state fluorescence intensity between the absence and presence of quencher at concentration $[Q]$. The dependence of $F_0/(F_0 - F)$ on the reciprocal value of the quencher concentration $[Q]^{-1}$ is linear, with slope equal to the value of $(f_a K_a)^{-1}$. Figure 4.6 B displays the modified Stern-Volmer plots and the corresponding binding constant (K_a) value for BSA-testosterone system, obtained from the slope of the linear-fit, was estimated to be $8.89 (\pm 1) \times 10^4 \text{ M}^{-1}$, which is in good agreement with that reported by Riahi and co-workers $5.5 \times 10^4 \text{ M}^{-1}$.²⁴

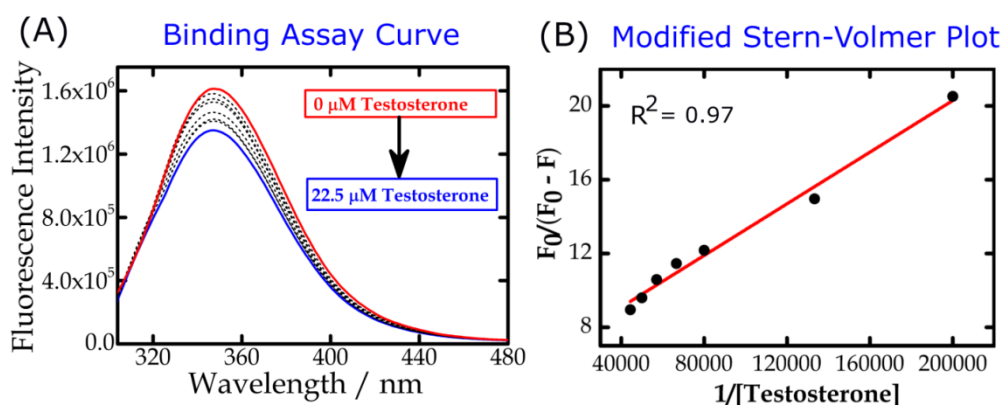


Figure 4.6 Fluorescence quenching study of the tryptophan residues in BSA by testosterone. (A) Steady-state fluorescence spectra of BSA (10μM) in 20mM aqueous phosphate buffer (pH 7.2) in the presence of testosterone with the concentration: (a) 0 μM, (b) 5 μM, (c) 7.5 μM, (d)12.5 μM, (e)15 μM, (f)17.5 μM, (g)20.0 μM, (h)22.5 μM. The fluorescence spectra were recorded in the wavelength range of 300-450 nm by exciting BSA at 290 nm. (B) Plot of $F_0/(F_0 - F)$ versus $1/[Testosterone]$ for tryptophan fluorescence quenching of the protein by testosterone.

4.3.4 Prediction of Electric Field inside Protein Interior

For the spectroscopic experiments of protein-steroid complex, 1 mM of testosterone was added to 1.5 mM BSA solution in phosphate buffer (pH = 7.0). At these concentrations >99% of the steroid is bound to the serum protein, implying that the detected spectroscopic signals of the ligand reflect that of the bound state. The $n-\pi^*$ absorption wavelength and the C=O stretching frequency of testosterone observed in 1:1 BSA-testosterone complex are 312.6 nm (Figure 4.7B) and 1661.7 cm^{-1} (Figure 4.7C), respectively. It is important to note that the experimentally observed C=O IR frequency shows excellent agreement with the frequency predicted from the $n-\pi^*$ wavelength, 1660.8 cm^{-1} , by the calibration curve in Figure 4.3A.

The corresponding electrostatic fields predicted from the peak maxima of the $n-\pi^*$ absorption spectrum and the C=O IR spectrum at the BSA binding site of testosterone are -18.70MV/cm and -18.03MV/cm (Figure 4.7D), respectively. A negligible ~3.5% error in the field estimation from the independent spectroscopic techniques illustrates that either of these non-invasive experimental methods can be used to predict the local electric field at the binding site of the protein.

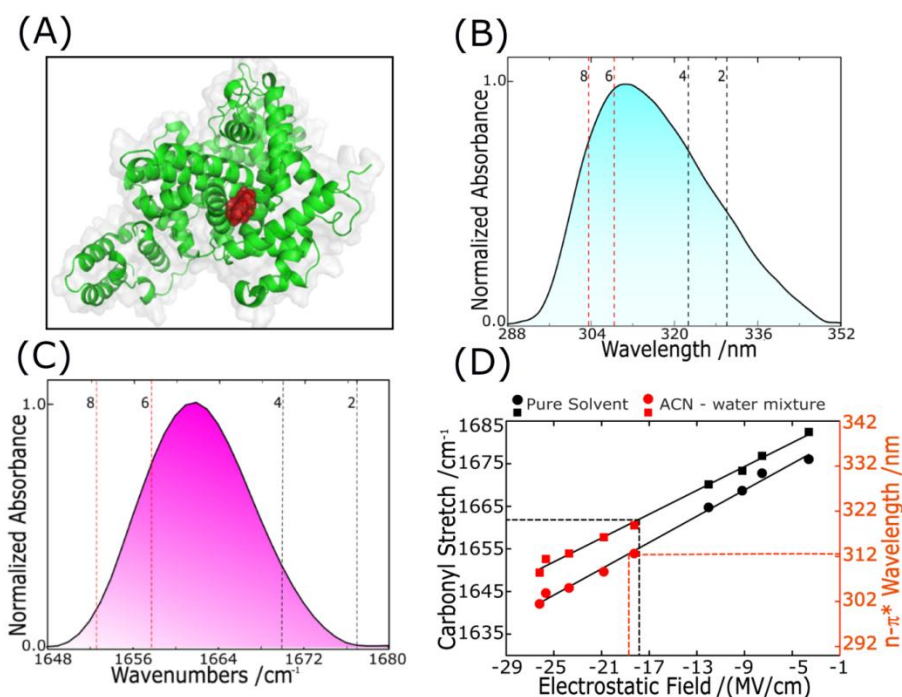


Figure 4.7 A cartoon of BSA-testosterone complex is shown in 4.7A. The protein is shown is green and the substrate is shown in red. (4.7B) The $n-\pi^*$ absorption spectra and (4.7C) the IR spectra of C=O stretch of testosterone in BSA-testosterone complex can be used to estimate the local polarity at the binding site of BSA using electric field (4.7D). The predicted electric fields from UV/VIS and IR experiments are within 0.7 MV/cm (error $\sim 3.5\%$). The dotted vertical lines in 4.7B and 4.7C represent the peak maxima of aprotic solvents and binary aqueous mixtures. The numbers (2, 4, 6, and 8) correspond to those in column 1 of Table 4.1.

Apparently, testosterone senses a large electric field at the binding site of BSA that is similar to that sensed by testosterone in a polar (10% acetonitrile/water) solvent. The electric fields in solution are homogeneous and increase with the overall solvent polarity. However, a nominally non-polar protein matrix with surface charges can produce an inhomogeneous electric field similar to that in polar solvation environment required for the spectroscopic shift. In a recent work by Boxer and coworkers, an extremely large electric field was found to be exerted on the substrate by the oxyanion hole at the active site of an enzyme.¹⁴ Semi-empirical polarity

parameters only provide a qualitative understanding and fail to depict a microscopic description of the structure function relation. The electrostatic field on the other hand serves as a quantitative and microscopic descriptor of local electrostatics and can be estimated from multiple choices of spectroscopic experiments as well as molecular dynamics (MD) simulations.

4.4 Conclusion

The implications of these results are manifold. We have shown that either of IR, UV/VIS, or ^{13}C NMR experimental techniques can be used to calibrate the local electric field within protein interiors. Choice of the spectroscopic technique depends on the concerned biological/chemical process. For example, $n-\pi^*$ absorption might be the favored technique to determine electric field for protein-ligand complexes where the absorption peak of the ligand can be monitored, as shown in this work. A long wavelength $n-\pi^*$ absorption of the ligand (as seen in testosterone) has less overlap with the protein absorption as compared with the overlap of the carbonyl stretch with the amide I protein IR band. Another inherent technical advantage of UV/VIS spectroscopy over IR spectroscopy in case of protein ligand complexes arises from the ease of subtracting the background protein spectra. The commonly used IR sandwich sample cells make it difficult to maintain the same path-length in individual IR measurements. However, no such error from the reproducibility of the path-length arises for the standard cuvettes (fixed path-length) used for UV/VIS absorption experiments. On the other hand, isotope editing ($^{13}\text{C}=\text{O}$ or $^{13}\text{C}=\text{O}^{18}$) has been extensively used to isolate the C=O frequencies of a specific amino acid in a protein. In such cases, both IR as well as ^{13}C NMR will be able to provide the local electric field within the protein interior. However, electric field should be projected along the

direction of the transition dipole of the amide normal mode which is not along the C=O bond as shown here for testosterone. These results are also significant from the computational viewpoint. When crystal structures are unavailable for protein-substrate complexes, molecular docking provides a snapshot of the orientation of the substrate with the biomolecule. However, multiple orientations of the ligand with respect to the receptor might be equally probable as predicted from docking studies. MD simulations of each of these conformers and subsequent electric field estimation when compared with the electric field predicted from the spectroscopic experiments can underpin the orientation of the substrate at the binding site and provide a molecular level picture of the biological process.

4.5 References

1. Warshel, A. Electrostatic Basis of Structure-Function Correlation in Proteins. *Acc. Chem. Res.* 1981, *14*, 284-290.
2. Perutz, M. Electrostatic Effects in Proteins. *Science* 1978, *201*, 1187-1191.
3. K A Sharp, a.; Honig, B. Electrostatic Interactions in Macromolecules: Theory and Applications. *Annu. Rev. Biophys. Biophys. Chem.* 1990, *19*, 301-332.
4. Honig, B.; Nicholls, A. Classical Electrostatics in Biology and Chemistry. *Science* 1995, *268*, 1144.
5. Simonson, T. Macromolecular Electrostatics: Continuum Models and Their Growing Pains. *Curr. Opin. Struct. Biol.* 2001, *11*, 243-252.
6. Warshel, A.; Papazyan, A. Electrostatic Effects in Macromolecules: Fundamental Concepts and Practical Modeling. *Curr. Opin. Struct. Biol.* 1998, *8*, 211-217.
7. Macgregor, R. B.; Weber, G. Estimation of the Polarity of the Protein Interior by Optical Spectroscopy. *Nature* 1986, *319*, 70-73.

8. Zhuang, Y.-D.; Chiang, P.-Y.; Wang, C.-W.; Tan, K.-T. Environment-Sensitive Fluorescent Turn-On Probes Targeting Hydrophobic Ligand-Binding Domains for Selective Protein Detection. *Angew. Chem., Int. Ed* 2013, *52*, 8124-8128.
9. Reichardt, C. Solvatochromic Dyes as Solvent Polarity Indicators. *Chem. Rev.* 1994, *94*, 2319-2358.
10. Grunwald, E.; Winstein, S. The Correlation of Solvolysis Rates. *J. Am. Chem. Soc.* 1948, *70*, 846-854.
11. Kosower, E. M. The Effect of Solvent on Spectra. I. A New Empirical Measure of Solvent Polarity: Z-Values. *J. Am. Chem. Soc.* 1958, *80*, 3253-3260.
12. Langhals, H. Polarity of Binary Liquid Mixtures. *Angew. Chem. Int. Ed. Engl.* 1982, *21*, 724-733.
13. de Dios, A.; Pearson, J.; Oldfield, E. Secondary and Tertiary Structural Effects on Protein NMR Chemical Shifts: an ab Initio Approach. *Science* 1993, *260*, 1491-1496.
14. Fried, S. D.; Bagchi, S.; Boxer, S. G. Extreme Electric Fields Power Catalysis in the Active site of Ketosteroid Isomerase. *Science* 2014, *346*, 1510-1514.
15. Fried, S. D.; Bagchi, S.; Boxer, S. G. Measuring Electrostatic Fields in Both Hydrogen-Bonding and Non-Hydrogen-Bonding Environments Using Carbonyl Vibrational Probes. *J. Am. Chem. Soc.* 2013, *135*, 11181-11192.
16. Renge, I. Solvent Dependence of $n-\pi^*$ Absorption in Acetone. *J. Phys. Chem. A* 2009, *113*, 10678-10686.
17. Fried, S. D.; Boxer, S. G. Measuring Electric Fields and Noncovalent Interactions Using the Vibrational Stark Effect. *Acc. Chem. Res.* 2015, *48*, 998-1006.
18. Deb, P.; Haldar, T.; Kashid, S. M.; Banerjee, S.; Chakrabarty, S.; Bagchi, S. Correlating Nitrile IR Frequencies to Local Electrostatics Quantifies Noncovalent Interactions of Peptides and Proteins. *J. Phys. Chem. B* 2016, *120*, 4034-4046.
19. Kashid, S. M.; Bagchi, S. Experimental Determination of the Electrostatic Nature of Carbonyl Hydrogen-Bonding Interactions Using IR-NMR Correlations. *J. Phys. Chem. Lett.* 2014, *5*, 3211-3215.

20. Boxer, S. G. Stark Realities. *J. Phys. Chem. B* 2009, *113*, 2972-2983.
21. Augspurger, J. D.; Dykstra, C. E.; Oldfield, E. Correlation of Carbon-13 and oxygen-17 Chemical shifts and the Vibrational Frequency of Electrically Perturbed Carbon monoxide: a Possible Model for Distal Ligand Effects in Carbonmonoxyheme Proteins. *J. Am. Chem. Soc.* 1991, *113*, 2447-2451.
22. Haldar, T.; Bagchi, S. Electrostatic Interactions Are Key to C=O n- π^* Shifts: An Experimental Proof. *J. Phys. Chem. Lett.* 2016, *7*, 2270-2275.
23. Lehrer, S. Solute Perturbation of Protein Fluorescence. Quenching of the Tryptophyl Fluorescence of Model Compounds and of Lysozyme by Iodide Ion. *Biochemistry* 1971, *10*, 3254-3263.
24. Chanphai, P.; Vesper, A. R.; Bekale, L.; Berube, G.; Tajmir-Riahi, H. A. Transporting Testosterone and its Dimers by Serum Proteins. *J. Photochem. Photobiol.* 2015, *153*, 173-183.

Chapter 5

Stark Consequences of Reichardt's Dye

5.1 Introduction

Solvatochromic dyes play a key role in the understanding of solvent polarity effects and are increasingly important as probes of complex biological systems.¹⁻³ The $E_T(30)$ scale, derived from the electronic absorption of the betaine dye 2,6-diphenyl-4-(2,4,6-triphenylpyridinium-1-yl)phenolate (Reichardt's dye), has been the most widely applied empirical solvent polarity scale.⁴⁻⁵ The linear correlation between the emission peak maxima of a fluorophore and the corresponding $E_T(30)$ values in different solvents allows us to determine the polarity within protein interiors.⁶⁻⁹ However, little has been understood regarding the origin of this universal correlation between $E_T(30)$ and almost any existing fluorophore, other than its solvent sensitivity is due to large dipolar difference between the ground and the excited state. In spite of the scarcity in adequate understanding behind its working principle, it has found its use in detecting polarity of active site of enzyme, solvation difference between minor and major groove of DNA, complex inhomogeneous solvation environment inside a reverse micelles, etc.^{4, 9-13} However, for those distinct environments, polarity on the basis of $E_T(30)$ parameter provides a vastly simplistic average picture and is inadequate to capture the micro heterogeneity due to specific interaction of charged and polar groups towards the fluorophore. We therefore need the understanding behind this remarkable solvent sensitivity and need to find more microscopic details of heterogeneous solvent environment.

Interestingly, Stark effect predicts linear sensitivity of the peak frequencies to the electric field exerted by the environment on the probe molecule.¹⁴⁻¹⁵ The solvatochromic shift in peak frequencies ($\Delta\bar{\nu}$) can be related to the change in the exerted electric fields ($\Delta\vec{F}$) through the relation:¹⁵⁻¹⁸ $\Delta\bar{\nu} = \Delta\vec{\mu} \cdot \Delta\vec{F}$, where $\Delta\vec{\mu}$, known

as the Stark tuning rate, is the change in dipole moment between the two states involved in the transition. The field-frequency correlation suggests that $\Delta\vec{\mu}$ is independent of the solvation environment. As $E_T(30)$ scale has been derived from the electronic absorption of Reichardt's dye, it is worth investigating whether this semi-empirical polarity scale has electronic Stark effect as its origin.

5.2 Materials and sample preparation

Coumarin 1 [7-Diethylamino-4-methyl coumarin], PRODAN [N,N-dimethyl-6-propionyl-2-naphthylamine], human serum albumin (HSA), solvents like diethyl ether (DEE), dibutyl ether (DBE), tetrahydrofuran (THF), valeronitrile (VLN), acetonitrile (ACN), dimethyl sulphoxide (DMSO), and D₂O were obtained from Sigma Aldrich and used without further purification. All the organic dyes were dissolved independently in neat organic solvents and protic binary aqueous mixtures (DMSO/water) such that the final concentration of liquid sample is 10 mM for the solvatochromic IR studies. As both dyes are not soluble (or sparingly soluble) in neat water or in dmsO/water mixtures (with high water content (> 60% v/v)), we have reported spectroscopic results up to 50% dmsO/water (v/v). For recording the IR spectra of organic dye in each solvent (or solvent mixture) 100 scans were collected.

5.3 Results and discussion

5.3.1 Origin of $E_T(30)$ parameter

Upon dissolving a dye molecule (e.g Reichardt's dye) with a permanent dipole moment in any solvent, the dipoles of the solvent molecules reorient to the same general direction as that of the solute, thereby minimizing the system's potential energy.¹⁹ Because the solvent molecules are no longer randomly oriented, the electric fields created by their own permanent dipoles no longer cancel out, and so they exert

a net electric field onto the dye. The exerted field depends on the magnitude of the dipole of the dye and the polarity of the solvent. Electronically excited state of the dye typically possesses a dipole of different magnitude and orientation relative to the ground state. However, for an instantaneous electronic absorption of the dye molecule, the solvent molecules are oriented in a way to stabilize the ground state's dipole moment (Frank Condon principle). The Stark tuning rate, $\Delta\vec{\mu}$, will thus be given by $\Delta\vec{\mu} = \mu_e \cos(\theta) - \mu_g$, where θ is the angle between the ground and the excited state dipole moments.

5.3.1.1 Correlation between π - π^* absorption frequency with electrostatic field for Reichardt's dye

To measure the difference dipole moment of Reichardt's dye molecule in the ground and the first excited electronic state, quantum calculations were performed on the pyridinium N-phenolate betaine dye in a wide range solvation environment of varying polarity. The results are presented in table 5.1.

It is forthcoming from the Table 5.1 that the difference dipole moment ($\Delta\vec{\mu}$) is solvent independent within the error limit, thereby showing electrostatic behavior according to linear Stark model. The $E_T(30)$ value is measured from the maximum wavelength of the π - π^* absorption band of this Reichardt's dye in a great variety of solvents using equation 1.⁴⁻⁵

$$E_T(30) / (Kcal mol^{-1}) = 28591 / \lambda_{max} (nm) \quad [1]$$

Table 5.1 Dipole moment in the ground and excited states, the angle (θ) between ground and the excited state dipole moments, and the change in dipole moment ($\Delta\vec{\mu}$) for the pyridinium N-phenolate betaine dye in different neat organic solvents with varying polarity.

Solvent name	State	μ_x	μ_y	μ_z	Angle(Θ)	$\Delta\vec{\mu}$
Tetrahydrofuran (THF)	Ground State	19.3995	12.5156	0.5162	10.71	-21.83
	Excited State	1.1163	0.5898	0.2404		
Hexane	Ground State	15.6556	10.3321	0.2683	175.94	-20.38
	Excited State	-1.3228	-0.9188	-0.1309		
Dibutyl ether (DBE)	Ground State	17.6539	11.4113	0.3427	162.09	-21.41
	Excited State	-0.2816	-0.2763	0.0897		
Dimethyl sulphoxide (DMSO)	Ground State	20.5570	13.1851	0.6000	6.59	-21.99
	Excited State	2.0919	1.2265	0.3232		

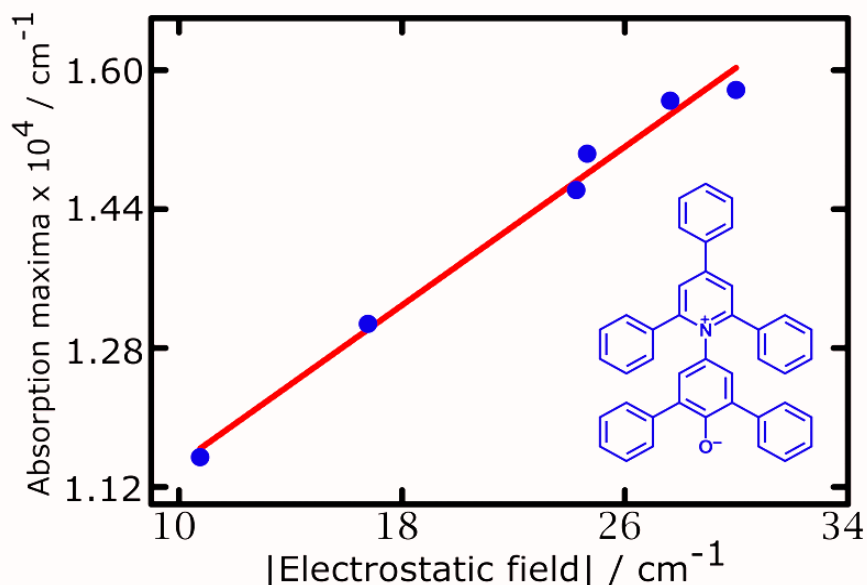


Figure 5.1 π - π^* absorption peak maxima plotted against electrostatic field along C-O axis of pyridinium N-phenolate betaine dye in different neat organic solvents (blue solid circles) of varying polarity. The regression values (R^2) of the fitted line is 0.97. The red solid line indicates best fit line. The equation for this best fitted line is $\bar{\nu}_{abs} = 256.1 |\vec{F}_{C=O}| + 9095.3$.

As the electronic absorption shows the characteristic of Stark behavior, the electric fields in different solvents with varying polarity should also correlate with the absorption values in the respective solvents.¹⁹ To further establish this point, we have estimated average electrostatic fields exerted on the Reichardt's dye along the C-O axis in all the different solvation environment using atomistic molecular dynamics (MD) simulations. The electrostatic fields calculated from MD simulations for the pyridinium N-phenolate dye in various solvents are tabulated (Table 5.2). Previously, the values of $E_T(30)$ parameter have been reported by Reichardt et.al and the corresponding maximum absorption frequency was calculated using equation 1. An excellent linear correlation is obtained between π - π^* absorption peak maxima and electrostatic fields (Figure 5.1) for Pyridinium N-phenolate betaine dye in aprotic solvation environments.

Table 5.2 Absolute values of the absorption peak maxima and the MD estimated electric fields along the C-O axis for pyridinium N-phenolate betaine dye in different neat organic solvents with varying polarity.

Solvent	$E_T(30)$ (Kcal mol ⁻¹)	Absorption Maxima(cm ⁻¹)	Electric Field / (MV/cm)
Dibutyl ether	33	11542.1	-10.75
Tetrahydrofuran	37.4	13081.1	-16.78
Propionitrile (PPN)	43.6	15249.5	-24.64
Acetonitrile (ACN)	45.6	15949.1	-27.62
DMSO	45.1	15774.2	-29.99
Valeronitrile (VLN)	41.8	14619.9	-24.25

5.3.2 Validation of Stark consequence for $E_T(30)$ dye

It is quite evident from the Stark explanation of $E_T(30)$ dye that the solvatochromic parameters are the manifestation of the solvent electric field on the dye molecule. So $\Delta\vec{\mu}$ for electronic transitions in different organic dye molecules causes the fluorescence peak maxima of dyes to change in solvents of varying polarity.¹⁹⁻²⁰ A similar solvatochromic shift has been reported for vibrational (IR) transitions like the carbonyl (C=O) stretch. Using vibrational Stark effect spectroscopy it has been proved that C=O IR stretching frequencies are sensitive towards the solvation environment.^{15, 17, 21} So, if the $E_T(30)$ series is solely due to the sensing of local electrostatics then carbonyl vibrational probe containing fluorescent dye should also show a similar type of linear correlation between IR and the fluorescence peak maxima.

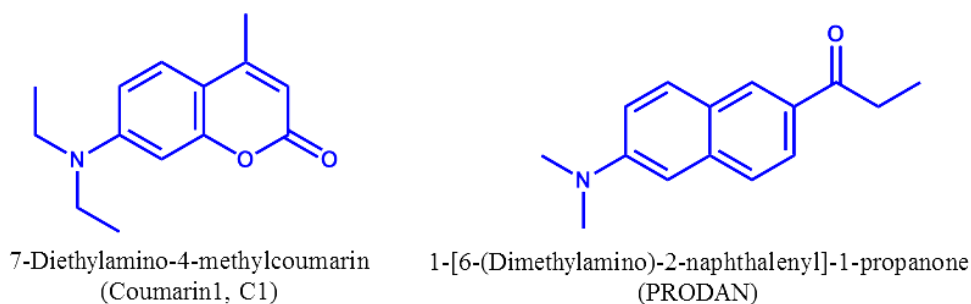


Figure 5.2 Molecular structure and abbreviations of the solvatochromic probes used.

In order to test our hypothesis, we have chosen two model C=O vibrational probe containing different fluorophores, such as coumarin dye i.e. coumarin1 (C1) and naphthalene dye i.e. N, N-dimethyl-6-propionyl-2-naphthylamine (PRODAN) (Figure 5.2). These molecules are commonly employed in determining local electrostatics in biomolecules and heterogeneous solvent mixture owing to its extremely environment-sensitive fluorescence property.²²⁻²³ Environment sensitivity of fluorescence on these dyes are attributed to the presence of an electron-donating substituted amino group at one end and an electron-accepting carbonyl (-C=O) group in the opposite position forming a donor- π - acceptor system having charge transfer transition from the donor to the acceptor moiety.

5.3.2.1 Steady-State Fluorescence Measurements

Both the fluorescent dyes (C1 and PRODAN) are dissolved in various solvents of varying polarity to perform the fluorescence experiments.

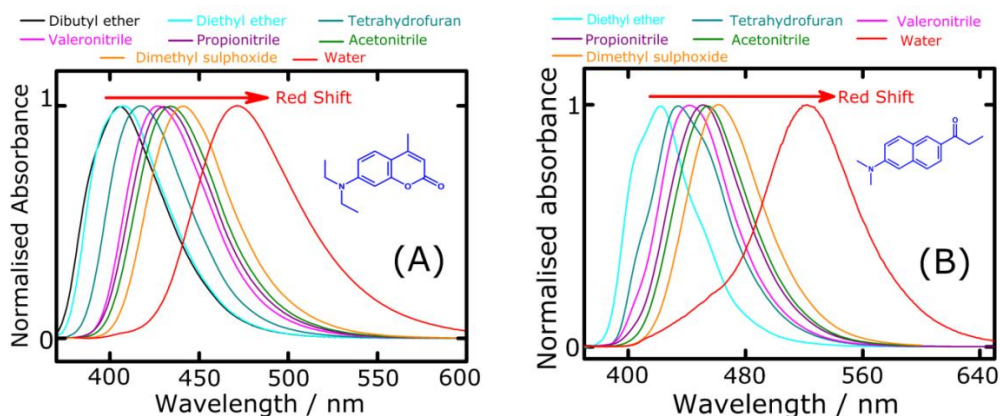


Figure 5.3 Solvatochromic π - π^* emission spectra of coumarin 1 (A) and PRODAN (B) in a number of neat organic solvents and water. The polarity increases in the direction of the arrow.

The emission peak positions of both the fluorescent dyes show a gradual red shift, thereby exhibiting a strong sensitivity towards the solvent polarity (Figure 5.2A & 5.2B). The red shifts in the emission peak maxima are in good agreement with the trend observed by Barik et al. and Weber et al.²²⁻²³ When both the fluorophores are dissolved in a polar protic solvent like water, emission peak maxima reveal a further red shift as compared with that in DMSO. To further understand the interactions in H-bonding environments, we have scanned the intermediate polarities between DMSO and water by using different DMSO/water solutions, where the percentage of water is gradually increased by 10% (v/v) increments.

5.3.2.2 Vibrational Solvatochromism

We have performed the IR solvatochromism trends on the C=O stretch of both the fluorophores in various neat organic solvents and aqueous DMSO (v/v) solutions.

The FTIR spectrum of C1 displays two bands in the carbonyl region (Figure 5.3A). The lower frequency peak arises from the C=O stretch and the higher frequency one has been previously attributed to Fermi resonance.²⁴ The dual absorption spectra are

fitted to two peaks with Voigt lineshape to obtain the carbonyl stretching frequency ($\bar{\nu}_{C=O}$), as shown in Figure 5.3B. The C=O stretch being ideal for the manifestation of the Stark effect shows a linear variation of peak maxima with the change in electrostatic field as evident from picture 5.5A. The C=O stretching frequency of C1 is progressively red-shifted as the solvation environment changes from a non-polar solvent (dibutyl ether) to a polar aprotic solvent (DMSO), with an overall frequency shift of 17.7cm^{-1} (Figure 5.3B). A further red shift was observed when C1 is dissolved in binary water mixtures which are capable of forming H-bond. How a specific interaction like H-bond perturbed micro electrostatic is a much sought after topic. In order to understand that systemic variation of the composition, experiments in DMSO-water mixtures are also performed. Since C1 was partially soluble in water, it has been studied up to 1:1 DMSO/water (v/v) solution. In the binary aqueous mixture, the C=O stretch shows a monotonic red shift with increasing water content (i.e. solvent polarity polarity).

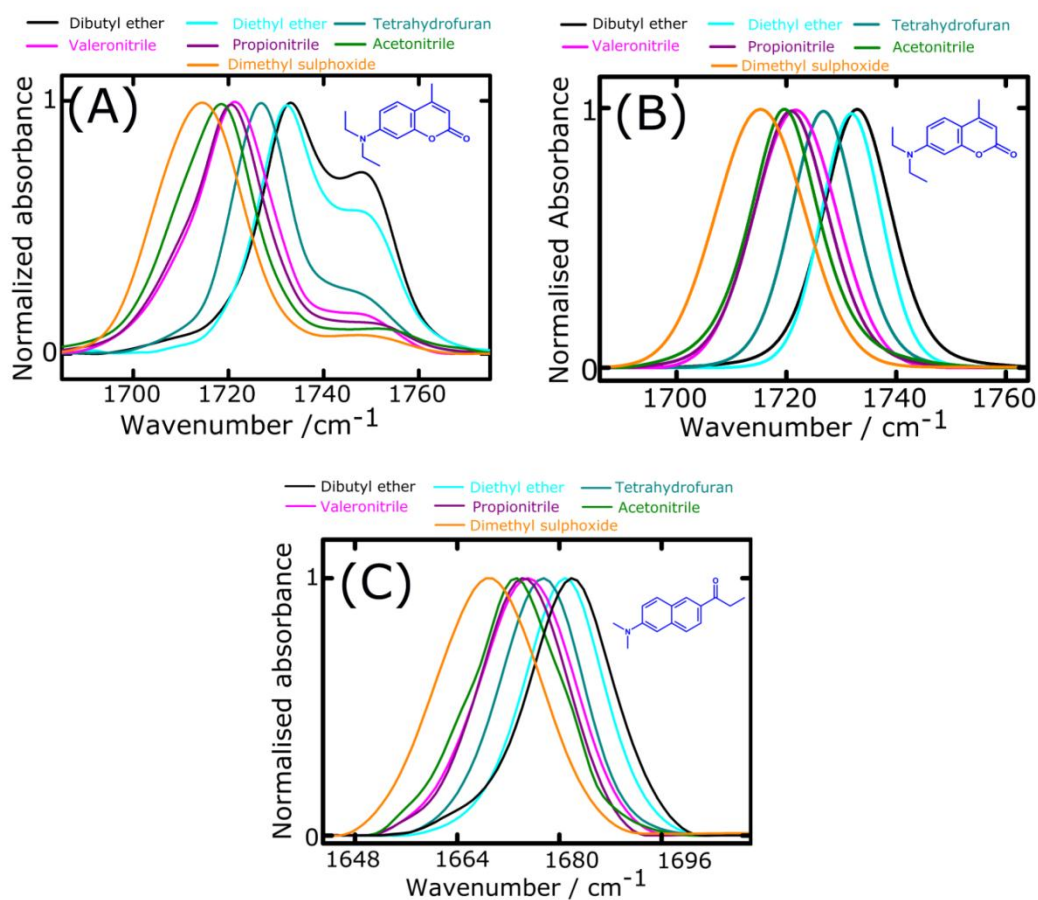


Figure 5.4 Solvatochromic IR studies of coumarin1 and PRODAN. (A) Area normalized FTIR absorption spectra of the C=O stretch of coumarin1 in non-hydrogen bonding solvation environments. (B) Fitted IR absorption spectra of the C=O stretch of coumarin1 in neat organic solvents of varying polarity. (C) Representative FTIR spectra of the C=O stretching band of PRODAN dissolved in a number of neat organic solvents at 10 mM concentration.

A 12.1 cm⁻¹ red shift in $\bar{\nu}_{C=O}$ is observed for PRODAN as the solvation environment is varied from the aprotic non polar solvent dibutyl ether (black) to the aprotic polar solvent DMSO (orange) (Figure 5.3C). However, due to the intrinsic overlap between C=O stretch and Fermi resonance peak, it is impossible to separated out C=O stretching frequency of PRODAN in the binary mixture of DMSO/water solutions.

Absolute values of fluorescence peak maxima and C=O stretching frequencies of both C1 and PRODAN in non-hydrogen-bonding and hydrogen-bonding solvation environments are tabulated in table 5.3 and 5.4 respectively.

Table 5.3 Absolute values of fluorescence peak maxima and C=O stretching frequencies of coumarin1 in non-hydrogen-bonding and hydrogen-bonding solvation environments.

Serial Number	Solvents	Carbonyl stretch / cm ⁻¹	π - π^* Emission Wavelength /nm	π - π^* Emission Wavenumber /(cm ⁻¹)
1	Di Butyl Ether	1732.9	405.6	24654.8
2	Di Ethyl Ether	1731.8	407.3	24551.9
3	Tetrahydrofuran	1726.8	417.7	23940.6
4	Valeronitrile	1721.7	427.3	23402.8
5	Propionitrile	1720.7	430.8	23212.6
6	Acetonitrile	1719.8	433.9	23046.8
7	Dimethyl sulphoxide	1715.2	441.2	22665.4
8	9:1 (D:W)	1711.4	444.6	22492.1
9	4:1 (D:W)	1706.8	449.1	22266.8
10	7:3 (D:W)	1702.3	453.6	22045.9
11	3:2 (D:W)	1699.5	456.3	21915.4
12	1:1 (D:W)	1697.4	458.5	21810.2
13	2:3 (D:W)	No IR peak	463.4	21579.6
14	1:4 (D:W)	No IR peak	467.3	21399.5
15	Water	No IR peak	471.1	21226.9

D: W represents dimethyl sulphoxide–water solution (v/v).

Table 5.4 Absolute values of fluorescence peak maxima and C=O stretching frequencies of PRODAN in non-hydrogen-bonding and hydrogen-bonding solvation environments.

Serial Number	Solvents	Carbonyl stretch / cm^{-1}	$\pi-\pi^*$ Emission Wavelength /nm	$\pi-\pi^*$ Emission Wavenumber /(cm^{-1})
1	Di Butyl Ether	1682.4	-	-
2	Di Ethyl Ether	1680.9	421.9	23700.1
3	Tetrahydrofuran	1677.2	435.1	22981.1
4	Valeronitrile	1675.2	442.2	22613.3
5	Propionitrile	1674.5	451.2	22163.1
6	Acetonitrile	1672.6	454.3	22010.4
7	Dimethyl sulphoxide	1670.3	461.5	21668.5
8	9:1 (D:W)	No IR peak	479.3	20863.1
9	4:1 (D:W)	No IR peak	486.4	20561.3
10	7:3 (D:W)	No IR peak	493.9	20247
11	3:2 (D:W)	No IR peak	497.9	20083
12	1:1 (D:W)	No IR peak	503.7	19853
13	2:3 (D:W)	No IR peak	508.9	19650
14	1:4 (D:W)	No IR peak	516.1	19379.2
15	Water	No IR peak	522.5	19138.7

D: W represents dimethyl sulphoxide–water solution (v/v)

5.3.2.3 Fluorescence – IR Frequency Correlation

As previously reported, the emission maxima ($\bar{\nu}_{emission}$) of the different fluorescent dye is linearly correlated with the $E_T(30)$ parameters in non-H-bonding solvation environments which is used to characterize the solvent polarity.^{3, 25-28} The $E_T(30)$ polarity parameter is an approximate semi-empirical approach and it is not deterministic of the nature of interaction. Recently, it has been also manifested that fluorescence spectroscopy based methodology can be used to measure the electrostatic field in complex solvation environment like deep eutectic solvents.²⁹ So we wanted to check whether a linear correlation exists between fluorescence peak maxima of the fluorophore and the IR peak maxima for C=O containing fluorescent dye molecule.

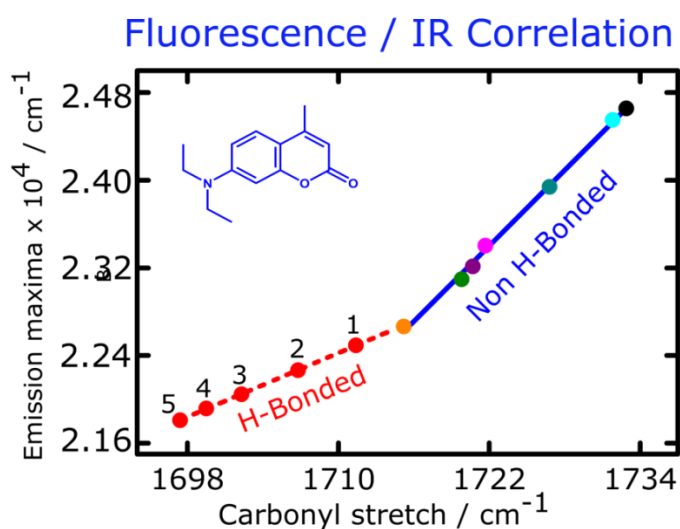


Figure 5.5 Experimentally obtained carbonyl stretching frequency of C1 is plotted against the corresponding emission peak maxima in non-H-bonding (blue line) and H-bonding (red dotted line) solvation environments. Linear correlation is observed (solid blue lines) for C1 in aprotic solvents (non H-bonded C=O), whereas, a deviation from linearity is observed in protic solvation environment (H-bonded C=O). The red circles represent protic binary solvent mixtures [(1) 9:1 (D:W), (2) 4:1 (D:W), (7) 7:3 (D:W), (8) 3:2 (D:W), (9) 1:1 (D:W)].

We have plotted between emission maxima ($\bar{\nu}_{emission}$) against the carbonyl stretching frequencies ($\bar{\nu}_{C=O}$) of C1 dye molecule in the respective aprotic solvents. It shows an excellent linear correlation with a regression coefficient (R^2) value of 0.99 (Figure 5.4). In case of protic solvents (i.e. aqueous DMSO solutions) that can form at least one H-bond with the ketone C=O, a deviation from the linear correlation is observed (Figure 5.4).

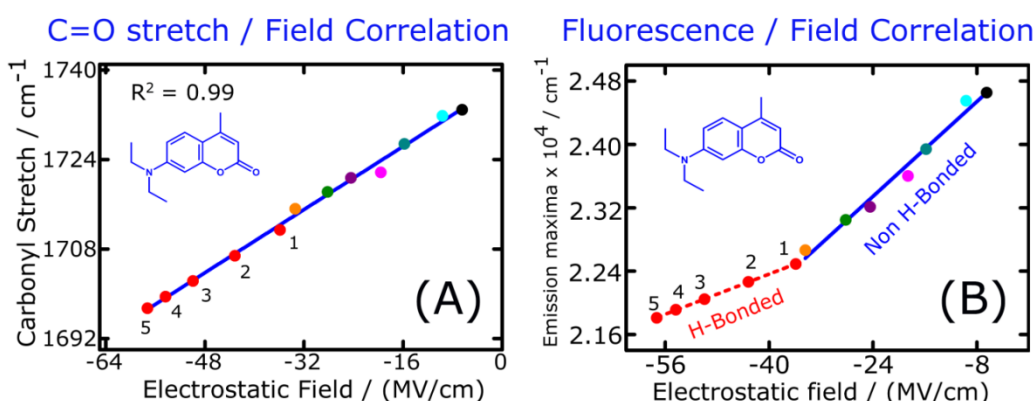


Figure 5.6 (A) Carbonyl stretching frequency versus electrostatic field exerted on the C=O of the C1 calculated by MD simulation of C1 dissolved in different non-hydrogen bonding and hydrogen bonding solvents. The regression values (R^2) of the fitted lines are shown in the figures. The blue line denotes best fitted line. The equation for this best fitted line is $\bar{\nu}_{C=O} = 0.703 (F_{C=O}) + 1737.6$. (B) Plot of fluorescence peak maxima C1 in different solvation environments compared against the average electrostatic field C=O experiences in each solvents, as calculated by MD simulation. Blue (solid) and red (dotted) lines indicate best fitted line of the Non H-bonded and H-bonded solvents respectively. The red circles represent protic binary solvent mixtures [(1) 9:1 (D:W), (2) 4:1 (D:W), (3) 7:3 (D:W), (4) 3:2 (D:W), (5) 1:1 (D:W)]. The equation of the best fit line for C1 in non H-bonding solvents is $\bar{\nu}_{emission} = 74.8 (F_{C=O}) + 25138, (R^2 = 0.987)$.

For H-bonded solvation environment, slope of the line changes indicating an inherent sensitivity of fluorescence with the H-bond. So from this dual experimental approach, we can easily to detect the coumarin1 C=O H-bonding status. A covariance of two

experimentally measurable observables, IR and emission frequencies, with different sensitivities to C=O H-bond provides an experimental way out toward conclusive detection of C=O H-bond.

5.3.2.4 Fluorescence – Electric field Correlation

To understand the dependency of electric field on microscopic heterogeneity, we have calculated the electrostatic field exerted along the C=O bond axis using MD simulations. A linear correlation is obtained between C=O stretching frequencies and the calculated electrostatic fields for coumarin1 in both protic and aprotic solvation environment (Figure 5.5A). These results go along with our previous studies and corroborate that no separated semi-empirical parameters are needed for the hydrogen bonding and non-hydrogen bonding solvent.³⁰ The linear dependency of the IR frequency shifts on the electrostatic fields raises the question about the nature of relationship between solvatochromic shift of emission maxima and the electrostatic fields. A strong linear correlation is observed between emission peak maxima and electrostatic field for C1 in aprotic solvents with R^2 value 0.98 but the correlation is violated when we have dissolved C1 dye in protic solvents (Figure 5.5). However, previous studies involving semi empirical scales could not accommodate specific interactions like H-bonding and also lacks the microscopic details necessary to understand heterogeneous solvent environment.^{3, 5} The electrostatic field being direct reporter of local electrostatic environment negates the reliance on any semi empirical parameters.

5.3.2.5 Prediction of Electric Field inside Protein Interior Using Fluorescence

Spectroscopy

To interrogate the local electrostatics inside protein interiors, the local electric field at the PRODAN binding site of human serum albumin (HSA) has been probed in the present study. The environmentally sensitive fluorescent probe, PRODAN, also shows an excellent linear correlation between the C=O IR stretch and the emission peak maxima in aprotic solvents with R^2 value 0.98 (Figure 5.6A).

Table 5.5 MD estimated and corrected electric fields experienced by the carbonyl for PRODAN in neat organic solvents and dimethyl sulphoxide/water binary mixtures (v/v).

Serial Number	Solvents	MD estimated electric field / (MV/cm)	*Corrected electric field / (MV/cm)
1	Di Butyl Ether	-6.87	-2.44
2	Di Ethyl Ether	-8.03	-2.86
3	Tetrahydrofuran	-14.68	-5.06
4	Valeronitrile	-17.21	-5.93
5	Propionitrile	-20.68	-7.13
6	Acetonitrile	-24.37	-8.40
7	Dimethyl sulphoxide	-27.44	-9.46
8	9:1 (D:W)	-30.1	-10.4
9	4:1 (D:W)	-33.7	-11.62
10	7:3 (D:W)	-40.08	-13.82
11	3:2 (D:W)	-42.28	-14.57
12	1:1 (D:W)	-46.36	-16.68
13	2:3 (D:W)	-51.11	-17.62
14	1:4 (D:W)	-57.4	-19.79
15	Water	-63.87	-22.02

*: MD estimated fields are divided by a correction factor of 2.81 for PRODAN to get the corresponding corrected electric fields.

Fluorescence / IR Correlation C=O stretch / Field Correlation

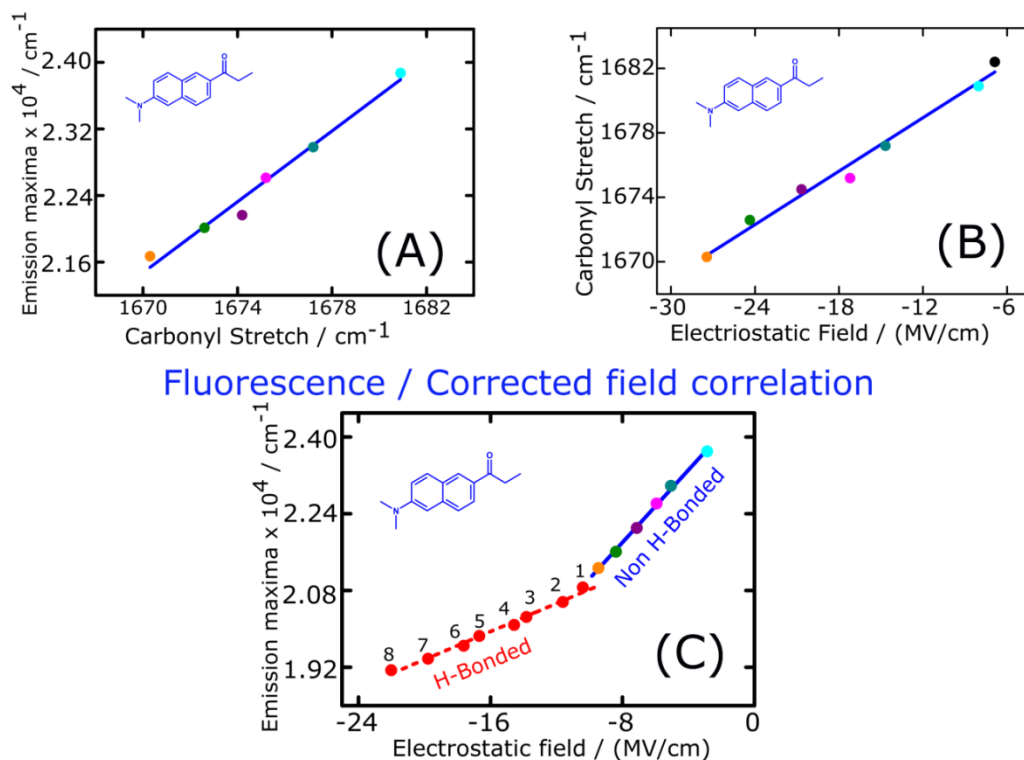


Figure 5.7 (A) Experimentally obtained carbonyl stretch of PRODAN is plotted against the corresponding emission peak maxima in non-H-bonding (blue line) solvation environments. Linear correlation is observed (solid blue lines) for PRODAN in aprotic solvents (non-H-bonded C=O). The regression value for best fit line is 0.98. (B) Carbonyl stretching frequency versus electrostatic field exerted on the C=O of the PRODAN calculated by MD simulation of PRODAN dissolved in different non-hydrogen bonding solvents. The regression value for best fit line is 0.99. The blue line denotes best fitted line. The equation for this best fitted line is $\bar{\nu}_{C=O} = 0.636 (F_{C=O}) + 1687.8$. (C) Plot of fluorescence peak maxima PRODAN in different solvation environments compared against the average electrostatic field C=O experiences in each solvents, as calculated by MD simulation. Blue (solid) and red (dotted) lines indicate best fitted line of the Non H-bonded and H-bonded solvents respectively. The red circles represent protic binary solvent mixtures [(1) 9:1 (D:W), (2) 4:1 (D:W), (3) 7:3 (D:W), (4) 3:2 (D:W), (5) 1:1 (D:W), (6) 2:3 (D:W), (7) 1:4 (D:W), (8) water]. The equation of the best fit line for PRODAN in non H-bonding solvents is $\bar{\nu}_{emission} = 377.7 (F_{C=O}) + 24824.2, (R^2 = 0.99)$.

ACEDAN (2-Acetyl-6-(dimethyl amino) naphthalene) is a fluorescent probe with a very similar structure to that of PRODAN. The connectivity around the C=O moiety is also near about the same for both the molecules. Boxer and coworkers have experimentally measured the Stark tuning rate of ACEDAN and the corresponding reported value is $1.8 \text{ cm}^{-1} / (\text{MV}/\text{cm})$.¹⁶ We have estimated the electrostatic field being exerted along the C=O of PRODAN using molecular dynamics (MD) simulations in all the different solvation environments of the solvatochromic experiments. When we plotted C=O stretching frequencies against the calculated electrostatic fields, it shows a linear correlation with slope ~ 0.64 (Figure 5.6B). The calculated electrostatic fields were scaled down by a factor of 2.81 to make the slope equal to the experimentally measured value. This divergence appears from the local field effect and is comparable with the reported value of the local field correction factor, $f \sim 2$.¹⁵ The electrostatic fields calculated from the MD simulations for all the different solvation environments, along with the corresponding corrected field values are listed in Table 5.5 and equations of the best fit line of the plot using the corrected field is given in the caption of Figure 5.6. $\bar{\nu}_{\text{emission}}$ of PRODAN shows an excellent linear sensitivity with the corrected electrostatic field in aprotic solvents (Figure 5.6C). Also similar trends are observed when we plotted fluorescence maxima against corrected electrostatic field in protic solvents as mentioned previously for C1 dye (Figure 5.6C). A deviation from the linear covariance of $\bar{\nu}_{\text{emission}}$ and corrected electrostatic field in protic solvents is indicative of the presence of C=O H-bond. So from this fluorescence/field correlation, we can easily detect the C=O hydrogen bonding status. Additionally, this also allows us to determine $\vec{F}_{\text{C=O}}$ using the experimentally measured $\bar{\nu}_{\text{emission}}$ in any unknown complex environment.

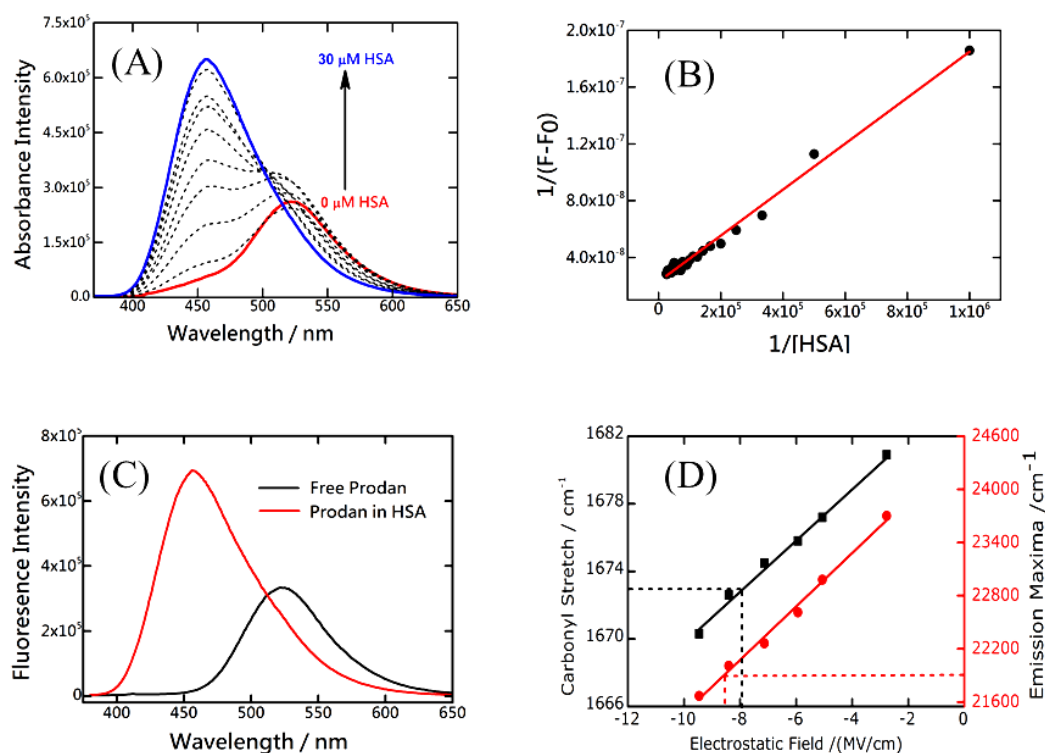


Figure 5.8 (A) Emission spectra of PRODAN (10 μ M) as a function of HSA concentration. (B) Plot of $1/(F-F_0)$ versus $1/[HSA]$. (C) Emission spectra of PRODAN-HSA 1:1 complex in buffer and free PRODAN in buffer. (D) The predicted electrostatic fields from both emission and IR experiments are within 0.6 MV/cm.

To extend the reach of the study, PRODAN is being used to locate the nature of interaction and local electrostatics inside the cavity of protein-ligand complex. Here we have reported the interaction at the binding site of PRODAN- human serum albumin (HSA) 1:1 inclusion complex (Figure 5.7A). The binding constant value (K_a) of the PRODAN with HSA has been determined from the integrated fluorescence intensity data using modified Benesi-Hildebrand equation:³¹

$$\frac{1}{(F_x - F_0)} = \frac{1}{(F_\infty - F_0)} + \frac{1}{(F_\infty - F_0)K_a L}$$

Where, F_0 , F_x , and F_∞ are the fluorescence intensities of the PRODAN in the absence of HSA, at an intermediate HSA concentration, and at a concentration of complete interaction, respectively, and $[L]$ is the HSA concentration. From the slope and

intercept of the above equation we calculated the binding constant value for HSA-PRODAN 1:1 complex of $1.5 \times 10^5 \text{ M}^{-1}$ (Figure 5.7B). This estimated value shows good agreement with the previously reported value of K_a by Ahmed H. Zewail and his co-workers,³² Gonzalez-Jimenez and his co-workers.³³ Using that binding constant value, concentration of PRODAN and HSA are optimized to make >99% fluorophores bound to the serum protein. Figure 5.7A shows that a monotonic enhancement in the fluorescence intensity of the PRODAN is observed along with hypsochromic (blue) shift upon gradual addition of HSA. The blue shift in the emission spectrum indicates the PRODAN binds in a less polar site of HSA. Also the enhancement of the fluorescence intensity is due to restriction of the internal motion within the cavity of HSA-PRODAN binding complex and thereby disfavoring non-radiative decay pathway.

In the bound state, the emission maxima of PRODAN is observed at 457 nm (Figure 5.7C). Also in the 1:1 HSA- PRODAN complex, the carbonyl stretching frequency of PRODAN is found to be at 1673 cm^{-1} . The corresponding electrostatic fields predicted from the peak maxima of the fluorescence spectrum and the C=O IR spectrum at the HSA binding site of PRODAN are -8.58 and -7.98 MV/cm respectively (Figure 5.7D). So using two independent spectroscopic methods we can predict the same electric field which acts as a microscopic polarity indicator within the error bar.

5.4 Summary

In summary, solvatochromic dyes are used ubiquitously to test polarity in solvent mixture with the correlation of dye parameter and peak maxima of fluorophore. The lack of reasoning being such correlation is addressed in this combination in the

framework of vibrational spectroscopy. It not only provides a large pool of potential fluorophore to choose for a polarity indicator in protein environment, it also provides a much improved local electrostatic picture by help of solvent induced electric field as a polarity indicator. Application of such correlation has many applications including investigation of solvent effect inside protein interior, DNA solvation, heterogeneous catalysis, and enzyme catalysis.

5. 5 References

1. Klymchenko, A. S. Solvatochromic and Fluorogenic Dyes as Environment-Sensitive Probes: Design and Biological Applications. *Acc. Chem. Res.* **2017**, *50*, 366-375.
2. Levitus, M.; Ranjit, S. Cyanine dyes in biophysical research: the photophysics of polymethine fluorescent dyes in biomolecular environments. *Quarterly Reviews of Biophysics* **2011**, *44*, 123-151.
3. Moog, R. S.; Kim, D. D.; Oberle, J. J.; Ostrowski, S. G. Solvent Effects on Electronic Transitions of Highly Dipolar Dyes: A Comparison of Three Approaches. *J. Phys. Chem. A* **2004**, *108*, 9294-9301.
4. Machado, V. G.; Stock, R. I.; Reichardt, C. Pyridinium N-Phenolate Betaine Dyes. *Chem. Rev.* **2014**, *114*, 10429-10475.
5. Reichardt, C. Solvatochromic Dyes as Solvent Polarity Indicators. *Chem. Rev.* **1994**, *94*, 2319-2358.
6. Langhals, H. Polarity of Binary Liquid Mixtures. *Angew. Chem. Int. Ed. Engl.* **1982**, *21*, 724-733.
7. Liu, B.; Bi, X.; McDonald, L.; Pang, Y.; Liu, D.; Pan, C.; Wang, L. Solvatochromic fluorescent probes for recognition of human serum albumin in

aqueous solution: Insights into structure-property relationship. *Sensors and Actuators B: Chemical* **2016**, *236*, 668-674.

8. Green, A. M.; Abelt, C. J. Dual-Sensor Fluorescent Probes of Surfactant-Induced Unfolding of Human Serum Albumin. *J. Phys. Chem. B* **2015**, *119*, 3912-3919.
9. Paul, B. K.; Samanta, A.; Guchhait, N. Exploring Hydrophobic Subdomain IIA of the Protein Bovine Serum Albumin in the Native, Intermediate, Unfolded, and Refolded States by a Small Fluorescence Molecular Reporter. *J. Phys. Chem. B* **2010**, *114*, 6183-6196.
10. Giordano, L.; Shvadchak, V. V.; Fauerbach, J. A.; Jares-Erijman, E. A.; Jovin, T. M. Highly Solvatochromic 7-Aryl-3-hydroxychromones. *J. Phys. Chem. Lett.* **2012**, *3*, 1011-1016.
11. Sarkar, A.; Kedia, N.; Bagchi, S. A novel water soluble solvatochromic probe as a micropolarity reporter for homogeneous and microheterogeneous media. *Journal of Luminescence* **2014**, *151*, 111-122.
12. Jara, F.; Domínguez, M.; Rezende, M. C. The interaction of solvatochromic pyridiniophenolates with cyclodextrins. *Tetrahedron* **2006**, *62*, 7817-7823.
13. Rao, V. G.; Ghosh, S.; Ghatak, C.; Mandal, S.; Brahmachari, U.; Sarkar, N. Designing a New Strategy for the Formation of IL-in-Oil Microemulsions. *J. Phys. Chem. B* **2012**, *116*, 2850-2855.
14. Boxer, S. G. Stark Realities. *J. Phys. Chem. B* **2009**, *113*, 2972-2983.
15. Fried, S. D.; Boxer, S. G. Measuring Electric Fields and Noncovalent Interactions Using the Vibrational Stark Effect. *Acc. Chem. Res.* **2015**, *48*, 998-1006.

16. Suydam, I. T.; Boxer, S. G. Vibrational Stark Effects Calibrate the Sensitivity of Vibrational Probes for Electric Fields in Proteins. *Biochemistry* **2003**, *42*, 12050-12055.
17. Fried, S. D.; Bagchi, S.; Boxer, S. G. Measuring Electrostatic Fields in Both Hydrogen-Bonding and Non-Hydrogen-Bonding Environments Using Carbonyl Vibrational Probes. *J Am Chem Soc* **2013**, *135*, 11181-11192.
18. Bagchi, S.; Fried, S. D.; Boxer, S. G. A solvatochromic model calibrates nitriles' vibrational frequencies to electrostatic fields. *J Am Chem Soc* **2012**, *134*, 10373-10376.
19. Liptay, W. Electrochromism and Solvatochromism. *Angew. Chem. Int. Ed. Engl.* **1969**, *8*, 177-188.
20. Callis, P. R. Electrochromism and Solvatochromism in Fluorescence Response of Organic Dyes: A Nanoscopic View. In *Advanced Fluorescence Reporters in Chemistry and Biology I: Fundamentals and Molecular Design*, Demchenko, A. P., Ed. Springer Berlin Heidelberg: Berlin, Heidelberg, **2010**; pp 309-330.
21. Fried, S. D.; Bagchi, S.; Boxer, S. G. Extreme electric fields power catalysis in the active site of ketosteroid isomerase. *Science* **2014**, *346*, 1510.
22. Weber, G.; Farris, F. J. Synthesis and spectral properties of a hydrophobic fluorescent probe: 6-propionyl-2-(dimethylamino)naphthalene. *Biochemistry* **1979**, *18*, 3075-3078.
23. Barik, A.; Nath, S.; Pal, H. Effect of solvent polarity on the photophysical properties of coumarin-1 dye. *J. Chem. Phys.* **2003**, *119*, 10202-10208.
24. Arjunan, V.; Puviarasan, N.; Mohan, S.; Murugesan, P. Fourier transform infrared and Raman spectral assignments and analysis of 7-amino-4-trifluoromethylcoumarin. *Spectrochim. Acta, Part A* **2007**, *67*, 1290-1296.

25. Liu, X.; Cole, J. M.; Low, K. S. Solvent Effects on the UV–vis Absorption and Emission of Optoelectronic Coumarins: a Comparison of Three Empirical Solvatochromic Models. *J. Phys. Chem. C* **2013**, *117*, 14731-14741.
26. Sarkar, A.; Kedia, N.; Purkayastha, P.; Bagchi, S. Photophysics of two structurally similar dyes containing substituted amino as donor and carbonyl as acceptor groups. *J. Lumin.* **2012**, *132*, 2345-2354.
27. Sarkar, A.; Kedia, N.; Purkayastha, P.; Bagchi, S. Synthesis and spectroscopic investigation of a novel solvatochromic dye. *J. Lumin.* **2011**, *131*, 1731-1738.
28. Kedia, N.; Sarkar, A.; Purkayastha, P.; Bagchi, S. Ketocyanine dyes as sensors for proticity and pH of a medium. *Spectrochim. Acta A* **2012**, *95*, 569-575.
29. Chatterjee, S.; Haldar, T.; Ghosh, D.; Bagchi, S. Electrostatic Manifestation of Micro-Heterogeneous Solvation Structures in Deep-Eutectic Solvents: A Spectroscopic Approach. *J. Phys. Chem. B* **2020**, *124*, 3709-3715.
30. Haldar, T.; Kashid, S. M.; Deb, P.; Kesh, S.; Bagchi, S. Pick and Choose the Spectroscopic Method to Calibrate the Local Electric Field inside Proteins. *J. Phys. Chem. Lett.* **2016**, *7*, 2456-2460.
31. Benesi, H. A.; Hildebrand, J. H. A Spectrophotometric Investigation of the Interaction of Iodine with Aromatic Hydrocarbons. *J Am Chem Soc* **1949**, *71*, 2703-2707.
32. Kamal, J. K. A.; Zhao, L.; Zewail, A. H. Ultrafast hydration dynamics in protein unfolding: Human serum albumin. *Proc. Natl. Acad. Sci. U. S. A* **2004**, *101*, 13411.
33. Moreno, F.; Cortijo, M.; González-Jiménez, J. The Fluorescent Probe Prodan Characterizes the Warfarin Binding Site on Human Serum Albumin. *Photochemistry and Photobiology* **1999**, *69*, 8-15.

Chapter 6

**Hydrogen Bonding Status of a Nitrile
Probe Using Infrared and Emission
Spectroscopy in Dual Tandem**

6.1 Introduction

Tryptophan (Trp) is the most commonly used fluorescence reporter in the investigation of protein structure, function and dynamics.¹⁻⁵ This is because (1) it has a relatively high fluorescence quantum yield and large molar extinction coefficient which allows the fluorescence measurement at lower concentration, (2) its fluorescence properties, such as emission peak maxima, Stokes shift, and life time, are highly sensitive towards the environment. However, if the protein contains more than one Trp residue, then it is very difficult to deconvolute the spectra of individual Trp residue. In such cases, we need to substitute tryptophan with a fluorophores that having different fluorescence properties (quantum yield, Stokes shift and emission wavelengths). It is important that the insertion of the substituent does not perturb the molecular architecture of native protein conformation and maintain the dimensions of Trp moiety. It has been demonstrated in the past decades that various cyano-tryptophans (CN-Trp), such as 4CN-Trp,⁶ 5CN-Trp,⁷ 6CN-Trp,⁸ and 7CN-Trp⁸⁻⁹ have been used as a sensitive fluorescence probe for biological spectroscopy. Recently, nitrile vibrational probe containing the indole moiety have proven interesting as fluorescent tryptophan mimics.

The vibrational frequency of certain chemical groups provides information regarding local environment.¹⁰⁻¹³ The solvent-induced vibrational frequency shifts are directly sensitive towards the change in the electric field through vibrational Stark effect (VSE).^{10, 14-17} Since the electric field is projected along the vibrational axis, it can serve as a microscopic and quantitative descriptor of non-covalent interaction.^{10, 18} Therefore, using IR spectroscopy we can predict the local electrostatic environment in biological macromolecules. Carbonyl (C=O) is one of the most abundant vibrational

probe which is very local and highly intense. C=O has been widely used to determine the electrostatic field in the biological macromolecules.¹⁵ Using VSE spectroscopy, it has been experimentally illustrated that C=O stretching frequencies are linearly sensitive towards the electrostatic field in both non H-bonding and H-bonding environments.^{10, 15, 19-22} But the limitation of carbonyl probe is the intrinsic overlap of the C=O stretch with the amide I protein IR band, making it difficult to estimate electric field in proteins. Nitrile (C≡N) groups are particularly powerful vibrational probes for investigation of protein structure, interaction and dynamics. C≡N absorbs in a convenient region of the IR spectrum which does not overlap with the intrinsic vibrations of biomolecules.²³⁻²⁷ This makes C≡N as directional and sensitive probes of electric field in biological macromolecules.

For the electronic transitions, electrostatics plays a crucial role towards the solute-solvent interaction for the dye molecule.²⁸⁻²⁹ Fluorescence peak maxima for many dye molecules shows a strong solvatochromic shift with varying solvent polarity.^{28, 30-33} Recently, it has been shown that emission spectroscopy based methodology can be used to measure the electrostatic field in the deep eutectic solvents.³⁴ In the present study, we have examined the correlation between IR stretching frequencies (ground electronic state phenomenon) and the fluorescence peak maxima (excited electronic state phenomenon) of different nitrile probe containing indole moieties to detect the nitrile H-bonding status. Also here we have shown that the sensitivity of the π - π^* emission wavelengths towards the electrostatic field along the C≡N bond for cyano indole compounds in different non H-bonding and H-bonding solvation environments.

6.2 Materials and sample preparation

4-cyanoindole, 5-cyanoindole and solvents like dibutyl ether, diethyl ether, tetrahydrofuran, N,N-dimethylformamide and dimethyl sulfoxide were obtained from Sigma Aldrich and used without further purification. Milli-Q water was used in this study. All micelles like, sodium dodecyl sulfate (SDS), cetyltrimethylammonium bromide (CTAB), and tritonX-100 (TX100) were purchased from Sigma-Aldrich and used without further purification. Each sample was dissolved independently in aprotic solvents and protic binary aqueous mixtures (DMSO/water) such that the final concentration of liquid sample is 10 mM for the IR studies.

6.3 Results and discussion

6.3.1 Steady-State Fluorescence Measurements

4CNI and 5CNI (Figure 6.0), nitrile group functionalized indole variants are dissolved in various solvents of varying polarity to perform the fluorescence experiments.

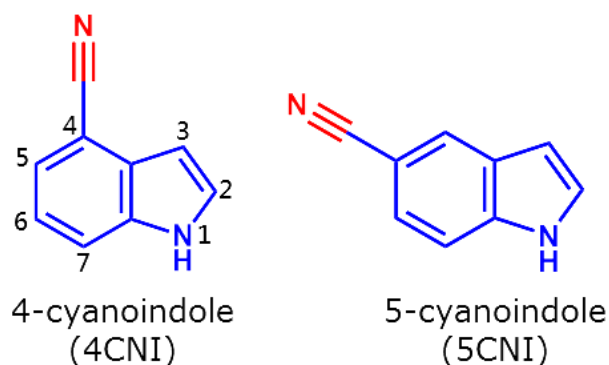


Figure 6.0. Molecular structure and abbreviations of the solvatochromic probes used. The atom numbering is given for 4-cyano indole.

The fluorescence peak position of those cyanoindoles exhibits a strong sensitivity towards the solvent polarity and show a gradual red shift with increasing solvent polarity (Figure 6.1A, Figure 6.1B). The red shift in the emission maxima is in good

agreement with the trend observed by Markiewicz et al and Hilaire et al.⁶⁻⁷ When both the fluorophores are dissolved in polar protic solvent like water, emission peak maxima reveal a further red shift as compared with that in DMSO (Figure 6.1 A & 6.1 B).

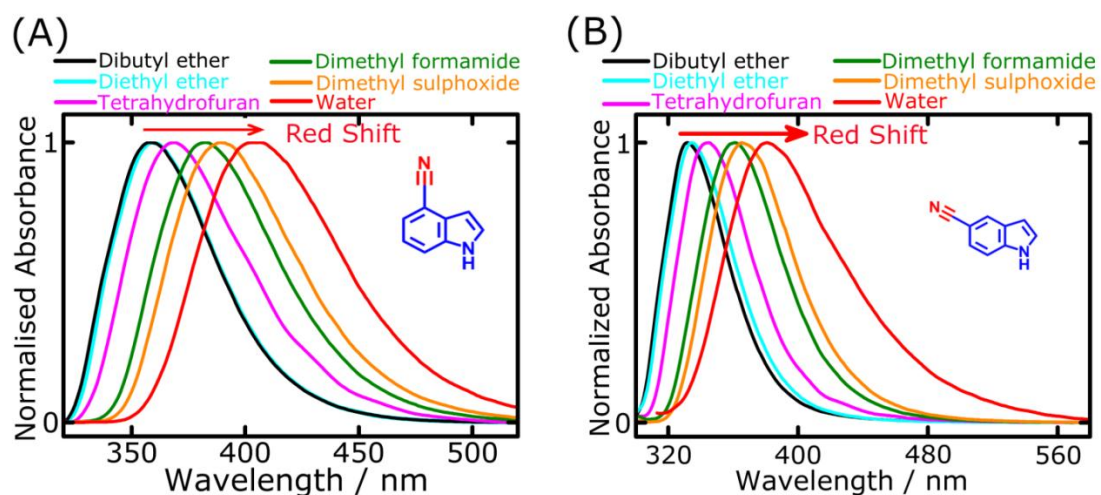


Figure 6.1 Solvatochromic π - π^* emission spectra of 4-cyano indole (A) and 5-cyano indole (B) in a number of organic solvents and water. The polarity increases in the direction of the arrow.

During the electronic transition of the indole ring, it produces a larger dipole moment in the excited electronic state as compared to that in the ground electronic state.⁹ Hence, the excited state is more stabilized than the ground state in a polar protic environment like water. To further interrogate the interaction in H-bonding solvation environments, we have scanned the intermediate polarities between DMSO and water by using different DMSO/water solutions, where the percentage of water is gradually increased by 20% (v/v) increments (Figure 6.2 A and 6.2 B).

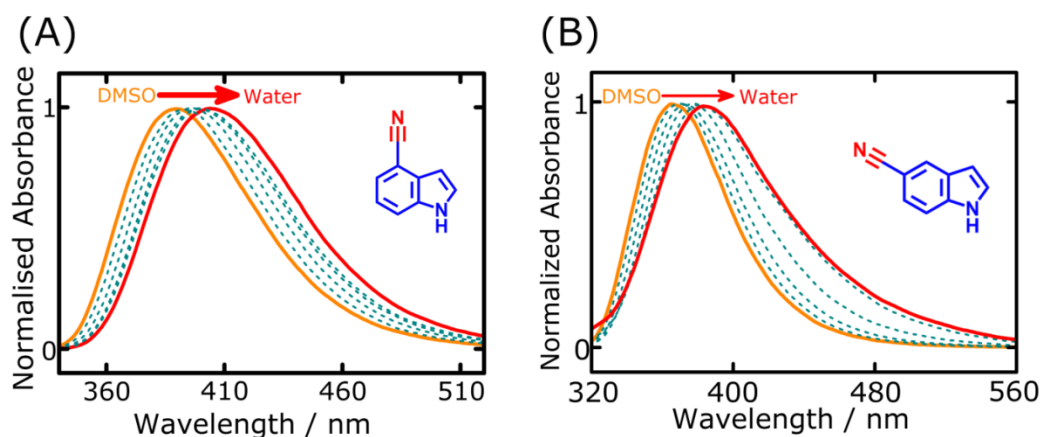


Figure 6.2 Normalized emission spectra of both (A) 4-cyano indole ($\lambda_{\text{ex}} = 300\text{nm}$) and (B) 5-cyano indole ($\lambda_{\text{ex}} = 275\text{nm}$) in various 8:2, 6:4, 4:6, 2:8 aqueous dimethyl sulphoxide solutions (v/v) (Dotted lines). Normalized emission spectra of both cyano-indoles in DMSO (solid orange line) and water (solid red line) are also shown for comparison. The polarity increases in the direction of the arrow.

6.3.2 Vibrational Solvatochromism

We have carried out the solvatochromic IR experiments on the $\text{C}\equiv\text{N}$ stretch of both 4CNI and 5CNI in different neat organic solvents, water, and aqueous DMSO solutions.

The FTIR spectrum of 4CNI in the $\text{C}\equiv\text{N}$ stretch region exhibits two distinct transitions (Figure 6.3 A), which is in good agreement with the previous observations.³⁵⁻³⁶ Prior studies indicated that the lower frequency peak corresponds to $\text{C}\equiv\text{N}$ stretching and the higher frequency peak arises due to the Fermi resonance between the fundamental nitrile stretching motion and ring breathing modes.³⁷⁻³⁸ Moreover, Density Functional Theory computational study shows that one vibrational mode in the $\text{C}\equiv\text{N}$ stretch region. The peaks are deconvolved to obtain the nitrile stretch ($\bar{\nu}_{\text{C}\equiv\text{N}}$), as shown in Figure 6.3B.

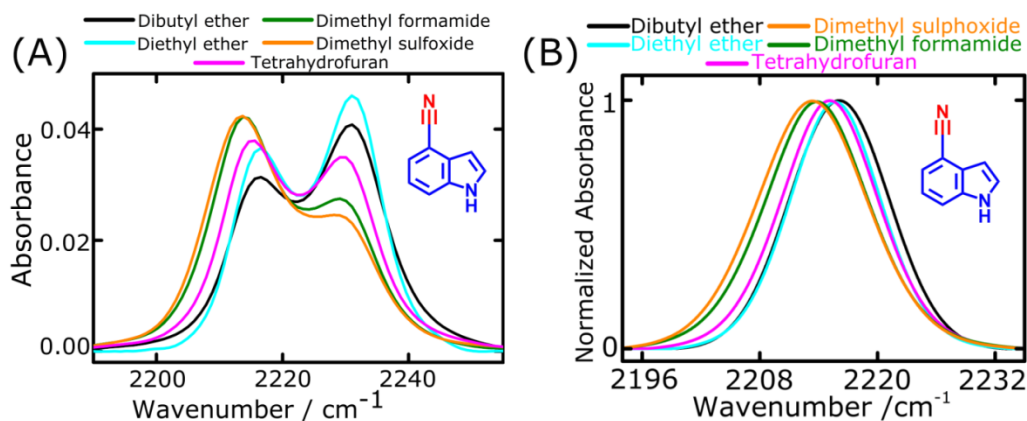


Figure 6.3 Solvatochromic IR studies of 4-cyano indole. (A) Area normalized FTIR absorption spectra of the C≡N stretch of 4-cyanoindole in non-hydrogen bonding solvation environments. (B) Fitted IR absorption spectra of the C≡N stretch of 4-cyano indole in pure organic solvents.

As previously reported, we observe gradually decrease in nitrile stretching frequencies of both 4CNI and 5CNI with increasing polarity of the aprotic solvents (Figure 6.3B & 6.4A).³⁵ A 2.8 cm⁻¹ red shift in $\bar{\nu}_{C\equiv N}$ is observed for 4CNI as the solvation environment is altered from the aprotic non polar solvent dibutyl ether (black) to the aprotic polar solvent DMSO (orange), whereas 5CNI exhibits a red shift of 6.6 cm⁻¹ for the same. When 5CNI is dissolved in water (red), where the C≡N can form an H-bond with water and $\bar{\nu}_{C\equiv N}$ is higher than that in non H-bond forming solvent, DMSO. Since 4CNI was partially soluble in water, the 4CNI have been studied up to 1:4 DMSO/water (20% DMSO, v/v) solutions. The nitrile stretching frequencies of both the cyano-indoles show a monotonically increasing blue shift with increasing polarity of DMSO/water mixture (with increasing water content by 20% v/v increments) (Figure 6.4B for 5CNI). Absolute values of fluorescence peak maxima and C≡N stretching frequencies of both 4-cyanoindole and 5-Cyanoindole in non-hydrogen-bonding and hydrogen-bonding solvation environments are tabulated in table 6.1 and 6.2 respectively.

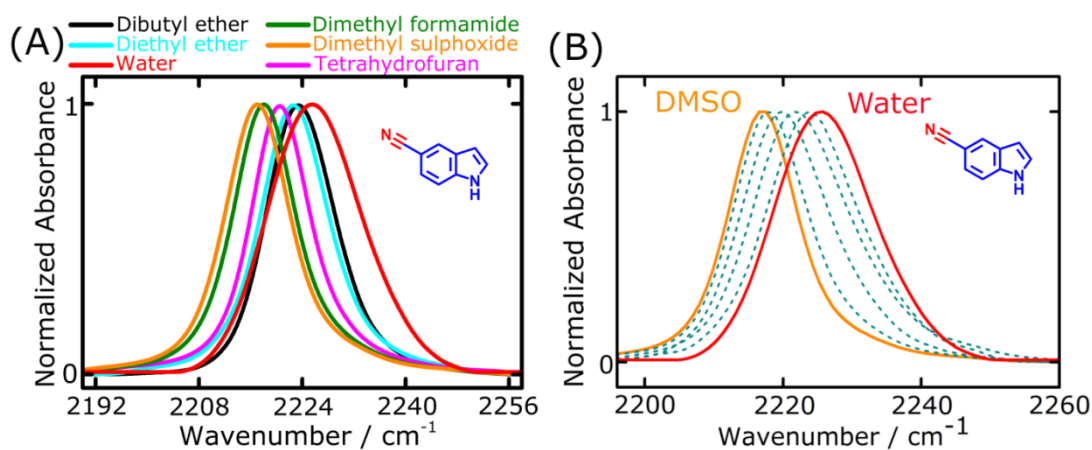


Figure 6.4 (A) Representative FTIR spectra of the C≡N stretching band of 5-cyanoindole dissolved in a number of aprotic solvents and water at 10 mM concentration. (B) Representative FTIR spectra of the C≡N stretch band of 5-cyanoindole in different DMSO-water (D: W) solutions (dotted lines). IR absorption spectra of the C≡N stretch of 5-cyanoindole in DMSO (solid orange line) and water (red solid line) are also displayed for easy comparison.

Table 6.1 Absolute values of fluorescence peak maxima and C≡N stretching frequencies of 4-Cyanoindole in non-hydrogen-bonding and hydrogen-bonding solvation environments.

Solvents	Nitrile stretch / cm^{-1}		$\pi-\pi^*$ Emission Wavelength / (nm)	$\pi-\pi^*$ Emission Wavenumber / (cm^{-1})
	1 st peak	2 nd peak		
Di Butyl Ether	2216.1	2230.8	358.9	27861.4
Di Ethyl Ether	2215.8	2230.1	360	27777.8
Tetrahydrofuran	2215.1	2229.5	367.7	27196.1
N,N dimethyl formamide	2213.8	2229.1	382.7	26130.1
Di methyl sulphoxide	2213.3	2228.9	389.7	25660.8

4:1 (D:W)	2214	2229.8	393.5	25413.0
3:2 (D:W)	2215.1	2231.7	396.5	25220.7
2:3 (D:W)	2216.4	2233.1	399.7	25018.8
3:7 (D:W)	2216.9	2233.9	400.1	24993.8
Water	No peak Insoluble	No peak insoluble	405.1	24685.3

D: W represents dimethyl sulphoxide–water solution (v/v).

Table 6.2 Absolute values of fluorescence peak maxima and C≡N stretching frequencies of 5-Cyanoindole in non-hydrogen-bonding and hydrogen-bonding solvation environments.

Solvents	Nitrile stretch / cm ⁻¹	$\pi-\pi^*$ Emission Wavelength /(nm)	$\pi-\pi^*$ Emission Wavenumber/(cm ⁻¹)
Di Butyl Ether	2223.7	333.1	30021.1
Di Ethyl Ether	2222.8	335.6	29797.4
Tetrahydrofuran	2220.5	345.1	28977.1
N,N dimethyl formamide	2218.1	361.1	27693.2
Dimethyl sulphoxide	2217.1	367.2	27233.1
4:1 (D:W)	2218.2	370.1	27019.7
3:2 (D:W)	2219.4	373.3	26788.1
2:3 (D:W)	2221.1	377.5	26490.1
1:4 (D:W)	2223.1	382.2	26164.3
Water	2224.4	384.8	25987.5

D: W represents dimethyl sulphoxide–water solution (v/v).

6.3.3 Electric Field-Vibrational Frequency Correlation

Using atomistic molecular dynamics (MD) simulations, we have estimated the average electrostatic field at the midpoint of the C≡N ($\vec{F}_{C\equiv N}$) of both cyano-indoles in all the different solvation environments. Electric fields in aprotic solvents show an excellent linear correlation with the experimentally determined nitrile stretching frequencies of both 4CNI (Figure 6.5A) and 5CNI (Figure 6.5B). The slopes of the best fit lines are $0.21 \text{ cm}^{-1}/(\text{MV}/\text{cm})$ and $0.40 \text{ cm}^{-1}/(\text{MV}/\text{cm})$ for Figure 6.5A and 6.5B respectively. The experimentally measured Stark tuning rate for 5CNI is $0.86 \text{ cm}^{-1}/(\text{MV}/\text{cm})$.¹⁸ Therefore, the slope of the solvatochromic line is 2.15 fold smaller than the experimentally determined Stark tuning rate. This divergence appears from the local field effect and is compatible with the reported value of the local field correction factor, $f \sim 2$.¹⁰ Although a plot of $\bar{\nu}_{C\equiv N}$ versus $\vec{F}_{C\equiv N}$ maintains a linear correlation for non H-bonded solvents, a deviation is observed for H-bonding protic solvents and solvent mixtures (Figure 6.5A, 6.5B). This observation is similar with the trends observed by Deb et al. for 4CNI (Figure 6.5A) and 5CNI (Figure 6.5B).³⁹ $\bar{\nu}_{C\equiv N}$ exhibits a linear correlation with $\vec{F}_{C\equiv N}$ in the aqueous DMSO solutions and water (R^2 values of 0.99 and 0.98, respectively). The slopes of the best fit lines obtained for protic environments are 0.17 and 0.24 for 4CNI and 5CNI respectively. It is to be noted that the slopes are opposite in sign to that obtained in the neat solvents. A plot of the paired points ($\bar{\nu}_{C\equiv N}, \vec{F}_{C\equiv N}$) for 4CNI and 5CNI in both non H-bonding and H-bonding solvation environments provides a V-shaped curve, which is similar to the previous result. In the V-shaped plot, blue solid line represents the behavior of nitriles in non H-bonding environments and red dotted line represents the same in H-bonding environments. However, prediction of $\vec{F}_{C\equiv N}$ using the experimental measured

$\bar{\nu}_{C\equiv N}$ from IR spectra in any unknown environment is difficult because a single value of $\bar{\nu}_{C\equiv N}$ can correspond to two values of the electrostatic field (Figure 6.5A, 6.5B). So the knowledge of H-bonding status of the nitrile is essential.

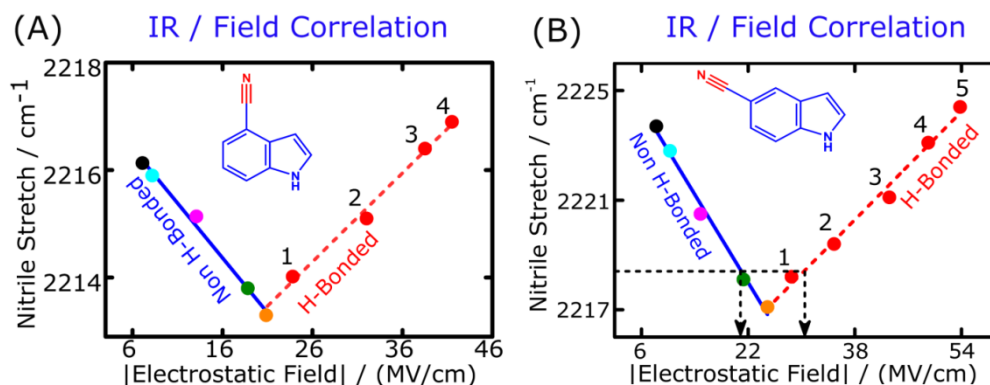


Figure 6.5 Field-frequency calibration curves for (A) 4CNI and (B) 5CNI in H-bonding and non-H-bonding environments. The blue (solid) and red (dotted) lines indicate the best fitted line in non H-bonding and H-bonding solvents respectively. The equations of the best-fit non-H-bonded lines for (A) 4CNI and (B) 5CNI are $\bar{\nu}_{C\equiv N} = -0.20 |\vec{F}_{C\equiv N}| + 2217.6$ ($R^2 = 0.99$) and $\bar{\nu}_{C\equiv N} = -0.40 |\vec{F}_{C\equiv N}| + 2226.8$ ($R^2 = 0.99$) respectively. The field-frequency paired points (red circle) for the nitriles dissolved in DMSO/water binary mixtures (v/v) (H-bonding environments) falls off the best-fit non-H-bonded lines. A linear correlation between $C\equiv N$ stretching frequency and the electrostatic field exerted by the H-bonding environments exists for both the cyano-indoles. The equations of the best fit H-bonded lines for (A) 4CNI and (B) 5CNI are $\bar{\nu}_{C\equiv N} = 0.17 |\vec{F}_{C\equiv N}| + 2210$, ($R^2 = 0.98$) and $\bar{\nu}_{C\equiv N} = 0.27 |\vec{F}_{C\equiv N}| + 2210.9$, ($R^2 = 0.98$) respectively.

6.3.4 Fluorescence-IR Frequency Correlation

To experimentally conquer this limitation, we have used fluorescence/IR correlation of both cyano-indoles in aprotic and protic solvents. For non H-bonding solvents, both ground and excited electronic states are only stabilized by the electrostatic interactions by the surrounding solvent molecules, which lead to a linear correlation between nitrile stretch and fluorescence peak maxima ($\bar{\nu}_{emission}$). The $\bar{\nu}_{C\equiv N}$ in aprotic

solvents show an excellent linear correlation with $\bar{\nu}_{emission}$ with correlation coefficient of 0.99 for both 4CNI (Figure 6.6A) and 5CNI (Figure 6.6B). In case of protic solvent (water), nitrile can form H-bonds with water, a deviation from linear correlation is observed (Figure 6.6A, 6.6B) for both cyano-indoles. When we plotted $\bar{\nu}_{C\equiv N}$ against $\bar{\nu}_{emission}$ for 4CNI (Figure 6.6A) and 5CNI (Figure 6.6B) in binary aqueous mixture of DMSO (v/v) show a distinct deviation from the respective non H-bonded line.

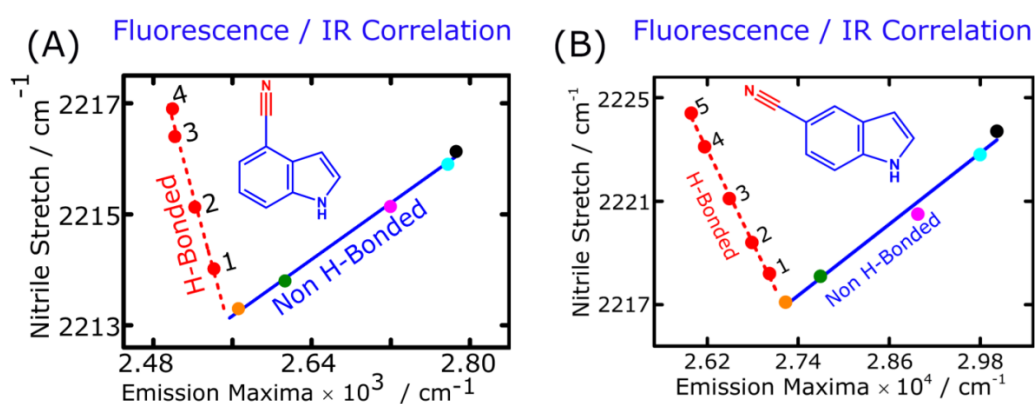


Figure 6.6 Experimentally obtained nitrile stretching frequencies of (A) 4CNI and (B) 5CNI are plotted against the corresponding π - π^* emission frequencies in non-H-bonding (blue line) and H-bonding (red line) solvation environments. Linear correlation is observed (solid blue lines) for cyano indoles in aprotic solvents (non-H-bonded C \equiv N), whereas, a deviation from linearity is observed in protic solvation environment (H-bonded C \equiv N).

A deviation from the linear covariance of nitrile stretching and emission frequencies represent the effect of specific interaction, which alters $\bar{\nu}_{C\equiv N}$ and $\bar{\nu}_{emission}$ differently. So, in the fluorescence/IR plot, the $(\bar{\nu}_{C\equiv N}, \bar{\nu}_{emission})$ ordered points that occur in the blue line corresponds to solvation environments free of H-bonds, while points that fall significantly off this line appear to experience a non-electrostatic contribution, assigned to H-bond effects.

6.3.5 Fluorescence-Electric Field Correlation

Previous studies have discussed the correlation of fluorescence peak maxima with the various semi-empirical solvent polarity scales in non-hydrogen bonded solvation environments.^{33, 40-42} But this empirical polarity parameter lacks the microscopic details necessary to understand heterogeneous solvent environment.²¹ Electric field being a direct reporter of local electrostatic environment negates the reliance on any semi empirical parameters.

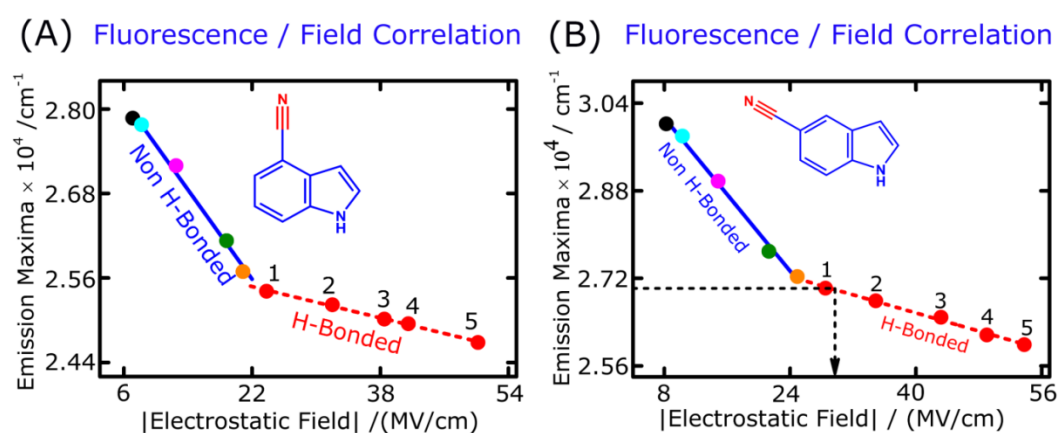


Figure 6.7 Plot of fluorescence peak maxima of 4-cyano indole (A) and 5-cyano indole (B) in different solvation environments compared against the average electrostatic field $\text{C}\equiv\text{N}$ experiences in each solvents, as calculated by MD simulation. Blue (solid) and red (dotted) lines indicate best fitted line of the Non H-bonded and H-bonded solvents respectively. The equations of the best fit lines for (A) 4-cyano indole and (B) 5-cyano indole in non H-bonding solvents are $\bar{\nu}_{emission} = -158.6 (|F_{\text{C}\equiv\text{N}}|) + 29072.6$, ($R^2 = 0.994$) and $\bar{\nu}_{emission} = -174.78 (|F_{\text{C}\equiv\text{N}}|) + 31526.7$, ($R^2 = 0.99$), respectively.

The fluorescence peak positions are strongly influenced by the electric field through electronic Stark effect.²⁸⁻²⁹ A linear correlation can be seen between shifts of emission peak maxima across aprotic solvents and the electric fields calculated along $\text{C}\equiv\text{N}$ molecular axis using MD simulation (R^2 values of 0.99 for both 4CNI (Figure 6.7A) and 5CNI (Figure 6.7B)). In cases of more specific interaction likes hydrogen

bonding, ground and excited interacts in a dissimilar manner causing slope to change between H-bonded and non H-bonded line. The values of $\vec{F}_{C\equiv N}$ for 4CI and 5CI in protic solvent, water, and binary aqueous mixture of DMSO to mimic the H-bonding solvation environments when plotted against the corresponding emission peak positions show a prominent deviation from the respective solid line. Interestingly, a new linear correlation ($R^2 = 0.99$) is observed between $\vec{F}_{C\equiv N}$ and $\bar{\nu}_{emission}$ in aqueous DMSO solution (v/v) and water for 4CI (Figure 6.7A) and 5CI (Figure 6.7B). For hydrogen bonded environment slope of the line changes indicating inherent sensitivity of fluorescence with specific interaction like hydrogen bonded. So from this fluorescence/field correlation, we can easily detect the nitrile hydrogen bonding status and also allows us to estimate $\vec{F}_{C\equiv N}$ using the experimentally measured $\bar{\nu}_{emission}$ in any unknown environment.

6.3.6 Validation of Fluorescence/Field Correlation

We have experimentally determined $\vec{F}_{C\equiv N}$ along the C \equiv N bond axis of both cyanoindoles in the micelle-water interface using fluorescence spectroscopy. Here, Cationic surfactant CTAB, anionic surfactant SDS and neutral surfactant TX-100 are used to prepare three micelle solutions in aqueous medium.

We have measured the fluorescence peak maxima and nitrile stretching frequencies of 5CNI in above mentioned micellar medium. The C \equiv N IR and fluorescence peak positions of 5CNI in various micellar environments are listed in Table 6.3. Further, we have independently predicted $\bar{\nu}_{C\equiv N}$ of 5CNI in these different micellar interface from $\bar{\nu}_{emission}$ using the fluorescence/IR calibration curve (Figure 6.6B). It is important to note that the experimentally observed the nitrile stretching frequencies agree well with the frequencies predicted from the fluorescence spectroscopy, by the

calibration curve in Figure 6.6B. The corresponding electrostatic fields predicted from the nitrile stretch (Figure 6.5B) and emission peak maxima (Figure 6.7B) in the various micellar interfaces are shown in Table 1. Prediction of electrostatic fields from IR spectroscopy shows an excellent agreement with the predicted electrostatic field from emission peak maxima.

Table 6.3 Emission maxima ($\bar{\nu}_{emission}$) and nitrile stretch ($\bar{\nu}_{C\equiv N}$) of 5CNI and 4CNI along with predicted electrostatic field ($\vec{F}_{C\equiv N}$) from emission maxima of different micellar interfaces.

Micelle	$\bar{\nu}_{C\equiv N}$ (cm^{-1})	$\bar{\nu}_{emission}$ (cm^{-1})	Predicted electric field from C \equiv N stretch /(MV/cm)	Predicted electric field from emission peak maxima /(MV/cm)
5CI in CTAB- water interface	2218.4	27021.8	30.37	29.03
5CI in SDS-water interface	2220.8	26680.3	40.09	37.28
5CI in TX100- water interface	2218.6	27012.9	31.18	29.24
4CI in CTAB- water interface	No IR peak	25403.3	-	24.71
4CI in SDS-water interface	No IR peak	25169.9	-	33.13
4CI in TX100- water interface	No IR peak	25400.2	-	24.82

However, in the case of 4CNI, which is partially soluble in water, therefore getting IR spectrum in the micellar medium is extremely difficult. But using the fluorescence/field calibration curve, we can easily estimate $\vec{F}_{C\equiv N}$ in the three micelle-water interfaces (Figure 6.7A). Table 6.3 manifested that both the cyano-indoles are follow similar trends in the above mentioned micellar medium.

6.3.7 Validation of Stark Tuning Rate

The value of Stark tuning rate ($|\Delta\vec{\mu}|$) implies the intrinsic sensitivity of the transition to an electrostatic field and also remains constant as long as the same connectivity towards the vibrational probe.^{10, 17} To establish this point, we have calculated the electrostatic field being exerted along the C≡N using molecular dynamics (MD) simulations of six nitrile group functionalized indole variants, such as 4CNI, 5CNI, 6-cyanoindole (6CNI), 7-cyanoindole (7CNI), *N*-acetyl-4-cyano tryptophan and *N*-acetyl-5-cyano tryptophan respectively. For non-H-bonded C≡N where the interactions are electrostatic in nature, we have observed a linear correlation between fluorescence shifts and shifts in electrostatic fields for different C≡N containing molecules with a negative slope as expected from VSE (Figure 6.8).

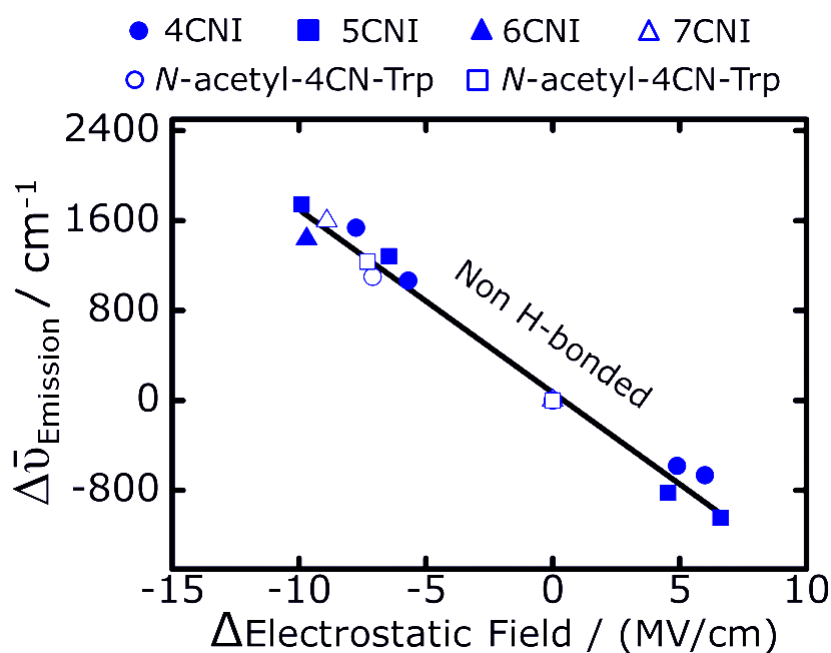


Figure 6.8 Shifts in emission wavenumber versus shifts in C=O electrostatic fields for 4-cyano indole (solid blue circle), 5-cyano indole (solid blue square), 6-cyano indole (solid blue triangle), 7-cyano indole (hollow triangle), *N*-acetyl-4-cyano tryptophan (hollow circle), *N*-acetyl-5-cyano indole (hollow square) in various non-hydrogen-bonding solvents. In purely electrostatic environment $\Delta\bar{\nu}_{emission}$ varies linearly with the electric field for various nitrile group containing indole compounds. The black

line indicates the best fitted line in non H-bonding solvents. The slope and intercept of best fit line for non H-bonded solvents are $-162.75 \text{ cm}^{-1}/(\text{MV}/\text{cm})$ and 69.869 cm^{-1} respectively. The regression value of the fitted line is 0.98.

6.4 Summary

This result cumulatively intimate that nitrile ($\text{C}\equiv\text{N}$) probes can quantitatively assess the electric fields involved in both non-H-bonded and H-bonded environments, making them promising for understanding the physical description of key bimolecular processes such as protein-ligand binding and organic catalysis. Also direct detection of nitrile ($\text{C}\equiv\text{N}$) H-bonds can provide critical information regarding mechanistic understanding of organic and biological reactions.

6.5 References

1. Chen, Y.; Barkley, M. D. Toward Understanding Tryptophan Fluorescence in Proteins. *Biochemistry* **1998**, *37*, 9976-9982.
2. Royer, C. A. Probing Protein Folding and Conformational Transitions with Fluorescence. *Chem. Rev.* **2006**, *106*, 1769-1784.
3. Zhong, D. Hydration Dynamics and Coupled Water-Protein Fluctuations Probed by Intrinsic Tryptophan. In *Advances in Chemical Physics*, **2009**; pp 83-149.
4. Simon-Lukasik, K. V.; Persikov, A. V.; Brodsky, B.; Ramshaw, J. A. M.; Laws, W. R.; Alexander Ross, J. B.; Ludescher, R. D. Fluorescence determination of tryptophan side-chain accessibility and dynamics in triple-helical collagen-like peptides. *Biophys. J.* **2003**, *84*, 501-508.
5. Callis, P. R. Binding phenomena and fluorescence quenching. II: Photophysics of aromatic residues and dependence of fluorescence spectra on protein conformation. *J. Mol. Struct.* **2014**, *1077*, 22-29.

6. Hilaire, M. R.; Ahmed, I. A.; Lin, C.-W.; Jo, H.; DeGrado, W. F.; Gai, F. Blue fluorescent amino acid for biological spectroscopy and microscopy. *Proc. Natl. Acad. Sci. U.S. A.* **2017**, *114*, 6005-6009.
7. Markiewicz, B. N.; Mukherjee, D.; Troxler, T.; Gai, F. Utility of 5-Cyanotryptophan Fluorescence as a Sensitive Probe of Protein Hydration. *J. Phys. Chem. B* **2016**, *120*, 936-944.
8. Talukder, P.; Chen, S.; Roy, B.; Yakovchuk, P.; Spiering, M. M.; Alam, M. P.; Madathil, M. M.; Bhattacharya, C.; Benkovic, S. J.; Hecht, S. M. Cyanotryptophans as Novel Fluorescent Probes for Studying Protein Conformational Changes and DNA–Protein Interaction. *Biochemistry* **2015**, *54*, 7457-7469.
9. Mukherjee, D.; Ortiz Rodriguez, L. I.; Hilaire, M. R.; Troxler, T.; Gai, F. 7-Cyanoindole fluorescence as a local hydration reporter: application to probe the microheterogeneity of nine water-organic binary mixtures. *Phys. Chem. Chem. Phys.* **2018**, *20*, 2527-2535.
10. Fried, S. D.; Boxer, S. G. Measuring Electric Fields and Noncovalent Interactions Using the Vibrational Stark Effect. *Acc. Chem. Res.* **2015**, *48*, 998-1006.
11. Thielges, M. C.; Case, D. A.; Romesberg, F. E. Carbon–Deuterium Bonds as Probes of Dihydrofolate Reductase. *J. Am. Chem. Soc.* **2008**, *130*, 6597-6603.
12. Park, E. S.; Andrews, S. S.; Hu, R. B.; Boxer, S. G. Vibrational Stark Spectroscopy in Proteins: A Probe and Calibration for Electrostatic Fields. *J. Phys. Chem. B* **1999**, *103*, 9813-9817.
13. Ye, S.; Huber, T.; Vogel, R.; Sakmar, T. P. FTIR analysis of GPCR activation using azido probes. *Nature Chemical Biology* **2009**, *5*, 397-399.
14. Fafarman, A. T.; Boxer, S. G. Nitrile Bonds as Infrared Probes of Electrostatics in Ribonuclease S. *J. Phys. Chem. B* **2010**, *114*, 13536-13544.

15. Fried, S. D.; Bagchi, S.; Boxer, S. G. Measuring Electrostatic Fields in Both Hydrogen-Bonding and Non-Hydrogen-Bonding Environments Using Carbonyl Vibrational Probes. *J. Am. Chem. Soc.* **2013**, *135*, 11181-11192.
16. Andrews, S. S.; Boxer, S. G. Vibrational Stark Effects of Nitriles I. Methods and Experimental Results. *J. Phys. Chem. A* **2000**, *104*, 11853-11863.
17. Boxer, S. G. Stark Realities. *J. Phys. Chem. B* **2009**, *113*, 2972-2983.
18. Suydam, I. T.; Boxer, S. G. Vibrational Stark Effects Calibrate the Sensitivity of Vibrational Probes for Electric Fields in Proteins. *Biochemistry* **2003**, *42*, 12050-12055.
19. Fried, S. D.; Bagchi, S.; Boxer, S. G. Extreme electric fields power catalysis in the active site of ketosteroid isomerase. *Science* **2014**, *346*, 1510.
20. Pazos, I. M.; Ghosh, A.; Tucker, M. J.; Gai, F. Ester Carbonyl Vibration as a Sensitive Probe of Protein Local Electric Field. *Angew. Chem. Int. Ed.* **2014**, *53*, 6080-6084.
21. Haldar, T.; Kashid, S. M.; Deb, P.; Kesh, S.; Bagchi, S. Pick and Choose the Spectroscopic Method to Calibrate the Local Electric Field inside Proteins. *J. Phys. Chem. Lett.* **2016**, *7*, 2456-2460.
22. Kashid, S. M.; Bagchi, S. Experimental Determination of the Electrostatic Nature of Carbonyl Hydrogen-Bonding Interactions Using IR-NMR Correlations. *J. Phys. Chem. Lett.* **2014**, *5*, 3211-3215.
23. Fafarman, A. T.; Sigala, P. A.; Schwans, J. P.; Fenn, T. D.; Herschlag, D.; Boxer, S. G. Quantitative, directional measurement of electric field heterogeneity in the active site of ketosteroid isomerase. *Proc. Natl. Acad. Sci. U. S. A* **2012**, *109*, E299.

24. Suydam, I. T.; Snow, C. D.; Pande, V. S.; Boxer, S. G. Electric Fields at the Active Site of an Enzyme: Direct Comparison of Experiment with Theory. *Science* **2006**, *313*, 200.
25. Bagchi, S.; Fried, S. D.; Boxer, S. G. A solvatochromic model calibrates nitriles' vibrational frequencies to electrostatic fields. *J. Am. Chem. Soc.* **2012**, *134*, 10373-10376.
26. Fafarman, A. T.; Sigala, P. A.; Herschlag, D.; Boxer, S. G. Decomposition of Vibrational Shifts of Nitriles into Electrostatic and Hydrogen-Bonding Effects. *J. Am. Chem. Soc.* **2010**, *132*, 12811-12813.
27. Getahun, Z.; Huang, C.-Y.; Wang, T.; De León, B.; DeGrado, W. F.; Gai, F. Using Nitrile-Derivatized Amino Acids as Infrared Probes of Local Environment. *J. Am. Chem. Soc.* **2003**, *125*, 405-411.
28. Callis, P. R. Electrochromism and Solvatochromism in Fluorescence Response of Organic Dyes: A Nanoscopic View. In *Advanced Fluorescence Reporters in Chemistry and Biology I: Fundamentals and Molecular Design*, Demchenko, A. P., Ed. Springer Berlin Heidelberg: Berlin, Heidelberg, **2010**; pp 309-330.
29. Liptay, W. Electrochromism and Solvatochromism. *Angew. Chem. Int. Ed.* **1969**, *8*, 177-188.
30. Sackett, D. L.; Wolff, J. Nile red as a polarity-sensitive fluorescent probe of hydrophobic protein surfaces. *Analytical Biochemistry* **1987**, *167*, 228-234.
31. Nad, S.; Kumbhakar, M.; Pal, H. Photophysical Properties of Coumarin-152 and Coumarin-481 Dyes: Unusual Behavior in Nonpolar and in Higher Polarity Solvents. *J. Phys. Chem. A* **2003**, *107*, 4808-4816.

32. Moog, R. S.; Kim, D. D.; Oberle, J. J.; Ostrowski, S. G. Solvent Effects on Electronic Transitions of Highly Dipolar Dyes: A Comparison of Three Approaches. *J. Phys. Chem. A* **2004**, *108*, 9294-9301.
33. Reichardt, C. Solvatochromic Dyes as Solvent Polarity Indicators. *Chem. Rev.* **1994**, *94*, 2319-2358.
34. Chatterjee, S.; Haldar, T.; Ghosh, D.; Bagchi, S. Electrostatic Manifestation of Micro-Heterogeneous Solvation Structures in Deep-Eutectic Solvents: A Spectroscopic Approach. *J. Phys. Chem. B* **2020**, *124*, 3709-3715.
35. van Wilderen, L. J. G. W.; Brunst, H.; Gustmann, H.; Wachtveitl, J.; Broos, J.; Bredenbeck, J. Cyano-tryptophans as dual infrared and fluorescence spectroscopic labels to assess structural dynamics in proteins. *Phys. Chem. Chem. Phys.* **2018**, *20*, 19906-19915.
36. Zhang, W.; Markiewicz, B. N.; Doerksen, R. S.; Smith, I. I. I. A. B.; Gai, F. C≡N stretching vibration of 5-cyanotryptophan as an infrared probe of protein local environment: what determines its frequency? *Phys. Chem. Chem. Phys.* **2016**, *18*, 7027-7034.
37. Chalyavi, F.; Gilmartin, P. H.; Schmitz, A. J.; Fennie, M. W.; Tucker, M. J. Synthesis of 5-Cyano-Tryptophan as a Two-Dimensional Infrared Spectroscopic Reporter of Structure. *Angew. Chem. Int. Ed.* **2018**, *57*, 7528-7532.
38. Rodgers, J. M.; Abaskharon, R. M.; Ding, B.; Chen, J.; Zhang, W.; Gai, F. Fermi resonance as a means to determine the hydrogen-bonding status of two infrared probes. *Phys. Chem. Chem. Phys.* **2017**, *19*, 16144-16150.
39. Deb, P.; Haldar, T.; Kashid, S. M.; Banerjee, S.; Chakrabarty, S.; Bagchi, S. Correlating Nitrile IR Frequencies to Local Electrostatics Quantifies Noncovalent Interactions of Peptides and Proteins. *J. Phys. Chem. B* **2016**, *120*, 4034-4046.

40. Langhals, H. Polarity of Binary Liquid Mixtures. *Angew. Chem. Int. Ed. Engl.* **1982**, *21*, 724-733.
41. Kosower, E. M. The Effect of Solvent on Spectra. I. A New Empirical Measure of Solvent Polarity: Z-Values. *J. Am. Chem. Soc.* **1958**, *80*, 3253-3260.
42. Grunwald, E.; Winstein, S. The Correlation of Solvolysis Rates. *J. Am. Chem. Soc.* **1948**, *70*, 846-854.

Chapter 7

Summary and Future Scope of the Thesis

7.1 Summary

Non-covalent interactions, in particular the specific chemical interactions (e.g. H-bonds) and nonspecific long-range electrostatic interactions, play a pivotal role toward biomolecular functions. A molecular understanding of the local electrostatic environment within the idiosyncratic interior of biological systems, consistently for both specific (H-bonding) and nonspecific electrostatic (local polarity) interactions are fundamental for a detailed understanding of these processes. Electrostatic field (local electrostatics) serves as a microscopic and quantitative descriptor of local polarity within the biomolecular interior. Electrostatic field is the common underlying phenomenon of nonbonding interactions which are responsible for various biomolecular functions. Various theoretical models do exist for the estimation of electric fields. However involvement of a large number of assumptions in semi-empirical models and the requirement of extensive computational time for atomistic simulations of biological macromolecules limit the theoretical approach of electric field calculation. On the contrary, vibrational Stark effect illustrates a direct experimental access to the electric field. Though Stark tuning rate can provide a direct relation between the change in the electric field and the IR frequency, there are technical limitations in VSE to estimate the electric field inside a range of bio-molecules. Throughout this thesis, non-covalent interactions between a given compound and its complex environment (including H-bonds) have been determined and quantified in terms of the electric field that the environment exerts on the molecule using a simple field- frequency calibration curve.

In chapter 3, 4 and 5 we have addressed the use of conventional spectroscopies like IR, UV/VIS, fluorescence and NMR, either used separately or in tandem, to estimate

polarity in terms of electrostatic field inside the protein interior and to determine the hydrogen bonding status of C=O. The knowledge of H-bonding status of carbonyl group will be extremely beneficial for understanding the mechanistic role of H-bonds in organic and biological reactions. However, the intrinsic overlap of carbonyl stretching frequency with the amide I protein backbone IR absorption band limits the use of C=O in electric field estimation quantitatively. Here, in chapter 4 and 5, we have shown that both $n-\pi^*$ absorption and $\pi-\pi^*$ emission of the ligand can be utilized to overcome the shortcoming of the overlap of the C=O stretch with the amide I protein IR band.

In chapter 6, we have discussed another vibrational probe (i.e. nitrile) which is highly intense, local, and absorbs in the convenient region of the IR spectrum and that is useful as directional and sensitive probes of electric field in biological macromolecules. In this chapter, using fluorescence/field calibration curve, we can easily detect the nitrile hydrogen bonding status and also allows us to estimate $\vec{F}_{C\equiv N}$ using the experimentally measured $\bar{\nu}_{emission}$ in any unknown complex environment.

7.2 Future Scope

In organic chemistry, it is extremely important to understand how the structure of an organic compound affects its chemical reactivity towards the various chemical reactions.¹⁻² In order to investigate the mechanism of a reaction using substituent effect, we need to study with a reactant in which a substituent has been changed, and see how this change alters the reactivity (function) of the molecule. These substituent effects are used to determine how the free energies of reaction and activation energy vary as a function chemical structure. These substituent effects are referred to as structure-reactivity relationship. This structure-reactivity relationship is very

informative about the mechanism of the reaction.³ Many experiments that were established to demonstrate the structure–reactivity relationship focused on the linear Gibbs energy relationship of the Hammett equation.⁴⁻⁷ In 1937, Hammett quantified that the electronic influence of a substituent on the reaction center of that substrate determined by studying reaction on meta- and para- substituted benzene derivative.² However, Hammett equation fails for the ortho substituted aromatic and open chain aliphatic compounds.⁸⁻¹⁰ So we have to identify alternatives to the Hammett parameter (σ) in order to remove the dependence on the empirically derived parameters.

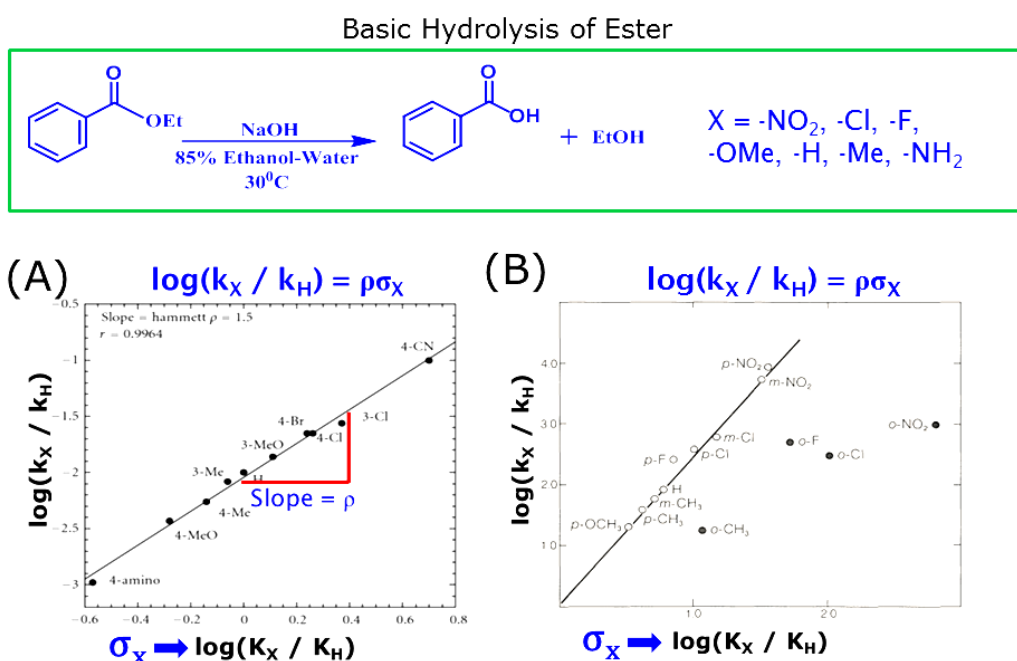


Figure 7.1 The empirically proposed Hammett equation is based on the ionization of benzoic acid in water at 25°C and is expressed as, $\log(k_X/k_H) = \rho\sigma_X$. The equation describing the linear correlation between a series of reactions with meta- and para-substituted aromatics and the hydrolysis of benzoic acids with the same substituents is known as the Hammett Equation (A). Ortho isomers do not fall on the line (B).

Hammett parameter (σ) has been commonly used by the organic chemistry community to express the effect of electronic charge density distribution throughout

the molecule upon changing the substituents on chemical system.⁹ Substitution at the aromatic ring exhibited two factors such as steric and electronic effect on the reaction rate.¹¹ Recently, Sigman et.al has shown that for the meta- and para- substituent benzoic acid only the electronic effect is present.¹² But for the ortho substituted benzoic acid, carbonyl group twisted out of plane from the aromatic ring due to the steric effects between the ortho substituent and carbonyl group.^{8, 12} So here both steric and electronic factor depends on the reaction rate. Since, in the presence of both electron withdrawing and donating substituent group, the electronic charge distribution throughout the ring changes, so that will also redistribute the charge on the carbonyl vibrational probe. So the vibrational frequency of the carbonyl group also changes. Vibrational frequency shift is sensitive to changes in the Hammett parameter.

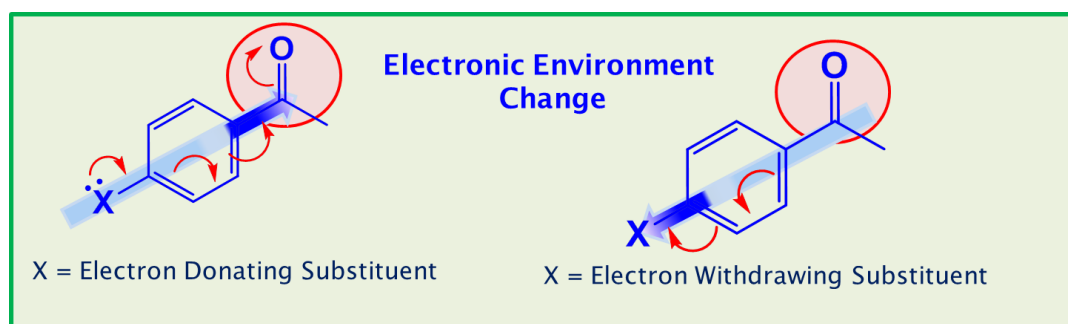


Figure 7.2 Cartoon demonstrating the influence of substituent on carbonyl vibration of acetophenone. In both cases (i.e. electron donating and withdrawing substituents) shown above, the carbonyl(C=O) vibration is a relatively local mode, indicated by the solid circle. The carbonyl group is conjugated with the highly polarizable benzene ring, and electron density can drift from benzene to the carbonyl group under the influence of a substituent. Therefore, the frequency of carbonyl is characteristic of the polarization of the entire benzene molecule.

The vibrational stark effect (VSE) spectroscopy, which describes the effect of an electric field towards the frequencies of certain vibrations (such as C=O, C≡N stretch

etc.).¹³⁻¹⁶ So the work described in the thesis can be utilized to check the possibility of replacement of the Hammett parameter by the electrostatic field.

7.3 References

1. Kreevoy, M. M. Structural Effects on Equilibrium in Organic Chemistry (Hine, Jack). *J. Chem. Educ.* **1976**, *53*, A200.
2. Hammett, L. P. The Effect of Structure upon the Reactions of Organic Compounds. Benzene Derivatives. *J. Am. Chem. Soc.* **1937**, *59*, 96-103.
3. Deno, N. C. Structure and mechanism in organic chemistry (Ingold, C.K.). *J. Chem. Educ.* **1971**, *48*, A218.
4. Wells, P. R. Linear Free Energy Relationships. *Chem. Rev.* **1963**, *63*, 171-219.
5. Hammett, L. P. Some Relations between Reaction Rates and Equilibrium Constants. *Chem. Rev.* **1935**, *17*, 125-136.
6. Hammett, L. P. Linear free energy relationships in rate and equilibrium phenomena. *Trans. Faraday Soc.* **1938**, *34*, 156-165.
7. Jaffe, H. H.; Jones, H. L. Applications of the Hammett Equation to Heterocyclic Compounds**This work was supported in part by a grant from the Petroleum Research Fund, administered by the American Chemical Society; this support is gratefully acknowledged. In *Advances in Heterocyclic Chemistry*, Katritzky, A. R., Ed. Academic Press: **1964**; Vol. 3, pp 209-261.
8. McDaniel, D. H.; Brown, H. C. A Quantitative Approach to the Ortho Effects of Halogen Substituents in Aromatic Systems^{1,2}. *J. Am. Chem. Soc.* **1955**, *77*, 3756-3763.
9. Hansch, C.; Leo, A.; Taft, R. W. A survey of Hammett substituent constants and resonance and field parameters. *Chem. Rev.* **1991**, *91* (2), 165-195.

10. Taft, R. W. Linear Free Energy Relationships from Rates of Esterification and Hydrolysis of Aliphatic and Ortho-substituted Benzoate Esters. *J. Am. Chem. Soc.* **1952**, *74*, 2729-2732.
11. Taft, R. W. Polar and Steric Substituent Constants for Aliphatic and o-Benzoate Groups from Rates of Esterification and Hydrolysis of Esters¹. *J. Am. Chem. Soc.* **1952**, *74*, 3120-3128.
12. Santiago, C. B.; Milo, A.; Sigman, M. S. Developing a Modern Approach To Account for Steric Effects in Hammett-Type Correlations. *J. Am. Chem. Soc.* **2016**, *138*, 13424-13430.
13. Boxer, S. G. Stark Realities. *J. Phys. Chem. B* **2009**, *113*, 2972-2983.
14. Fafarman, A. T.; Sigala, P. A.; Herschlag, D.; Boxer, S. G. Decomposition of Vibrational Shifts of Nitriles into Electrostatic and Hydrogen-Bonding Effects. *J. Am. Chem. Soc.* **2010**, *132*, 12811-12813.
15. Fried, S. D.; Bagchi, S.; Boxer, S. G. Measuring Electrostatic Fields in Both Hydrogen-Bonding and Non-Hydrogen-Bonding Environments Using Carbonyl Vibrational Probes. *J. Am. Chem. Soc.* **2013**, *135*, 11181-11192.
16. Fried, S. D.; Bagchi, S.; Boxer, S. G. Extreme Electric Fields Power Catalysis in the Active Site of Ketosteroid Isomerase. *Science* **2014**, *346*, 1510-1514.

ABSTRACT

Name of the Student: Tapas Haldar

Registration No.: 10CC16A26031

Faculty of Study: Chemical Sciences

Year of Submission: 2021

AcSIR academic centre/CSIR Lab: NCL, Pune

Name of the Supervisor: Dr. Sayan Bagchi

Title of the thesis: Spectroscopic Determination of Electrostatic and Hydrogen Bonding Interactions in Chemical and Biological Systems

Understanding the molecular details of the biological process is of critical consequence to modern biophysics. Non-covalent interactions (such as hydrogen bonding, electrostatic and hydrophobic interaction etc.) are more ubiquitous in biological system and which are govern by the chemical interactions between host-guest molecule, or molecular recognition, protein folding, and self-assembly of Nano-materials. The propensity to understand and predict the interaction is essential because functions of the molecules are influenced by the interaction. However, experimentally it has been extremely problematic for chemists to identify and measure the non-covalent interaction in the complex organized system such as protein.

Local electrostatics within protein interiors affects protein's interactions with ligands, substrates, and other proteins, making it a critical determinant of structure, stability and activity. Electrostatic interactions being prevalent in biomolecular systems, research efforts have focused to quantify and describe local polarity within protein cavities and to further relate that to biological processes.

A most fundamental concept from physics, electric field, which can be proxy to the local polarity within the biomolecular interior. Since the electric field is projected along the vibrational axis, so it can serve as a microscopic and quantitative descriptor of non-covalent interaction. Vibrational Stark Effect (VSE) Spectroscopy is an inherent infrared (IR) based experimental technique that is used to predict the electrostatic field experienced by a molecular vibration due to its surrounding environment. Using vibrational probes, VSE quantifies the effect of an externally applied electrostatic field on vibrational frequency. Thus non-covalent interaction is determined in a quantitative and microscopic manner by means of electric field. The concept of VSS has been used to study the local electrostatics inside the protein interiors.

Throughout this thesis, non-covalent interactions between a given compound and its complex environment (including H-bonds) have been determined and quantified in terms of the electric field that the environment exerts on the molecule using a simple field- frequency calibration curve.

List of Publication(s) in SCI Journal(s) Emanating from the Thesis Work

- (I) **Haldar, T.**; Kashid, S. M.; Deb, P.; Kesh, S.; Bagchi, S. Pick and choose the spectroscopic method to calibrate the local electric field inside proteins. *J. Phys. Chem. Lett.*, **2016**, 7, 2456–2460.
- (II) **Haldar, T.**; Bagchi, S. Electrostatic interactions are key to C=O n- π^* shifts: an experimental proof. *J. Phys. Chem. Lett.*, **2016**, 7, 2270–2275.
- (III) Chatterjee, S.; **Haldar, T.**; Ghosh, D.; Bagchi, S. Electrostatic manifestation of micro-heterogeneous solvation structures in deep eutectic solvents: a spectroscopic approach. *J. Phys. Chem. B*, **2020**, 124, 3709–3715.

List of Other Publication(s) in SCI Journal(s)

- (I) Deb, P.; **Haldar, T.**; Kashid, S. M.; Banerjee, S.; Chakrabarty, S.; Bagchi, S. Correlating Nitrile IR Frequencies to Local Electrostatics Quantifies Non covalent Interactions of Peptides and Proteins. *J. Phys. Chem. B*, **2016**, 120, 4034–4046.
- (II) Chatterjee, S.; Ghosh, D.; **Haldar, T.**; Deb, P.; Sakpal, S. S.; Deshmukh, S. H.; Kashid, S. M.; Bagchi, S. Hydrocarbon Chain Length Dependence of Solvation Dynamics in Alcohol-Based Deep Eutectic Solvents: A Two-Dimensional Infrared Spectroscopic Investigation. *J. Phys. Chem. B*, **2019**, 123, 9355–9363.

List of papers with abstract presented (oral or poster) at national or international conferences/seminars.

- (III) “**Science Day Celebration 2019**” held at CSIR National Chemical laboratory Pune.
(Presented poster)
- (IV) “**Spectroscopy and Dynamics of Molecules and Clusters (SDMC). 2019**” organized by IISER Mohali and IIT Kanpur, Shimla, India. (Presented poster)

(V) **“NCL-RF Annual Students conferences 2019”** held at CSIR National Chemical laboratory Pune. (Presented oral)

(VI) **“Spectroscopy and Dynamics of Molecules and Clusters (SDMC). 2017”** organized by IIT Madras and Indian Institute of Science, Bangalore, Pondicherry, India. (Presented poster)

(VII) **“Divisional day celebration 2017”** held at CSIR National Chemical laboratory Pune. (Presented poster)

(VI) **“Science day celebration 2017”** held at CSIR National Chemical laboratory Pune. (Presented poster)

Electrostatic Manifestation of Micro-Heterogeneous Solvation Structures in Deep-Eutectic Solvents: A Spectroscopic Approach

Srijan Chatterjee, Tapas Haldar, Deborin Ghosh, and Sayan Bagchi*

Cite This: *J. Phys. Chem. B* 2020, 124, 3709–3715

Read Online

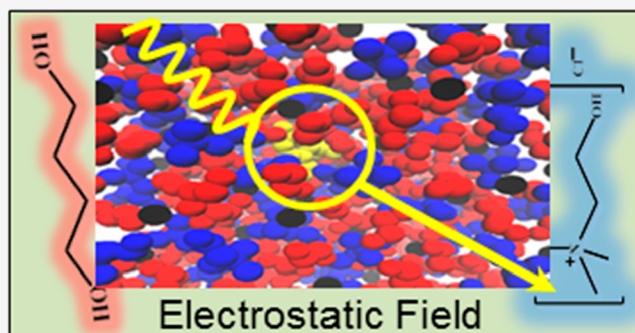
ACCESS |

Metrics & More

Article Recommendations

Supporting Information

ABSTRACT: Deep eutectic solvents have emerged as inexpensive green alternatives to conventional solvents for diverse applications in chemistry and biology. Despite their importance as useful media in various applications, little is known about the microscopic solvation structures of deep eutectic solvents around solutes. Herein, we show that the electrostatic field, which can be estimated both from infrared experiments and theory, can act as a unified concept to report on the microscopic heterogeneous solvation of deep eutectic solvents. Using a fluorophore containing the carbonyl moiety as the solute and the electrostatic field as a descriptor of the solvation structure of the deep eutectic solvents, we report the residue-specific distribution, orientation, and hydrogen bonding in deep eutectic solvents constituting of choline chloride and alcohols of varying chain-lengths. We observe that an increase in alcohol chain-length not only affects the alcohol's propensity to form hydrogen bond to the solute but also alters the spatial arrangement of choline cations around the solute, thereby leading to a microheterogeneity in the solvation structure. Moreover, to extend our electrostatic field based strategy to other deep eutectic solvents, we report an emission spectroscopy based method. We show that this method can be applied, in general, to all deep eutectic solvents, irrespective of their constituents. Overall, this work integrates experiments with molecular dynamics simulations to provide insights into the heterogeneous DES solvation.



INTRODUCTION

Deep eutectic solvent (DES), a neoteric class of environmentally benign solvents, has gained significant popularity as a suitable alternative to organic solvents.^{1–3} A typical DES consists of two or more components mixed in a certain mole ratio, with at least one hydrogen bond acceptor (HBA) and a hydrogen bond donor (HBD).^{2–4} DES, owing to extensive interspecies HB interactions, shows a large depression in melting point which allows the formation of a stable solvent at the room temperature.^{2,3} Commonly used DESs are composed of quaternary ammonium salts like choline chloride (ChCl) as the HBA and amides, alcohols, and acids as the HBD. The green character of DES has attracted potential applications in diverse fields of chemistry and biology which include organic synthesis,^{5,6} catalysis,^{7,8} biotransformations,^{9,10} and nanoscience^{11,12} among many others. Moreover, protein stability^{13–15} and enzyme activity^{16,17} have been successfully explored in DES as an alternative to water.

In recent times, studies have been performed to unravel heterogeneous nature of deep eutectic microstructure both from spectroscopic and computational standpoint.^{18–25} The effect of the hydrogen bonding partner on DES property and its relation with nanoscale heterogeneity has been analyzed using classical MD simulation^{19,26,27} and ab initio MD simulation.^{28,29} Microscopic structure and solute–DES inter-

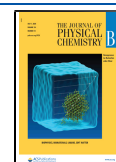
action are also discussed in conjunction with the polarity of the HBD partner.^{30–35} A few recent interesting studies also discuss the stability of DES in the aqueous presence of water.^{27,36,37}

As the choice of an appropriate DES for any given process depends on the DES solvation properties, insights into the DES solvation structures around a solute is desired.^{32,38,39} Alcohol-based (as HBD) eutectic systems are used as media in various applications due to their significantly low viscosity compared to other DESs.^{32,40} It has been suggested that changes in the hydrocarbon chain-length of the alcohol significantly influence the properties of alcohol-based DES.^{30,41} However, little is known about how the residue specific distribution and the hydrogen bonding of the DES constituents (ChCl and alcohol) are altered by the alcohol chain length. Thus, it is critical to obtain a molecular understanding of how the solvation structures of alcohol-based DES with varying chain-lengths influence the solute–

Received: December 7, 2019

Revised: February 29, 2020

Published: April 10, 2020

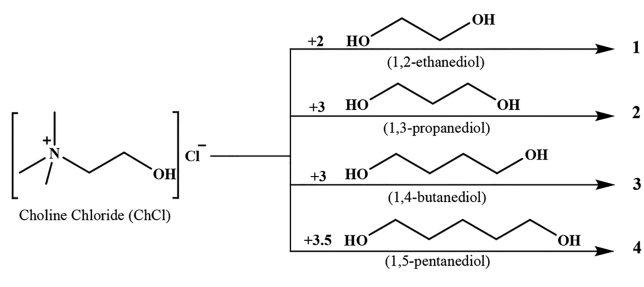


solvent interactions. To gauge solute–solvent interactions, spectroscopic responses of fluorophores have been commonly used to assess the polarity of DES through semiempirical polarity scales.^{35,40,42–44} Although these studies are informative, the continuum semiempirical polarity parameters do not account for the microscopic nature of the solvent. Moreover, these parameters cannot be computed from simulations and thus cannot provide the microscopic details of the DES solvation structures. To overcome this limitation, we require an experimental, yet microscopic, observable of solute–solvent interactions, which can independently be estimated from simulations.

It has been recently shown that electrostatic field (\vec{F}) can serve as a quantitative and microscopic descriptor of solute–solvent interactions in neat solvents and solvent mixtures.^{45,46} Carbonyl (C=O) groups, ubiquitous in chemistry and biology, has been reported to show a linear correlation between the C=O infrared (IR) frequencies ($\bar{\nu}_{\text{C=O}}$) and the corresponding electrostatic fields ($\vec{F}_{\text{C=O}}$ along the C=O bond through vibrational Stark effect (VSE)).^{47,48} As $\vec{F}_{\text{C=O}}$ depends both on the distances of all other solvent atoms from the C=O and the residual partial charges on each solvent atom, it can be directly mapped to the DES solvation structure. Moreover, $\vec{F}_{\text{C=O}}$ exerted by the DES on the solute's C=O can be independently estimated from molecular dynamics (MD) simulations. The electrostatic field estimated from simulations can be compared with that measured from experiment to benchmark the MD force fields.⁴⁷ A good agreement between the common microscopic parameter ($\vec{F}_{\text{C=O}}$) obtained independently from experiments and simulations would allow us to get insights into the variation in the solvation structures of alcohol-based DES with varying chain lengths.

In this report, we have experimentally determined $\vec{F}_{\text{C=O}}$ along the C=O bond of a fluorophore, coumarin 151 (C151), exerted by the four alcohol-based DESs (Scheme 1) from

Scheme 1. Molecular Structures of the Constituents of the DES Used in This Study



infrared (IR) spectroscopy. We have compared the experimentally determined $\vec{F}_{\text{C=O}}$ with those estimated from MD simulations. Furthermore, we have decomposed the total electrostatic field into contributions from individual HBA and HBD constituents to obtain an in-depth understanding of the microscopic heterogeneous solvation of the DESs around the solute molecule. Moreover, in order to obtain a general strategy for $\vec{F}_{\text{C=O}}$ estimation in any DES, irrespective of its constituents, we have successfully used the emission peak maxima of the fluorophore to estimate electrostatic fields in three non-alcohol-based DESs.

MATERIALS AND METHODS

Materials. Coumarin151(C151), choline chloride (ChCl), 1,2-ethanediol, 1,3-propanediol, 1,4-butanediol, 1,5-pentanediol, urea, malonic acid, and oxalic acid and solvents like dibutyl ether (DBE), diethyl ether (DEE), tetrahydrofuran (THF), valeronitrile (VLN), and acetonitrile (ACN) were purchased from Sigma-Aldrich. All chemicals other than ChCl were used without further purification. Milli-Q water was used in this study.

Sample Preparation. All of the deep eutectic solvents were synthesized by following a reported procedure.^{41,49} Choline chloride was dried in a vacuum oven at 90 °C for 24 h before use. All of the deep eutectic solvents were prepared in an argon-filled glovebox. ChCl were mixed with respective diols, urea and acids with a specific molar ratio. Then the mixtures were heated and stirred at 60–70 °C until fully homogeneous colorless liquids were formed. The reaction mixture was allowed to cool to room temperature before any measurements were taken. Water content was measured by using a Metrohm Karl Fischer titrator and results indicated that water contents are less than 0.5% by weight (Table S1). Full IR absorption spectra of DESs are shown in Figure S1 (Supporting Information). The absence of the water band (OH bend) near 1700 cm^{-1} in pure DES spectra as compared to that in pure water and DES water mixtures (2:1 v/v) (Figure S2, Supporting Information) validates the results obtained from water content measurement in DESs.

Spectroscopy. IR absorption spectra were recorded on a FTIR-Bruker Vertex 70 spectrometer with 2 cm^{-1} resolution at room temperature. For each sample, ~60 μL of the sample solution was loaded into a demountable cell consisting of two windows (CaF_2 , 3 mm thickness, Shenzen Laser), separated by a mylar spacer of 56 μm thickness. IR cells were prepared in Argon filled glovebox to minimize the water contamination. Fluorescence was obtained with a calibrated Spectrofluorometer FS5 (Edinburgh Instruments).

Molecular Dynamics Simulations. Classical molecular dynamics simulations were performed by GROMACS 2016.5 package.⁵⁰ Parameters for pure solvents and coumarin 151 dye were taken from our previous work based on AMBER framework.⁵¹ Force field parameters for ChCl, 1,2-ethanediol, urea, malonic acid, and oxalic acid are taken from the work of Brian et al.,²⁶ and for 1,3-propanediol and 1,4-butanediol, we have used force field parameters for alcohol generated by the automatic server by Jorgensen and co-workers.⁵² Cubic simulation boxes are defined by 100 choline chloride ion pair and varying number of hydrogen bond donor according to the experimental mole fraction using GROMACS build in tool. Prior to each simulation step, we have performed energy minimization by steepest descent algorithm with 2 fs step size. *NVT* ensemble was performed at 300 K for 1 ns with a velocity rescale thermostat and was followed by the *NPT* ensemble at 300 K temperature and 1 bar pressure using a Parrinello–Rahman barostat for 5 ns. LINCS is used to constrain all the hydrogen atoms which are covalently bonded. Production runs are carried out for a minimum of 10 ns.

Hydrogen bond analysis are performed on GROMACS of last 5 ns of trajectory where position outputs are saved every 500 ps. The distance cutoff of 3.5 Å and angle cutoff of 30° are used for the hydrogen bond calculation. Represented snapshots are obtained by using GROMACS cluster analysis tool to get the most probable arrangement. Electric field on carbonyl

bonds of coumarin151 have been calculated according to our previous work.⁴⁸

RESULTS AND DISCUSSION

Coumarin 151 (C151), a common fluorophore containing an ester C=O moiety is dissolved in the synthesized DESs to perform the spectroscopic experiments. The emission peak positions of C151 in the DESs (Figure S3 in the Supporting Information) are similar to those of C151 in acetonitrile–(ACN–) water mixtures (Figure S4) and show a gradual blue-shift with increasing hydrocarbon chain-length of the alcohols.

The blue-shift in the emission maxima is consistent with an earlier report, albeit using different fluorophores.³² Furthermore, the IR spectra in the C=O stretch region of C151 are measured in neat solvents and aqueous ACN solutions (Figure S4 in the Supporting Information). The C=O stretch region in C151 shows overlapping transitions (Figure S5A in the Supporting Information) arising from the C=O stretch (lower frequencies) and Fermi resonance peaks (higher frequencies).⁵³ The peaks are deconvolved to obtain the C=O peak positions ($\bar{\nu}_{C=O}$), as shown in Figure S5B in the Supporting Information. A gradual red-shift in $\bar{\nu}_{C=O}$ is observed with the increasing polarity of the solvents. We have also estimated $\bar{F}_{C=O}$ from MD simulations in the same solvents and aqueous ACN solutions.⁵⁴ A plot of the paired points ($\bar{\nu}_{C=O}, \bar{F}_{C=O}$) shows a linear correlation ($R^2 = 0.98$) with a slope of $0.32 \text{ cm}^{-1}/(\text{MV}/\text{cm})$ (Figure 1A). This is in excellent agreement with the reported Stark tuning rates [$\Delta\bar{\nu}_{C=O}/\Delta\bar{F}_{C=O} \sim 1.0 \text{ cm}^{-1}/(\text{MV}/\text{cm})$] of ester C=O,⁵⁵ independently measured from vibrational Stark spectroscopy, containing a local field

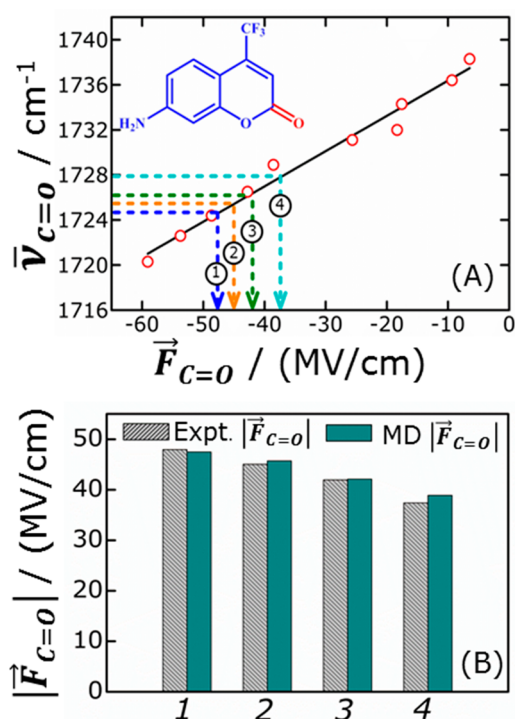


Figure 1. (A) C=O IR stretching frequencies ($\bar{\nu}_{C=O}$) in neat solvents and ACN-water mixtures show a linear correlation with the corresponding $\bar{F}_{C=O}$ of C151. The black line indicates the best fit line ($R^2 = 0.98$). $\bar{F}_{C=O}$ in **1**, **2**, **3**, and **4** are estimated from their respective $\bar{\nu}_{C=O}$. (B) Bar plots of IR estimated and MD predicted $\bar{F}_{C=O}$ in **1**, **2**, **3**, and **4** show excellent agreement.

factor of ~ 3 .⁵⁶ The best-fit straight line in Figure 1A acts as a calibration line and allows us to estimate $\bar{F}_{C=O}$ using the experimentally measured $\bar{\nu}_{C=O}$ in any unknown environment.⁴⁷ To estimate the average electrostatic fields exerted along the solute C=O bond by the alcohol-based DESs with varying hydrocarbon chain-lengths, we obtain the values of $\bar{\nu}_{C=O}$ of C151 in **1**, **2**, **3**, and **4** (Figure S6 in the Supporting Information). Similar to the emission peak maxima, $\bar{\nu}_{C=O}$ also show a gradual blue-shift with increasing hydrocarbon chain-length of the alcohols. Using, the calibration line in Figure 1A, we estimate the fields to be -47.9 , -45.1 , -41.9 , and $-37.4 \text{ MV}/\text{cm}$ in **1**, **2**, **3**, and **4**, respectively. This result indicates that $\bar{F}_{C=O}$ exerted by the DES decreases with the increase in the chain-length of the alcohols, plausibly due the increase in hydrophobicity arising from the longer hydrocarbon chains. Furthermore, we have generated the force-fields for **1**, **2**, **3**, and **4** and performed MD simulations to predict $\bar{F}_{C=O}$ on C151 in the four alcohol-based DESs. Figure 1B and Table S1 in the Supporting Information show that the $\bar{F}_{C=O}$ estimated from the IR spectra are in excellent agreement with those predicted from MD simulations.

As the IR estimated electrostatic fields are validated by the independently measured Stark tuning rate (from the slope in Figure 1A), this agreement between theory and experiment allows us to obtain further insights about the variation in HB, distribution, and orientation of the DES constituents around C151 as a function of alcohol chain-length. First, we decomposed the total $\bar{F}_{C=O}$ estimated from MD simulations to the contributions from the individual constituents (HBA and HBD) for all the alcohol-based DESs (Figure 2A and Table S2

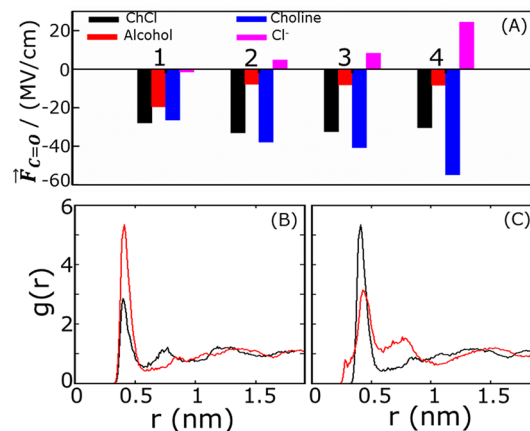


Figure 2. (A) Contributions from ChCl, alcohol, choline cation, and chloride anion to the total $\bar{F}_{C=O}$. (B) RDF between the C=O oxygen of C151 and the choline nitrogen in 1,2-ethanediol (**1**, black) and 1,5-pentanediol (**4**, red). (C) RDF between the C=O oxygen of C151 and the choline nitrogen in 1,5-pentanediol (**4**, black) and between the C=O oxygen of C151 and the choline oxygen in 1,5-pentanediol (**4**, red).

in the Supporting Information). It is observed that the exerted field arises predominantly (60–80%) from ChCl across all DESs. Despite the apparent change in hydrophobicity with the variation in alcohol chain-length, the diols have a smaller contribution to the overall $\bar{F}_{C=O}$ experienced by the solute. The largest contribution of the alcohol constituent is observed in **1**; the electrostatic field (a greater negative indicates larger stabilization) drops off to about half the value in **1** for larger chain alcohols. However, the electrostatic fields exerted by

ChCl almost remain constant and no apparent trend can be observed in as a function of alcohol chain-length. When we further decompose the total field arising from ChCl field into contributions from the choline cations and the chloride anions (Figure 2A and Table S2 in the Supporting Information), we find an interesting trend. A monotonic increase in the stabilizing field from the choline cations (C=O-cation attraction) as a function of increasing alcohol chain-length is accompanied by a subsequent increase in the destabilizing field from the chloride anions (C=O-anion repulsion). This result suggests ChCl remains as an ion-pair, as also reported in a recent study.⁵⁷ Furthermore, as the electrostatic field is inversely proportional to the square of the distance, the result indicates that the choline concentration around the C151 C=O increases with increase in the chain-length of the alcohol constituent. To obtain a greater insight into this, radial distribution function (RDF) is calculated between the C=O oxygen (O) of C151 and the choline nitrogen (N) for all DESs. As surmised from the changes in the electrostatic fields exerted by choline in the alcohol-based DESs, we observe that the RDF peak intensity increases with increase in the alcohol chain-length (Figure 2B). The variation in the RDF peak intensities for different alcohol chain-lengths correlates with the variation observed in $\bar{F}_{C=O}$ exerted by choline. Additionally, to investigate the orientation of the choline molecules with respect to the solute C=O, we have calculated the RDF between the carbonyl oxygen of C151 and the choline O in in 1, 2, 3, and 4. Figure 2C shows that the N atom of the choline cation is predominantly oriented toward the solute carbonyl. The small peak in the RDF between C=O oxygen and choline O within 3.5 Å indicates a small population of the choline cation where the hydroxyl groups are oriented toward the solute C=O, plausibly forming HB to the C=O. As both the choline and the alcohol constituents of the DESs contain OH groups it will be interesting to understand which is the preferred hydrogen bond partner to C151 C=O. We have performed hydrogen bond analysis, and it demonstrates that preferential hydrogen bonding occurs between C151 C=O and alcohol OH (Table S3 in the Supporting Information). However, the HB propensity monotonically decreases with increase in the alcohol chain-length. Thus, it can be concluded that the increase in alcohol chain-length not only perturbs the HB affinity but it also affects the spatial arrangement of choline cation around the solute leading to a microheterogeneity in the solvation structure. The overall solvation environment is manifested in the total $\bar{F}_{C=O}$ experienced by the solute C=O, however, decomposition of the total field into residue-specific contributions unfolds the microheterogeneity of the solvation structure. Representative MD snapshots in Figure 3 show the heterogeneous solvation structure around the solute in four different alcohol-based DESs with varying chain length.

Even though we have established an electrostatic field based methodology to obtain molecular insights into the solvation structure of DES, this strategy requires experimental determination of $\bar{\nu}_{C=O}$ from the IR spectra to estimate the electrostatic fields exerted of the solute. However, the HBD constituent of DES is not restricted to alcohols. Amides and carboxylic acids, which have also been reported as common HBD constituents in DESs, themselves contain the C=O group. As it is not feasible to decipher $\bar{\nu}_{C=O}$ of the solute in the presence of the broad and intense IR signal from the solvent C=O group, our strategy is limited to alcohol-based DES. In search of an alternate strategy applicable to all DES, we

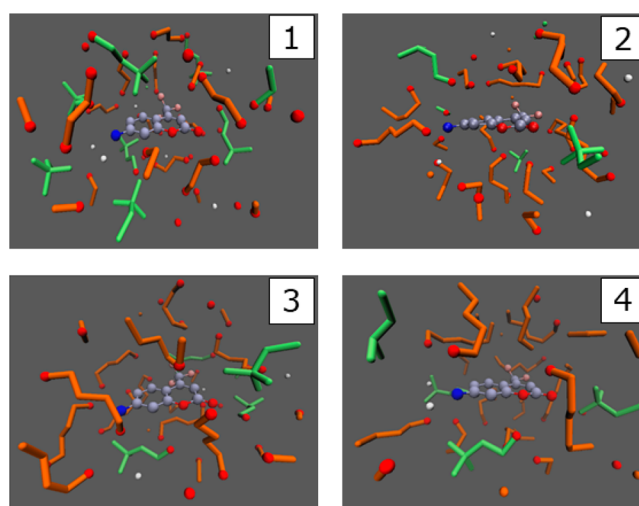


Figure 3. Representative snapshots of 1, 2, 3, and 4 from MD trajectories. The snapshots are obtained by averaging the coordinates of a 5 ns long simulation.

decided to plot $\bar{\nu}_{C=O}$ of 1, 2, 3, and 4 against the corresponding emission frequencies (Figure 4A) as both

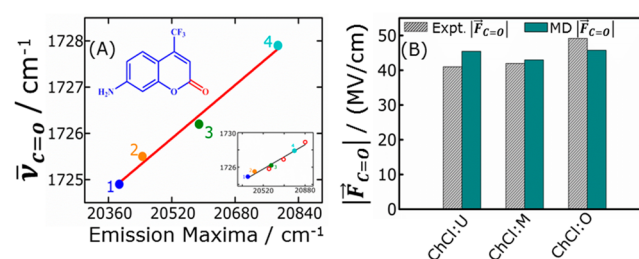
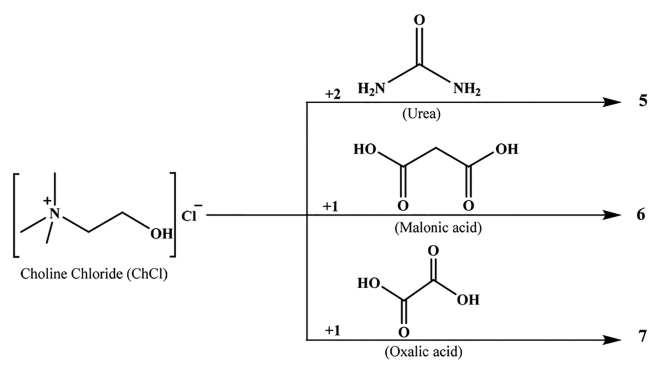


Figure 4. (A) C=O IR stretching frequencies ($\bar{\nu}_{C=O}$) in 1, 2, 3, and 4 and aqueous acetonitrile solutions (v/v) {80% acetonitrile, 60% acetonitrile, 40% acetonitrile} [red circle, inset] show a linear correlation with the corresponding emission peak maxima of C151. The red line indicates the best fit line ($R^2 = 0.98$). (B) Bar plot of $\bar{F}_{C=O}$ estimated from emission peak maxima and MD simulations in ChCl:U, ChCl:M, and ChCl:O show good agreement

emission and IR peak maxima in alcohol-based DESs show blue shifts with increasing chain length. Interestingly, a linear correlation ($R^2 = 0.98$) is observed between $\bar{\nu}_{C=O}$ and the emission peak maxima. As the other commonly used DESs contain a C=O moiety, they cannot be used to check the generality of this linear relation between $\bar{\nu}_{C=O}$ and the emission frequencies. However, when points from noneutectic solutions, containing a HBD and a HBA (binary mixtures of ACN and water), are included (Figure 4A, inset), the excellent linear correlation ($R^2 = 0.97$) between $\bar{\nu}_{C=O}$ and the emission peak maxima validates the generality of the aforesaid linearity. This observation implies that $\bar{F}_{C=O}$ can also be estimated using the emission peak maxima. The origin of this linear relationship is itself an interesting topic of investigation, however, it falls outside the scope of this work. Instead, we have compared the experimental $\bar{F}_{C=O}$ from emission peak maxima with those estimated from simulations to inspect the generality of this approach for DES constituents containing the C=O group.

Combining the linear relationships from Figures 1A and 4A, we have estimated $\bar{F}_{C=O}$ in three more DESs (Scheme 2): 5

Scheme 2. Molecular Structures of Other Constituents of the DES Used in This Study



(ChCl:U), 6 (ChCl:M), and 7 (ChCl:O), where the HBD constituents contain the C=O group. The estimated values of $\bar{F}_{C=O}$ on C151 in these three DESs are given in Table S4 in the Supporting Information. Furthermore, we have independently predicted $\bar{F}_{C=O}$ in these C=O-containing DESs from MD simulations. Figure 4B shows that the experimentally estimated fields agree well with the MD predicted fields. This agreement demonstrates that a molecular level understanding of the DES solvation structures can indeed be obtained for other DESs using the electrostatic field based approach, independent of the DES constituents.

CONCLUSION

To understand changes in solute–solvent interactions in different DESs, earlier reports assessed empirical solvent parameters depicting polarity, HBD acidity, and HBA basicity using responses of fluorescent probes.^{21,31,34,35} However, these empirical parameters cannot be computed from MD simulations, and thus they cannot provide further insights into the heterogeneous solvation structure of the DES. We have successfully demonstrated that electrostatic field can be used a unified concept to decipher the microheterogeneity as well as the subtle changes in the solvation structures of the alcohol-based DESs with varying hydrocarbon chain length. We have obtained a molecular understanding of the distribution, orientation, and HB of the constituents with respect to DES solvation. Furthermore, we have shown that an emission spectroscopy based methodology allows us to determine the electrostatic fields in any DES, irrespective of the constituents. Recent experimental and theoretical studies have shown that electrostatic fields play key roles in chemical and enzymatic processes.^{58–60} This electrostatic field based strategy will enable us to connect theoretical and experimental results and to provide insights into the various applications of DES in chemistry and biology.

ASSOCIATED CONTENT

Supporting Information

The Supporting Information is available free of charge at <https://pubs.acs.org/doi/10.1021/acs.jpbc.9b11352>.

Figures showing FTIR spectra, emission spectra, fluorescence emission spectra, IR absorption spectra, and radial distribution functions and tables of spectral data, deconvolution of total electric field, calculated number of hydrogen bonds, and emission maxima (PDF)

AUTHOR INFORMATION

Corresponding Author

Sayan Bagchi – Physical and Materials Chemistry Division, CSIR-National Chemical Laboratory (CSIR-NCL), Pune 411008, India; Academy of Scientific and Innovative Research (AcSIR), Ghaziabad 201002, India; orcid.org/0000-0001-6932-3113; Phone: +91-20-25903048; Email: s.bagchi@ncl.res.in; Fax: +91-20-25902636

Authors

Srijan Chatterjee – Physical and Materials Chemistry Division, CSIR-National Chemical Laboratory (CSIR-NCL), Pune 411008, India; Academy of Scientific and Innovative Research (AcSIR), Ghaziabad 201002, India

Tapas Haldar – Physical and Materials Chemistry Division, CSIR-National Chemical Laboratory (CSIR-NCL), Pune 411008, India; Academy of Scientific and Innovative Research (AcSIR), Ghaziabad 201002, India

Deborin Ghosh – Physical and Materials Chemistry Division, CSIR-National Chemical Laboratory (CSIR-NCL), Pune 411008, India

Complete contact information is available at:

<https://pubs.acs.org/10.1021/acs.jpbc.9b11352>

Notes

The authors declare no competing financial interest.

ACKNOWLEDGMENTS

S.B. acknowledges SERB India (EMR/2016/000576). D.G. acknowledges SERB India (PDF/2018/000046). We would like to thank Debranj Mandal and Dr. Arup Kumar Rath, CSIR-NCL, Pune, for their support in DES synthesis.

REFERENCES

- (1) Francisco, M.; van den Bruinhorst, A.; Kroon, M. C. Low-transition-temperature Mixtures (LTTMs): A New Generation of Designer Solvents. *Angew. Chem., Int. Ed.* **2013**, *52*, 3074–3085.
- (2) Smith, E. L.; Abbott, A. P.; Ryder, K. S. Deep eutectic solvents (DESs) and their applications. *Chem. Rev.* **2014**, *114* (21), 11060–11082.
- (3) Zhang, Q.; De Oliveira Vigier, K.; Royer, S.; Jerome, F. Deep eutectic solvents: syntheses, properties and applications. *Chem. Soc. Rev.* **2012**, *41* (21), 7108–7146.
- (4) Abbott, A. P.; Boothby, D.; Capper, G.; Davies, D. L.; Rasheed, R. K. Deep Eutectic Solvents Formed Between Choline Chloride and Carboxylic Acids: Versatile Alternatives to Ionic Liquids. *J. Am. Chem. Soc.* **2004**, *126* (29), 9142–7.
- (5) Alonso, D. A.; Baeza, A.; Chinchilla, R.; Guillena, G.; Pastor, I. M.; Ramón, D. J. Deep Eutectic Solvents: The Organic Reaction Medium of the Century. *Eur. J. Org. Chem.* **2016**, *2016* (4), 612–632.
- (6) Ruß, C.; König, B. Low melting mixtures in organic synthesis - an alternative to ionic liquids? *Green Chem.* **2012**, *14* (11), 2969–2982.
- (7) Abbott, A. P.; Capper, G.; Davies, D. L.; Rasheed, R. K.; Tambyrajah, V. Quaternary ammonium zinc- or tin-containing ionic liquids: water insensitive, recyclable catalysts for Diels-Alder reactions. *Green Chem.* **2002**, *4* (1), 24–26.
- (8) Gu, Y.; Jérôme, F. Bio-based solvents: an emerging generation of fluids for the design of eco-efficient processes in catalysis and organic chemistry. *Chem. Soc. Rev.* **2013**, *42* (24), 9550–9570.
- (9) Dominguez de Maria, P.; Maugeri, Z. Ionic liquids in biotransformations: from proof-of-concept to emerging deep-eutectic-solvents. *Curr. Opin. Chem. Biol.* **2011**, *15* (2), 220–225.

- (10) Gorke, J. T.; Srienc, F.; Kazlauskas, R. J. Hydrolase-catalyzed biotransformations in deep eutectic solvents. *Chem. Commun.* **2008**, No. 10, 1235–1237.
- (11) Liao, H.-G.; Jiang, Y.-X.; Zhou, Z.-Y.; Chen, S.-P.; Sun, S.-G. Shape-Controlled Synthesis of Gold Nanoparticles in Deep Eutectic Solvents for Studies of Structure-Functionality Relationships in Electrocatalysis. *Angew. Chem.* **2008**, *120* (47), 9240–9243.
- (12) Wagle, D. V.; Zhao, H.; Baker, G. A. Deep eutectic solvents: sustainable media for nanoscale and functional materials. *Acc. Chem. Res.* **2014**, *47* (8), 2299–2308.
- (13) Esquembre, R.; Sanz, J. M.; Wall, J. G.; del Monte, F.; Mateo, C. R.; Ferrer, M. L. Thermal unfolding and refolding of lysozyme in deep eutectic solvents and their aqueous dilutions. *Phys. Chem. Chem. Phys.* **2013**, *15* (27), 11248–11256.
- (14) Monhemi, H.; Housaindokht, M. R.; Moosavi-Movahedi, A. A.; Bozorgmehr, M. R. How a protein can remain stable in a solvent with high content of urea: insights from molecular dynamics simulation of *Candida antarctica* lipase B in urea: choline chloride deep eutectic solvent. *Phys. Chem. Chem. Phys.* **2014**, *16* (28), 14882–14893.
- (15) Parnica, J.; Antalík, M. Urea and guanidine salts as novel components for deep eutectic solvents. *J. Mol. Liq.* **2014**, *197*, 23–26.
- (16) Harifi-Mood, A. R.; Ghobadi, R.; Divsalar, A. The effect of deep eutectic solvents on catalytic function and structure of bovine liver catalase. *Int. J. Biol. Macromol.* **2017**, *95*, 115–120.
- (17) Wu, B. P.; Wen, Q.; Xu, H.; Yang, Z. Insights into the impact of deep eutectic solvents on horseradish peroxidase: Activity, stability and structure. *J. Mol. Catal. B: Enzym.* **2014**, *101*, 101–107.
- (18) Mjalli, F. S.; Naser, J.; Jibril, B.; Alizadeh, V.; Gano, Z. Tetrabutylammonium Chloride Based Ionic Liquid Analogues and Their Physical Properties. *J. Chem. Eng. Data* **2014**, *59* (7), 2242–2251.
- (19) Kaur, S.; Malik, A.; Kashyap, H. K. Anatomy of Microscopic Structure of Ethaline Deep Eutectic Solvent Decoded through Molecular Dynamics Simulations. *J. Phys. Chem. B* **2019**, *123* (39), 8291–8299.
- (20) Dou, J.; Zhao, Y.; Yin, F.; Li, H.; Yu, J. Mechanistic Study of Selective Absorption of NO in Flue Gas Using EG-TBAB Deep Eutectic Solvents. *Environ. Sci. Technol.* **2019**, *53* (2), 1031–1038.
- (21) Das, A.; Biswas, R. Dynamic Solvent Control of a Reaction in Ionic Deep Eutectic Solvents: Time-Resolved Fluorescence Measurements of Reactive and Nonreactive Dynamics in (Choline Chloride + Urea) Melts. *J. Phys. Chem. B* **2015**, *119* (31), 10102–10113.
- (22) Guchhait, B.; Das, S.; Daschakraborty, S.; Biswas, R. Interaction and dynamics of (alkylamide + electrolyte) deep eutectics: Dependence on alkyl chain-length, temperature, and anion identity. *J. Chem. Phys.* **2014**, *140* (10), 104514.
- (23) Das, A.; Das, S.; Biswas, R. Density relaxation and particle motion characteristics in a non-ionic deep eutectic solvent (acetamide + urea): Time-resolved fluorescence measurements and all-atom molecular dynamics simulations. *J. Chem. Phys.* **2015**, *142* (3), 034505.
- (24) Das, A.; Das, S.; Biswas, R. Fast fluctuations in deep eutectic melts: Multi-probe fluorescence measurements and all-atom molecular dynamics simulation study. *Chem. Phys. Lett.* **2013**, *581*, 47–51.
- (25) Mukherjee, K.; Das, A.; Choudhury, S.; Barman, A.; Biswas, R. Dielectric Relaxations of (Acetamide + Electrolyte) Deep Eutectic Solvents in the Frequency Window, $0.2 \leq \nu/\text{GHz} \leq 50$: Anion and Cation Dependence. *J. Phys. Chem. B* **2015**, *119* (25), 8063–8071.
- (26) Doherty, B.; Acevedo, O. OPLS Force Field for Choline Chloride-Based Deep Eutectic Solvents. *J. Phys. Chem. B* **2018**, *122* (43), 9982–9993.
- (27) Kumari, P.; Shobhna; Kaur, S.; Kashyap, H. K. Influence of Hydration on the Structure of Reline Deep Eutectic Solvent: A Molecular Dynamics Study. *ACS Omega* **2018**, *3* (11), 15246–15255.
- (28) Fetisov, E. O.; Harwood, D. B.; Kuo, I. F. W.; Warrag, S. E. E.; Kroon, M. C.; Peters, C. J.; Siepmann, J. I. First-Principles Molecular Dynamics Study of a Deep Eutectic Solvent: Choline Chloride/Urea and Its Mixture with Water. *J. Phys. Chem. B* **2018**, *122* (3), 1245–1254.
- (29) Stefanovic, R.; Ludwig, M.; Webber, G. B.; Atkin, R.; Page, A. J. Nanostructure, hydrogen bonding and rheology in choline chloride deep eutectic solvents as a function of the hydrogen bond donor. *Phys. Chem. Chem. Phys.* **2017**, *19* (4), 3297–3306.
- (30) Chatterjee, S.; Ghosh, D.; Haldar, T.; Deb, P.; Sakpal, S. S.; Deshmukh, S. H.; Kashid, S. M.; Bagchi, S. Hydrocarbon Chain-Length Dependence of Solvation Dynamics in Alcohol-Based Deep Eutectic Solvents: A Two-Dimensional Infrared Spectroscopic Investigation. *J. Phys. Chem. B* **2019**, *123* (44), 9355–9363.
- (31) Hossain, S. S.; Paul, S.; Samanta, A. Liquid Structure and Dynamics of Tetraalkylammonium Bromide-Based Deep Eutectic Solvents: Effect of Cation Chain Length. *J. Phys. Chem. B* **2019**, *123* (31), 6842–6850.
- (32) Hossain, S. S.; Samanta, A. How do the hydrocarbon chain length and hydroxyl group position influence the solute dynamics in alcohol-based deep eutectic solvents? *Phys. Chem. Chem. Phys.* **2018**, *20* (38), 24613–24622.
- (33) Pandey, A.; Bhawna; Dhingra, D.; Pandey, S. Hydrogen Bond Donor/Acceptor Cosolvent-Modified Choline Chloride-Based Deep Eutectic Solvents. *J. Phys. Chem. B* **2017**, *121* (16), 4202–4212.
- (34) Pandey, A.; Pandey, S. Solvatochromic Probe Behavior within Choline Chloride-Based Deep Eutectic Solvents: Effect of Temperature and Water. *J. Phys. Chem. B* **2014**, *118* (50), 14652–14661.
- (35) Pandey, A.; Rai, R.; Pal, M.; Pandey, S. How polar are choline chloride-based deep eutectic solvents? *Phys. Chem. Chem. Phys.* **2014**, *16* (4), 1559–1568.
- (36) Hammond, O. S.; Bowron, D. T.; Edler, K. J. The Effect of Water upon Deep Eutectic Solvent Nanostructure: An Unusual Transition from Ionic Mixture to Aqueous Solution. *Angew. Chem., Int. Ed.* **2017**, *56* (33), 9782–9785.
- (37) Posada, E.; López-Salas, N.; Jiménez Riobóo, R. J.; Ferrer, M. L.; Gutiérrez, M. C.; del Monte, F. Reline aqueous solutions behaving as liquid mixtures of H-bonded co-solvents: microphase segregation and formation of co-continuous structures as indicated by Brillouin and ¹H NMR spectroscopies. *Phys. Chem. Chem. Phys.* **2017**, *19* (26), 17103–17110.
- (38) Cui, Y.; Fulfer, K. D.; Ma, J.; Weldeghiorghis, T. K.; Kuroda, D. G. Solvation dynamics of an ionic probe in choline chloride-based deep eutectic solvents. *Phys. Chem. Chem. Phys.* **2016**, *18* (46), 31471–31479.
- (39) Baz, J. r.; Held, C.; Pleiss, J. r.; Hansen, N. Thermophysical properties of glyceline-water mixtures investigated by molecular modelling. *Phys. Chem. Chem. Phys.* **2019**, *21* (12), 6467–6476.
- (40) Abbott, A. P.; Harris, R. C.; Ryder, K. S.; D'Agostino, C.; Gladden, L. F.; Mantle, M. D. Glycerol eutectics as sustainable solvent systems. *Green Chem.* **2011**, *13* (1), 82–90.
- (41) Harris, R. M. *Physical Properties of Alcohol Based Deep Eutectic Solvents*; University of Leicester: 2008.
- (42) Dimroth, K.; Reichardt, C.; Siepmann, T.; Bohlmann, F. About Pyridinium N-Phenolic Betaines and Their Use for Characterizing the Polarity of Solvents. *Justus Liebigs Annalen der Chemie* **1963**, *661* (1), 1–37.
- (43) Kamlet, M. J.; Abboud, J. L.; Taft, R. W. The solvatochromic comparison method. 6. The π^* scale of solvent polarities. *J. Am. Chem. Soc.* **1977**, *99* (18), 6027–6038.
- (44) Kamlet, M. J.; Taft, R. W. The solvatochromic comparison method. I. The β -scale of solvent hydrogen-bond acceptor (HBA) basicities. *J. Am. Chem. Soc.* **1976**, *98* (2), 377–383.
- (45) Deb, P.; Haldar, T.; Kashid, S. M.; Banerjee, S.; Chakraborty, S.; Bagchi, S. Correlating Nitrile IR Frequencies to Local Electrostatics Quantifies Noncovalent Interactions of Peptides and Proteins. *J. Phys. Chem. B* **2016**, *120* (17), 4034–4046.
- (46) Fried, S. D.; Boxer, S. G. Measuring Electric Fields and Noncovalent Interactions Using the Vibrational Stark Effect. *Acc. Chem. Res.* **2015**, *48* (4), 998–1006.
- (47) Fried, S. D.; Bagchi, S.; Boxer, S. G. Measuring Electrostatic Fields in Both Hydrogen-Bonding and Non-Hydrogen-Bonding Environments Using Carbonyl Vibrational Probes. *J. Am. Chem. Soc.* **2013**, *135* (30), 11181–11192.

(48) Haldar, T.; Kashid, S. M.; Deb, P.; Kesh, S.; Bagchi, S. Pick and Choose the Spectroscopic Method to Calibrate the Local Electric Field inside Proteins. *J. Phys. Chem. Lett.* **2016**, *7* (13), 2456–2460.

(49) HÄkkinen, R.; Abbott, A. Solvation of carbohydrates in five choline chloride-based deep eutectic solvents and the implication for cellulose solubility. *Green Chem.* **2019**, *21* (17), 4673–4682.

(50) Abraham, M. J.; Murtola, T.; Schulz, R.; Pall, S. r.; Smith, J. C.; Hess, B.; Lindahl, E. GROMACS: High performance molecular simulations through multi-level parallelism from laptops to supercomputers. *SoftwareX* **2015**, *1–2*, 19–25.

(51) Wang, J.; Wolf, R. M.; Caldwell, J. W.; Kollman, P. A.; Case, D. A. Development and testing of a general amber force field. *J. Comput. Chem.* **2004**, *25* (9), 1157–74.

(52) Dodda, L. S.; Vilseck, J. Z.; Tirado-Rives, J.; Jorgensen, W. L. 1.14*CM1A-LBCC: Localized Bond-Charge Corrected CM1A Charges for Condensed-Phase Simulations. *J. Phys. Chem. B* **2017**, *121* (15), 3864–3870.

(53) Arjunan, V.; Puviarasan, N.; Mohan, S.; Murugesan, P. Fourier transform infrared and Raman spectral assignments and analysis of 7-amino-4-trifluoromethylcoumarin. *Spectrochim. Acta, Part A* **2007**, *67* (5), 1290–1296.

(54) Haldar, T.; Bagchi, S. Electrostatic Interactions Are Key to C=O $n-\pi^*$ Shifts: An Experimental Proof. *J. Phys. Chem. Lett.* **2016**, *7* (12), 2270–2275.

(55) Schneider, S. H.; Boxer, S. G. Vibrational Stark Effects of Carbonyl Probes Applied to Reinterpret IR and Raman Data for Enzyme Inhibitors in Terms of Electric Fields at the Active Site. *J. Phys. Chem. B* **2016**, *120* (36), 9672–9684.

(56) Olson, J. Z.; Schneider, S. H.; Johansson, P. K.; Luk, T. S.; Schlenker, C. W. Stark Tuning Rates of Organic Carbonates Used in Electrochemical Energy Storage Devices. *J. Phys. Chem. C* **2019**, *123* (18), 11484–11492.

(57) Shaukat, S.; Fedotova, M. V.; Kruchinin, S. E.; Bester-Rogac, M.; Podlipnik, C.; Buchner, R. Hydration and ion association of aqueous choline chloride and chlorocholine chloride. *Phys. Chem. Chem. Phys.* **2019**, *21* (21), 10970–10980.

(58) Fried, S. D.; Bagchi, S.; Boxer, S. G. Extreme electric fields power catalysis in the active site of ketosteroid isomerase. *Science* **2014**, *346* (6216), 1510–1514.

(59) Aragonès, A. C.; Haworth, N. L.; Darwish, N.; Ciampi, S.; Bloomfield, N. J.; Wallace, G. G.; Diez-Perez, I.; Coote, M. L. Electrostatic catalysis of a Diels-Alder reaction. *Nature* **2016**, *531*, 88.

(60) Wang, Z.; Danovich, D.; Ramanan, R.; Shaik, S. Oriented-External Electric Fields Create Absolute Enantioselectivity in Diels-Alder Reactions: Importance of the Molecular Dipole Moment. *J. Am. Chem. Soc.* **2018**, *140* (41), 13350–13359.

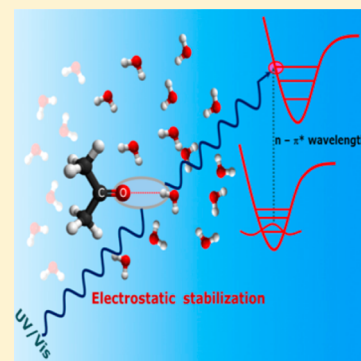
Electrostatic Interactions Are Key to C=O $n-\pi^*$ Shifts: An Experimental Proof

Tapas Haldar and Sayan Bagchi*

Physical and Materials Chemistry Division, CSIR-National Chemical Laboratory, Dr. Homi Bhabha Road, Pune 411008, India

S Supporting Information

ABSTRACT: Carbonyl $n-\pi^*$ transitions are known to undergo blue shift in polar and hydrogen-bonding solvents. Using semiempirical expressions, previous studies hypothesized several factors like change in dipole moment and hydrogen-bond strength upon excitation to cause the blue shift. Theoretically, ground-state electrostatics has been predicted to be the key to the observed shifts, however, an experimental proof has been lacking. Our experimental results demonstrate a consistent linear correlation between IR (ground-state phenomenon) and $n-\pi^*$ frequency shifts (involves both ground and excited electronic-states) of carbonyls in hydrogen-bonded and non-hydrogen-bonded environments. The carbonyl hydrogen-bonding status is experimentally verified from deviation in $n-\pi^*$ /fluorescence correlation. The IR/ $n-\pi^*$ correlation validates the key role of electrostatic stabilization of the ground state toward $n-\pi^*$ shifts and demonstrates the electrostatic nature of carbonyl hydrogen bonds. $n-\pi^*$ shifts show linear sensitivity to calculated electrostatic fields on carbonyls. Our results portray the potential for $n-\pi^*$ absorption to estimate local polarity in biomolecules and to probe chemical reactions involving carbonyl activation/stabilization.



Solute–solvent interactions are widely known to have significant effects on the behavior of molecular systems. In the near-ultraviolet (UV) region, anomalous solvatochromic shifts of carbonyl (C=O) electronic absorption bands to shorter wavelengths with increasing solvent polarity were first reported in the 1920s.¹ Later it was recognized that such absorption bands arise from $n-\pi^*$ transitions, where the nonbonding electron localized on the oxygen atom of the carbonyl (C=O) is excited to the antibonding π^* orbital.^{2,3} The largest sensitivity to solvents arises when the lone pair on C=O is available for hydrogen bonding (H-bonding) in protic solvents. The blue shift in $n-\pi^*$ electronic transition of C=O has been of great interest for a long time, from both theoretical and experimental points of view. Several factors like change in the dipole moment and H-bonding in the excited state,⁴ size of the solvent molecules,⁴ H-bonding of the solvent with the solute,⁵ Franck–Condon principle, and the changes in H-bond strength upon excitation⁶ have been proposed to cause the solvatochromic blue shifts in C=O $n-\pi^*$ transition. Several semiempirical expressions have been derived to dissect the role of H-bonding and electrostatics toward the $n-\pi^*$ blue shifts in carbonyls.^{7,8} Recently, Catalan and coworkers have proposed a new photophysical model that includes solvent acidity, dipolarity, and polarizability to explain the spectroscopic data.⁹ Various other theoretical studies have also contributed to the understanding of the solvatochromic blue shifts of $n-\pi^*$ transitions of carbonyls.^{10–12} It has been theoretically postulated that the solute–solvent interactions in the excited state do not appreciably contribute to the blue shift of the $n-\pi^*$ transitions;¹³ however, to the best of our knowledge, a direct experimental demonstration of the origin of the blue shift in $n-\pi^*$ transitions has never been reported. Because C=O

chromophore is present in a wide range of chemical/biological molecules, experimental determination of the interactions leading to the blue shift will have an immense effect on the molecular level mechanistic understanding of chemical/biological reactions involving C=O stabilization/activation by the catalyst/solvent.^{14–16}

The C=O chromophore is potentially a versatile spectroscopic probe to intermolecular interactions by means of UV, IR, ¹³C NMR, and Raman spectroscopy. The high sensitivity of the spectroscopic observables involved in spectroscopic transitions localized on C=O toward solvent polarity, H-bonding, and formation of donor–acceptor complex have been reported.^{17,18} These shifts have been explained either through theoretical calculations or through indirect semiempirical models derived from experimental data. In this study, we report direct experimental results using IR/ $n-\pi^*$ correlations on various C=O molecules to explain the C=O $n-\pi^*$ solvatochromic shifts. Previous studies have dissected electrostatic and H-bonding contribution to $n-\pi^*$ transitions. Our experimental results show a unique correlation for both protic and aprotic solvents to underpin the electrostatic nature of carbonyl H-bonds in a consistent manner. Moreover, we demonstrate that the H-bonding status of C=O can be experimentally probed using deviations in $n-\pi^*$ /fluorescence correlations.

Ground state electrostatic interactions have been hypothesized to cause the solvatochromic blue shift in C=O $n-\pi^*$ transitions from direct reaction field (DRF) calculations.¹³

Received: May 16, 2016

Accepted: June 1, 2016

Published: June 1, 2016

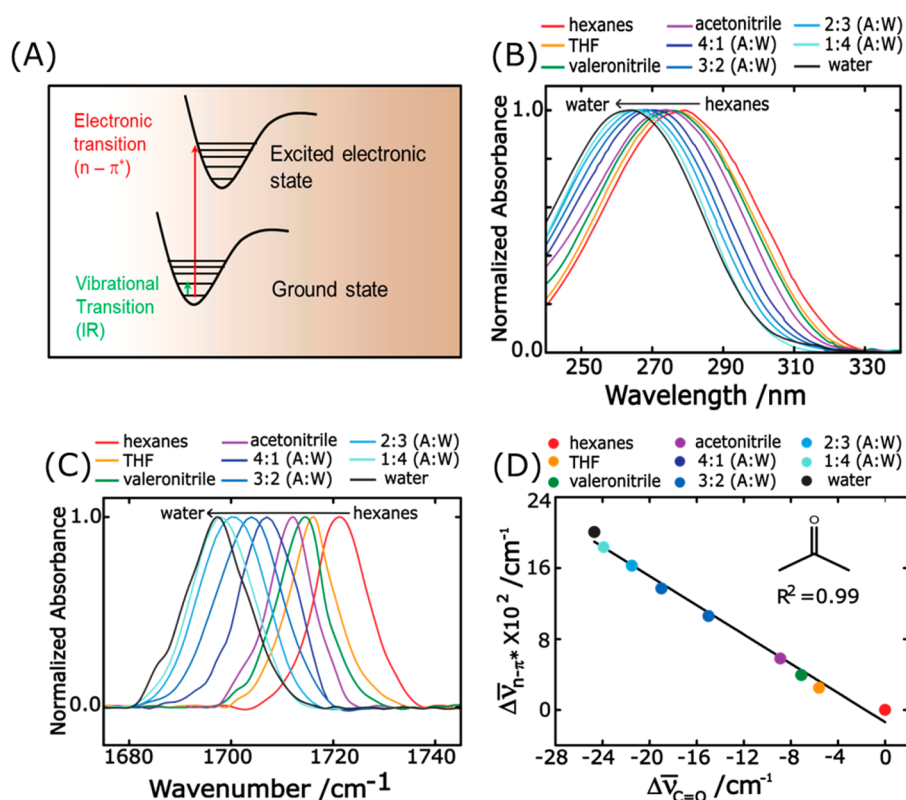


Figure 1. (A) Energy diagram representation of the IR transition (a ground-state phenomenon) and the $n-\pi^*$ transition (involves ground and excited electronic states). Solvatochromic (B) $n-\pi^*$ electronic absorption spectra and (C) IR absorption spectra of the C=O stretch of acetone in aprotic and protic solvation environments. (D) Shifts of $n-\pi^*$ absorption ($\Delta\bar{\nu}_{n-\pi^*}$) plotted against shifts of C=O IR stretching frequencies ($\Delta\bar{\nu}_{C=O}$) of acetone in different solvation environments. The black line indicates best fit line. The regression value (R^2) of the fitted line is shown in the figure.

Table 1. Absolute Values and Shifts in $n-\pi^*$ and C=O Stretching Frequencies of Acetone in Non-Hydrogen-Bonding and Hydrogen-Bonding Solvation Environments

solvent	carbonyl stretch ($\bar{\nu}_{C=O}$)/ cm^{-1}	($\bar{\nu}_{C=O}$)/ cm^{-1b}	$n-\pi^*$ wavelength ($\lambda_{n-\pi^*}$)/nm	$n-\pi^*$ wavenumber ($\bar{\nu}_{n-\pi^*}$)/ cm^{-1}	($\Delta\bar{\nu}_{n-\pi^*}$)/ cm^{-1}
hexanes	1721.6	0.0	278.0	35971	0.0
tetrahydrofuran	1716.0	-5.6	276.1	36219	248
valeronitrile	1714.5	-7.1	275.0	36364	393
acetonitrile	1712.7	-8.9	273.6	36550	579
4:1 A:W ^a	1706.6	-15.0	270.0	37030	1059
3:2 A:W ^a	1702.6	-19.0	267.8	37341	1370
2:3 A:W ^a	1700.1	-21.5	266.0	37598	1627
1:4 A:W ^a	1697.7	-23.9	264.5	37807	1836
water	1696.9	-24.7	263.3	37979	2008

^aA:W represents acetonitrile–water solution (v/v). ^bNegative sign represents red shift with respect to hexane.

From an experimental viewpoint, parameters derived from solvent dielectric constant have shown reasonable linear correlation with the shift in $n-\pi^*$ transition frequencies in a selected set of aprotic solvents;^{7,8} however, using the semiempirical parameter, similar correlation could not be seen for protic solvents that can form a H-bond with the carbonyl. C=O stretching frequencies have also been reported to show linear sensitivity with similar semiempirical expressions for aprotic solvents.¹⁹ Other semiempirical polarity parameters/scales like Kosower's Z scale and Onsager reaction field have been extensively used to correlate the solvent effects on $n-\pi^*$ and C=O stretching frequencies;^{20,21} however, H-bonding pose a challenging task to describe solute–solvent interactions. The continuum semiempirical models do not account for the microscopic nature of the solvent and thereby cannot describe specific chemical interactions like H-bonding. Electrostatic field

can serve as a quantitative and microscopic descriptor of solute–solvent interactions.²² Stark effect provides a calibration of the transition frequency to the electrostatic field in terms of the difference dipole associated with the transition. Recent studies from vibrational Stark effect (VSE), arising from IR transitions) have demonstrated that the field arising from electrostatic interactions varies linearly with C=O IR frequency in both H-bonding and non-H-bonding environments;²³ however, deviations from linear field–frequency correlation have been observed for nitriles in protic solvents.^{24–26} Because both the solvatochromic shifts in C=O IR frequencies and $n-\pi^*$ frequencies have shown linear sensitivity to multiple semiempirical expressions for aprotic solvents, we wanted to check whether a linear correlation exists between $n-\pi^*$ and IR shifts in carbonyls. On the basis of the results of VSE on C=O, we hypothesized that a correlation

between IR shift (ground electronic state phenomenon) and $n-\pi^*$ shift (involves both ground and excited states) would provide model-free direct experimental evidence of the role of ground-state electrostatic interactions toward the solvatochromic blue shifts observed for carbonyls (Figure 1A). Incorporating both protic and aprotic solvents in our study will enable us to confirm if electrostatic interactions are key toward the spectral shifts in both H-bonding and non-H-bonding solvation environments.

Acetone is chosen as the model carbonyl because the C=O stretching frequencies and $n-\pi^*$ frequencies of acetone have been extensively characterized in various solvents of varying polarity.^{9,27–29} As previously reported, we observe a gradual increase in $n-\pi^*$ frequencies and a decrease in C=O stretching frequencies with increasing polarity of the aprotic solvents (Figure 1B,C). The $n-\pi^*$ frequencies are obtained using the methodology provided by Renge.²⁹ The overall frequency dispersion observed from the aprotic nonpolar solvent hexane to the aprotic polar solvent acetonitrile in the IR experiment is ca. 9 cm^{-1} (Table 1). For $n-\pi^*$ transitions, the dispersion is ca. 579 cm^{-1} (Table 1). When acetone is dissolved in water, where the C=O can form a H-bond with water, a further red shift and blue shift are observed in IR and $n-\pi^*$ frequencies, respectively. To further understand the interactions in H-bonding environment, we have scanned the polarity range between acetonitrile and water using acetonitrile/water solutions, where the percentage of water is gradually increased by 20% (v/v) increments. The C=O IR and $n-\pi^*$ frequencies of acetone in various solvents/solvent mixtures are listed in Table 1. The reported frequencies shifts (as shown in Table 1) are calculated with respect to hexane, as it is the most nonpolar solvent in the solvatochromic series. Moreover, theoretical calculations have predicted approximately zero electrostatic field along the C=O in hexane.²³ The solvatochromic red shifts in IR frequencies show a linear correlation with the corresponding $n-\pi^*$ blue shifts (Figure 1D). The linear sensitivity, as seen in aprotic solvents, where the interactions are predominantly electrostatic, continues in protic solvation environments, and the regression value of the best-fit line is 0.99. The solvatochromic C=O IR shifts has been previously shown to arise from VSE, where the local electrostatic field from the solvation environment affects the vibrational frequencies.²³ Thus, the observed linear correlation between a ground state phenomenon and $n-\pi^*$ shifts in Figure 1D demonstrates that the electrostatic interactions are key toward the acetone $n-\pi^*$ blue shift in both H-bonding and non-H-bonding environments.

To check the generality of the role of electrostatics toward the $n-\pi^*$ blue shifts in carbonyls, we have carried out similar solvatochromic UV and IR absorption experiments on other molecules containing the C=O moiety. C=O connected to an aromatic ring (acetophenone), α,β -unsaturated ketone (mesityl oxide), and ester (ethyl acetate) are the different carbonyls chosen to check the validity of the IR/ $n-\pi^*$ correlation in a similar sets of solvents/solvent mixtures. Because the $n-\pi^*$ absorption frequency of ethyl acetate is within the solvent cutoff limit in most solvents, the solvatochromic response of ethyl acetate has been studied in hexane, acetonitrile, water, and acetonitrile/water solutions (Figure 2A). Excellent IR/ $n-\pi^*$ correlation in ethyl acetate, as shown in Figure 2B, demonstrates that electrostatic stabilization of the ground state also determines the $n-\pi^*$ blue shifts of ester C=O. Acetophenone and mesityl oxide also show excellent linear

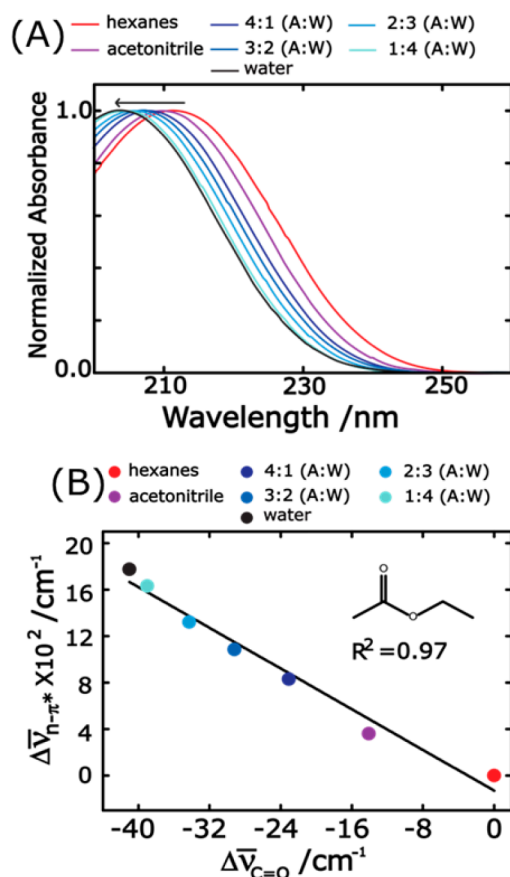


Figure 2. (A) $n-\pi^*$ electronic absorption spectra of ethyl acetate in non-hydrogen-bonding and hydrogen-bonding solvation environments. The polarity increases in the direction of the arrow. (B) Shifts of $n-\pi^*$ absorption ($\Delta\bar{\nu}_{n-\pi^*}$) plotted against shifts of C=O IR stretching frequencies ($\Delta\bar{\nu}_{\text{C=O}}$) of ethyl acetate in different solvation environments. The black line indicates best fit line. The regression value (R^2) of the fitted line is shown in the figure.

correlations between shifts in IR and $n-\pi^*$ frequencies (Figure 3A,B) in aprotic as well as protic solvation environments. $n-\pi^*$ electronic absorption spectra of mesityl oxide and acetophenone in non-H-bonding and H-bonding solvation environments are shown in the Supporting Information (Figures S1 and S2); however, because of the intrinsic overlap of the $n-\pi^*$ and $\pi-\pi^*$ bands of acetophenone and mesityl oxide in polar protic solvation environments, the conjugated ketones have been studied up to 1:1 acetonitrile/water (50% v/v). For acetophenone and mesityl oxide, the water concentration in binary solvent mixtures has been increased by 10% (v/v) to maintain the same number of data points in the linear fit. The IR and $n-\pi^*$ frequencies for acetophenone, ethyl acetate, and mesityl oxide, along with their shifts with respect to hexane, are listed in the Supporting Information (Tables S1–S3).

The explanation of the above-mentioned experimental correlation is as follows. During the ultrafast $n-\pi^*$ excitation process, the solvent shells cannot reorient and adapt to the excited state dipole, and thus the carbonyl moiety in the excited state is surrounded by the solvent molecules adapted to the ground state electrostatic interactions. A better stabilization of the ground state C=O dipole in polar solvation environment as compared with a nonpolar solvent leads to the $n-\pi^*$ blue shift with increasing solvent polarity. This stability can be associated with a greater electrostatic field exerted by the

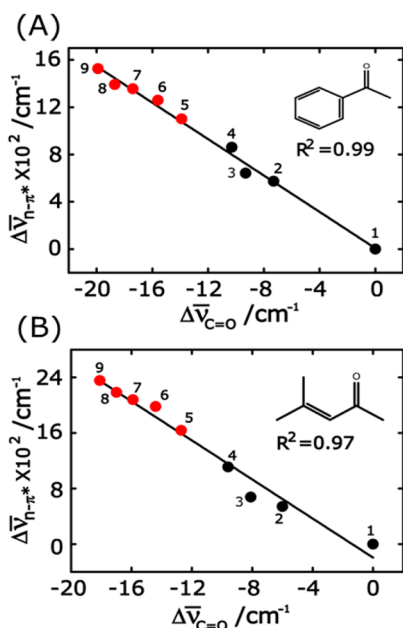


Figure 3. Plots of $n-\pi^*$ frequency shifts ($\Delta\bar{\nu}_{n-\pi^*}$) versus IR frequency shifts ($\Delta\bar{\nu}_{\text{C=O}}$) of (A) acetophenone and (B) mesityl oxide in different solvents and binary solvent mixtures. The black lines indicate the best-fit lines. The black solid circles represent aprotic solvents [(1) hexanes, (2) tetrahydrofuran, (3) valeronitrile, (4) acetonitrile] and red solid circles represent aqueous acetonitrile solutions (v/v) [(5) 90% acetonitrile, (6) 80% acetonitrile (7) 70% acetonitrile, (8) 60% acetonitrile, (9) 50% acetonitrile]. The regression values (R^2) of the fitted lines are shown in the figures.

solvents along the C=O bond dipole through VSE. The larger stability in protic solvation environments of C=O can be rationalized by considering that a H-bond positions a large dipole near the IR probe due to the small van der Waals radius of hydrogen, which, in turn, exerts a greater stabilizing electrostatic field on the C=O. The linear sensitivity of IR frequency shifts with that of $n-\pi^*$ frequency in a range of different C=O compounds demonstrates that electrostatic interactions in the ground electronic state play a key role toward the $n-\pi^*$ blue shifts in carbonyls. Being a function of the coordinates of the individual atoms of the solvent molecules as well as their partial charges, the electrostatic field provides a microscopic description of the solute–solvent interaction and accounts for specific chemical interactions like H-bonding. Thus, the IR/ $n-\pi^*$ linearity obtained in the aprotic solvents can be extended to the protic solvation environments. Very recently, Boxer and coworkers have demonstrated a linear correlation between electrostatic field and C=O IR stretching frequencies using VSE, consistently for both H-bonding and non-H-bonding solvents.²³ Theoretical calculations have predicted a redistribution of electron density along the C=O bond in the excited state, leading to a reduced dipole moment that in turn reduces the electrostatic interactions.³⁰ A smaller dipole moment would result in a blue shift with increasing solvent polarity through electronic Stark effect. In Stark effect interpretation the slope of the IR/ $n-\pi^*$ plot would be related to the difference dipoles of the two transitions. Considering the slopes of the IR/ $n-\pi^*$ plots along with the reported values of the difference dipoles for IR transitions (from VSE), the difference dipoles for the C=O $n-\pi^*$ transitions are on the order of $\sim 3\text{--}5$ D (see Table S5 in the Supporting Information), which is consistent with the reported values for

other electronic transitions.³¹ The similarity in difference dipoles supports the argument that the observed linear correlations arise from the underlying solvent electrostatic field. To further establish this point, we have calculated the electrostatic fields being exerted along the C=O using molecular dynamics (MD) simulations, and a linear correlation is obtained between $n-\pi^*$ shifts and shifts in electrostatic fields for different C=O-containing molecules (Figure 4) in both

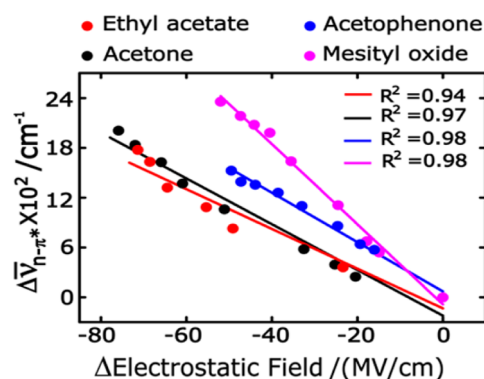


Figure 4. Shifts in $n-\pi^*$ absorption wavenumber ($\Delta\bar{\nu}_{n-\pi^*}$) versus shifts in C=O electrostatic fields ($\Delta\bar{F}_{\text{C=O}}$) for ethyl acetate, acetone, acetophenone, and mesityl oxide. The solid circles represent the [$\Delta\bar{\nu}_{n-\pi^*}$, $\Delta\bar{F}_{\text{C=O}}$] paired points and the solid lines denote best linear fits. The regression values (R^2) of the fitted lines are shown in the Figure.

protic and aprotic solvation environments; however, previous studies involving semiempirical scales could not accommodate specific interactions like H-bonding, and thus the linearity between absorption frequencies and the polarity parameter was confined within a selected set of non-H-bonding solvents. The slopes of the best-fit lines in Figure 4 also provide us an estimate of the difference dipole for the C=O $n-\pi^*$ transitions. The values of the slopes obtained using the calculated electrostatic fields (listed in Table S4 of the Supporting Information) are smaller by a factor of ~ 2.5 (see Table S6 of the Supporting Information). This factor is consistent with the correction factor arising from local field effect.^{16,23,26}

Our experimental results show that the linearity is extendable from non-H-bonding to H-bonding environments of C=O, and thus it is unnecessary to consider separately the contribution from electrostatic interactions and H-bonding interactions for C=O spectroscopic probes. These results support the electrostatic nature of C=O H-bonding interactions.¹⁷ Because both the axes in IR/ $n-\pi^*$ correlation are experimental observables, there are no assumptions involved in elucidating the highly debated origin of the $n-\pi^*$ blue shifts. The only assumption is whether the C=O is H-bonded in acetonitrile/water solutions. To experimentally prove this assumption, we have used UV/fluorescence covariance of acetone in protic and aprotic solvents. An acetone molecule that is H-bonded in the ground state probably cannot sustain the H-bond in the excited state as one of the electrons in the n -orbital is removed during the $n-\pi^*$ transition. Two lone pairs on C=O oxygen can presumably form two H-bonds; however, a previous study reported negligible contribution of solvent acidity to fluorescence solvatochromism of acetone. For aprotic solvents, both the ground and excited states are not H-bonded and are stabilized by the electrostatic interactions by the surrounding solvent molecules, leading to a linear correlation between $n-\pi^*$ shifts

and fluorescence shifts. According to this explanation, a plot of $n-\pi^*$ shifts versus fluorescence shifts will maintain a linear correlation for aprotic solvents, whereas a deviation from linearity will occur for H-bonding protic solvents/solvent mixtures (Figure 5), where the ground state involves a specific

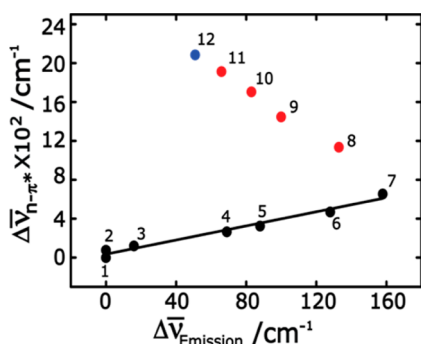


Figure 5. Shifts in $n-\pi^*$ absorption ($\Delta\bar{\nu}_{n-\pi^*}$) versus shifts of emission wavenumber ($\Delta\bar{\nu}_{em}$) for acetone in protic and aprotic solvation environments. Black solid circles represent aprotic solvents [(1) cyclohexane, (2) hexanes, (3) *n*-pentane, (4) diethyl ether, (5) tetrahydrofuran, (6) valeronitrile, (7) acetonitrile], red solid circles represent aqueous acetonitrile solutions (v/v) [(8) 80% acetonitrile, (9) 60% acetonitrile, (10) 40% acetonitrile, (11) 20% acetonitrile], and blue solid circle represents water. Black line indicates best fit line in different non-hydrogen-bonding aprotic solvents. The regression value (R^2) of the best fit equals to 0.97.

chemical interaction (H-bonding) that is missing in the excited state. A plot of ($\Delta\bar{\nu}_{n-\pi^*}$) versus fluorescence (emission) shifts ($\Delta\bar{\nu}_{em}$) demonstrates deviation from the linear correlation for all acetonitrile/water mixtures, thereby providing evidence that C=O is H-bonded in binary aqueous solutions of acetonitrile. The emission spectra and emission frequencies of acetone are shown in Figure S3 and Table S6 of the [Supporting Information](#).

In summary, using IR/ $n-\pi^*$ correlations in a range of different compounds with C=O functionalities, we have provided the first experimental evidence regarding the origin of the C=O $n-\pi^*$ solvatochromic shifts. Our results demonstrate that increasing solute–solvent electrostatic interactions in the ground electronic state is the key to the blue shifts in $n-\pi^*$ transitions. We have also experimentally demonstrated the H-bonding status of the C=O using $n-\pi^*$ /fluorescence correlations. The implications of these results are manifold. These results demonstrate that $n-\pi^*$ frequencies can predict the electrostatic fields experienced by the carbonyl moiety. Electrostatic field has been recently proposed to be a microscopic and quantitative descriptor of noncovalent interactions and local polarity.²³ To date, IR spectroscopy has been used to predict electrostatic fields through vibrational Stark effect; however, the intrinsic overlap of the ligand C=O frequency with the amide-I band of the protein makes it extremely difficult to experimentally determine the C=O stretching frequency of the carbonyl.¹⁶ On the contrary, long wavelength $n-\pi^*$ transition of ligand carbonyls (e.g., in steroids) has considerable less overlap with the protein absorption and can be a suitable alternative for determining the local polarity at the binding site of the protein. Moreover, several organic reactions are predicted to involve C=O activation through the H-bond. Metal-free organocatalysis has seen tremendous growth in recent times.³² Recently, $n-\pi^*$ frequencies have

been shown to correlate with organic reaction rates.³³ Our results might provide the mechanistic understanding of these organic reactions.

■ ASSOCIATED CONTENT

Supporting Information

The Supporting Information is available free of charge on the ACS Publications website at DOI: [10.1021/acs.jpcllett.6b01052](https://doi.org/10.1021/acs.jpcllett.6b01052).

Experimental methods and simulation protocol, table for IR frequencies and $n-\pi^*$ frequencies for acetophenone, ethyl acetate, and mesityl oxide, and table for MD estimated electric fields of acetone, acetophenone, mesityl oxide, and ethyl acetate in different solvation environments (PDF)

■ AUTHOR INFORMATION

Corresponding Author

*E-mail: s.bagchi@ncl.res.in.

Notes

The authors declare no competing financial interest.

■ ACKNOWLEDGMENTS

This work was financially supported by CSIR-NCL (Grant No. MLP028126). S.B. thanks the Department of Science and Technology (DST), (SR/S2/RJN-142/2012) for Ramanujan Fellowship.

■ REFERENCES

- (1) Scheibe, G. Influencing of Absorption Spectrum, Reaction Rate and Equilibrium by Solvents. *Ber. Dtsch. Chem. Ges. B* **1927**, *60*, 1406–1419.
- (2) McConnell, H. Effect of Polar Solvents on the Absorption Frequency of $n-\pi^*$ Electronic Transitions. *J. Chem. Phys.* **1952**, *20*, 700–704.
- (3) Kasha, M. Characterization of Electronic Transitions in Complex Molecules. *Discuss. Faraday Soc.* **1950**, *9*, 14–19.
- (4) Bayliss, N. S.; McRae, E. G. Solvent Effects in the Spectra of Acetone, Crotonaldehyde, Nitromethane and Nitrobenzene. *J. Phys. Chem.* **1954**, *58*, 1006–1011.
- (5) Brealey, G. J.; Kasha, M. The Role of Hydrogen Bonding in the $n \rightarrow \pi^*$ Blue-shift Phenomenon. *J. Am. Chem. Soc.* **1955**, *77*, 4462–4468.
- (6) Pimentel, G. C. Hydrogen Bonding and Electronic Transitions - the Role of the Franck-Condon Principle. *J. Am. Chem. Soc.* **1957**, *79*, 3323–3326.
- (7) Ito, M.; Inuzuka, K.; Imanishi, S. Effect of Solvent on $n-\pi^*$ Absorption Spectra of Ketones. *J. Am. Chem. Soc.* **1960**, *82*, 1317–1322.
- (8) McRae, E. G. Theory of Solvent Effects on Molecular Electronic Spectra - Frequency Shifts. *J. Phys. Chem.* **1957**, *61*, 562–572.
- (9) Catalan, J.; Pablo Catalan, J. On the Solvatochromism of the $n-\pi^*$ Electronic Transitions in Ketones. *Phys. Chem. Chem. Phys.* **2011**, *13*, 4072–4082.
- (10) Grozema, F. C.; van Duijnen, P. T. Solvent Effects on the $n-\pi^*$ Transition of Acetone in Various Solvents: Direct Reaction Field Calculations. *J. Phys. Chem. A* **1998**, *102*, 7984–7989.
- (11) Martin, M. E.; Sanchez, M. L.; Olivares del Valle, F. J.; Aguilar, M. A. A Multiconfiguration Self-Consistent Field/Molecular Dynamics Study of the $n-\pi^*$ Transition of Carbonyl Compounds in Liquid Water. *J. Chem. Phys.* **2000**, *113*, 6308–6315.
- (12) Aidas, K.; Kongsted, J.; Osted, A.; Mikkelsen, K. V.; Christiansen, O. Coupled Cluster Calculation of the $n-\pi^*$ Electronic Transition of Acetone in Aqueous Solution. *J. Phys. Chem. A* **2005**, *109*, 8001–8010.

(13) Van Duijnen, P. T.; de Vries, A. H. Direct Reaction Field Force Field: A Consistent Way to Connect and Combine Quantum-Chemical and Classical Descriptions of Molecules. *Int. J. Quantum Chem.* **1996**, *60*, 1111–1132.

(14) Wittkopp, A.; Schreiner, P. R. Metal-Free, Noncovalent Catalysis of Diels-Alder Reactions by Neutral Hydrogen Bond Donors in Organic Solvents and in Water. *Chem. - Eur. J.* **2003**, *9*, 407–414.

(15) Tuerkmen, Y. E.; Rawal, V. H. Exploring the Potential of Diarylacetylenediols as Hydrogen Bonding Catalysts. *J. Org. Chem.* **2013**, *78*, 8340–8353.

(16) Fried, S. D.; Bagchi, S.; Boxer, S. G. Extreme Electric Fields Power Catalysis in the Active Site of Ketosteroid Isomerase. *Science* **2014**, *346*, 1510–1514.

(17) Kashid, S. M.; Bagchi, S. Experimental Determination of the Electrostatic Nature of Carbonyl Hydrogen-Bonding Interactions Using IR-NMR Correlations. *J. Phys. Chem. Lett.* **2014**, *5*, 3211–3215.

(18) Balasubramanian, A.; Rao, C. N. R. Evaluation of Solute-Solvent Interactions from Solvent Blue-shifts of $n \rightarrow \pi^*$ Transitions of C=O, C=S, NO₂ and N=N Groups: Hydrogen Bond Energies of Various Donor-acceptor Systems. *Spectrochim. Acta* **1962**, *18*, 1337–1352.

(19) Inuzuka, K. z.; Ito, M.; Imanishi, S. Effect of Solvent on Carbonyl Stretching Frequency of Ketones. *Bull. Chem. Soc. Jpn.* **1961**, *34*, 467–471.

(20) Dilling, W. L. The Effect of Solvent on the Electronic Transitions of Benzophenone and Its o- and p-Hydroxy Derivatives. *J. Org. Chem.* **1966**, *31*, 1045–1050.

(21) Elenewski, J. E.; C Hackett, J. Solvatochromism and the Solvation Structure of Benzophenone. *J. Chem. Phys.* **2013**, *138*, 224308.

(22) Fried, S. D.; Boxer, S. G. Measuring Electric Fields and Noncovalent Interactions Using the Vibrational Stark Effect. *Acc. Chem. Res.* **2015**, *48*, 998–1006.

(23) Fried, S. D.; Bagchi, S.; Boxer, S. G. Measuring Electrostatic Fields in Both Hydrogen-Bonding and Non-Hydrogen-Bonding Environments Using Carbonyl Vibrational Probes. *J. Am. Chem. Soc.* **2013**, *135*, 11181–11192.

(24) Fafarman, A. T.; Sigala, P. A.; Herschlag, D.; Boxer, S. G. Decomposition of Vibrational Shifts of Nitriles into Electrostatic and Hydrogen-Bonding Effects. *J. Am. Chem. Soc.* **2010**, *132*, 12811–12813.

(25) Bagchi, S.; Fried, S. D.; Boxer, S. G. A Solvatochromic Model Calibrates Nitriles' Vibrational Frequencies to Electrostatic Fields. *J. Am. Chem. Soc.* **2012**, *134*, 10373–10376.

(26) Deb, P.; Haldar, T.; Kashid, S. M.; Banerjee, S.; Chakrabarty, S.; Bagchi, S. Correlating Nitrile IR Frequencies to Local Electrostatics Quantifies Noncovalent Interactions of Peptides and Proteins. *J. Phys. Chem. B* **2016**, *120*, 4034–4046.

(27) Kun Cha, D.; Kloss, A. A.; Tikanen, A. C.; Ronald Fawcett, W. Solvent-Induced Frequency Shifts in the Infrared Spectrum of Acetone in Organic Solvents. *Phys. Chem. Chem. Phys.* **1999**, *1*, 4785–4790.

(28) Nyquist, R. A. Infrared Studies of Ketones: Parameters Affecting the Induced Carbonyl Stretching Vibration by Solute/Solvent Interaction. *Appl. Spectrosc.* **1990**, *44*, 433–438.

(29) Renge, I. Solvent Dependence of $n-\pi^*$ Absorption in Acetone. *J. Phys. Chem. A* **2009**, *113*, 10678–10686.

(30) Pasteka, L. F.; Melicherick, M.; Neogrady, P.; Urban, M. CASPT2 and CCSD(T) Calculations of Dipole Moments and Polarizabilities of Acetone in Excited States. *Mol. Phys.* **2012**, *110*, 2219–2237.

(31) Boxer, S. G. Stark Realities. *J. Phys. Chem. B* **2009**, *113*, 2972–2983.

(32) Sohtome, Y.; Nagasawa, K. The Design of Chiral Double Hydrogen Bonding Networks and Their Applications to Catalytic Asymmetric Carbon-Carbon and Carbon-Oxygen Bond-Forming Reactions. *Synlett* **2010**, *2010*, 1–22.

(33) Walvoord, R. R.; Huynh, P. N. H.; Kozlowski, M. C. Quantification of Electrophilic Activation by Hydrogen-Bonding Organocatalysts. *J. Am. Chem. Soc.* **2014**, *136*, 16055–16065.

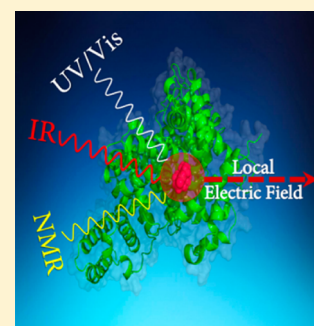
Pick and Choose the Spectroscopic Method to Calibrate the Local Electric Field inside Proteins

Tapas Haldar, Somnath M. Kashid, Pranab Deb, Sandeep Kesh, and Sayan Bagchi*

Physical and Materials Chemistry Division, CSIR-National Chemical Laboratory, Dr. Homi Bhabha Road, Pune 411008, India

Supporting Information

ABSTRACT: Electrostatic interactions in proteins play a crucial role in determining the structure–function relation in biomolecules. In recent years, fluorescent probes have been extensively employed to interrogate the polarity in biological cavities through dielectric constants or semiempirical polarity scales. A choice of multiple spectroscopic methods, not limited by fluorophores, along with a molecular level description of electrostatics involving solute–solvent interactions, would allow more flexibility to pick and choose the experimental technique to determine the local electrostatics within protein interiors. In this work we report that ultraviolet/visible-absorption, infrared-absorption, or ^{13}C NMR can be used to calibrate the local electric field in both hydrogen bonded and non-hydrogen bonded protein environments. The local electric field at the binding site of a serum protein has been determined using the absorption wavelength as well as the carbonyl stretching frequency of its natural steroid substrate, testosterone. Excellent agreement is observed in the results obtained from two independent spectroscopic techniques.



The polarity within protein interiors affects the protein's interactions with ligands, substrates, and other proteins, making it a critical determinant of protein structure, stability, and activity. Because electrostatic interactions are prevalent in any biomolecular system,^{1–3} computational and experimental studies have focused on describing local electrostatics and polarity within biological cavities. Protein polarity is often described by a low dielectric constant ($\epsilon = 2–4$); however, electrostatics calculations suggest large electric fields are produced by charged and polar groups in folded proteins that can vary from site to site in magnitude and direction.^{4–6} Experimental studies for protein polarity determination have mostly relied on the sensitivity of the fluorescent probes to the microenvironment.^{7,8} These studies are informative and report on protein polarity by correlating peak emission wavelength to dielectric constant or semiempirical solvent polarity parameters and scales.^{9–12} However, there are a few limitations: (a) Polarity measurement in protein depends on efficient fluorophore insertion, thus limited by the affinity of the ligand binding site. (b) The fluorescent probe might alter the molecular architecture of the native protein and thereby change the function and stability. (c) The dielectric constant is a bulk solvent property and cannot define the local microenvironment around the optical probe. (d) Most of the semiempirical polarity parameters [with a few exceptions, e.g., $E_T(30)$] cannot account for the specific intramolecular and intermolecular interactions like hydrogen bonding. We therefore require a noninvasive label-free spectroscopic method that probes chemical groups preferably either present in the native proteins or in their natural substrates. We would also require a microscopic and quantitative descriptor of electrostatic interactions inside proteins that is dependent on the molecular architecture of the biomolecule and the coordinates of the

surrounding solvent molecules. Moreover, a direct coupling, understood on a theoretical basis and independently verified by experiments, should exist between the spectroscopic observable and the local electrostatics descriptor.

Carbonyl ($\text{C}=\text{O}$) groups are ubiquitous in biomolecules and are also common in the natural substrates of the proteins. Probing $\text{C}=\text{O}$ moieties paves the way to use label free spectroscopic techniques. Here, we focus on noninvasive spectroscopic methods like infrared (IR) spectroscopy, nuclear magnetic resonance (NMR) spectroscopy, and ultraviolet/visible (UV/vis) $n-\pi^*$ absorption spectroscopy that provide spectral signatures of the $\text{C}=\text{O}$ moiety. Moreover, the spectroscopic observables like $\text{C}=\text{O}$ IR frequencies, ^{13}C NMR chemical shifts of the $\text{C}=\text{O}$ carbon, or $n-\pi^*$ wavelengths are sensitive to the immediate surroundings of the $\text{C}=\text{O}$ group and therefore should be ideal to report on the local electrostatics within proteins.^{13–16} The electric field estimated at any point inside the protein depends on the distances of all the other atoms in the system (both solute and solvent atoms) from that point as well as the residual partial charges on each atom and has been reported to influence every aspect of protein function.^{17,18} Because biomolecules consist of polar, polarizable, and charged residues, the electric field experienced by $\text{C}=\text{O}$ from its environment can provide microscopic insight about how enzymes function within the highly heterogeneous protein environment.¹⁴ For example, a small change in the environment, such as a modification in the protonation state or a conformational rearrangement upon

Received: April 20, 2016

Accepted: June 13, 2016

Published: June 13, 2016



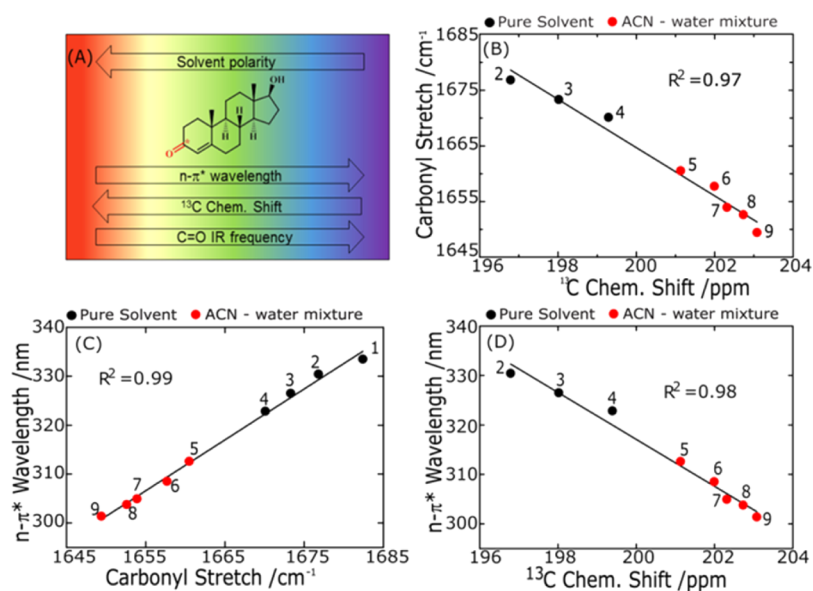


Figure 1. For carbonyls, the spectroscopic observables of IR spectroscopy, NMR spectroscopy, and UV/vis absorption spectroscopy change with the solvent polarity. Panel A represents the shift (and the direction of the shifts) in the observables for testosterone with the varying solvent polarity. Linear correlations exist among the three independent spectroscopic observables of testosterone, namely, (B) C=O stretching frequency and ^{13}C chemical shift of the C=O carbon, (C) C=O stretching frequency and $n-\pi^*$ wavelength, and (D) $n-\pi^*$ wavelength and ^{13}C chemical shift of the C=O carbon in hydrogen bonding and non-hydrogen bonding solvents. The black lines denote the best-fit lines; the black circles represent aprotic solvents [(1) DBE, (2) THF, (3) VLN, (4) ACN], and red circles represent protic solvent mixtures [(5) A10W, (6) A20W, (7) A30W, (8) A40W, (9) A50W]. The regression values of the fitted lines are shown in the figures.

ligand binding, would result in a change in the electric field experienced by C=O. Moreover, because C=O hydrogen bonding interactions are electrostatic,^{15,19} the electric field at C=O includes specific solute–solvent interactions like hydrogen bonding. In this work, we have shown independent linear correlations of IR, NMR, and UV/vis spectroscopic observables to the electric field exerted on C=O. Depending on the biomolecular system, we can pick and choose the spectroscopic method to determine the local electric field within biomolecules.

Serum albumins, one of the most abundant proteins in the circulatory system, maintain osmotic pressure and pH of blood and transport several lipophilic compounds, such as fatty acids, drugs, and steroid hormones. Testosterone, a steroid hormone, is one of the natural substrates of serum albumins. The association of testosterone with serum proteins regulates its biological activity. The steroid–protein interaction has major biological implications, and the local electric field at the testosterone binding site of bovine serum albumin (BSA) has been probed in the present work.

To interrogate the local electrostatics at the binding site of BSA, solvatochromic IR, ^{13}C NMR, and UV/vis experiments were performed for testosterone in a wide range of solvation environments of varying polarity. Testosterone was dissolved in various organic solvents and binary aqueous mixtures of acetonitrile/water to mimic non-hydrogen bonding and hydrogen bonding solvation environments of the substrate. Due to the change in polarity, a shift in the respective peak positions is observed in each of the spectroscopic techniques (Figure 1A). The $n-\pi^*$ absorption wavelength of testosterone shows a monotonically increasing blue-shift with the increasing polarity of the aprotic solvents and the protic aqueous binary mixtures (with increasing water content) (Table 1). The C=O stretching frequency of testosterone shows a monotonic red shift with the increasing polarity of the same set of neat solvents

Table 1. $n-\pi^*$ Absorption Wavelength, C=O Stretching Frequencies, and ^{13}C NMR Chemical Shifts for Testosterone in Non-hydrogen Bonding and Hydrogen Bonding Solvents

serial no.	solvent	$n-\pi^*$ wavelength (nm)	carbonyl stretch (cm^{-1})	^{13}C chemical shift (ppm)
1	dibutyl ether (DBE)	333.47	1682.4	No peak
2	tetrahydrofuran (THF)	330.39	1676.8	196.79
3	valeronitrile (VLN)	326.50	1673.3	198.02
4	acetonitrile (ACN)	322.80	1670.1	199.39
5	90% ACN + 10% water (A10w)	312.57	1660.5	201.39
6	80% ACN + 20% water (A20W)	308.50	1657.7	201.99
7	70% ACN + 30% water (A30W)	304.93	1653.9	202.31
8	60% ACN + 40% water (A40W)	303.77	1652.6	202.73
9	50% ACN + 50% water (A50W)	301.37	1649.4	203.08

and solvent mixtures (Table 1). The ^{13}C NMR chemical shift of the carbonyl carbon shows a downfield shift with the increasing polarity of the solvation environment (Table 1). We observe linear cross correlations within the spectroscopic observables in various non-hydrogen bonded as well as hydrogen bonded environments (Figure 1B–D). This result illustrates that measurement of one of the spectroscopic observables can directly predict the other observables from the calibrations shown in Figure 1. To verify the generality of the linear correlation between independent spectroscopic variables as seen for testosterone C=O, we have performed solvatochromic experiments on small molecule ketones, esters, and amides, and the results show trends similar to those found in testosterone (shown in the Supporting Information). Thus, a

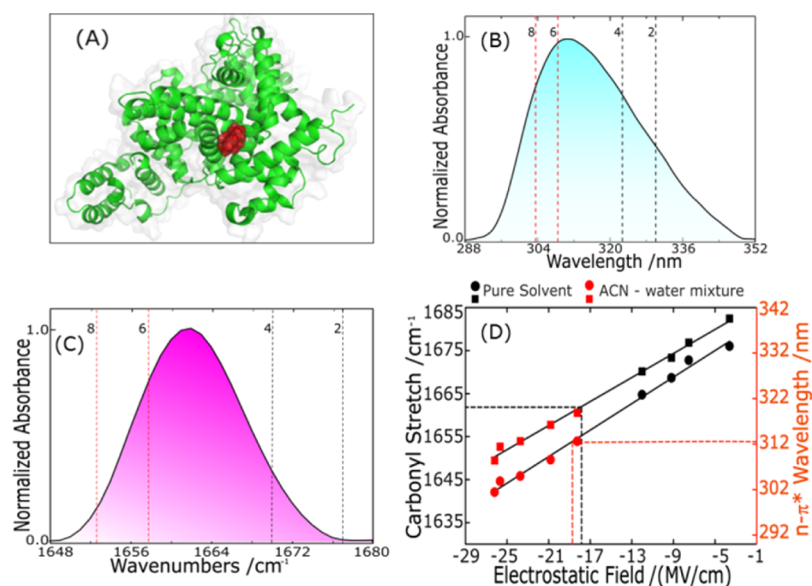


Figure 2. (A) Cartoon of BSA–testosterone complex. The protein is shown in green, and the substrate is shown in red. (B) The $n-\pi^*$ absorption spectra and (C) the IR spectra of C=O stretch of testosterone in BSA–testosterone complex can be used to estimate the local polarity at the binding site of BSA using electric field (D). The predicted electric fields from UV/vis and IR experiments are within 0.7 MV/cm (error $\sim 3.5\%$). The dotted vertical lines in panels B and C represent the peak maxima of aprotic solvents and binary aqueous mixtures. The numbers (2, 4, 6, and 8) correspond to those in column 1 of Table 1.

direct coupling of any of these spectroscopic variables to the local electric field within the biomolecular interior would allow us to quantify local electrostatics by performing any one of the above-mentioned noninvasive spectroscopic experiments.

Interestingly, the C=O IR frequencies are known to show linear sensitivity toward the electrostatic field through vibrational Stark effect (VSE).²⁰ A change in the local environment modifies the electrostatic field exerted on the IR probe, thereby causing a shift in the IR transition energy. Moreover, vibrational Stark tuning rate, the change in IR frequency caused by a unit change in field, can be measured independently from vibrational Stark spectroscopy (VSS). For a diatomic chemical moiety like C=O, the varying electrostatic field along the C=O bond in solvatochromic experiments polarizes the charge density and changes the perpendicular elements of the shielding tensor.²¹ The change in charge density changes the shielding on the C=O carbon nucleus, and the ¹³C chemical shift has been reported to vary linearly with the field. Thus, while the linear sensitivity of C=O to electrostatic field is the difference dipole (VSE) that for ¹³C NMR is the shielding polarizability. Because both C=O stretching frequencies and ¹³C chemical shifts of the C=O carbon show linear sensitivity toward electrostatic field, the electrical and magnetic properties of the ground electronic state tend to vary linearly (Figure 1B). The linear correlation between C=O IR frequencies and the $n-\pi^*$ absorption wavelengths arises as the solvent shell orientation in the Franck–Condon state is adapted to the electrostatic interactions of the ground state. The excitation process is much faster than the solvent shell reorientation process, and the solvatochromic shifts of the $n-\pi^*$ transitions are dominated by the ground-state electrostatic stabilization of the spectroscopic probe.²²

The tuning rate of 19-nortestosterone (another steroid with a similar structure) has been measured and reported by Boxer and co-workers.¹⁴ Using molecular dynamics (MD) simulations, we have calculated the electrostatic field at the midpoint of the C=O of testosterone in all the different solvation

environments of the solvatochromic experiments. The calculated fields, corrected using the experimentally measured Stark tuning rate (see Supporting Information for details) show a linear correlation with the C=O IR frequencies (Figure 2). ¹³C NMR chemical shifts of the C=O carbon and the $n-\pi^*$ absorption wavelengths also show similar linear sensitivities to the calculated electrostatic fields as expected from Figure 1. The straight lines shown in Figure 2D can independently calibrate the sensitivities of C=O IR frequency, ¹³C chemical shift (shown in Figure S15 of the Supporting Information), and $n-\pi^*$ wavelength to the electrostatic field exerted on the carbonyl at the testosterone binding site of the serum protein.

The binding constant (K_a) of $8.89 (\pm 1) \times 10^4 \text{ M}^{-1}$ is obtained for BSA-testosterone complex using tryptophan fluorescence quenching of the protein. This result shows good agreement with the previously reported value of K_a by Tajmir-Riahi and co-workers.²³ For the spectroscopic experiments of the protein–steroid complex, 1 mM of testosterone was added to 1.5 mM BSA solution in phosphate buffer (pH 7.0). At these concentrations, >99% of the steroid is bound to the serum protein, implying that the detected spectroscopic signals of the ligand reflect that of the bound state. The $n-\pi^*$ absorption wavelength and the C=O stretching frequency of testosterone observed in 1:1 BSA-testosterone complex are 312.6 nm (Figure 2A) and 1661.7 cm⁻¹ (Figure 2B), respectively. It is important to note that the experimentally observed C=O IR frequency shows excellent agreement with the frequency predicted from the $n-\pi^*$ wavelength, 1660.8 cm⁻¹, by the calibration curve in Figure 1B. The corresponding electrostatic fields predicted from the peak maxima of the $n-\pi^*$ absorption spectrum and the C=O IR spectrum at the BSA binding site of testosterone are -18.70 and -18.03 MV/cm (Figure 2C), respectively. A negligible $\sim 3.5\%$ error in the field estimation from the independent spectroscopic techniques illustrates that either of these noninvasive experimental methods can be used to predict the local electric field at the binding site of the protein.

Apparently, testosterone senses a large electric field at the binding site of BSA that is similar to that sensed by testosterone in a polar (10% acetonitrile/water) solvent. The electric fields in solution are homogeneous and increase with the overall solvent polarity. However, a nominally nonpolar protein matrix with surface charges can produce an inhomogeneous electric field similar to that in polar solvation environment required for the spectroscopic shift. In a recent work by Boxer and co-workers, an extremely large electric field was found to be exerted on the substrate by the oxyanion hole at the active site of an enzyme.¹⁴ Semiempirical polarity parameters provide only a qualitative understanding and fail to depict a microscopic description of the structure–function relation. The electrostatic field on the other hand serves as a quantitative and microscopic descriptor of local electrostatics and can be estimated from multiple choices of spectroscopic experiments as well as molecular dynamics (MD) simulations.

The implications of these results are manifold. We have shown that IR, UV/vis, or ¹³C NMR experimental techniques can be used to calibrate the local electric field within protein interiors. Choice of the spectroscopic technique depends on the concerned biological/chemical process. For example, $n-\pi^*$ absorption might be the favored technique to determine electric field for protein–ligand complexes where the absorption peak of the ligand can be monitored, as shown in this work. A long wavelength $n-\pi^*$ absorption of the ligand (as seen in testosterone) has less overlap with the protein absorption as compared with the overlap of the carbonyl stretch with the amide I protein IR band. Another inherent technical advantage of UV/vis spectroscopy over IR spectroscopy in the case of protein ligand complexes arises from the ease of subtracting the background protein spectra. The commonly used IR sandwich sample cells make it difficult to maintain the same path length in individual IR measurements. However, no such error from the reproducibility of the path length arises for the standard cuvettes (fixed path length) used for UV/vis absorption experiments. On the other hand, isotope editing (¹³C=O or ¹³C=¹⁸O) has been extensively used to isolate the C=O frequencies of a specific amino acid in a protein. In such cases, both IR as well as ¹³C NMR will be able to provide the local electric field within the protein interior. However, the electric field should be projected along the direction of the transition dipole of the amide normal mode which is not along the C=O bond as shown here for testosterone. These results are also significant from the computational viewpoint. When crystal structures are unavailable for protein–substrate complexes, molecular docking provides a snapshot of the orientation of the substrate with the biomolecule. However, multiple orientations of the ligand with respect to the receptor might be equally probable as predicted from docking studies. MD simulations of each of these conformers and subsequent electric field estimation when compared with the electric field predicted from the spectroscopic experiments can underpin the orientation of the substrate at the binding site and provide a molecular level picture of the biological process.

EXPERIMENTAL SECTION

Testosterone; bovine serum albumin; and solvents, such as dibutyl ether, tetrahydrofuran, valeronitrile, acetonitrile, and D₂O, were obtained from Sigma-Aldrich and used without further purification. UV absorption spectra were measured on a Shimadzu UV 3600 Plus spectrophotometer using a quartz cell

of 1 cm path length. The concentration of testosterone used for solvatochromic UV/vis absorption experiments was 5 mM. The ¹³C NMR spectra were obtained on a 400 MHz JEOL ECX NMR spectrometer. Here, peak positions were reported as the maximum value. IR absorption spectra were recorded on a FTIR-8300 (Shimadzu) spectrometer with 2 cm⁻¹ resolution at room temperature. For each sample (testosterone), ~60 μL of the sample solution was loaded into a demountable cell consisting of two windows (CaF₂, 3 mm thickness, Shenzen Laser), separated by a mylar spacer of 56 μm thickness. Testosterone was dissolved independently in aprotic solvents and protic binary aqueous mixtures (acetonitrile/water) such that the final concentration of liquid sample is 10 mM for the solvatochromic IR studies. More details about the IR spectroscopy are given in the [Supporting Information](#). The details of the MD simulations and electric field calculations are given in the [Supporting Information](#).

ASSOCIATED CONTENT

Supporting Information

The Supporting Information is available free of charge on the ACS Publications website at DOI: [10.1021/acs.jpcllett.6b00852](https://doi.org/10.1021/acs.jpcllett.6b00852).

Experimental methods and simulation protocol, spectroscopic correlations for other carbonyls, binding constant determination, and table for dielectric constants in various acetonitrile/water mixtures ([PDF](#))

AUTHOR INFORMATION

Corresponding Author

*E-mail: s.bagchi@ncl.res.in.

Notes

The authors declare no competing financial interest.

ACKNOWLEDGMENTS

This work was financially supported by CSIR-NCL (Grant MLP028126) and SERB, India (SR/S2/RJN-142/2012). Dr. Santosh Kumar Jha (CSIR-NCL) and Dr. Partha Hazra (IISER-Pune) are acknowledged for helpful discussions. P.D. thanks DST for INSPIRE fellowship.

REFERENCES

- (1) Warshel, A. Electrostatic Basis of Structure-Function Correlation in Proteins. *Acc. Chem. Res.* **1981**, *14*, 284–290.
- (2) Perutz, M. Electrostatic Effects in Proteins. *Science* **1978**, *201*, 1187–1191.
- (3) Sharp, K. A.; Honig, B. Electrostatic Interactions in Macromolecules: Theory and Applications. *Annu. Rev. Biophys. Biophys. Chem.* **1990**, *19*, 301–332.
- (4) Honig, B.; Nicholls, A. Classical Electrostatics in Biology and Chemistry. *Science* **1995**, *268*, 1144–1149.
- (5) Simonson, T. Macromolecular Electrostatics: Continuum Models and Their Growing Pains. *Curr. Opin. Struct. Biol.* **2001**, *11*, 243–252.
- (6) Warshel, A.; Papazyan, A. Electrostatic Effects in Macromolecules: Fundamental Concepts and Practical Modeling. *Curr. Opin. Struct. Biol.* **1998**, *8*, 211–217.
- (7) Macgregor, R. B.; Weber, G. Estimation of the Polarity of the Protein Interior by Optical Spectroscopy. *Nature* **1986**, *319*, 70–73.
- (8) Zhuang, Y.-D.; Chiang, P.-Y.; Wang, C.-W.; Tan, K.-T. Environment-Sensitive Fluorescent Turn-On Probes Targeting Hydrophobic Ligand-Binding Domains for Selective Protein Detection. *Angew. Chem., Int. Ed.* **2013**, *52*, 8124–8128.
- (9) Reichardt, C. Solvatochromic Dyes as Solvent Polarity Indicators. *Chem. Rev.* **1994**, *94*, 2319–2358.

- (10) Grunwald, E.; Winstein, S. The Correlation of Solvolysis Rates. *J. Am. Chem. Soc.* **1948**, *70*, 846–854.
- (11) Kosower, E. M. The Effect of Solvent on Spectra. I. A New Empirical Measure of Solvent Polarity: Z-Values. *J. Am. Chem. Soc.* **1958**, *80*, 3253–3260.
- (12) Langhals, H. Polarity of Binary Liquid Mixtures. *Angew. Chem., Int. Ed. Engl.* **1982**, *21*, 724–733.
- (13) de Dios, A.; Pearson, J.; Oldfield, E. Secondary and Tertiary Structural Effects on Protein NMR Chemical Shifts: An ab Initio Approach. *Science* **1993**, *260*, 1491–1496.
- (14) Fried, S. D.; Bagchi, S.; Boxer, S. G. Extreme Electric Fields Power Catalysis in the Active Site of Ketosteroid Isomerase. *Science* **2014**, *346*, 1510–1514.
- (15) Fried, S. D.; Bagchi, S.; Boxer, S. G. Measuring Electrostatic Fields in Both Hydrogen-Bonding and Non-Hydrogen-Bonding Environments Using Carbonyl Vibrational Probes. *J. Am. Chem. Soc.* **2013**, *135*, 11181–11192.
- (16) Renge, I. Solvent Dependence of $n-\pi^*$ Absorption in Acetone. *J. Phys. Chem. A* **2009**, *113*, 10678–10686.
- (17) Fried, S. D.; Boxer, S. G. Measuring Electric Fields and Noncovalent Interactions Using the Vibrational Stark Effect. *Acc. Chem. Res.* **2015**, *48*, 998–1006.
- (18) Deb, P.; Haldar, T.; Kashid, S. M.; Banerjee, S.; Chakrabarty, S.; Bagchi, S. Correlating Nitrile IR Frequencies to Local Electrostatics Quantifies Noncovalent Interactions of Peptides and Proteins. *J. Phys. Chem. B* **2016**, *120*, 4034–4046.
- (19) Kashid, S. M.; Bagchi, S. Experimental Determination of the Electrostatic Nature of Carbonyl Hydrogen-Bonding Interactions Using IR-NMR Correlations. *J. Phys. Chem. Lett.* **2014**, *5*, 3211–3215.
- (20) Boxer, S. G. Stark Realities. *J. Phys. Chem. B* **2009**, *113*, 2972–2983.
- (21) Augspurger, J. D.; Dykstra, C. E.; Oldfield, E. Correlation of Carbon-13 and Oxygen-17 Chemical Shifts and the Vibrational Frequency of Electrically Perturbed Carbon Monoxide: a Possible Model for Distal Ligand Effects in Carbonmonoxyheme Proteins. *J. Am. Chem. Soc.* **1991**, *113*, 2447–2451.
- (22) Haldar, T.; Bagchi, S. Electrostatic Interactions Are Key to C=O $n-\pi^*$ Shifts: An Experimental Proof. *J. Phys. Chem. Lett.* **2016**, *7*, 2270–2275.
- (23) Chanphai, P.; Vesper, A. R.; Bekale, L.; Berube, G.; Tajmir-Riahi, H. A. Transporting Testosterone and its Dimers by Serum Proteins. *J. Photochem. Photobiol., B* **2015**, *153*, 173–183.